Terahertz and Infrared Spectroscopy of Thin Film Cuprate Superconductors

Von der Fakultät Mathematik und Physik der Universität Stuttgart
zur Erlangung der Würde eines Doktors der Naturwissenschaften
(Dr. rer. nat.) genehmigte Abhandlung

Vorgelegt von

Robert David Dawson

aus Fullerton, Kalifornien, Vereinigte Staaten

Hauptberichter:	Prof. Dr. Bernhard Keimer
Mitberichter:	Prof. Dr. Martin Dressel
Prüfungsvorsitzende:	Prof. Dr. Maria Daghofer

Tag der Einreichung:	06.08.2021
Tag der mündlichen Prüfung:	06.10.2021

Max-Planck-Institut für Festkörperforschung
Universität Stuttgart

Stuttgart 2021

To my grandmother, Pauline Wendt

Contents

Abbreviations

1D	one-dimensional
2D	two-dimensional
3D	three-dimensional
AHNS	Ambegaokar-Halperin-Nelson-Siggia
ARPES	angle-resolved photoemission spectroscopy
ASOPS	asynchronous optical sampling
BCS	Bardeen-Cooper-Schrieffer
BKT	Berezinskii-Kosterlitz-Thouless
BSCCO	$Bi_2Sr_2CaCu_2O_{8+\delta}$
BWO	backward wave oscillator
CW	continuous wave
DyBCO	$DyBa_2Cu_3O_{7-\delta}$
FFT	fast Fourier transform
FROG	frequency resolved optical gating
FTIR	Fourier transform infrared spectrometer
FWHM	full-width at half-maximum
GDD	group delay dispersion
GL	Ginzburg-Landau
GVD	group velocity dispersion
KK	Kramers-Kronig
LSAT	$(LaAlO_3)_{0.3}(Sr_2AlTaO_6)_{0.7}$
LSCO	$La_{2-x}Sr_xCuO_4$
MBE	molecular beam epitaxy
MI	mutual inductance
NMR	nuclear magnetic resonance
OAP	off-axis parabolic mirror
***R*BCO**	$R Ba_2Cu_3O_{7-\delta}$, where R = *rare earth element*
RF	radio frequency
TTDS	terahertz time-domain spectroscopy
XRD	X-ray diffraction
YBCO	$YBa_2Cu_3O_{7-\delta}$

Zusammenfassung

Das Forschung an Quantenmaterialien hat eine grundsätzliche Erneuerung der Physik der kondensierten Materie eingeleitet. Diese neue Klasse von Materie—definiert als Materialsysteme mit Elektronenwellenfunktionen mit neuartigen verschränkten und topologischen Eigenschaften—bietet Forschern die Möglichkeit, sowohl reichhaltige neue Physik, als auch fortschrittliche Gerätefunktionalitäten zu verfolgen [1]. Während bestimmte konventionelle Festkörpersysteme, wie beispielsweise Halbleiter-Heterostrukturen, ebenfalls neuartige quantenmechanische Eigenschaften aufweisen können, leiten komplexe Quantenmaterialien ihre Eigenschaften typischerweise von starken Elektron-Elektron-Wechselwirkungen und eingeschränkter Dimensionalität ab. Neue Materialien und Zustände wie beispielsweise topologische Isolatoren, Graphen, Hochtemperatur-Supraleitung, neuartige Ladungs- und Stromordnungen sowie Spintexturen, die Skyrmionen genannt werden, wurden in das wissenschaftliche Lexikon aufgenommen und haben eigene Forschungsteilgebiete der hervorgebracht. Starke Elektronenkorrelationen und -verschränkungen implizieren auch, dass eine Vielzahl unterschiedlicher Eigenschaften aus ähnlichen Systemkonfigurationen hervorgehen können und dass durch die Feinabstimmung externer Parameter Systeme so manipuliert werden können, dass sie sehr unterschiedliche Ordnungsformen aufweisen. Solche Verhaltensmerkmale deuten direkt darauf hin, dass Quantenmaterialien einen Platz in der nächsten Generation technologischer Anwendungen und als Analoga zur Erforschung von Fragestellungen in anderen Bereichen der Physik finden werden.

Die Erforschung von Quantenmaterialien begann in den späten 1980er Jahren mit der Entdeckung der Hochtemperatur-Supraleitung in Perowskitverbindungen auf Kupferoxidbasis durch Georg Bednorz und Alex Müller [2]. Bei dem Versuch ein Verständnis der Eigenschaften sowohl des supraleitenden als auch des "normalen" Zustands oberhalb von T_c zu erlangen, wurde erkannt, dass die Kupferoxide durch elektronische Eigenschaften definiert werden, die nicht durch die Standardquantentheorie von Festkörpern erklärt werden können; eine Theorie, die einen der größten wissenschaftlichen Triumphe des 20. Jahrhunderts darstellt. Neben der Hochtemperatur-Supraleitung, deren Mechanismus nicht in die Bardeen-Cooper-Schrieffer-Theorie für konventionelle Supraleiter passte, wurde beobachtet, dass Kupferoxide eine Vielzahl anderer verblüffender Zustände beherbergen, wie Spindichtewellen, zwei- und dreidimensionale Ladungsordnung, einen ungewöhnlichen metallischen ("Strange Metal")-Zustand und eine mysteriöse "Pseudogap"-Phase, die keine bekannte Symmetrieform zu brechen scheint [3]. Alle diese Zustände sind in einem relativ kompakten Bereich des Phasenraums vorhanden und scheinen miteinander verflochten zu sein; manchmal sogar miteinander konkurrierend. Starke Elektron-Elektron-Wechselwirkungen und die quasi-zweidimensionale Kristallstruktur wurden als Schlüsselfaktoren für die Entstehung dieser unüblichen Eigenschaften identifiziert, so dass die Kupferoxide als

"stark korrelierte Elektronenmaterialien" bekannt wurden. Später, als viele weitere Familien solcher Materialien entdeckt wurden und die Bedeutung unkonventioneller Eigenschaften der Elektronenwellenfunktion allgemein anerkannt wurde, nahm diese Klasse von Systemen den einfacheren Namen "Quantenmaterialien" an. Jedoch bleibt das grundlegende Wesen der Elektron-Elektron-Wechselwirkungen wenig verstanden; nicht nur in den Kupferoxiden. Es wurden einige theoretische Erfolge beim Verständnis des stark korrelierten Elektronenproblems in einer Dimension (1D) und Quasi-1D erzielt, aber diese Lösungen sind nicht vollständig auf höhere Dimensionen übertragbar [4]. Es ist mittlerweile allgemein anerkannt, dass ein vollständiges Verständnis der Hochtemperatur-Supraleitung in den Kupferoxiden ein umfassendes Verständnis der stark korrelierten Elektronenphysik erfordert und umgekehrt. Diese Dissertation leistet durch präzise Messungen der optischen Eigenschaften dünner Kuprat-Schichten einen Beitrag zu diesem Forschungsfeld.

Die Messung der Submillimeter-Mikrowellen- und Infrarot-Eigenschaften konventioneller Supraleiter ist eine der Krönungen der modernen optischen Physik und Spektroskopie. Mitte der 1950er Jahre konnten Rolfe Glover und Michael Tinkham, die sowohl mit Mikrowellen-Resonanz- als auch mit ferninfraroten optischen Techniken arbeiteten, die Öffnung der optischen Energielücke bei niedrigen Frequenzen unterhalb von T_c in dünnen supraleitenden Metallschichten beobachten [5, 6]. Die Arbeit zeigte, dass die optische Energielücke genau 2Δ entspricht, wobei Δ die supraleitende Energielücke ist, und ebnete den Weg für das spätere Verständnis der mikroskopischen Theorie von Bardeen, Cooper und Schrieffer im Jahr 1957. Später bestätigten zusätzliche Messungen der Infrarotleitfähigkeit einen Reihe von Summenregeln für die Erhaltung des spektralen Gewichts beim Übergang vom Normalzustand in den supraleitenden Zustand [7] und lieferten direkte Messungen von Kohärenzeffekten in der elektromagnetischen Absorption [8]. Diese Ergebnisse, zusammen mit denen aus komplementären experimentellen Techniken, führten zu der voreiligen Annahme, dass Supraleitung ein weitgehend gelöstes Problem sei. Mit dem Aufkommen von Hochtemperatur-Supraleitung und Quantenmaterialien besteht erneut die Notwendigkeit, die niederenergetische Elektrodynamik des supraleitenden Zustands zu verstehen um Einblicke in den grundlegenden Mechanismus zu gewinnen. Anders als bei konventioneller Supraleitung stellt jedoch die Reihe an verflochtener und konkurrierender Ordnungszustände, die für stark korrelierte Elektronenmaterialien charakteristisch sind, eine weitere Herausforderung an die Forschung dar. Viele der in Kupferoxiden und anderen Quantenmaterialien relevanten Energieskalen liegen im Terahertz-Bereich des elektromagnetischen Spektrums [9], das historisch experimentell schwer zu erreichen war, da es in dem Frequenzbereich liegt, in dem herkömmliche elektronische und optische Quellen schwach sind. Darüber hinaus sorgen die starken Elektronenwechselwirkungen und die Verschränkung dafür, dass der niederenergetische Spektralbereich intrinsisch mit hochenergetischen Anregungen verbunden ist, die bei mehreren eV oder darüber liegen. In den letzten Jahren sind neue spektroskopische Techniken im Terahertz-Bereich durch die Kombination von Elementen elektronischer und optischer Quellen aufgekommen und diese haben nun den Entwicklungspunkt erreicht, an dem eine hohe Genauigkeit und Geschwindigkeit der Messung möglich ist [10]. Durch die Zusammenführung dieser hochmodernen Terahertz-Techniken mit anderen etablierten spektroskopischen Werkzeugen über einen weiten Energiebereich von sub-meV bis zu mehreren eV wird es möglich sein, die verschiedenen gekoppelten Energieskalen in Quantenmaterialien zu entflechten, um die Beziehung zwischen

Hochtemperatur-Supraleitung und anderer miteinander verknüpfter Ordnungen zu erforschen.

Eine weitere Herausforderung für die Untersuchung stark korrelierter Elektronenmaterialien war die Herstellung reiner und qualitativ hochwertige Proben. Viele der charakteristischen Eigenschaften korrelierter Elektronen- und Quantenmaterialien leiten sich von einer eingeschränkten Dimensionalität ab—das heißt, die Systeme sind dreidimensional, aber sie besitzen eine Kristallstruktur oder Probengeometrie, die in einer oder mehreren Dimensionen beschränkt ist. Traditionell, war die Herstellung von niederdimensionalen Systemen schwierig, da volatiler Sauerstoff für die kristalline Struktur von enormer Bedeutung ist und dessen Verlust dazu führt, dass Proben leicht zerfallen und kristalline Unordnung die elektronischen Zustände dramatisch verändert. In letzter Zeit haben Fortschritte in der Oxid-Molekularstrahlepitaxie (engl. "molecular beam epitaxy", kurz MBE) das Wachstum ultradünner Schichten mit präziser Kontrolle der Unordnung und hoher Qualität ermöglicht, die von anderen Techniken, wie zum Beispiel dem Laserstrahlverdampfen oder Magnetronsputtern nicht erzielt werden können [11]. Der Erfolg der Oxid-MBE ermöglicht nun den Zugang zu neuen Materialsystemen, wie z.B. ultradünnen Schichten. Kombiniert mit den Fortschritten der breitbandigen phasensensitiven Terahertzspektroskopie erlaubt dies eine genaue Untersuchung der Auswirkungen reduzierter Dimensionalität auf die stark korrelierte Elektronenphysik.

In dieser Frage wurden in der Tat bereits viele wissenschaftliche Fortschritte erzielt. Untersuchungen des optischen Verhaltens, der Infraroteigenschaften und der Summenregeln in den Kupferoxiden bilden ein zentrales Thema in der Erforschung der Hochtemperatur-Supraleitung, das bis in die späten 1980er und frühen 1990er Jahre zurückreicht. Ferninfrarot-Leitfähigkeitsmessungen waren der Schlüssel um die Bedeutung der quasi-zweidimensionalen Kristallstruktur für die elektronischen Eigenschaften festzustellen und trugen dazu bei, die teilweise Unterdrückung der für die sog. Pseudogap-Phase charakteristischen Zustandsdichte zu identifizieren. Die starke Kopplung in Hochtemperatur-Supraleitern lässt jedoch vermuten, dass die herkömmlichen optischen Summenregeln in den Kupferoxiden nicht eingehalten werden, da durch die hohen Energieskalen der Korrelationseffekte hoch- und niederenergetische optische Anregungen stark verflochten sind. Dies hat zu Theorien der unkonventionellen Supraleitung geführt, die auf der Idee einer minimalen kinetischen Energie basieren, bei dem das spektrale Gesamtgewicht bei niedrigen Energien im supraleitenden Zustand gegenüber dem Normalzustandswert [12, 13] ansteigt. Mehrere Gruppen haben Studien basierend auf optischer Breitbandspektroskopie durchgeführt, um dieses Problem zu lösen [14–16], aber die berichteten Ergebnisse sind abhängig von Gittereffekten, dem subtilen Zusammenspiels zwischen verschiedenen Kopplungsparametern und dem Spektralbereich, über den die Antwortfunktionen gemessen wird [17]. Um diese Fragen vollständig zu beantworten, sind spektroskopische Breitbandmessungen erforderlich, die sowohl amplituden- als auch phasenempfindlich sind, um Energien unter $\sim$1 meV und über mehreren eV zu erreichen und die Änderungen des spektralen Gewichts der optischen Leitfähigkeit mit der Bildung des supraleitenden Zustands ins Verhältnis zu setzten.

Spektroskopische Methoden haben auch bereits einige Ergebnisse bei der Untersuchung der reduzierten Dimensionalität in den Kupferoxiden erzielt. Im ersten Jahrzehnt nach der Entdeckung der Hochtemperatur-Supraleitung halfen Messungen der magnetischen Eindringtiefe im Submillimeter-, Mikrowellen- und Radiobereich,

um die Supraleitung in Volumenproben der 3D-XY-Universalitätsklasse zuzuordnen [18, 19]. Bei Annäherung an den zweidimensionalen Grenzfall sollten Fluktuationen der 2D-XY-Universalitätsklasse zusammen mit dem charakteristischen Berezinskii-Kosterlitz-Thouless-Übergang auftreten, bei dem Wirbel und magnetische Flusslinien sich spontan lösen und vermehren, wodurch die supraleitende Elektronendichte abrupt auf Null getrieben wird. Während mehrere Studien Anzeichen des Berezinskii-Kosterlitz-Thouless-Übergangs in der supraleitenden Elektronendichte einiger Kupferoxide [20–22] gefunden haben, beschränken sich die berichteten Messungen überwiegend auf die stark unterdotierte Seite des Phasendiagramms, wo quantenkritische Fluktuationen in der Nähe des unterdotierten quantenkritischen Punktes die Kosterlitz-Thouless-Physik verschleiern. Experimente mit optimal dotierten und überdotierten Kupferoxiden sind erforderlich, wurden jedoch aufgrund der Nichtverfügbarkeit qualitativ hochwertiger Dünnschichtproben noch nicht durchgeführt. Solche Messungen würden die Möglichkeit eröffnen, die Entwicklung verschiedener Parameter, die für das Lösen der Wirbel entscheidend sind, über das gesamte Phasendiagramm zu verfolgen und einen Bereich zwischen quasi-1D und 3D erschließen, mit dem Modelle stark korrelierter Elektronensysteme getestet werden können.

Die in dieser Dissertation präsentierten Ergebnisse konzentrieren sich auf breitbandige phasensensitive spektroskopische Messungen von ultradünnen $DyBa_2Cu_3O_{7-\delta}$-Supraleiterfilmen, die das gesamte elektromagnetische Spektrum vom submillimetermikrowellen bis zum UV Bereich (0.1 meV bis 6.5 eV) abdecken. Die Analyse dieser Ergebnisse zielt darauf ab, sowohl die Fragen der optischen Summenregeln in Kupferoxid-Hochtemperatur-Supraleitern als auch das Verhalten von nahezu optimal dotierten Kupferoxiden im 2D-Limit durch das "Schließen der Terahertz-Lücke" zu beantworten. Hierbei ist besonders die Phasensensitivität dieser Messungen hervorzuheben; alle hier verwendeten spektroskopischen Techniken messen sowohl den Real- als auch den Imaginärteil der komplexen dielektrischen Funktion, wodurch sowohl die dissipative als auch die induktive Reaktion unabhängig voneinander extrahiert werden können, ohne dass Modellannahmen oder Kramers-Kronig-Beziehungen erforderlich sind. Obwohl bereits verschiedene phasenempfindliche Techniken verwendet wurden, um sowohl Volumen- als auch Dünnschicht-Kupferoxide über nahezu das gesamte Spektrum zu messen, konzentrieren sich die bisherigen Ergebnisse in der Literatur typischerweise auf stückweise Analysen oder Messungen nur in einem Teilbereich des optischen Spektrums. Die Stärke der hier vorgestellten Versuchstechnik besteht darin, dass wir erstmals die Antwortfunktion lückenlos über das gesamte Spektrum und der gleichen Proben bestimmt haben. Wir kombinieren diese Technik mit Dünnschichtproben von extrem hoher Qualität, die mit einem kürzlich entwickelten, hochmodernen Oxid-MBE-System synthetisiert wurden.

In Kapitel 2 stellen wir den wissenschaftlichen Hintergrund vor, welcher der in unseren Ergebnissen behandelten Physik zugrunde liegt. Nach einer kurzen Einführung in die strukturellen Details, physikalischen Eigenschaften und das Phasendiagramm der Hochtemperatur-Kupferoxid-Supraleiter wenden wir uns der Physik supraleitender Fluktuationen zu. Es folgt eine detaillierte Diskussion der theoretischen Grundlagen für das 2D-XY-Modell, den Berezinskii-Kosterlitz-Thouless Flusswirbel-Entkopplungsübergang und das 2D Coulomb-Gas. Die Ausweitung der Theorie der Flusswirbelentkopplung auf 2D-Supraleiter unterscheidet sich von ihrer Manifestation in neutralen 2D-Suprafluiden, daher widmen wir mehrere Seiten einer Diskussion des Effekts in konventionellen Supraleitern, um einen Bezugspunkt zu bieten, bevor

wir zu einer detaillierten Bestandsaufnahme der aktuellen Forschung zum Berezinskii-Kosterlitz-Thouless-Übergang in Kupferoxid-Supraleitern übergehen. Schließlich behandeln wir kurz die wichtigsten Punkte der Ferrell-Glover-Tinkham-Summenregel für Supraleiter und ihren Zusammenhang mit der Hochtemperatur-Supraleitung.

Kapitel 3 beschreibt die zur Datenakquirierung und -analyse eingesetzten experimentellen Methoden. Drei separate experimentelle Ansätze wurden verwendet: quasioptische Submillimeter-Interferometrie, Terahertz-Zeitbereichsspektroskopie und spektroskopische Ellipsometrie vom fernen Infrarot bis UV. Für quasioptische Interferometriemessungen im Submillimeterbereich wurde ein Mach-Zehnder-Interferometer mit einem Rückwärtswellenoszillator als Quelle verwendet. Die Terahertz-Zeitbereichsspektroskopie wurde mit einem hochauflösenden Hochgeschwindigkeitsspektrometer von Laser Quantum GmbH durchgeführt. Dieses Spektrometer basiert auf der asynchronen optischen Abtastdetektionstechnik und bietet ein Messfenster von 1 ns und eine Zeitauflösung von 20 fs mit einer spektralen Bandbreite von 1 GHz bis 20 THz. Spektroskopische Ellipsometrie-Messungen wurden an drei separaten Instrumenten erhalten; die Ferninfrarotmessungen wurden an der IR-1-Beamline des KARA-Synchrotrons am Karlsruher Institut für Technologie durchgeführt, Mittel- und Nahinfrarot an einem nahezu identischen In-House-Setup am Max-Planck-Institut für Festkörperforschung in Stuttgart, und an einem kommerziellen VASE-Spektrometer (J.A. Woollam Co.) für sichtbares bis UV-Licht. Dieses Kapitel enthält eine detaillierte Diskussion der technischen Aspekte und der Datenanalyse sowohl der quasioptischen Submillimeter-Interferometrie als auch der Terahertz-Zeitbereichsspektroskopie, sowie einen Unterabschnitt über die Auflösungsgrenzen, denen das Terahertz-Zeitbereichsmessverfahren unterliegt. Ein kurzer Überblick über die spektroskopische Ellipsometrie ist ebenfalls enthalten.

Der Hauptteil unserer experimentellen Ergebnisse wird in Kapitel 4 präsentiert. Die Ergebnisse werden konzeptionell in zwei verwandte Themenbereiche unterteilt. Zuerst wird in den Abschnitten 4.1–4.3 die Gültigkeit der Ferrell-Glover-Tinkham-Summenregel und des Zwei-Fluid-Modells in ultradünnen $DyBa_2Cu_3O_{7-\delta}$ Filmen analysiert. Dies beginnt mit einer detaillierten Untersuchung der Qualität und des Unordnungsniveaus in einer Reihe von Filmen mit Dicken von 7 bis 60 Elementarzellen. Obwohl in den Filmen definitiv Unordnung vorhanden ist, stellen wir fest, dass das Unordnungsniveau für alle Filme in der Serie moderat bleibt und deutlich unter den stark ungeordneten Bereich fällt, bei dem quantenkritische Fluktuationen beginnen, die Phase des supraleitenden Ordnungsparameters zu beeinflussen. Als nächstes wird die gemessene optische Leitfähigkeit als Funktion der Temperatur dargestellt. Diese Daten werden dann verwendet, um eine Kramers-Kronig-Konsistenzprüfung der unabhängig gemessenen komplexen dielektrischen Funktion durchzuführen. Die Ergebnisse dieses Verfahrens zeigen, dass die Ferrell-Glover-Tinkham-Summenregel und das Zwei-Fluid-Modell im Dünnfilm $DyBa_2Cu_3O_{7-\delta}$ mit einem Fehler von 0,2% erfüllt sind. Zweitens wird in den Abschnitten 4.4–4.6 das Verhalten der Suprafluiddichte in den Filmen bei Annäherung an die 2D-Grenze untersucht. Die Gültigkeit der Ferrell-Glover-Tinkham-Summenregel ermöglicht es uns, die Suprafluiddichte als Funktion der Temperatur mit sehr hoher Genauigkeit zu extrahieren, da die Summenregel das integrierte Gesamtspektralgewicht anstelle der Spektralantwort bei einer einzelnen Frequenz behandelt. Wir stellen fest, dass die Temperaturabhängigkeit der Suprafluiddichte in Proben mit einer Dicke von 10 Elementarzellen und mehr einer "universellen" Temperaturabhängigkeit folgt, die für das kritische 3D-XY-Verhalten charakte-

ristisch ist. Auf der anderen Seite beobachten wir unterhalb von 10 Elementarzellen eine erhöhte Steigung der temperaturabhängigen Suprafluiddichte bei Annäherung an T_c von unten. Wir argumentieren, dass dieses Verhalten auf das Vorhandensein eines Berezinskii-Kosterlitz-Thouless-Flusswirbel-Entkopplungsübergangs in nahezu optimal dotierten, ultradünnen $DyBa_2Cu_3O_{7-\delta}$-Filmen hinweist. Messungen des Effekts in Gegenwart eines transversalen externen Magnetfelds scheinen qualitativ konsistent mit der Abbildung des 2D-XY-Modells auf das 1D-Sinus-Gordon-Problem zu sein, bei dem sich die Wirbelkernenergie aufgrund des Vorhandenseins des Feldes verschiebt. Schließlich berichten wir über unsere Messungen zur Skalierung des Homes-Gesetzes in ultradünnen $DyBa_2Cu_3O_{7-\delta}$ Filmen. Unsere Leitfähigkeitsmessungen legen nahe, dass das Homes-Gesetz in dünnen Kupferoxidschichten tatsächlich eingehalten wird. Wir stellen jedoch fest, dass die Skalierungskonstante für die Filme um den Faktor 3 kleiner ist als die Skalierungskonstante in massiven Supraleitern. Aus diesen Ergebnissen argumentieren wir, dass in allen Proben eine nicht-supraleitende, $\sim$4 Elementarzellen dicke Schicht an der Substratgrenzfläche verbleibt, welche jedoch nicht einfach mit epitaktisch induzierten Sauerstofffehlstellenverteilungen zusammenhängt. Die vollständige Natur dieser nicht-supraleitenden Schicht bleibt unbekannt, aber wir geben einige Spekulationen über ihren Ursprung.

Schließlich fasst Kapitel 5 unsere Ergebnisse kurz und bündig zusammen. Die Anhänge enthalten detailliertere Informationen zu experimentellen Details und zum Aufbau unseres Terahertz-Zeitbereichsspektrometers.

Chapter 1

Introduction

1.1 General Overview

The emergence of quantum materials has ushered in a great revolution in modern condensed matter physics. This new class of matter—defined as material systems that possess electron wavefunctions with novel entanglement and topological properties—offers researchers the opportunity to pursue both rich new physics and advanced device functionalities alike [1]. While certain conventional solid state systems such as semiconductor heterojunctions and classic superconductors can also be said to harbor novel quantum-mechanical properties, quantum materials typically derive their traits from strong electron-electron interactions and constrained dimensionality. Furthermore, they are characterized by what Philip W. Anderson famously termed "more is different:" the macroscopic properties of quantum materials are more than simply the sum of their parts, meaning that a constructionist approach from elementary principles is not sufficient to properly quantify and explain their physics as a whole [23]. The fascinating array of effects that are observed in quantum materials are examples of *emergent phenomena* that reflect new kinds of broken symmetry that only become evident when many-body systems are brought together in specific ways. New objects and states such as topological insulators, graphene, high-temperature superconductivity, novel types of charge and current ordering, and spin textures called skyrmions have entered the scientific lexicon and spawned entire research subfields of their own. Strong electron correlations and entanglement also imply that a wide variety of different properties are likely to emerge from similar system configurations, and that by tuning external parameters by only a small amount systems can be manipulated to exhibit vastly different forms of order. Such traits immediately suggest that quantum materials will find a place in the next generation of technological applications and as analogs to explore the physics of complicated systems in other branches of physics.

Research on quantum materials was kicked off in the late 1980's with the discovery of high-temperature superconductivity in copper-oxide based perovskite compounds [2]. At the time, the importance of the discovery of a new type of superconductivity was immediately understood, but the more far-reaching implications of the compounds' electronic structure beyond superconductivity only came to be grasped by the scientific community some time later. In the quest to catalog and understand the properties of both the superconducting state and the "normal" state above T_c, it was realized that the copper oxides are defined by electronic properties that cannot be ex-

plained by the standard quantum theory of solids, a theory that represented one of the greatest scientific triumphs of the twentieth century. In addition to high-temperature superconductivity, whose mechanism did not fit the Bardeen-Cooper-Schrieffer theory for conventional superconductors, copper oxides were observed to host a wide variety of other perplexing states, such as spin density waves, two and three dimensional charge order, a "strange metal" state, and a mysterious "pseudogap" phase that does not appear to break any known form of symmetry [3]. Additionally, all these states are found in a relatively compact region of phase space and appear to be intertwined, sometimes even competing with one another. Strong electron-electron interactions and the quasi-two-dimensional crystal structure were identified as the key factors giving rise to the odd properties, so the copper oxides became known as "strongly correlated electron materials." Later, when many more families of strongly correlated electron materials were discovered and the importance of unconventional properties of the electron wavefunction became more widely appreciated, this class of systems took on the simpler name "quantum materials." However, the fundamental nature of the electron-electron interactions remains poorly understood. Some theoretical successes have been achieved in understanding the strongly correlated electron problem in 1D and quasi-1D but these solutions are not fully generalizable to higher dimensions [4]. It has now become widely accepted that a complete understanding of high-temperature superconductivity in the copper oxides requires a full understanding of strongly correlated electron physics, and vice versa.

By contrast, the study of electricity, magnetism, and the optical properties of materials is a very old science. The electric attraction of chaff to amber and the magnetic force between lodestone and iron were known to the ancients, and through the works of Plato, Aristotle, Euclid, Theon, and Ptolemy they were able to deduce the rectilinear propagation of light, the law of reflection, and the existence of refraction [24]. In fact, our modern words to describe electricity and magnetism originate from the ancient Greek words for amber and lodestone: ἤλεκτρον, *ēlektron*, and μαγνῆτις λίθος, *magnêtis lithos*. The study of optics can be traced back to the Islamic scholar Ibn al-Haytham in the early eleventh century and English Franciscan Roger Bacon in the thirteenth century [25], although it was not until the late nineteenth century when the modern science of optics took anything close to its present form. With the completion of the quantum theory of solids in the first part of the twentieth century, research on optical properties of materials flourished: measurements of the response functions of all kinds of materials across nearly the full electromagnetic spectrum from radio to X-ray matched the theory remarkably well and enabled rapid scientific progress in many fields, from astrophysics, to solid state physics, to biology, greatly expanding our understanding of the fundamental mechanisms of the physical world. Technological progress in such diverse applications as telecommunications, computing, medicine, remote sensing, and security soon followed. It is only natural, then, to turn the techniques of the study of optical properties to superconductivity and quantum materials.

The measurement of the submillimeter-microwave and infrared properties of conventional superconductors is one of the crowning achievements of modern optical physics and spectroscopy. In the mid-1950's, working with both microwave cavity resonance and far-infrared optical techniques, Rolfe Glover and Michael Tinkham were able to observe the opening of the optical gap at low frequencies below T_c in thin superconducting metal films [5,6]. The work showed that the optical gap is equivalent

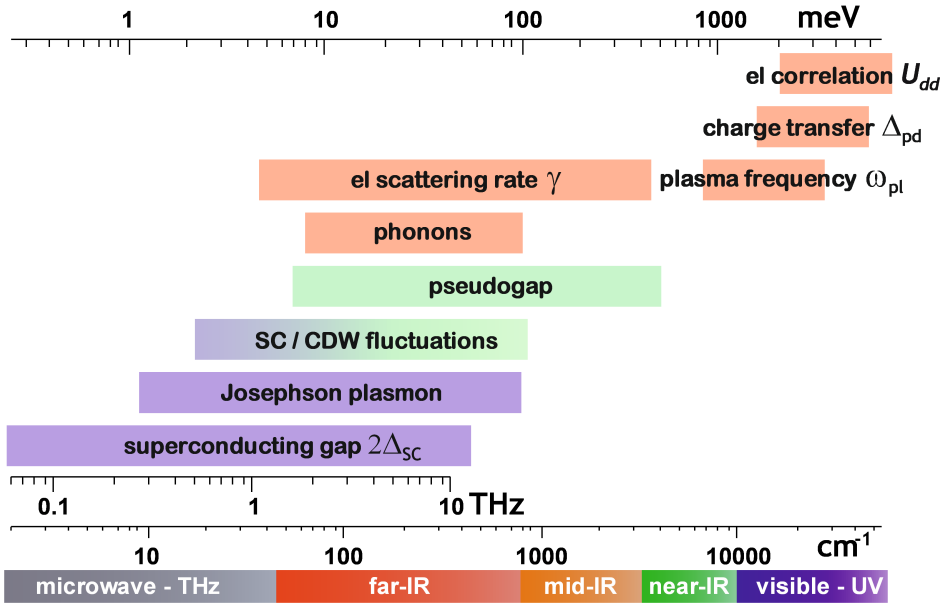

Figure 1.1 Strongly correlated electron materials harbor an array of intertwined and competing forms of order that gives rise to a number of energy scales. Many of these energy scales are found in the terahertz portion of the electromagnetic spectrum, but it is common to find relevant excitations as high as several eV or above. The experimental challenge in untangling these intertwined orders involves finding simple ways to relate changes in the spectrum at low energies to changes that occur at energies several magnitudes higher.

to exactly 2Δ, where Δ is the superconducting energy gap, and paved the way for the subsequent understanding of the microscopic theory by Bardeen, Cooper, and Schrieffer in 1957. Later, additional measurements of the infrared conductivity confirmed a set of sum rules for the conservation of spectral weight upon crossing over from the normal state to the superconducting state [7] and provided direct measurements of coherence effects in the electromagnetic absorption [8]. These results, along with those from complementary experimental techniques, led to the premature belief that superconductivity was a largely solved problem. With the advent of high-temperature superconductivity and quantum materials there is again the need to understand the low energy electrodynamics of the superconducting state in order to gain insight into the fundamental mechanism. But, unlike in the case of conventional superconductivity, the array of intertwined and competing orders that are characteristic of strongly correlated electron materials presents an unfortunate roadblock. Many of the energy scales relevant in the copper oxides and other quantum materials lie in the terahertz portion of the electromagnetic spectrum (see Fig. 1.1) [9], which has historically been difficult to reach experimentally because it lies in the frequency range where traditional electronic and optical sources are weak. Furthermore, the strong electron interactions and entanglement ensures that the low energy response is intrinsically linked to high energy excitations that lie at several eV or above. In recent years new spectroscopic techniques have emerged in the terahertz range by combining elements of both electronic and optical sources, and these have now reached the point of development where high accuracy and speed of measurement are possible [10]. By merging these state-of-the-art terahertz techniques with other established spectroscopic tools

across a wide energy range from sub-meV to several eV it will be possible to disentangle the various coupled energy scales in quantum materials in order to explore the relationship between high-temperature superconductivity and other intertwined orders.

Another challenge for the study of strongly correlated electron materials has been the ability to obtain suitably clean and high quality samples. Many of the characteristic properties of correlated electron and quantum materials derive from constrained dimensionality—that is, the systems are three-dimensional but they possess crystal structure or sample geometry that frustrate one or several of these dimensions. Examples of such systems include layered materials, thin films, nanowires, and quantum dots, where upon each reduction in dimensionality additional physical properties emerge. The difficulties for fabricating such materials are two-fold. First, there is the question of how to grow dimensionally confined samples while maintaining the proper crystallographic structure. Correlated electron materials such as the copper oxides are typically constructed from complicated unit cells that contain many substructure components and elemental species, such as metal-oxide layers, charge reservoir slabs, oxygen chains or tetrahedra, and rare earth ions. Successfully assembling all components in the correct order into a structure that is only a few unit cells across must compete against the tendency of the samples to degrade or chemically break down as the system attempts to find its most energetically favored configuration. Second, samples of reduced dimensionality are highly susceptible to disorder because of the outsized influence of edge and surface effects compared to the bulk properties. This is further compounded by the intrinsic nature of correlated electron materials; the intertwining and competition between various forms of order and strong electron interactions implies that small changes in disorder level can easily push the system from one state into another. As a result, fabrication techniques must find a way to reduce disorder stemming from not only extrinsic defects and chemical species, but also the formation of structural impurities and oxides that are composed of the same species as the desired material. On this front atomic layer-by-layer oxide molecular beam epitaxy (ALL-MBE) has made great strides in the past decade [11]. Unlike other growth techniques such as pulsed laser deposition or reactive magnetron sputtering, ALL-MBE takes advantage of low deposition energies and precise layer control to routinely achieve pristine layers as thin as a single monolayer. In fact, ALL-MBE grown $La_{1-x}Sr_xCuO_4$ films have been used to demonstrate that high-temperature superconductivity can survive in a single CuO_2 plane [26]. The success of oxide MBE now allows new material regimes to be accessed, and coupling ultrathin films grown by this method with the advances in terahertz and wide band phase sensitive spectroscopy opens the door to precise investigation of the effects of reduced dimensionality on strongly correlated electron physics.

Much scientific progress has indeed already been made on these issues. Studies of the optical response, infrared properties, and sum rules in the copper oxides constitute a central theme in high-temperature superconductivity research, stretching back to the late 1980's and early 1990's. Far-infrared conductivity measurements were key to establishing the importance of the quasi-2D crystal structure for the electronic properties and were instrumental in identifying the partial suppression of the density of states characteristic of the pseudogap phase. In the absence of a comprehensive theory of high-temperature superconductivity, scaling relationships were optically investigated between various physical quantities across the phase diagram.

One of these, known as Homes' law, established a linear relationship between the density of superconducting electrons and the product of T_c with the dc conductivity: $\rho_{s0} \propto \sigma_{\rm dc} T_c$ [27]. Interestingly, both copper oxides and conventional superconductors were found to obey this relationship with the same proportionality constant irrespective of their doping or disorder levels. Since the conventional superconductors are known to obey the optical conductivity sum rules, Homes' law seems to suggest that the high-temperature superconductors do too. However, the density of superconducting electrons in some copper oxides is nearly four orders of magnitude smaller than that in conventional metallic superconductors, which implies that the T_c is large in high-temperature superconductors because their electronic dissipation approaches the largest values allowed by quantum mechanics [28]. Furthermore, the strong coupling nature of high-temperature superconductivity raises the prospect that the conventional two-fluid model and optical sum rules are not obeyed in a simple way in the copper oxides, because the intertwining of various energy scales allows the possibility that optical spectral weight may redistribute between very high and very low energies. This has led to theories of unconventional superconductivity based on the idea of a kinetic energy saving mechanism, where the total spectral weight at low energies in the superconducting state increases compared to the normal state value [12, 13]. Several groups have performed wide band optical spectroscopy studies to settle this issue [14–16], but the reported results are sensitive to lattice effects, the nature of the fine interplay between coupling parameters, and the spectral range over which the response functions are measured [17]. Far-infrared spectroscopic experiments have also found that lattice effects and electron-phonon interactions may give rise to low energy modes at frequencies below 100 cm^{-1} that complicate the analysis of the optical data due to the accumulation of appreciable low frequency spectral weight, despite these modes not strongly affecting either the density of superconducting electrons or T_c [29]. Unfortunately, traditional far-infrared reflectivity techniques are not well-suited to exploring these low energy electrodynamics because they require model dependent assumptions in the limit $\hbar\omega \rightarrow 0$ and Kramers-Kronig transformations in order to extract the full complex conductivity. Rather, measurements below 100 cm^{-1} are needed that are fully amplitude and phase sensitive in order to relate the evolution of the spectral weight to meV or sub-meV excitations. Questions regarding the validity of the optical sum rules, kinetic energy saving mechanism, and the nature of the scaling laws in thin films will then be able to be accurately explored.

Spectroscopic techniques have also already borne fruit in the study of reduced dimensionality in the copper oxides. In the first decade after the discovery of high-temperature superconductivity, measurements of the magnetic penetration depth in the submillimeter, microwave, and radio portions of the spectrum were vital for assigning the superconductivity in bulk samples to the 3D-XY universality class [18,19]. This universality class, which high-temperature superconductivity shares with other types of materials such as certain magnetic systems, establishes that the critical scaling behavior obeys specific material independent trends; in particular, the superconducting electron density is proportional to $T^{2/3}$ near T_c. Upon approaching the two-dimensional limit fluctuations belonging to the 2D-XY universality class should appear along with the characteristic Berezinskii-Kosterlitz-Thouless transition, where vortices and magnetic flux lines spontaneously unbind and proliferate, driving the superconducting electron density to zero with different scaling behavior. Such 2D-XY fluctuations have only been observed in optimally doped copper ox-

ide samples at thicknesses less than 100 nm in $Bi_2Sr_2CaCu_2O_{8+\delta}$ [20]. It has been shown that 2D-XY fluctuations are more visible in underdoped copper oxides where the superconducting electron density is dramatically smaller [21], but near the underdoped quantum critical point where $T_c \to 0$ quantum critical fluctuations place the superconducting state into the $(3+1)$D-XY universality class and obscure signatures of the Berezinskii-Kosterlitz-Thouless transition [20, 22]. Recently, theoretical work mapping the 2D-XY model to the 1D sine-Gordon problem with variable vortex core energy and T_c inhomogeneity has been performed and successfully fits experimental data in both conventional superconductors and heavily underdoped copper oxides [30–33]. However, similar application of the sine-Gordon model of 2D-XY fluctuations to copper oxides in the optimally doped and overdoped regimes has not yet been carried out, largely due to the inavailability of data that definitively display signatures of 2D vortex unbinding. Quality measurements in these doping ranges have been difficult to obtain because sample disorder and dynamical vortex pinning due to fixed probe frequencies (such as those in mutual inductance experiments) tends to strongly obscure signatures of 2D fluctuations, and in samples where the superconducting electron density is large the fluctuation regime is expected to exist only in a narrow temperature range below T_c. More accurate studies of 2D superconductivity in optimally doped and overdoped copper oxides will require pristine thin film samples with a higher degree of control over sample disorder, as well as measurements of the superconducting electron density carried out across a broad range of frequencies to avoid issues related to dynamical vortex pinning. Such measurements would enable the possibility to chart the evolution of the vortex core energy and couplings across the full phase diagram, and offer an intermediate case between quasi-1D and 3D by which to test models of strongly correlated electron systems.

The study of the fundamental phenomena and processes in high-temperature superconductors and the dramatic interplay between the myriad forms of order in strongly correlated electron materials promises to allow us to move beyond simply understanding the physics of this class of matter to manipulating the phenomena and engineering *functional* quantum materials. Studies of the effects of constrained dimensionality and optical properties lie at the core of these future directions. The devices of tomorrow will most likely take advantage of multiple advanced properties—topology, dimensionality, novel phases, optical response, strain, etc.—to achieve multifaceted capabilities. The strong intertwining of different orders and the interaction between various effects enable the possibility to exploit these traits for functionalities as diverse as more efficient logic gates, versatile quantum sensors, better linkages to optical communications, and even completely new computing paradigms such as quantum computing.

1.2 Scope of the Thesis

The results presented in this thesis focus on wide band phase sensitive spectroscopic measurements of ultrathin $DyBa_2Cu_3O_{7-\delta}$ superconducting films that span the full electromagnetic spectrum from the submillimeter-microwave to UV (0.1 meV to 6.5 eV). The analysis of these results seeks to address the salient issues regarding both the optical sum rules in copper oxide high-temperature superconductors and the behavior of the same in the 2D limit by "closing the terahertz gap" to directly relate changes

of the low energy electodynamics between the superconducting and normal states to shifts of the optical spectral weight at higher energies. The *phase sensitive* nature of these measurements must be emphasized; all spectroscopic techniques used here measure both the real and imaginary part of the complex dielectric function, which allows both the dissipative and inductive response to be extracted independently without need for model assumptions or Kramers-Kronig relations. While various phase sensitive techniques have indeed been used before to measure both bulk and thin film copper oxides across nearly the full spectrum, the prior results given in the literature typically focus on piecemeal analysis or measurements in only a subset of our spectral range. The strength of the experimental technique presented here is that, for the first time, we are able to obtain the response functions across the full spectrum, without gaps, of the same samples. We pair this technique with thin film samples of ultra high quality grown by a recently developed, state-of-the-art ALL-MBE system.

In Chapter 2 we introduce the scientific background that underpins the physics treated in our results. After a brief introduction to the structural details, physical properties, and phase diagram of the high-temperature copper oxide superconductors, we turn our attention to the physics of superconducting fluctuations. A detailed discussion of the theoretical basis for the 2D-XY model, Berezinskii-Kosterlitz-Thouless vortex unbinding transition, and 2D Coulomb gas is given. The extension of the theory of vortex unbinding to 2D superconductors differs from its manifestation in neutral 2D superfluids, so we dedicate several pages to a discussion of the effect in conventional superconductors to provide a point of reference before moving on to a detailed survey of the status of current research on the Berezinskii-Kosterlitz-Thouless transition in copper oxide superconductors. Finally, we briefly treat the key points of the Ferrell-Glover-Tinkham sum rule for superconductors and how it relates to high-temperature superconductivity.

Chapter 3 describes the experimental technique used to obtain and analyze the data. Three separate experimental approaches were used: submillimeter quasioptical interferometry, terahertz time-domain spectroscopy, and far-infrared to UV spectroscopic ellipsometry. Submillimeter quasioptical interferometry measurements were obtained by means of a Mach-Zehnder interferometer with a backward wave oscillator as the source. Terahertz time-domain spectroscopy was performed with a high resolution, high speed spectrometer purchased from Laser Quantum GmbH. This spectrometer, based on the asynchronous optical sampling detection technique, boasts a 1 ns measurement window and a 20 fs time resolution, with a spectral bandwidth spanning 1 GHz to 20 THz. Spectroscopic ellipsometry measurements were obtained on three separate instruments; the far-infrared measurements were performed at the IR-1 beamline of the KARA synchrotron at the Karlsruhe Institute of Technology, mid- and near-infrared on a nearly identical in-house setup at the Max Planck Institute for Solid State Research in Stuttgart, and a commercial visible-to-UV VASE purchased from J. A. Woollam, Co. This chapter contains detailed discussion of the technical aspects and data analysis in both submillimeter quasioptical interferometry and terahertz time-domain spectroscopy, as well as a subsection on the resolution limits inherent in the terahertz time-domain measurement process. A brief overview of spectroscopic ellipsometry is also included.

The main body of our experimental results are presented in Chapter 4. The results are conceptually separated into two related themes. First, as discussed in Sections 4.1–4.3, the validity of the Ferrell-Glover-Tinkham sum rule and two-fluid model in

ultrathin $DyBa_2Cu_3O_{7-\delta}$ films are analyzed. This begins with a detailed investigation of the quality and disorder level in a series of films with thicknesses varying from 7 to 60 unit cells. While disorder is certainly present in the films, we find that the disorder level for all films in the series remains moderate and falls well below the highly disordered regime where quantum critical fluctuations begin to affect the phase of the superconducting order parameter. Next, the measured optical conductivity as a function of temperature is presented. This data is then used to perform a Kramers-Kronig consistency check of the independently measured complex dielectric function. The results of this procedure indicate that the Ferrell-Glover-Tinkham sum rule and two-fluid model are satisfied in thin film $DyBa_2Cu_3O_{7-\delta}$ to within 0.2% error. Second, an exploration of the behavior of the superfluid density in the films upon approaching the 2D limit is given in Sections 4.4–4.6. The validity of the Ferrell-Glover-Tinkham sum rule allows us to extract the superfluid density to very high accuracy as a function of temperature because the sum rule treats the integrated total spectral weight rather than the spectral response at a single frequency. We find that the temperature dependence of the superfluid density in samples 10 unit cells thick and greater follows a "universal" temperature dependence that is characteristic of 3D-XY critical behavior. On the other hand, below 10 unit cells we observe a steepening of the superfluid density temperature dependence upon approaching T_c from below. We argue that this behavior is indicative of the presence of a Berezinskii-Kosterlitz-Thouless vortex unbinding transition in near optimally doped, ultrathin $DyBa_2Cu_3O_{7-\delta}$ films. Measurements of the effect in the presence of a transverse external magnetic field appear to be qualitatively consistent with the mapping of the 2D-XY model to the 1D sine-Gordon problem, where the vortex core energy shifts due to the presence of the field. Finally, we report our measurements relating to Homes' law scaling in ultrathin film $DyBa_2Cu_3O_{7-\delta}$. Our conductivity measurements suggest that Homes' law is indeed obeyed in thin copper oxide films. However, we find that the scaling constant for the films is smaller than the scaling constant in bulk superconductors by a factor of 3. From these findings we argue that a non-superconducting, $\sim$4 unit cell thick layer at the substrate interface remains in all samples, but which is not simply related to epitaxially induced oxygen vacancy distributions. The full nature of this non-superconducting layer remains unknown, but we provide some speculations as to its origin.

Lastly, Chapter 5 succinctly summarizes and concludes our findings. The Appendices are reserved for more detailed information regarding experimental details and construction of our terahertz time-domain spectrometer.

Chapter 2

High-Temperature Superconductivity in Cuprate Thin Films

In the early 1980's, spurred on by the prediction of a possible bipolaronic to superconducting transition in strongly coupled electron-phonon systems [34], as well as their own experience in working with perovskite oxides, Georg Bednorz and Alex Müller set out to find a new kind of superconductor with a T_c much higher than that of previously known materials. They reasoned that, since in the BCS theory $T_c = 1.13\theta_{\mathrm{D}}e^{-1/N(0)V}$, the T_c could be strongly enhanced if the density of states $N(0)$ and the coupling V could be increased. They succeeded in 1986 with the discovery of $La_{2-x}Ba_xCuO_{4+y}$; the new material showed a transition temperature in excess of 30 K [2]. Their report contained evidence of only a resistive transition with no Meissner data, but within just a few weeks the discovery was confirmed independently by groups working in Tokyo and Houston. The following year C. W. Chu and M. K. Wu discovered [35] and isolated the compound $YBa_2Cu_3O_{7-\delta}$, which was observed to have a T_c as high as 93 K.

The discovery of high-T_c copper oxide superconductors ignited a firestorm of research activity that has lasted for more than 35 years. The importance of the discovery was immediately recognized and Bednorz and Müller were awarded the Nobel Prize in Physics in 1987. At first, the existence of superconductivity in oxide systems surprised and confounded the scientific community, because until then it had been understood that oxide materials were highly insulating and that superconductivity was a phase that nucleated out of a *metallic* parent state. Copper oxides, it turned out, are not only bad conductors, but exhibit bizarre properties and extreme complexity that cannot be described within the standard framework of the quantum theory of solids. Much of the activity of the past 35 years has been devoted to unraveling and understanding the underlying physics of this class of materials.

The purpose of this chapter is to introduce the materials and concepts that form the basis of the experimental results presented in this thesis. In Section 2.1 the general properties and phase diagram of the copper oxide superconductors are discussed. Section 2.2 then introduces the ideas of phase fluctuations and reduced dimensionality in superconductors and, based on these concepts, develops a description of the Berezinskii-Kosterlitz-Thouless vortex unbinding transition. The nature of this transition in conventional superconductors is discussed as a point of reference before

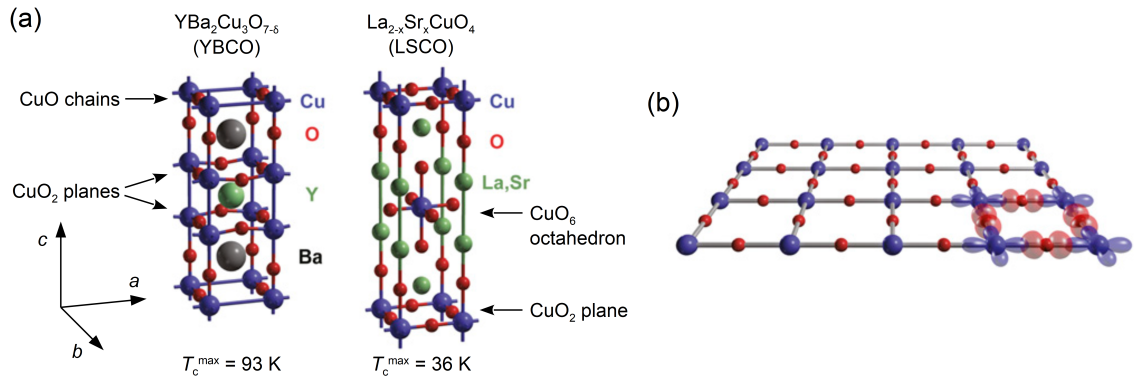

Figure 2.1 (a) The crystal structure of the copper oxide high-temperature superconductors $La_{2-x}Sr_xCuO_4$ and $YBa_2Cu_3O_{7-\delta}$. (b) The structure of an individual CuO_2 plane, with the Cu $3d_{x^2-y^2}$ (blue) and O $2p_{x,y}$ (red) orbitals shown. Figure adapted from Ref. [37].

turning to the details of the Berezinskii-Kosterlitz-Thouless phenomenon in high-T_c copper oxide superconductors. Finally, in Section 2.3, the optical conductivity sum rules in the cuprates are introduced and the relationship between the superfluid density and the conductivity is discussed.

2.1 Copper Oxide Superconductors

Since the original discovery of $La_{2-x}Ba_xCuO_{4+y}$ more than 200 cuprates grouped into 7 families have been discovered [36]. While specific details of the various compounds vary considerably, all are known to share the same basic structure, which consists of a system of conducting CuO_2 planes separated by insulating charge reservoir layers. This structure, illustrated in Fig. 2.1 for $La_{2-x}Sr_xCuO_4$ (LSCO) and $YBa_2Cu_3O_{7-\delta}$ (YBCO), is the prime defining feature of the high-T_c copper oxides and ensures that they have a fundamentally two-dimensional (2D) character, even in bulk. For sufficient charge concentration (doping) the superconductivity resides in the CuO_2 planes. In the so-called hole doped cuprates, which are the focus of this thesis, chemical substitutions in the charge reservoir layers draw electrons out of the CuO_2 planes leaving holes, or charge vacancies. In LSCO this is done by substituting several percent of La with Sr (or Ba) around the CuO_6 octahedra. In YBCO, on the other hand, the doping takes place by oxygen inclusion (or removal) in the CuO chains, which run along the crystallographic b-axis. This difference leads to structural variation between LSCO and YBCO. LSCO has tetragonal symmetry at high temperatures with $a = b = 3.78$ Å and $c = 13.2$ Å in the I4/mmm space group, although at low temperatures distortions of the CuO_6 octahedra result in a structural transition to a low-temperature tetragonal phase. The CuO chains in YBCO break four-fold rotational symmetry and the structure of that compound is instead orthorhombic, with $a = 3.828$ Å, $b = 3.888$ Å, and $c = 11.65$ Å, belonging to the Pmmm space group. Importantly, the non-stoichiometric nature of the compounds and dependence of the superconductivity on dopant concentration imply that disorder will be very relevant to the physical properties of the cuprates.

The two compounds also differ in their numbers of CuO_2 planes per unit cell, and this has important implications for superconductivity. The LSCO family, with its

single CuO_2 plane per unit cell, sports a maximum T_c of 36 K at ambient pressure [36], but the aforementioned distortions of the CuO_6 octahedra at low temperatures can produce a corrugated potential that leads to the formation of stripe phases and a suppressed T_c in certain doping ranges [4]. The YBCO family contains two CuO_2 layers per unit cell with the O atoms displaced somewhat above and below the planes formed by the Cu atoms, as depicted in Fig. 2.1(a). This bilayer structure is further characterized by the placement of the Y^{3+} ion between the two CuO_2 planes. It was realized early on [38] that substitution of Y with Gd, the most magnetic of the rare earth elements, did not suppress T_c by much more than one or two K. This led to the understanding that the rare earth ion is electronically isolated from the CuO_2 planes and does not play a role in superconductivity, but rather serves to stabilize the crystal structure. As a result Y can be replaced with any of the rare earth elements with minimal change to the superconducting properties, and we denote the YBCO family instead as RBCO (where R = Y, La, Nd, Sm, Eu, Gd, Tb, Dy, Ho, Er, Tm, Yb, or Lu). The few notable exceptions are Pr and Ce, where superconductivity is rapidly destroyed with just a few percent substitution of Y with these rare earths. It has been speculated that Pr/Ce $4f$ to O $2p$ hybridization, carrier localization, or rare earth substitution on the Ba site (due to the similarity of the ionic radii) destroys superconductivity without significant lattice distortion [39, 40].

As illustrated by the depiction of a single CuO_2 plane in Fig. 2.1(b), the relevant electronic states involve the Cu $3d_{x^2-y^2}$ and O $2p_{x,y}$ orbitals. By contrast, conventional superconductors are polyelectronic, three-dimensional (3D) metals whose superconductivity is characterized by an s-wave order parameter. Inelastic neutron scattering studies in the YBCO system reported observation of a spin resonance peak that suggested magnetic scattering was intimately tied to the superconducting state and provided evidence for an unconventional pairing mechanism in the copper oxides [41–44]. Indeed, since the relevant electrons for Cooper pairing lie in a band constructed from Cu $d_{x^2-y^2}$ orbitals, $d_{x^2-y^2}$ symmetry became the leading candidate for the symmetry of the order parameter. Later experiments confirmed this hypothesis and definitively revealed the pairing symmetry in the cuprates to be d-wave [45].

The much broader implications of the electronic structure on the physics of copper oxides are that, in addition to the appearance of an unconventional superconducting state, the strong electron interactions in the cuprates place them into a much larger overarching category of highly correlated "quantum materials" that are characterized by a complicated phase diagram with many competing and intertwined orders [3]. For the cuprates, these intertwined orders are summarized by the phase diagram in Fig. 2.2. The undoped parent compounds of the cuprates (RBa$_2$Cu$_3$O$_6$ in the case of RBCO and La_2CuO_4 in the case of LSCO), located at $p = 0$ in the diagram, are antiferromagnetic charge-transfer Mott insulators with the magnetic moments lying on the Cu sites in the CuO_2 planes. With a small amount of hole doping, however, the bewildering array of intertwined orders appears. The normal state at temperatures above the superconducting dome is nominally metallic but badly conducting. Indeed, this "strange metal" phase contains a number of anomalies that suggest it cannot be described by the conventional Fermi liquid theory, such as the $\varrho \propto T$ dependence of the resistivity (instead of $\varrho \propto T^2$) [46, 47]. This T-linear behavior is observed to extend from very low temperatures (when superconductivity is suppressed in high magnetic fields) up to very high temperatures, with no sign of saturation as is seen in standard metals, indicating that the strange metal regime likely terminates at $T = 0$

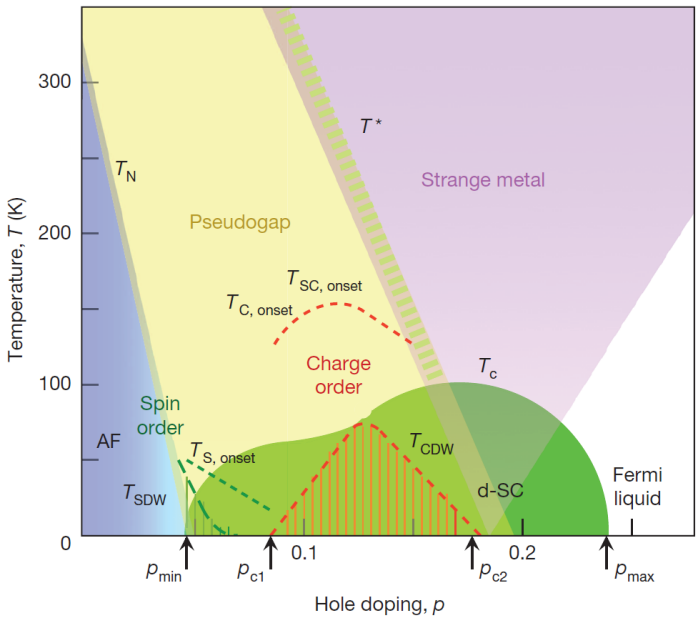

Figure 2.2 The phase diagram of the copper oxide high-temperature superconductors [3].

beneath the peak of the superconducting dome. At very high dopant concentrations, beyond the upper limit of the superconducting dome, the metallic behavior crosses over to that of the usual Fermi liquid description.

Specific to the copper oxide superconductors is the so-called pseudogap state that lies on the underdoped side of the phase diagram between the antiferromagnetic and strange metal regimes. This state is characterized by a partial reduction in the density of states below the temperature T^*, and was first observed in measurements of the nuclear magnetic resonance Knight shift and c-axis polarized infrared conductivity [48–50]. Later, scanning tunneling spectroscopy (STS) and angle-resolved photoemission spectroscopy (ARPES) also provided strong evidence for the existence of the pseudogap [51,52]. In particular, for a wide range of dopings, the ARPES measurements show the absence of any quasiparticle peaks along the antinodal directions (where the superconducting gap function is the largest), while distinct quasiparticle peaks appear on the Fermi surface in the nodal directions that trace out an arc shape (the so-called "Fermi arcs"). This behavior reflects the opening of a partial gap below T^* that evolves to become like the superconducting gap below T_c and at higher dopings. The pseudogap state is especially notable in that it is not accompanied by any known patterns of symmetry breaking, which, together with the ARPES data, gave rise to the hypothesis that the pseudogap represents a state of incoherent, phase-fluctuating preformed Cooper pairs where T^* is the initial pairing temperature and T_c is instead the temperature where the Cooper pair phase locks, making macroscopic superconductivity appear [53].

Evidence suggests that within the pseudogap a variety of additional intertwined order can be found [4]. Data from resonant inelastic X-ray scattering and inelastic neutron scattering experiments indicate that antiferromagnetic order is at least partially coexistent with superconductivity at low temperatures in a wide variety of cuprate families [3,54–57]. Additional X-ray and neutron scattering studies point to the presence of charge density wave (CDW), spin density wave (SDW), and electron

nematic order at temperatures below T^* [3]. Charge order, in particular, has been observed to compete with superconductivity; X-ray diffraction peaks corresponding to an incommensurate CDW display a substantial reduction in scattering intensity below T_c, but the X-ray signal is recovered after superconductivity is suppressed with the application of a magnetic field [58]. Stripe order in LSCO is observed to appear in the underdoped and pseudogap regime around the "dip" or "plateau" in the superconducting dome. In LBCO the dip extends all the way down to $T_c = 0$ at the doping level $x = 1/8$, constituting the "1/8 anomaly" in that material. Such stripy charge ordering has also recently been found to appear in YBCO in the presence of a magnetic field [59], after application of uniaxial strain [60], and in thin films by epitaxial stabilization [61]. It has thus been proposed that the suppression of the superconductivity in the underdoped regime is indicative of a competition between superconductivity and different forms of order that crystallize out of the pseudogap phase. Indeed, the stripe order itself may signal the existence of a "pair-density wave" state, a potential new state of matter where CDW, SDW, and superconducting order are all intertwined such that superconductivity is strongly spatially modulated, with the phase of the superconducting order parameter alternating from one stripe to the next [4].

There are also indications that the pseudogap T^* line in the phase diagram reaches $T = 0$ near optimal doping beneath the superconducting dome. This quantum critical point appears to be located at the same point where the strange metal phase also extrapolates to zero temperature. It is known from the physics of phase transitions that the existence of a quantum critical point is associated with quantum critical fluctuations that are characterized by spatial and temporal scale invariance; this property leads to the critical scaling laws of the various classes of physical systems [62]. In the copper oxide high-T_c materials, the scaling of the superfluid density with the normal state dissipation (known as Homes' law) implies that the energy relaxation time is independent of the specific material details and is instead given by $\hbar/k_BT$, which is the quantum mechanical limit of how short the dissipation timescale can physically be [27, 28]. Thus, directly above the quantum critical point, the temperature scale where the fluctuations are scale invariant is arbitrarily large, and a quantum critical region opens upward in the phase diagram. It is possible, then, that the strange metal phase of cuprates can be interpreted as a quantum critical fluctuation region of a more fundamental order parameter [3]. However, a more well-developed understanding of the strange metal and critical fluctuations in the optimally and overdoped region of the phase diagram is needed to determine if this is indeed the case.

Theoretical models describing the physics of strong correlations have mostly been solved in one dimension, but the mathematical techniques needed to elucidate the problem in higher dimensions are largely undeveloped. While an understanding of the pseudogap, strange metal, and superconductivity in bulk copper oxides is the ultimate goal, an understanding of the system in 2D or quasi-2D marks a clear intermediate step. It is expected that in 2D the pair-density wave state, if it indeed exists, will spawn a proliferation of topological transitions between different kinds of CDW, superconducting, and nematic electronic states as a function of temperature and phase stiffness of the various order parameters [4]. Recent advancements in thin film materials synthesis have enabled precise control of the electronic structure in the copper oxides and have opened the door to atomic-level engineering and dimensionally constrained studies of the correlations in these materials [26, 63, 64]. Importantly,

such techniques provide the ability to tune the disorder level, which makes it possible to also explore the complicated interplay between inhomogeneity and unconventional order [1].

2.2 Fluctuations in High-T_c Superconductors

2.2.1 The Ginzburg-Landau Theory

The phenomenological Ginzburg-Landau (GL) theory [65] was the first serious attempt to approach the problem of superconductivity from a quantum mechanical perspective. Based on Landau's theory of second order phase transitions [66], the GL theory treats the superconducting transition through an expansion of the free energy in powers of the order parameter, which is taken to be the wavefunction $\psi_s(\mathbf{r})$ of the superconducting state ($|\psi_s|^2$ is assumed to be proportional to the density of superconducting electrons ρ_s). Specifically, the free energy expansion is taken in powers of $|\psi_s(\mathbf{r})|^2$ and $|\nabla\psi_s(\mathbf{r})|^2$, leading to two coupled differential equations in terms of $\psi_s(\mathbf{r})$ and the vector potential $\mathbf{A}(\mathbf{r})$. As a result, the theory is only valid close to the phase transition where $T_c - T \ll T_c$, but the inclusion of the spatial dependence, gradients, and vector potential make the theory useful in situations where superconductivity is inhomogenous or the nonlinear response to fields is strong enough to affect $\rho_s(\mathbf{r})$. The microscopic BCS theory, by contrast, can quickly become difficult or computationally burdensome in these situations. Thus, while phenomenological, the GL theory is advantageous for treating the macroscopic behavior of the magnetic field dependence and superfluid density in situations where the BCS theory is of limited utility. Notably this also includes situations where the BCS theory has no applicability at all, such as in the case of high-T_c and unconventional superconductors.

For an inhomogenous superconductor in a uniform external magnetic field H, the Gibbs free energy density $\mathcal{F}$ is expanded as

$$\mathcal{F}_{sH} = \mathcal{F}_n + \int \left[\alpha |\psi_s|^2 + \frac{\beta}{2} |\psi_s|^4 + \frac{1}{4m} \left| \left(-i\hbar\nabla - \frac{2e}{c}\mathbf{A} \right) \psi_s \right|^2 + \frac{H^2}{8\pi} \right] d^3\mathbf{r}$$

with expansion coefficients α and β, and dropping the explicit spatial dependence in $\psi_s(\mathbf{r})$ and $\mathbf{A}(\mathbf{r})$. Minimizing $\mathcal{F}_{sH}$ with respect to ψ_s and $\mathbf{A}$ using standard variational approaches leads to the GL equations

$$0 = \xi_{\mathrm{GL}}^2 \left(i\nabla + \frac{2\pi}{\Phi_0}\mathbf{A} \right)^2 \psi_s - \psi_s + |\psi_s|^2 \psi_s \tag{2.1}$$

$$\mathbf{J} = \frac{\Phi_0 c}{16\pi^2\lambda^2 i} \left(\psi_s^* \nabla\psi_s - \psi_s \nabla\psi_s^* \right) - \frac{c}{4\pi\lambda^2} |\psi_s|^2 \mathbf{A}, \tag{2.2}$$

where the Ginzburg-Landau coherence length ξ_{GL} and effective London penetration depth λ are defined as

$$\xi_{\mathrm{GL}}(T) = \frac{\hbar c}{2\sqrt{2} e H_c(T) \lambda(T)} \tag{2.3}$$

$$\lambda^2(T) = \frac{mc^2}{8\pi e^2 |\psi_s(T)|^2}. \tag{2.4}$$

The GL coherence length represents the characteristic length scale over which variations in $\psi_s(\mathbf{r})$ occur while the effective London penetration depth is the characteristic depth to which a weak external magnetic field and hence the supercurrent penetrate into the superconductor.

The quantity $\Phi_0 = hc/2e$ is the fluxoid quantum. Quantization of the fluxoid rather than the magnetic flux $\Phi = \oint_C \mathbf{A} \cdot d\ell$ follows from spontaneous symmetry breaking of the wavefunction in the superconducting state and the gauge invariance of the GL equations. Here, the term *spontaneously broken symmetry* refers to the property that the Hamiltonian of a given system is invariant under a specific symmetry transformation in the thermodynamic limit while the ground state of the Hamiltonian is itself not invariant under this symmetry transformation [67]. However, according to Elitzur's theorem, spontaneous breaking of local symmetry for a symmetric gauge theory is impossible [68]. The Hamiltonian of a superconductor is symmetric with respect to gauge choice, so gauge symmetry is a local symmetry and hence cannot be broken. On the other hand, the $U(1)$ symmetry (continuous rotational symmetry about a single axis) of the phase φ of the wavefunction *can* be spontaneously broken. To see this, we note that the BCS ground state of a superconductor,

$$|\psi_\varphi\rangle = \prod_k \left(u_k + v_k e^{i\varphi} c^\dagger_{k\uparrow} c^\dagger_{-k\downarrow}\right)|0\rangle\,,$$

is not invariant under the phase transformation $\varphi(\mathbf{r}) \to \varphi(\mathbf{r}) + \vartheta$ for ϑ independent of spacetime, but it is gauge invariant because a proper gauge transformation requires *both* [67]

$$c^\dagger_{k\uparrow} \to e^{i\frac{e}{\hbar c}\Lambda} c^\dagger_{k\uparrow} \quad \text{and} \quad \varphi \to \varphi - \frac{2e}{\hbar c}\Lambda.$$

The corresponding gauge transformations of the GL equations are then written as $\mathbf{A} \to \mathbf{A}' + \Phi_0 \nabla\varphi/2\pi$ and $\psi_s \to \psi_s' e^{i\varphi(\mathbf{r})}$, where $\varphi(\mathbf{r})$ is arbitrary. The function $|\psi_s|$ is then single-valued as is required by the constraint that the observable penetration depth λ is single-valued, and the order parameter ψ_s is in general complex. Rewriting the second GL equation (Eq. 2.2) as

$$\mathbf{J} = \frac{c}{4\pi\lambda^2}\left(\frac{\Phi_0}{2\pi}\nabla\varphi - \mathbf{A}\right)|\psi_s|^2$$

and integrating $\mathbf{J}$ around an arbitrary closed contour yields

$$n\Phi_0\,|\psi_s|^2 = \oint_C \left(\frac{4\pi\lambda^2}{c}\mathbf{J} + \mathbf{A}\,|\psi_s|^2\right)\cdot d\ell.$$

The gradient of the phase $\nabla\varphi$ is multiple-valued so $2\pi n = \oint_C \nabla\varphi \cdot d\ell$ must equal an integer multiple of 2π to ensure single-valuedness of $|\psi_s|$. If the contour encloses a simply connected area that contains no holes or normal state regions, then the contour of integration C can be shrunk down without crossing a boundary until it encloses a single point, at which $n\Phi_0 = 0$ and zero net flux is enclosed, as expected in the Meissner state. On the other hand, if the contour of integration encloses a cavity or a non-superconducting region, then the presence of the boundary forces $n\Phi_0$ to take a nonzero integer multiple value of Φ_0. If C is taken to lie everywhere along its loop further than $\sim\lambda$ from the cavity walls, then the supercurrent $\mathbf{J} = 0$ and $n\Phi_0 = \Phi$ so that the fluxoid is indistinguishable from the total enclosed flux. Therefore, the

opening of a small cavity or the appearance of a small non-superconducting region allows the superconductor to admit a single quantum of flux and the phase slips by 2π. Or, equivalently, a phase fluctuation of the wavefunction by 2π is accompanied by the appearance of a supercurrent *vortex* that supports a single quantum of flux passing through the non-superconducting vortex core of cross sectional area $\sim\xi_{\mathrm{GL}}^2$.

Deep in the superconducting state at $T \ll T_c$ the free energy cost to create a vortex and admit flux is high and phase fluctuations have negligible effect on the superconducting wavefunction. This is evident because the energy density of a flux line including the kinetic energy of the circulating supercurrent is $U = H_c^2 \ln(\lambda/\xi_{\mathrm{GL}})/2\pi = 4(\mathcal{F}_n - \mathcal{F}_s)\ln(\lambda/\xi_{\mathrm{GL}})$ [8], and for typical high-T_c superconductors $\lambda \gg \xi_{\mathrm{GL}}$. However, close to T_c, $H_c(T \to T_c)$ approaches zero and thermal fluctuations allow the system to sample states which are within $\sim k_B T$ of the minimum free energy state, making thermally activated vortices and phase slips possible. Still, the total energy required for such a phase slip is on the order $H_c^2(T)\xi_{\mathrm{GL}}^2 R$ for a sample size R, so for an arbitrarily large bulk sample the superconducting state will not admit vortices in the absence of an applied external magnetic field even very close to T_c. For thin superconducting films, on the other hand, the energy needed to excite a vortex by thermal fluctuation may be considerably less than $k_B T_c$.

2.2.2 The Berezinskii-Kosterlitz-Thouless Transition

In a very general sense, physical systems can be classified by how they are described in a D-dimensional n-vector framework, termed the O(n) model, first elucidated in 1968 by Eugene Stanley [69]. The basic properties of the model are that given a classical D-dimensional lattice, each site on the lattice is described by an n-dimensional unit vector that is coupled to its neighbors. For example, the O(1) model describes Ising systems, O(2) corresponds to the XY model, and O(3) represents the Heisenberg model. The O(n) model is immensely important in physics because it serves as a cornerstone in our contemporary understanding of phase transitions. In fact, by studying a generalization of the D-dimensional O(n) model and searching for its critical behavior, Kenneth G. Wilson was led to the discovery of the renormalization group [70,71], for which he was awarded the 1982 Nobel Prize in Physics. Application of the renormalization group to 2D systems turned out to be crucial for the later discovery of an entirely new type of phase transition that is not defined by its pattern of symmetry breaking.

Early work by Peierls [72] and Landau [73,74] showed, using heuristic arguments, that 2D solids cannot host spontaneous breaking of continuous symmetry on the grounds that the mean-square fluctuations increase logarithmically with the size of the system. For a 2D crystal this physically corresponds to a scenario where the thermal motion of long wavelength phonons destroys the long-range positional order of the atoms at the lattice sites. Similarly, in 2D magnets the long-range magnetic correlations are destroyed by long wavelength spin waves. Later, Mermin, Wagner, and Hohenberg were able to rigorously prove by the use of Bogoliubov's inequality, without the simplifying assumptions of either a harmonic approximation or an order parameter expansion, that long-range order vanishes in the thermodynamic limit for *all* 2D systems [75,76]. However, while the mean-square fluctuations scale with the size of the system, the fluctuation instabilities are weak and positional order persisting over mesoscopic length scales is not ruled out. Long-range *directional*

order, on the other hand, is still transmitted infinitely far in a 2D crystal, so the definition and direction of crystalline axes is preserved [77]. Furthermore, at $T = 0$ the ground state of the system must be ordered in the thermodynamic limit because the fluctuation correlation function tends to a finite value [66]. As a result one would expect the existence of some type of phase transition at a nonzero temperature that is characterized by the destruction of long-range order over macroscopic length scales.

Inconclusive evidence for the existence of such a transition in 2D systems first appears in the results of numerical calculations which show a phase transition between a solid state and a fluid state in a 2D array of elastic particles [78]. Low-temperature expansions of 2D spin models further indicate that magnetization $M \propto H^{\alpha}$ for some power $0 < \alpha < 1$ as $T \to 0$, rather than the $M \propto H$ dependence found at high temperatures [79,80]. Consequently, high-temperature expansions of such spin models provide similar evidence, with a divergence in the magnetic susceptibility at low but finite temperatures [81]. However, results simultaneously point to either an absence or a weakening of the transition in the 2D Heisenberg model as compared to a 2D system of planar rotators, implying that a phase transition is more favorable in the 2D-XY model [69, 82].

Vortex Unbinding

It turns out that there is a strong similarity between certain types of planar 2D magnets and superfluid films. First Berezinskii [83] and then Kosterlitz and Thouless [84] rigorously showed that superfluids and systems characterized by the XY model in 2D do indeed exhibit long-range order at finite temperatures with a critical temperature T_{BKT} where the rigidity modulus drops to zero. They were able to do this by considering a straightforward argument based on the balance of free energy in a generic 2D-XY model system. In the 2D-XY model the Hamiltonian of a system described by a simple square lattice of lattice spacing a is given by

$$\mathcal{H} = -J \sum_{\langle ij \rangle} \mathbf{S}_i \cdot \mathbf{S}_j = -J \sum_{\langle ij \rangle} \cos\left(\varphi_i - \varphi_j\right) \to \frac{1}{2} J \int \left(\nabla \varphi(r)\right)^2 d^2 r, \tag{2.5}$$

where J is the coupling energy, $\mathbf{S}_i$ are the moments of the planar rotators, φ_i are orientation angles of the rotators, and the sum is taken over nearest neighbors only (the final element in Eq. 2.5 is the generalization of the Hamiltonian to the continuum limit). The presence of a dislocation or defect will cause $\varphi_i - \varphi_j$ to take nonzero values in the vicinity of the defect location. For a superfluid $\varphi_i - \varphi_j$ corresponds to the relative phase difference of the wavefunction at two adjacent lattice sites. As discussed above, to ensure single-valuedness of the complex wavefunction, the total phase difference must be an integer value of 2π when the sum in Eq. 2.5 is taken around any arbitrary closed loop. Thus, for a closed loop of radius r running along $2\pi r/a$ lattice sites and enclosing a single dislocation (or vortex), the relative phase difference between any two pairs of adjacent lattice sites is $\varphi_i - \varphi_j = a/r$ and the Hamiltonian can be expanded to second order about the minimum energy as

$$\mathcal{H} - E_0 \approx \frac{1}{2} J \sum_{\langle ij \rangle} \left(\varphi_i - \varphi_j\right)^2 = \frac{\pi J a}{r}$$

for small angles $\varphi_i - \varphi_j$. The total energy U in the array is then found by integrating $\mathcal{H}$ over all possible closed loops with radii extending from the size of a single unit cell

(corresponding to the radius of a single dislocation) to the total sample size R, giving

$$U = \pi J \ln \frac{R}{a} + E_0. \tag{2.6}$$

The creation of a single vortex is therefore associated with an energy that diverges logarithmically with increasing sample size. Deep inside the interior of a sample, then, the energy cost to create a single vortex becomes enormous and prohibitive. On the other hand, single vortex excitations may persist in a thin region of thickness L along the edge of the sample where $k_B T/\pi J \sim \ln L/a$. When *two* vortices of opposite handedness are present in the system $\varphi_i - \varphi_j$ is zero at distances much larger than the inter-vortex separation distance R_{12} due to cancellation from the opposite circulations and the integral over r can be cut off at $\sim R_{12}$. In this case the total energy in the system becomes

$$U = 2\pi J \ln \frac{R_{12}}{a} + 2E_0 \tag{2.7}$$

where $2E_0$ is the energy cost associated with the creation of two opposite vortices separated by a distance a and the force between the two vortices is $-\nabla U = -2\pi J/R_{12}$, indicating a net attractive interaction. Thus, with a finite excitation energy, *bound vortex-antivortex pairs* will form via thermal fluctuations and will persist until the vortices pass within a minimum distance a of each other, at which point they annihilate.

The behavior of the vortex-antivortex pairs is governed by the balance of the internal energy and entropy of the vortices. Above a certain temperature the decrease of the free energy associated with the entropy of pair breaking exceeds the free energy gain from the creation of more vortices. Given that there are $N \approx R^2/a^2$ total lattice sites in the system, the number of states available to bound and unbound vortex pairs are proportional to R^2/a^2 and R^4/a^4, respectively. The free energy difference $\mathcal{F}_{\text{unbound}} - \mathcal{F}_{\text{bound}} = \Delta U - T\Delta S$ between unbound and bound vortex-antivortex pairs is then

$$\mathcal{F}_{\text{unbound}} - \mathcal{F}_{\text{bound}} \approx 2\left(\pi J - k_B T\right) \ln \frac{R}{a}. \tag{2.8}$$

At low temperatures where $k_B T < \pi J$ the free energy difference $\Delta\mathcal{F} \to +\infty$ for large sample size R and the formation of broken vortex-antivortex pairs is thermodynamically excluded. On the other hand, for $k_B T > \pi J$ the free energy difference $\Delta\mathcal{F} \to -\infty$ for large R and broken pairs are strongly favored. The system therefore experiences a vortex unbinding transition at the Berezinskii-Kosterlitz-Thouless (BKT) critical temperature

$$T_{BKT} = \frac{\pi J}{k_B} \tag{2.9}$$

as the runaway formation of free vortices at higher temperatures produces a vortex plasma state in order to minimize the total free energy.

The BKT transition is conceptually illustrated in Fig. 2.3. The existence of the long-range ordered vortex-antivortex bound state at low but finite temperatures is remarkable because the Mermin-Wagner theorem rigorously rules out any form of long-range order on account of large-amplitude fluctuations (spin waves) that scale with the size of the system [75]. This implies that the vortex correlations must be insensitive to the surrounding spin fluctuations. In fact, Kosterlitz and Thouless were able to show that in the 2D-XY model the spin fluctuations and phase fluctuations

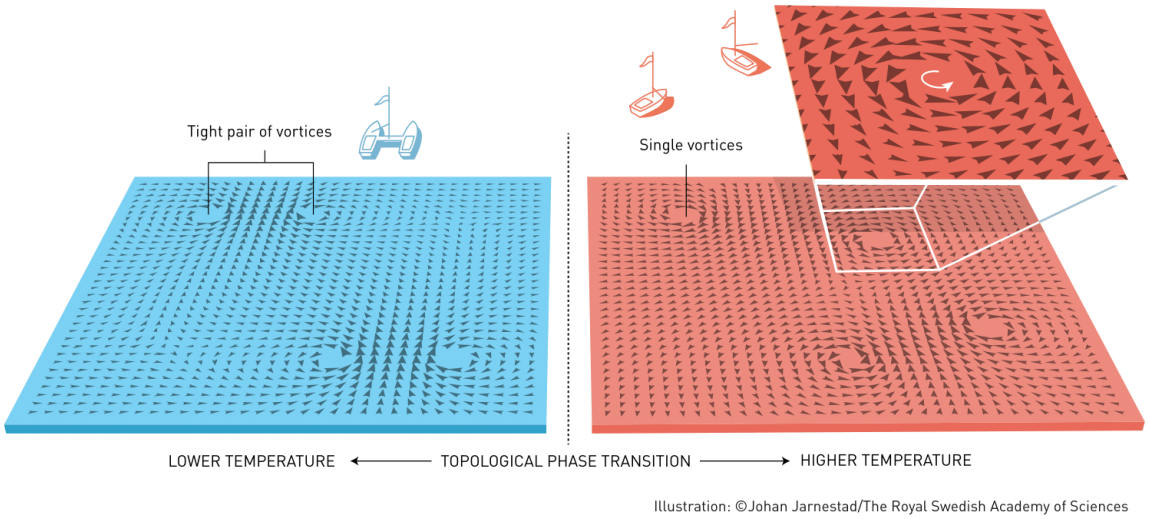

Figure 2.3 A conceptual illustration of the Berezinskii-Kosterlitz-Thouless vortex unbinding transition in the 2D-XY model. At temperatures below the BKT transition, $T_{BKT} = \pi J/k_B$, vortices may only thermodynamically form in bound vortex-antivortex pairs that move together through the system much like the linked hulls of a catamaran on the ocean. On the other hand, above the BKT temperature, the vortex-antivortex pairs spontaneously unbind and move freely through the system as independent entities. Image credit: The Royal Swedish Academy of Sciences, Nobel Prize in Physics 2016 [85].

are indeed separable and therefore do not interact [84]. The BKT transition is enabled in the 2D-XY model because, while the spin-spin correlations are not long-ranged, the phase correlations are.

Analogy to the 2D Coulomb Gas Model

The logarithmic dependence of the system energy on R in Eqs. 2.6 and 2.7 implies that the problem of vortex dynamics in the 2D-XY model draws a natural analogy to that of a Coulomb gas in two dimensions [84], where Poisson's equation for a point charge, $\nabla^2 V(r) = -2\pi\delta(r)$, also leads to a potential of the form $V(r) \propto \ln r$. In many cases it is actually more instructive to treat the properties of vortex dynamics via the 2D Coulomb gas model because the construction of the 2D Coulomb gas model is straightforward and provides an intuitive basis for understanding in terms of simple charges as opposed to complicated vortex structures. The model is constructed from a grand canonical description of a gas of $n = n_+ + n_-$ positively and negatively charged particles per unit volume, with each particle carrying a charge of equal magnitude q and with the interaction potential renormalized by linear screening. The complete description makes use of a set of self-consistent renormalization equations developed by Kosterlitz [86]. However, a simpler description in terms of the Poisson-Boltzmann equation is informative and provides an adequate picture of the critical behavior of the charge gas near T_{BKT} [87]. In the presence of a small test charge δq, the Poisson-Boltzmann equation for the system is given by

$$\delta q \nabla^2 V(r) = -\frac{2\pi\delta q}{\epsilon} f(r) - \frac{2\pi n_f^+}{\epsilon} e^{-\delta q V/k_B T} + \frac{2\pi n_f^-}{\epsilon} e^{\delta q V/k_B T} \tag{2.10}$$

where $f(r)$ is the Coulomb gas single-particle charge distribution, ϵ is the dielectric constant due to the polarization of bound charge pairs, and $n_f = n_f^+ + n_f^-$ is the number density of free charges. This description is in general not analytically tractable, but if we consider the limit where the Coulomb gas is overall neutrally charged and δq is infinitesimal, then the solution to this equation (in terms of its Fourier transform) is

$$V(k) = \frac{2\pi}{\epsilon} \frac{1}{k^2 + \lambda_s^{-2}} f(k), \tag{2.11}$$

where $\lambda_s = \sqrt{k_B T \epsilon / 2\pi n_f}$ is a screening length determined by the influence of the free charges. It is important to note that the definition of λ_s obtained from the long-range ($k \to 0$) limit of Eq. 2.11 is precise and does not assume *a priori* the existence of a charge unbinding transition. The screening length arises because bound pairs that are quite extended in space are likely to have other charges located within their spatial extent, especially when the fugacity for the free charges $e^{-\delta q V / k_B T} \approx 1$. These free charges polarize in the field of the pairs and act to reduce the interaction. As a result the spatial extent of $V(r)$ is bounded on the order $\sim\lambda_s$. The density of free charges $n_f \simeq 2e^{\mu_{\text{eff}}/k_B T}/ca^2$ is itself dependent upon the effective chemical potential μ_{eff} and the long-range energy of the form represented by Eq. 2.6, with c a constant and the factor of 2 arising from the fact that a free charge can take either a positive or negative value of q. The form of λ_s which satisfies the Poisson-Boltzmann equation is then found to be [87]

$$\left(\frac{\lambda_s}{a}\right)^{-2} = \begin{cases} \left(\frac{4\pi}{c k_B T \epsilon}\right)^{1/(1-1/4k_B T\epsilon)} & T > T_{BKT} \\ 0 & T < T_{BKT} \end{cases} \tag{2.12}$$

Eq. 2.12 is complementary to Eq. 2.8, as both describe a system where free (unbound) charges are thermodynamically forbidden at temperatures below the critical threshold T_{BKT}, while above T_{BKT} such free charges are favored. This is evident from Eq. 2.12 because as $T \to T_{BKT}^+$ the inverse screening length diverges, signalling that the Coulomb gas charges are only correlated on very short length scales and are thus free to screen out the interaction potential of any bound charges. As $T \to T_{BKT}^-$ the inverse screening length is zero implying that the interaction is long ranged. This behavior is illustrated in Fig. 2.4. Eq. 2.12 therefore contains the anticipated result of a divergent susceptibility upon approaching T_{BKT} from above.

An effective dielectric constant ϵ_{eff} can be defined from the Poisson equation $\nabla^2 V(r) = -2\pi f(r)/\epsilon_{\text{eff}}$ and Eq. 2.11 by

$$\frac{2\pi}{\epsilon_{\text{eff}}(k,T)} \frac{f(k)}{k^2} = \frac{2\pi}{\epsilon} \frac{f(k)}{k^2 + \lambda_s^{-2}}. \tag{2.13}$$

In the long-range ($k \to 0$) limit, this leads to the result

$$\frac{1}{\epsilon_{\text{eff}}(0,T)} = \begin{cases} 0 & T > T_{BKT} \\ \frac{1}{\epsilon} & T < T_{BKT} \end{cases} \tag{2.14}$$

which implies that above T_{BKT} the effective charge density of the 2D Coulomb gas jumps abruptly to zero from a finite value. Therefore, the vortex unbinding transition given in Eq. 2.9 is necessarily accompanied by a jump of the rigidity modulus to zero

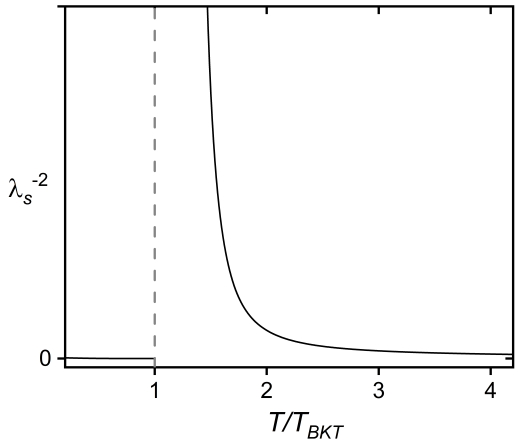

Figure 2.4 The behavior of the inverse Coulomb gas screening length as a function of temperature, with constant ϵ. As T approaches T_{BKT} from above the inverse screening length diverges, implying the divergence of the susceptibility due to free Coulomb gas charges which screen the interaction potential. At $T \leq T_{BKT}^{-}$ the inverse screening length is zero and the system is in the long-range ordered state. The dashed line marks T_{BKT}.

[88]. In 2D superfluids this corresponds to a suppression of the superfluid density. The physical mechanism responsible for such a jump is the divergence of the susceptibility above T_{BKT} which causes the polarizability of the Coulomb gas to become infinite and thus perfectly screen out long-range interactions.

The Universal Superfluid Density Jump

It was pointed out by Nelson and Kosterlitz that in neutral superfluids the superfluid density jump above T_{BKT} is *universal*, in that the magnitude of the jump is given only by constants and is independent of the size of the cutoff a that defines the spatial extent of the vortex cores [89]. The argument is based on a scaling analysis of the interaction potential treated within Kosterlitz's renormalization group theory approach. Since the interaction potential is screened in the 2D Coulomb gas, this corresponds to an analysis of the scale dependence of the effective dielectric constant.

The first step in the analysis is to derive the relationship between the effective dielectric constant of the 2D Coulomb gas model and the density of the 2D superfluid. The Hamiltonian for the neutral 2D Coulomb gas allows the dielectric constant of Eq. 2.14 to be defined in terms of the unscreened interaction potential, the mass density ρ, and the density-density correlation function as

$$\frac{1}{\epsilon_{\text{eff}}(0,T)} = \lim_{k\to 0}\left(1 - \frac{2\pi\rho}{k_B T}\left(\frac{\hbar}{m}\right)^2 V(k)\langle n(k)n(-k)\rangle\right), \tag{2.15}$$

where the Coulomb gas charge $q^2 \to 2\pi\rho\hbar^2/k_B T m^2$ [90]. By comparing this result to a similar one obtained from the Hamiltonian of the neutral 2D superfluid the relationship between ρ_s of the superfluid and ϵ_{eff} can be determined. The superfluid Hamiltonian,

$$\mathcal{H}_s = \frac{1}{2\rho k_B T}\int \vec{g}^2(\vec{r})d^2r, \tag{2.16}$$

depends upon a mass-current density operator $\vec{g}(\vec{r})$ that represents a mass-carrying velocity field. The operator $\vec{g}(\vec{r})$ is defined such that it can be split into its longitudinal and transverse components, $\vec{g}(\vec{r}) = \vec{g}_{\parallel}(\vec{r}) + \vec{g}_{\perp}(\vec{r})$, where $\nabla \times \vec{g}_{\parallel}(\vec{r}) = 0$ and $\nabla \cdot \vec{g}_{\perp}(\vec{r}) = 0$. This definition implies that $\vec{g}_{\parallel}(\vec{r})$ is the gradient of a scalar potential,

$$\vec{g}_{\parallel}(\vec{r}) = \rho \frac{\hbar}{m} \nabla \phi(\vec{r}),$$

and that $\vec{g}_{\perp}(\vec{r})$ corresponds to a vortex vector potential,

$$\vec{g}_{\perp}(\vec{r}) = \rho \frac{\hbar}{m} \nabla \times \hat{z} \int n(\vec{r}') V(|\vec{r} - \vec{r}'|) d^2 r',$$

where $\hat{z}$ is a unit vector oriented normal to the 2D plane. The potential $V(|\vec{r} - \vec{r}'|) \propto \ln(|r - r'|/a)$ is assumed to have a hard-core cutoff at a distance a corresponding to the spatial extent of the vortex cores, as discussed above. The mass-current density operator is used in lieu of the velocity field itself because it is well behaved inside the vortices and avoids singularities. Further, the boundary condition on $\vec{g}_{\parallel}(\vec{r})$ can be chosen such that $\phi(\vec{r})$ is constant at the sample edges, which allows the cross term $\vec{g}_{\parallel}(\vec{r})\vec{g}_{\perp}(\vec{r})$ to be dropped from the Hamiltonian. As a result the Hamiltonian depends only on the mass-current density correlation functions

$$\begin{aligned} \int \langle \vec{g}_{\parallel}(\vec{r}) \cdot \vec{g}_{\parallel}(0) \rangle d^2 r &= \rho k_B T \\ \int \langle \vec{g}_{\perp}(\vec{r}) \cdot \vec{g}_{\perp}(0) \rangle d^2 r &= 2\pi \left(\frac{\rho \hbar}{m} \right)^2 \lim_{k \to 0} V(\vec{k}) \langle n(\vec{k}) n(-\vec{k}) \rangle. \end{aligned} \tag{2.17}$$

The superfluid density ρ_s is defined as the mass density associated with the increase in free energy caused by a mass current $\mathcal{J}$, so it is sufficient to find the free energy of the system corresponding to $\mathcal{H}_s$ with an imposed infinitesimal scalar field that induces an infinitesimal mass current $\rho \delta \vec{v}$ [90]. This free energy is given by

$$\Delta \mathcal{F} = \frac{1}{\rho_s} \left(\frac{\mathcal{J}^2}{2\Omega} \right),$$

where Ω is a unit 2D volume. Solving for ρ_s it can be found that

$$\rho_s = \frac{1}{k_B T} \int \left[\langle \vec{g}_{\parallel}(\vec{r}) \cdot \vec{g}_{\parallel}(0) \rangle - \langle \vec{g}_{\perp}(\vec{r}) \cdot \vec{g}_{\perp}(0) \rangle \right] d^2 r, \tag{2.18}$$

and, making use of the mass-current density correlation functions in Eqs. 2.17, it is clear that this expression for ρ_s becomes identical to the expression for $1/\epsilon_{\text{eff}}$ given in Eq. 2.15. Thus, the superfluid density of the neutral 2D superfluid is related to the effective dielectric constant of the 2D Coulomb gas model as

$$\frac{\rho_s}{\rho} = \frac{1}{\epsilon_{\text{eff}}}, \tag{2.19}$$

putting on firm ground the assertion made above that the jump of $1/\epsilon_{\text{eff}}$ to zero at T_{BKT} corresponds to a suppression of the superfluid density. Furthermore, the identification of the superfluid density with the rigidity modulus raises an additional

physical interpretation of ρ_s. The value of ρ_s quantifies a *superfluid stiffness* that describes the minimum energy required to twist the phase of the superfluid wavefunction by 2π.

With the relationship between the superfluid density and effective dielectric constant established, the scaling analysis of ϵ_{eff} proceeds by considering the solution of the Kosterlitz renormalization group equations for the fugacity z_ℓ of the 2D Coulomb gas in the infinite-range limit [89]. The fugacity $z_\ell = e^{-\mu/k_BT}$ incorporates the superfluid Hamiltonian $\mathcal{H}_s$ through the chemical potential μ and represents the probability for creating a single Coulomb gas charge (vortex) in a unit volume. When $z_\ell \to 0$, then, the system is in the ordered state because the probability to spontaneousy create an unbound vortex is zero. Following Eq. 2.6 the chemical potential is defined as $\mu = \pi\rho\hbar^2/k_BTm^2\ln(\lambda_s/a) + E_0$; the fugacity becomes zero at T_{BKT} because the inverse screening length diverges (see Eq. 2.12). The renormalization group equations are obtained by expanding the effective current-current correlation function, $K_{\text{eff}}^{-1} = m^2/\hbar^2\rho^2\int\langle\vec{g}(\vec{r})\cdot\vec{g}(0)\rangle d^2r$, as a power series in z_ℓ and then repartitioning the energy by scaling the hard-core radius as $r_\ell = ae^\ell$. The power series,

$$K_{\text{eff}}^{-1} = \frac{k_BTm^2}{\rho_s\hbar^2} + 4\pi^3 z_\ell^2\int_a^\infty\left(\frac{dr}{a}\right)\left(\frac{r}{a}\right)^{3-2\pi\rho_s\hbar^2/k_BTm^2} + \mathcal{O}\left(z_\ell^4\right),$$

contains an integral which can be broken into two parts, with a small-r part running over the bounds $a \to ae^\ell$ and a large-r part running from $ae^\ell \to \infty$ [91]. The small-r part can be absorbed into the leading constant term (the bare coupling, which we call K^{-1}) while the large-r integral can be rescaled so that it once again runs over $a \to \infty$ by renormalizing z_ℓ. Since the solution in the $z_\ell \to 0$ limit will be sought the higher order corrections can be safely discarded. This rescaling can therefore be captured by a set of parameter renormalizations for the scale-dependent core energy and fugacity,

$$(K^{-1})' = K^{-1} + 2\pi^3 z_\ell^2\ell$$

$$z_\ell' = z_\ell + (2 - \pi K)z_\ell\ell.$$

By recursively iterating this rescaling with successive application of $r_\ell = ae^\ell$ for small ℓ, the renormalization group equations are obtained [86]:

$$\begin{aligned}\frac{d}{d\ell}\left(\frac{\epsilon_\ell k_BTm^2}{\rho\hbar^2}\right) &= 4\pi^3 z_\ell^2 \\ \frac{dz_\ell}{d\ell} &= \left[2 - \pi\left(\frac{\rho\hbar^2}{\epsilon_\ell k_BTm^2}\right)\right]z_\ell\end{aligned} \tag{2.20}$$

The quantity of interest here is the behavior of z_ℓ as $\ell \to \infty$. Integrating Eqs. 2.20 yields the renormalization group flows that allow physically relevant quantites to be extracted. The flows are a family of equations which relate the fugacity to the core energy as a function of ℓ. The specific behavior of a given flow is set by the value of the initial condition (the constant of integration), which is determined by the temperature and the $T = 0$ value of the superfluid density. Thus each flow corresponds to a single temperature. Following these flows to their limiting behavior as $\ell \to \infty$ allows the nature of the system to be identified and the critical behavior to be found. Several

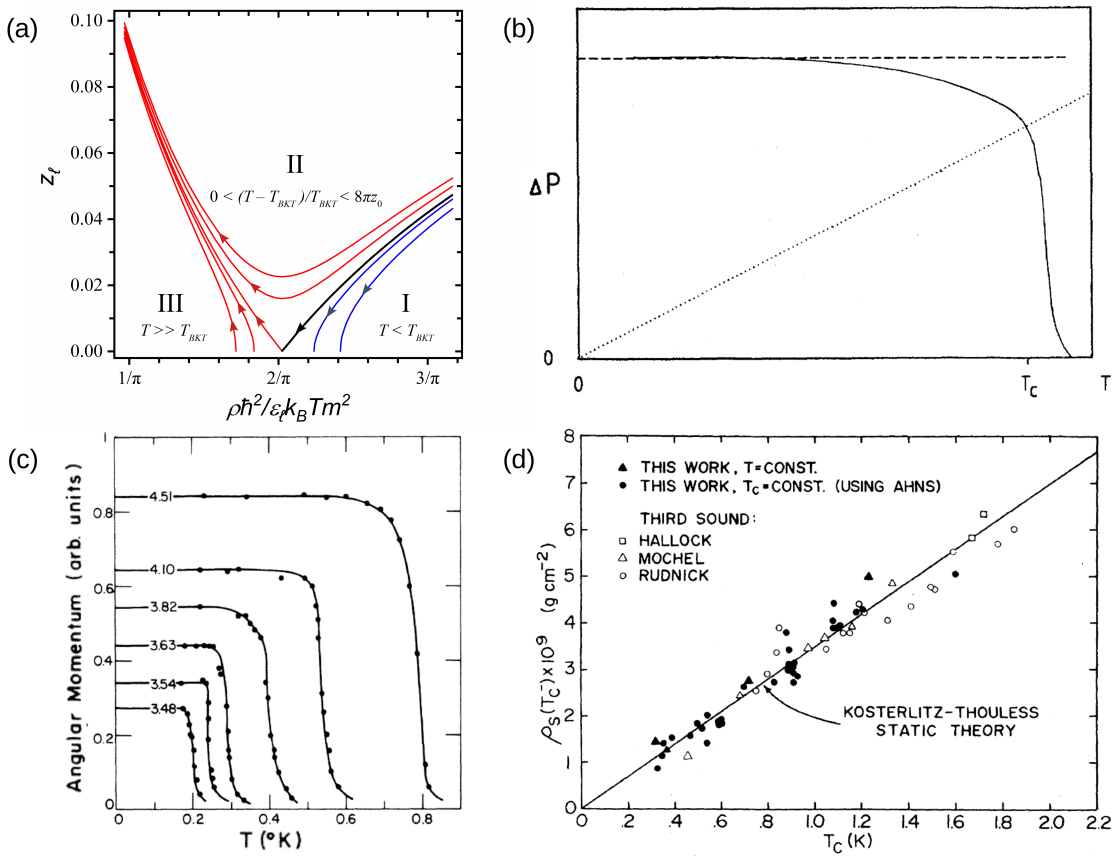

Figure 2.5 The universal jump in a neutral superfluid. (a) Kosterlitz renormalization group flows calculated for several different values of T. Arrows indicate the direction of increasing ℓ. Blue flows correspond to $T < T_{BKT}$ and tend to $z_\ell = 0$ with increasing ℓ, indicating a stable long-range ordered state at low temperatures (region I). The black flow corresponds to $T = T_{BKT}$ and tends exactly to the value $2/\pi$ as $\ell \to \infty$. The red flows correspond to $T > T_{BKT}$ and tend to $z_\ell \to \infty$ as $\ell \to \infty$, characteristic of a vortex plasma state. This high temperature regime can be subdivided into two regions. The flows in Region II contain a minimum in z_ℓ for some intermediate value of ℓ and characterize the critical fluctuation regime in a narrow temperature band above T_{BKT}, where $0 < (T - T_{BKT})/T_{BKT} < 8\pi z_0$. Region III corresponds to the very high temperature region, $T \gg T_{BKT}$, where the flows are unstable and the vortex plasma is completely uncorrelated. Figure adapted from Ref. [92]. (b) The expected qualitative temperature dependence of the superfluid density in a thin ^{4}He film. The dotted line corresponds to the BKT line (Eq. 2.22) and the dashed line denotes the $T = 0$ superfluid density. The universal jump and T_{BKT} (marked here as T_c) occur where the BKT line intersects the superfluid density [87]. (c) Experimental measurements of the superfluid density in a variety of thin ^{4}He films with different coverages, obtained via measurements of the angular momentum of persistent currents in helium condensed onto a rotating ring (coverages are indicated in units of 10^{-5} mol m^{-2}). The magnitude of the superfluid density jump is proportional to T_{BKT} [93]. (d) Collected results for the measured universal superfluid jump from several torsion oscillator experiments and third-sound measurements. The BKT line of Eq. 2.22 fits the data to better than 10% [94, 95].

such flows calculated for different values of the temperature, with arrows indicating the direction of increasing ℓ, are shown in Fig. 2.5(a). It can be seen that at high temperatures (corresponding to the red colored flows) the fugacity $z_\ell \to \infty$ as $\ell \to \infty$. At $T \gg T_{BKT}$ the flows are completely unstable and the system is in the normal state (marked as Region III). Just above T_{BKT}, in Region II, the flows contain a minimum for some value of ℓ, pointing to the formation of a vortex plasma state with zero superfluid density. It is in this second region where the system is characterized by the Kosterlitz vortex correlation length,

$$\xi_+ \simeq a e^{\pi/\sqrt{4z_0 t}} \tag{2.21}$$

($t = T/T_{BKT} - 1$ is the reduced temperature) that notably depends upon the square root of T. At low temperatures (blue colored flows in Region I), on the other hand, $z_\ell \to 0$ as $\ell \to \infty$. The highest temperature where this limiting behavior holds is shown by the black curve and corresponds to the temperature defined by $\rho\hbar^2/\epsilon_\ell k_B T m^2 = 2/\pi$. As T approaches T_{BKT} from below the Kosterlitz vortex correlation length $\xi_- \to \infty$. Therefore, for all temperatures $k_B T \leq \pi\rho\hbar^2/2\epsilon_\ell m^2$ the system is in a long-range ordered state without free vortices. As a result, from Eq. 2.19, the magnitude of the superfluid density jump at T_{BKT} is defined as

$$\rho_s = \frac{2m^2 k_B T_{BKT}}{\pi\hbar^2}. \tag{2.22}$$

This jump is considered to be universal because it depends only on the constants 2 and π, which were obtained by repartitioning the total energy of the vortices between the core energy and potential energy in a scale-independent way. The universality of the jump was confirmed experimentally by measurements of the superfluid density in thin films of superfluid ^{4}He [93–96]. The results of these measurements are summarized in Fig. 2.5(c) and (d), which show that for a variety of ^{4}He films with different superfluid densities and measured via different techniques the magnitude of the superfluid jump at T_{BKT} is always given by the result in Eq. 2.22 to within 10% accuracy. It must be stressed that this result presupposes a *neutral* superfluid; the derivation rests upon the requirement that the interaction potential is of the form $V(|\vec{r} - \vec{r}'|) \propto \ln(|r - r'|/a)$.

2.2.3 BKT Transition in Superconductors

In the most general sense, the existence of a transition that destroys long-range order at $T \neq 0$ in a 2D system requires that it be possible to describe such a system as an effective 2D Coulomb gas. This is because the interaction potential in the 2D Coulomb gas model is logarithmic in r. Systems that can be classified in the so-called *2D-XY universality class* satisfy this requirement because the 2D-XY Hamiltonian (see Eq. 2.5) produces the necessary logarithmic potential when integrated over the sample volume. The 2D-XY model treats a system as an array of planar rotators whose states are specified by only a single variable, φ (the in-plane orientation angle of a rotator). The restriction of the rotators to lie in the plane forces the boundary conditions to be defined such that integration along a closed path gives a total phase which must be an integer multiple of 2π. Furthermore, the topology of the system implies that this integer value of the phase is a *topological invariant*; because the allowed values of the total phase are discrete and disconnected, it is not possible to

obtain one state of the system from another simply through a smooth transformation or deformation of the rotators. Transitions from one state to another require a discrete tear or dislocation in the system that is associated with a large energy cost. As a result it can be said that the long-range ordered state at low temperatures in 2D systems is *topologically protected*, and the transition corresponds to a change to a state that is defined by continuous rather than discrete phase rotations. However, as shown by Wegner, spontaneous symmetry breaking does not occur at finite temperatures in the 2D-XY model [79]. This kind of phase transition therefore stands in contrast to usual phase transitions, which are characterized by a definite change in the symmetry of the system.

Various types of transitions and exotic states can be characterized as forms of topological order in addition to the neutral 2D superfluid already discussed [97]. Of the many kinds of topological order that are theoretically possible, quantum Hall states [98], topological insulators [99], and Weyl and Dirac semimetals [100] in particular have been experimentally realized. Thus, the work by Berezinskii, Kosterlitz, and Thouless on vortex unbinding transitions [83, 84] and the development of the renormalization group theory by Kosterlitz [86] laid the ground work for the discovery of new phases of matter which cannot be classified by their patterns of symmetry breaking [85]. For this contribution Kosterlitz and Thouless were awarded the Nobel Prize in Physics in 2016.

As pointed out by Kosterlitz and Thouless in their seminal paper, however, certain classes of 2D models do not show long-range order or a topological phase transition [84]. Foremost among these is the 2D Heisenberg model, where the rotators are not completely confined to the plane but may take on out-of-plane magnetization components. Formally this is because the Heisenberg model is described by the O(3) n-vector model whereas the XY model is an O(2) system. In this case the orientation of the rotators is described by two polar angles θ and φ such that the energy of a single dislocation (in the continuum limit) is given by

$$U_{\text{Heisenberg}} \propto \frac{1}{2} \int \int \left[(\nabla\theta)^2 + \sin^2\theta (\nabla\varphi)^2 \right] dxdy.$$

In this system $\int \nabla\varphi dx$ is not a topological invariant because a twist by 2π in the variable φ can be smoothly undone by a transformation of θ. The energy turns out to be finite without a logarithmic dependence and so there can be no transition. A second system in which a topological phase transition should not occur is that of a 2D superconductor, although for different reasons than for the Heisenberg model. While vortices in a 2D superconductor can be described by the 2D-XY model, the total interaction energy of a vortex-antivortex pair must include the coupling energy of the electric current to the magnetic field of the flux lines. Following Abrikosov's description of the magnetic flux lines in a superconductor, it can be shown that the interaction energy of such a vortex pair in 2D is given by

$$U_{\text{Abrikosov}} = \left(\frac{\Phi_0}{2\pi} \right)^2 \frac{1}{|\vec{r} - \vec{r}'|}$$

at large distances, where Φ_0 is the flux quantum [101, 102]. This result clearly differs from that of the neutral superfluid, which does not contain an energy contribution from the magnetic field and so has a logarithmic dependence of the interaction energy.

Put another way, the energy associated with the diamagnetism in the Meissner state of a superconductor interferes with the vortex dynamics in a 2D superconductor such that the system can no longer be fully described by the neutral 2D Coulomb gas model.

Following Kosterlitz and Thouless it was soon realized by Beasley, Mooij, and Orlando that the universal superfluid jump observed in ^{4}He is indeed also observable in a 2D superconductor if the superconductivity is considered in a certain limit [103]. The limiting factor in this case isn't the London penetration depth λ but rather the transverse penetration depth (Pearl length) $\lambda_\perp = \lambda^2/d$, where d is the thickness of the thin superconducting film, because the diamagnetism in a thin superconducting film is reduced by a factor d/λ. When $\lambda_\perp \approx \lambda$ the diamagnetic screening bounds the supercurrents to tightly circle the vortex cores and the energy is dominated by the magnetic vector potential. However, as λ increases (or as d decreases) the magnetic vector potential has a diminishing contribution and the range of the supercurrents extends further and further from the vortex cores. In the limit $\lambda_\perp \gg \lambda$ the vortex energy becomes dominated by the contribution from the superfluid velocity field and the description of the superconducting vortices becomes formally similar to that of neutral superfluid vortices in ^{4}He [104]. When the transverse penetration depth is significantly larger than the typical inter-vortex separation distance, $\lambda_\perp \gg |\vec{r} - \vec{r}'|/2$, the interaction energy is given by [101]

$$U_{\text{Pearl}} \approx \left(\frac{\Phi_0}{2\pi}\right)^2 \frac{1}{\lambda_\perp} \left(\ln \frac{\lambda}{|\vec{r} - \vec{r}'|}\right)$$

and the logarithmic dependence of the interaction on r is recovered. The criteria to observe the universal superfluid jump in a 2D superconductor, therefore, is that the thickness d of the film be thin enough such that $\lambda_\perp$ be comparable to the lateral dimensions of the sample.

For a thin film of thickness d, the internal energy of a single vortex is

$$U = \left(\frac{\Phi_0}{4\pi}\right)^2 \frac{d}{\lambda^2} \ln \frac{\lambda}{\xi_{\text{GL}}}.$$

In the absence of an applied external magnetic field vortex-antivortex pairs consisting of two vortices of opposite handedness will be spontaneously generated from thermodynamic fluctuations such that the total flux passing through the film remains zero, as in the case outlined above for the neutral superfluid. The total internal energy of a vortex-antivortex pair is therefore given by

$$U = 2\left(\frac{\Phi_0}{4\pi}\right)^2 \frac{d}{\lambda^2} \ln \frac{R_{12}}{\xi_{\text{GL}}}.$$

As before, the cutoff of the integration of the vortex kinetic energy is at the vortex-antivortex separation distance R_{12}, yielding $\ln R_{12}/\xi_{\text{GL}}$ rather than $\ln \lambda/\xi_{\text{GL}}$, because beyond $\sim R_{12}$ the net supercurrent flow is zero. From this internal energy, then, the BKT transition temperature for the 2D superconductor is

$$k_B T_{BKT} = \frac{{\Phi_0}^2}{32\pi^2} \frac{d}{\lambda^2} \tag{2.23}$$

with a Nelson-Kosterlitz superfluid jump given by

$$\rho_s = \frac{32\pi^2 k_B T_{\mathrm{BKT}}}{{\Phi_0}^2 d}. \tag{2.24}$$

To quantify the typical penetration depths and sample dimensions needed to observe the vortex unbinding transition in a superconductor, it is helpful to cast Eq. 2.23 for superconductors in the dirty limit as [103]

$$\lambda_\perp = \frac{0.98}{T}\ [\mathrm{cm}].$$

For conventional BCS superconductors with $T_{BKT} \approx T_c \sim 10$ K we find that $\lambda_\perp$ must be on the order of ∼1 mm or larger. To observe the universal superfluid jump in a superconductor, therefore, it is necessary to study samples which have large London penetration depths or very small thicknesses. Typically this involves samples with high normal-state sheet resistances or thicknesses that approach only a single unit cell.

In addition to the size of the superfluid density jump at T_{BKT}, the functional form of $\rho_s(T)$ below the vortex unbinding transition is of interest. From the solution of the Kosterlitz renormalization equations (Eqs. 2.20) and expanding z_ℓ to first order in the reduced temperature $t = (T_{BKT} - T)/T_{BKT}$, it is found that below T_{BKT}

$$\lim_{\ell\to\infty} \frac{\hbar^2 \rho_s(T)}{k_B T m^2} = \frac{2}{\pi}\left[1 + (2Bt)^{1/2}\right] \tag{2.25}$$

where B is a function of $\epsilon_c = \epsilon_{\ell\to\infty}(T_{BKT})$. This "square-root cusp" behavior is the second hallmark of the BKT transition [105]. It is well known that phase slips due to vortex motion give rise to finite electrical resistance in superconductors and superconducting arrays below the mean-field critical temperature T_{c0} [106,107]. Vortex motion can also lead to dissipation at temperatures above the resistive transition in thin film superconductors [108]. To describe this behavior Ambegaokar, Halperin, Nelson, and Siggia (AHNS) developed a dynamic theory of the vortex unbinding transition by combining Kosterlitz's equilibrium renormalization group theory with the Ginzburg-Landau understanding of vortex dynamics in superfluids [109–111]. An analogous theory was developed by Shenoy for Josephson junction arrays and superconducting wire networks [112]. Importantly, the AHNS theory predicts a nonlinear resistance below T_{BKT}, where $V \propto I^{\alpha(T)}$, with $\alpha(T_{BKT}) = 3$. The resistance is linear at temperatures $T \geq T_{c0}$ so the vortex plasma state between T_{BKT} and T_{c0} is evidenced by a crossover regime. In the vicinity of the transition $\alpha(T) \approx 3 + (8Bt)^{1/2}$; comparing to Eq. 2.21 it is evident that $\alpha(T)$ identifies with the Kosterlitz vortex correlation length ξ_+, which depends on $t^{-1/2}$. This square-root temperature dependence of the vortex correlation length is in marked contrast to the Ginzburg-Landau coherence length and its power-law temperature dependence, $\xi_{\mathrm{GL}}^2 \simeq 1/(T - T_c)$. This raises the possibility that the square-root cusp (and BKT transition) may be identified through a scaling analysis of nonlinear I–V data.

Dc transport studies on a variety of conventional thin film superconductors (Hg-Xe [113, 114], In/InO_x [115], Pb [116], NbN [117, 118]) and Josephson-coupled arrays [119,120] appear to agree with the AHNS scaling predictions. As seen in Fig. 2.6, temperatures where $\alpha(T)$ deviates from 1 are identified with the BCS mean-field critical temperature T_{c0} and temperatures where $\alpha(T)$ crosses 3 are identified as T_{BKT},

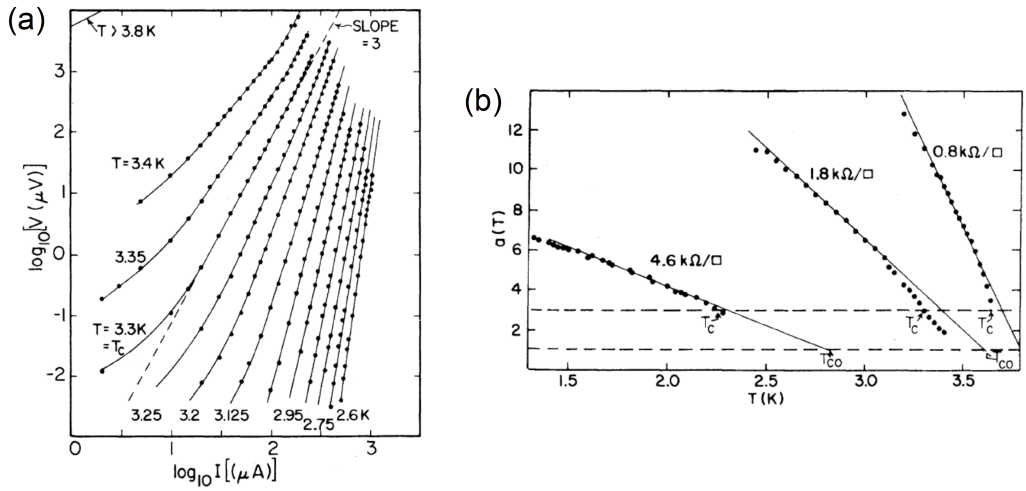

Figure 2.6 In a classic experiment, Kadin *et al.* [113] measured the noninear I–V behavior from vortex fluctuations in a series of Hg-Xe alloys. (a) In a representative 150 Å film the nonlinear exponent $\alpha(T)$, $V \propto I^{\alpha(T)}$, reaches a value of $\alpha = 3$ at $T_{BKT} = 3.3$ K (labeled here as "T_c"). The crossover behavior from $\alpha = 1$ to $\alpha = 3$ for isotherms above T_{BKT} is characteristic of the vortex plasma state. (b) A plot of the exponents $\alpha(T)$ extracted from (a) as a function of temperature, for several different samples. The temperature where $\alpha = 1$ is identified as the BCS mean-field critical temperature T_{c0}. Samples with increasing sheet resistances have increasing distance between T_{BKT} and T_{c0}, reflecting that larger sheet resistances imply longer transverse penetration depths $\lambda_\perp$. Figure adapted from Ref. [113].

with $T_{BKT} < T_{c0}$. Furthermore, scaling analysis shows that the measured resistance does indeed scale with $t^{1/2}$ below T_{BKT}, at least over the temperature ranges investigated, suggestive of the existence of the square-root cusp (see Fig. 2.7). Several groups thus reported the observation of the BKT vortex unbinding transition in thin film superconductors based primarily on the results of such I–V scaling analyses. However, several factors complicate the analysis of the I–V measurements and the correct interpretation of the data is not clear. First, reports of the vortex unbinding transition based on dc transport measurements are at most an indirect probe of BKT physics because the superfluid density must be deduced from the scaling exponent. Second, the degree of homogeneity of the samples plays an important role, as granularity and disorder introduce additional resistance and broaden the transition. Third, the range of overlap of the critical region with the domain of applicability of the Ginzburg-Landau theory, and hence the proper way to correct the analysis at low temperatures, is unclear, as is the proper method of accounting for strong-coupling effects [114]. Reports of the effective vortex dielectric constant ranging from $\epsilon_c = 1.2$ to as high as $\epsilon_c = 1.9$ indicate nonuniversality and strong renormalization of the superfluid density [113, 121]. Large values of ϵ_c also imply high vortex fugacity that calls into question the validity of the BKT theory in the analysis, because the BKT theory in its standard form lies in the dilute $z_\ell \to 0$ limit. Fourth, the I–V data and scaling analysis turn out to be sensitive to finite-size effects and the details of the noise floor of the measurements [122–124]. Measurements that feature a lower noise floor (a larger dynamic range) result in artificially lower extracted values of T_{BKT} and higher values of the vortex fugacity. The I–V curves at temperatures below the transition may also appear to collapse together in the scaling analysis, which should not

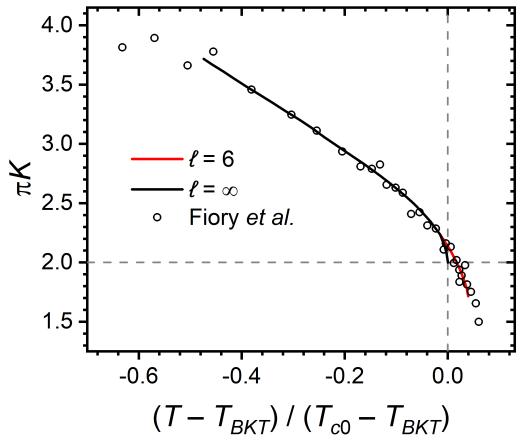

Figure 2.7 Observation of the characteristic "square-root cusp behavior" below T_{BKT} in a 100 Å thick In/InO_x thin film with $T_{BKT} = 3.234$ K. One signature of the BKT transition is the square root temperature dependence of the superfluid density ($K = \rho_s \hbar^2 / k_B T m^2$) upon approaching T_{BKT} from below. The data are extracted from nonlinear I–V measurements. Fits of the data to Eq. 2.25 for $\ell = 6$ and $\ell = \infty$ (red and black curves, respectively) illustrate that the system is more properly described by a finite rather than infinite length scale. Gray dashed lines mark the position of the Nelson-Kosterlitz universal jump at $K = 2/\pi$. The lack of a sharp jump at $T = T_{BKT}$ is due to finite-size effects. Figure adapted from Ref. [125].

occur because the vortex correlation length ξ_- below T_{BKT} is infinite. Thus it is clear that more direct, smoking-gun experimental signatures are needed to establish the existence of the vortex unbinding transition and BKT physics in 2D superconducting systems.

These considerations leave direct measurement of the superfluid density jump as the most natural way forward. The Nelson-Kosterlitz universal jump, first observed for superconductors in thin Al films [126], has since been observed in InO_x [125], NbN [127, 128], and highly disordered $MoGe_x$ films [129–131], although reports remain scarce. As depicted in Fig. 2.8(a), measurements typically show a broadening of the jump and a characteristic frequency dependence in the temperature at which the jump occurs. When combined with the time-dependent Ginzburg-Landau theory the AHNS theory gives a prediction for the frequency dependence of the conductivity that includes a smooth jump in the inductance and the appearance of a peak in the dissipation at T^{ω}_{BKT}, with the apparent T^{ω}_{BKT} increasing with increasing probe frequency [110, 111]. The salient feature of the AHNS dynamical theory is the frequency dependent vortex diffusion length $l_\omega = \sqrt{14\mathcal{D}/\omega}$, where $\mathcal{D} = 2e^2\xi^2_{GL} k_B T/\pi\hbar^2\sigma_n$ is the vortex diffusion constant [132]. The vortex response at ω is dominated by vortices separated by a distance $r \sim l_\omega$, so the peak in the dissipation and T^{ω}_{BKT} occur above the dc T_{BKT} when $\xi_+(T) \sim l_\omega$. This dynamical theory successfully fit the measurements of the superfluid density jump and current dissipation in thin ^{4}He films [95]. However, probes of vortex thermal relaxation in the vortex plasma state of thin film superconductors have shown that the thermal relaxation times are temperature independent and shorter than the prediction of the AHNS theory by almost two orders of magnitude [133]. A thorough study of In/InO_x films, which compared the superfluid density jump obtained from two-coil mutual inductance techniques to dc transport

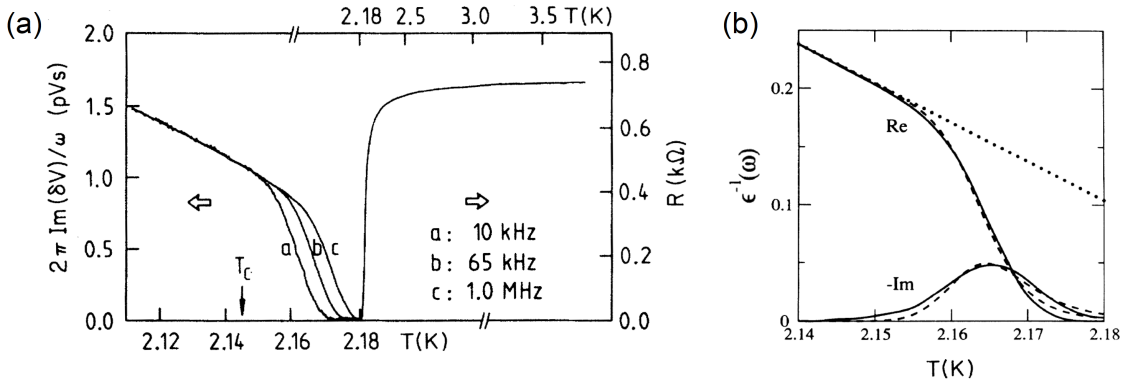

Figure 2.8 High resolution measurements of the universal superfluid density jump in superconducting Al wire networks obtained from two-coil mutual inductance. Superconducting wire networks are prototypical realizations of the 2D-XY universality class and so their behavior represents the ideal response. (a) The dependence of the superfluid density jump on probe frequency, at 10 kHz, 65 kHz, and 1.0 MHz. With increasing probe frequency the temperature T_ω of the jump shifts higher but the broadness of the jump remains unchanged. Figure adapted from Ref. [135]. (b) The measured superfluid density jump, $\mathrm{Re}[\epsilon^{-1}(\omega)]$, compared with the magnitude of the dissipation peak height, $\mathrm{Im}[\epsilon^{-1}(\omega)]$, near T_{BKT} for a probe frequency of 65 kHz (solid lines). The dashed lines correspond to fits calculated from Minnhagen's interacting 2D Coulomb gas phenomenology. The phenomenological fits qualitatively describe both the real and imaginary parts of the dynamical conductivity and are Kramers-Kronig consistent. The dotted line represents the initial parameter $\epsilon_0(T)$, which is an input to the model. Figure adapted from Ref. [136].

measurements, was unable to find agreement between values of T_{BKT} obtained from the dynamical conductivity and I–V scaling analyses [125]. On the other hand, the magnetoresistance and the temperature dependence of the critical field H_{c1} were found to be in accord with a separate dynamical phenomenology based on the interacting 2D Coulomb gas model, put forward by Minnhagen [134].

High resolution studies of the superfluid density jump and dissipation peak obtained by two-coil mutual inductance measurements in Al wire networks [135], shown in Fig. 2.8, demonstrated that the discrepancies of the AHNS dynamical theory lie in the treatment of the scaling in the Kosterlitz renormalization equations when a finite-range cutoff is encountered [136]. The Kosterlitz-Thouless theory in its standard form is valid as $\ell \to \infty$ so the AHNS dynamical theory is applicable in the infinite-range limit. However, when the logarithmic interaction potential between vortices is modified by a finite-size cutoff, as in the case for superconductors, the shape of the jump is distorted. The AHNS model contains five fit parameters and so can be made to agree with conductivity data to a high degree of accuracy despite the fact that the contributions from bound and free vortices enter the model separately (no interactions between bound and free vortices are considered). When a finite-range cutoff ℓ_{cut} is used to model finite-size effects above T_{BKT} the resulting real and imaginary parts of the complex conductivity $\tilde{\sigma}(\omega) = \sigma_1(\omega) + i\sigma_2(\omega)$ are no longer Kramers-Kronig consistent, demonstrating a loss of causality. Causality can be restored by introducing a long-range dielectric constant $\mathrm{Re}\,[\epsilon(\ell)] = \mathrm{Re}\,[\epsilon(\ell_{\mathrm{cut}})]$ for the bound vortex-antivortex pairs at $\ell > \ell_{\mathrm{cut}}$ in a piecewise fashion, but this procedure introduces a discontinuity in the fits of both $\sigma_1(\omega)$ and $\sigma_2(\omega)$. The Coulomb gas model of Minnhagen, on the

other hand, constructs a fully Kramers-Kronig consistent description of the dynamical conductivity by treating the Coulomb gas charges with the Langevin equation and defining the dissipation as the Kramers-Kronig transform of $\mathrm{Re}\,[\epsilon(\omega)]$ [87]. A consequence of this definition is that the ratio of the dissipation peak height to the superfluid density (calculated at the temperature of the dissipation peak) is given by

$$\frac{-\,\mathrm{Im}[\epsilon^{-1}(\omega)]}{\mathrm{Re}[\epsilon^{-1}(\omega)]} = \frac{2}{\pi}. \tag{2.26}$$

This treatment of the dynamic vortex response, which has zero adjustable parameters, agrees with the temperature dependence of the superfluid density jump and dissipation peak measured in Al wire networks [136]. The fit of Minnhagen's model to the measurements on Al networks is shown in Fig. 2.8(b). However, in real superconducting films, the temperature dependence of $\rho_s(T)$ is influenced by a variety of other interactions and excitations, such as phase fluctuations, BCS-like quasiparticle excitations, or interlayer Josephson coupling. The results therefore point to the need for modified Kosterlitz renormalization group equations for superconductors which properly take into account the finite-scale cutoff of the logarithmic vortex interaction potential.

Extensions to the Kosterlitz-Thouless theory have been developed by numerous groups by considering the next higher order terms of the renormalization group expansion. It turns out that the 1D Luttinger liquid problem is in the same universality class as the 2D Coulomb gas and XY models, so the BKT problem can be mapped into the 1D sine-Gordon model [138]. This is advantageous because in the Coulomb gas and XY models the vortex core energy is fixed by the Pearl energy and the short-range cutoff, while in the sine-Gordon model the vortex core energy is defined through the fugacity and can take a range of values. Minnhagen and coworkers developed such a phenomenology in the late 1980s which predicted that the superfluid density jump is nonuniversal and that the BKT line terminates in an Ising-like critical end point at high fugacities [139–142]. However, numerous Monte Carlo simulations have shown that the Minnhagen phenomenology is not consistent with obtained results and that its validity is questionable, because in its mapping of the Coulomb gas (which is exact only for point charges) to the sine-Gordon field theory the short-range repulsion is added in *post facto* [143, 144]. Nevertheless, there have been experimental reports of nonuniversal superfluid density behavior in InO_x thin films [121, 145], and measurements of the superfluid density jump in thin NbN films show a jump that is smeared out instead of sharp and begins at a temperature below the T_{BKT} value expected from the pure XY model [127].

More recently, Benfatto and coworkers have developed a sine-Gordon description of the BKT problem in both conventional and layered superconducting thin films by carefully considering the role of vortex core energy and disorder [30, 31]. In the pure XY model the vortex core energy μ is related to the energy of the superfluid stiffness J as $\mu_{XY} \approx 4.9J$ (see Eq. 2.9). For a vortex in a 2D BCS superconductor in the sine-Gordon treatment, on the other hand, $\mu_{\mathrm{BCS}} \approx 0.95J$. By including Gaussian-distributed homogeneous disorder it is possible to fit the experimental NbN data of Ref. [127] with vortex core energies $\mu \lesssim J$. Examples of these fits are depicted in Fig. 2.9. The disorder accounts for the broadening of the superfluid density jump while the reduction in μ from μ_{XY} accounts for the shift in T_{BKT}; a smaller value of μ results in a shift of T_{BKT} below the pure XY value, while a larger μ shifts T_{BKT} to

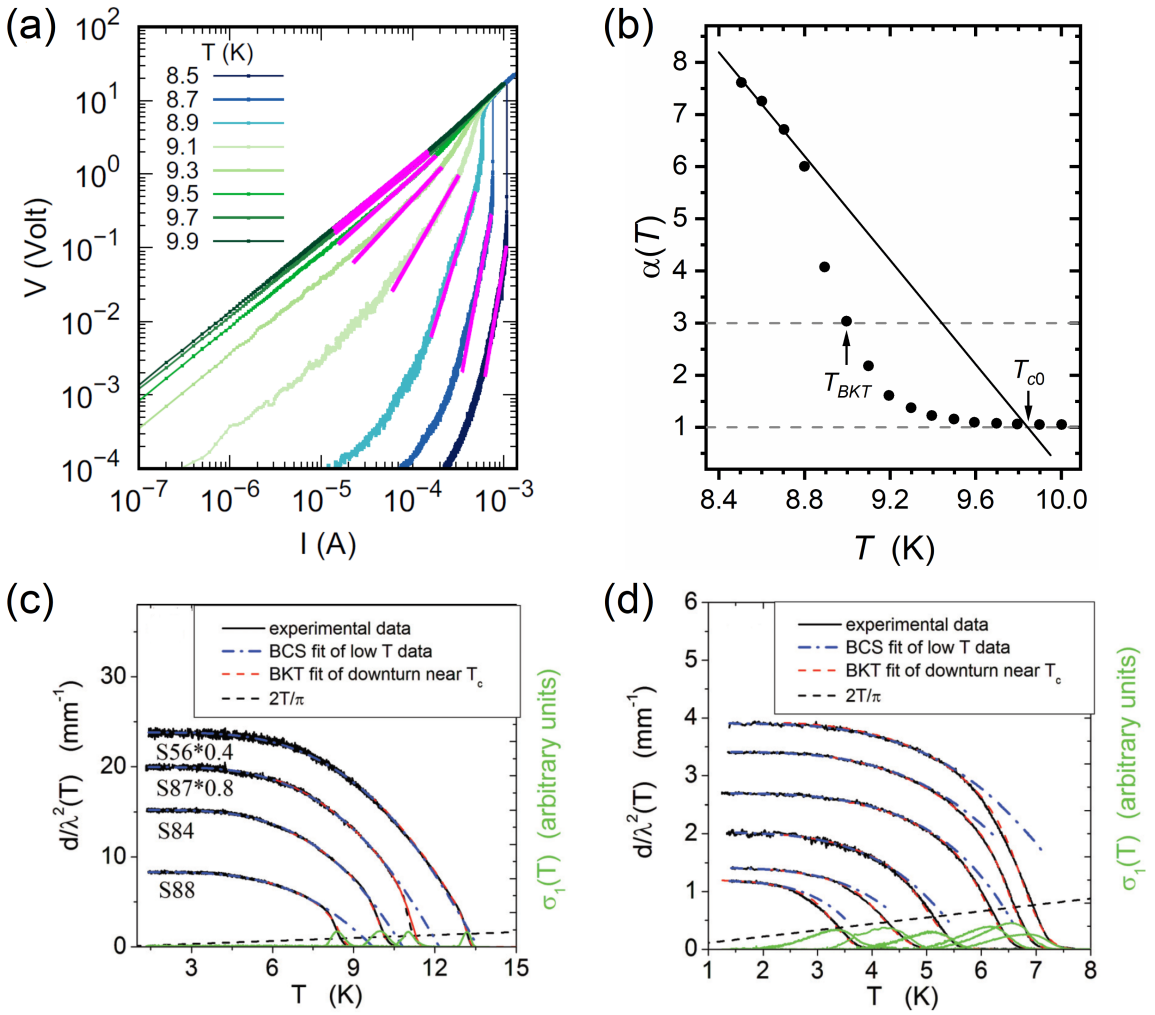

Figure 2.9 The "paradigmatic" case: BKT transition in NbN. (a) Dc transport measurements of the nonlinear resistivity $V \propto I^{\alpha(T)}$ in a 3 nm thick NbN film. The slopes of the pink lines give the values of the exponent $\alpha(T)$. Figure from Ref. [118]. (b) The exponent of the nonlinear resistivities extracted from (a) plotted as a function of temperature. The point where $\alpha(T)$ crosses 3 gives $T_{BKT} \approx 9.0$ K, while the linear extrapolation of the low temperature data to $\alpha = 1$ gives $T_{c0} \approx 9.9$ K. These values agree with T_{BKT} and T_{c0} obtained from more detailed sine-Gordon renormalization group procedures. Data and figure adapted from Ref. [118]. (c) The superfluid density in several moderately disordered NbN films as measured by two-coil mutual inductance. At low temperatures the data (black curves) show good agreement with a BCS fit (blue dashed curves), while near T_{c0} the data deviates from the expected BCS curve. Importantly, the deviation from the BCS curve begins at temperatures below the value of T_{BKT} expected from the pure 2D-XY model (black dashed line). The data in the full temperature range is well-described, on the other hand, by the sine-Gordon renormalization group model taking into account Gaussian-distributed disorder and significantly reduced vortex core energy (red dashed curve). Deviations of the superfluid density are only found in a narrow temperature range within $\sim 0.1 T_{c0}$ of the mean-field critical temperature. The dissipation peaks in the dynamical conductivity at T_{BKT} are shown in green. (d) The same as in (c), but for a series of highly disordered NbN films. The highly disordered films show broader deviations from the BCS model that begin at lower temperatures than for moderately disordered films. The width of the dissipation peaks is accordingly also significantly broadened. Still, the data is well fit by the phenomenological model of Benfatto *et al.* [30, 31]. Panels (c) and (d) are adapted from Ref. [128].

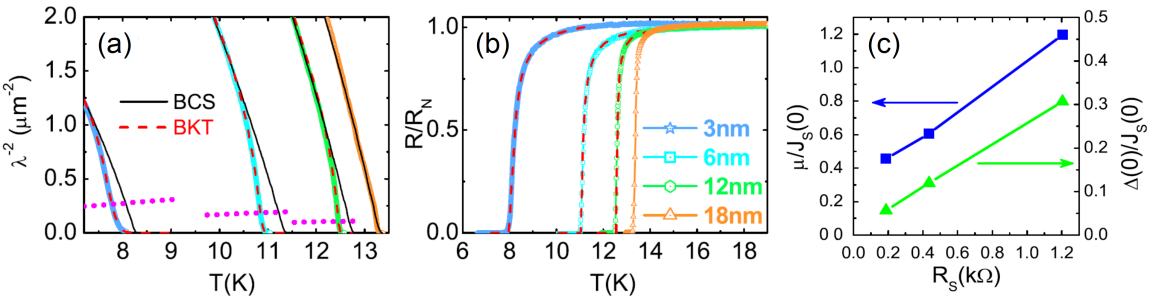

Figure 2.10 Thickness dependence measurements of the BKT transition for NbN films with thickness 3 nm, 6 nm, 12 nm, and 18 nm. (a) Measurements of the superfluid density jump show that with decreasing thickness T_{c0} decreases and the quantity $T_{c0} - T_{BKT}$ increases. Also, disorder is larger and broadens the jump more with decreasing thickness. Nevertheless, the full temperature dependence for each film can be fit accurately with the phenomenology of Benfatto *et al.* [30, 31]. Black lines correspond to a BCS fit of the low-temperature data and pink dotted lines represent the expected T_{BKT} in the pure 2D-XY model. (b) The phenomenological model simultaneously fits the resistivity measurements of each film above T_{BKT}. (c) As a function of film sheet resistance, the ratio of the vortex core energy μ to the superfluid stiffness J_s (blue squares) tracks the ratio of the BCS gap Δ to the superfluid stiffness (green triangles). The increase of μ with increasing disorder is caused by the separation between the energy scales Δ and J_s. Figure from Ref. [137].

higher temperatures. Furthermore, thickness-dependence measurements on NbN thin films reveal that the value of μ/J tracks the ratio of the gap energy to the superfluid stiffness, Δ/J, indicating that the increase in vortex core energy with decreasing film thickness is explained by a separation of the energy scales corresponding to pairing and phase coherence [137]. These measurements are illustrated in Fig. 2.10. Since μ scales with Δ it means that the strength of the Cooper pair coupling controls the position of T_{BKT}. An extension of the Benfatto phenomenology to time-dependent vortex dynamics has shown that film disorder once again plays a crucial role in the complex conductivity by limiting the characteristic vortex diffusion length to the length scale of the disorder-induced superconducting inhomogeneities, a value notably less than the diffusion length of the normal electrons residing in the vortex cores [146]. Most recently, Monte Carlo simulations have provided evidence suggesting that while disorder does not change the universality class, superconducting inhomogeneities associated with *correlated* disorder broaden the superfluid density jump around T_{BKT} in contrast to uncorrelated disorder, which plays a minimal role [147, 148]. This result is in agreement with Harris's long-standing prediction [149] that small amounts of random disorder should not change the critical behavior (the "Harris criterion"). To further elucidate the role of correlated disorder and vortex core energy it will be necessary to apply the model to the temperature dependence of the superfluid density and complex conductivity in other conventional superconductors such as InO_x and $MoGe_x$, as well as the cuprate high-T_c materials. The case of the cuprates, however, appears more challenging due to the complicated role played in those materials by the many competing orders that exist across their phase diagram in addition to the interlayer Josephson coupling.

2.2.4 The BKT Transition in Cuprate Thin Films

As discussed in the previous section, vortex unbinding is dominant when superfluid densities are low and the system is 2D-like, implying that the BKT transition should be more visible in layered superconductors with weak interplane coupling because the Pearl transverse penetration depth $\lambda_\perp$ is large. It is thus a natural extention to look for the BKT transition in the layered cuprate materials. Details of the transition, such as scaling behavior and the shape of the superfluid density jump, will give insight into the role of disorder, competing orders, and the nature of the Cooper pair coupling because these will all modify the vortex core energy and superfluid stiffness. Ideally, to gain the greatest insight into BKT physics in cuprates, the BKT transition should be studied in both bulk crystalline and thin film samples as well as across the full phase diagram.

Until this point the discussion has focused entirely on conventional thin film superconductors and superfluids, systems that are characterized by the 2D-XY universality class. Bulk superconductors, on the other hand, being fully three-dimensional, may fall within a different universality class. In conventional 3D systems, the "Ginzburg criterion" that determines the range about T_c where fluctuations dominate over mean-field behavior is only on the order $\delta T/T_c \sim (T_c/E_F)^4 \sim 10^{-12}$, an inaccessibly narrow temperature range [150]. Indeed, in Fig. 2.10(a, b) the BKT transition is no longer present already at film thicknesses of just $d \gtrsim 18$ nm (orange curves). In contrast to type-I superconductors, however, type-II superconductors experience a reduction of dimensionality from D to $D-2$ in the presence of an applied magnetic field [151]. The critical behavior of a bulk 3D type-II superconductor becomes effectively one-dimensional at fields below H_{c2} because the electrons become confined to Landau orbits that lie on cylinders centered on the flux lines [152]. In highly type-II superconductors, where $\lambda \gg \xi_{\mathrm{GL}}$, the magnetic screening is weak so the system is characterized by a very small effective charge $e_{\mathrm{GL}} = \xi_{\mathrm{GL}}/\lambda$. Upon approaching T_c from below, then, there is an initial crossover from GL mean-field behavior to the regime of a weakly charged superfluid that is described by the XY model. Such a bulk system is therefore expected to fall within the 3D-XY universality class with $\lambda \sim |T - T_c|^{(2-D)\nu/2}$, where the critical exponent $\nu = 2/3$ [153].

In the presence of a moderate applied magnetic field, $H_{c1} < H \ll H_{c2}$, the flux lines in a type-II superconductor form a vortex lattice with lattice spacing $a_v = \sqrt{\Phi_0/H}$. As H increases the flux lattice melts into a vortex fluid when a_v becomes comparable to the characteristic wavelength of the vortex fluctuations. For a layered superconductor the out-of-plane coherence length ξ_c is typically smaller than the in-plane one ξ_{ab} and the layered system is described by the anisotropy parameter $\eta = \xi_c/\xi_{ab}$; the out-of-plane vortex lattice spacing is therefore smaller than a_v by the factor η. In the presence of strong anisotropy where $\eta \ll 1$ the system can exhibit 2D behavior if ηa_v becomes less than the interlayer spacing d, since the individual superconducting layers become uncorrelated. However, experimental measurements of the transport properties, magnetization, heat capacity, magnetoresistance, penetration depth, and thermal expansion in bulk $YBa_2Cu_3O_{7-\delta}$ samples confirm that the RBCO system remains in the 3D-XY universality class despite significant anisotropy ($\eta \approx 1/6$) [154, 155]. In particular, as illustrated in Fig. 2.11(a) the magnetization, heat capacity, and magnetoresistance measured at different values of applied magnetic field all collapse onto the same universal curves with the scaling exponent $\nu = 2/3$ [18].

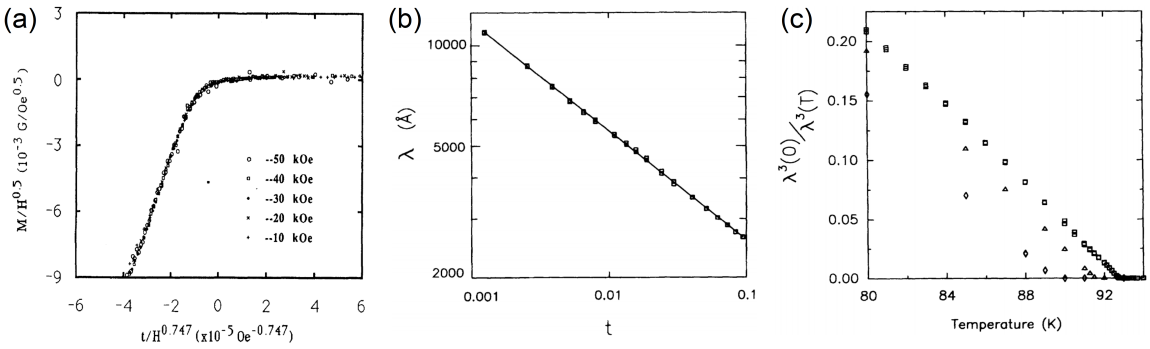

Figure 2.11 Experimental evidence that the *R*BCO family of cuprates falls within the 3D-*XY* universality class. Data was measured in clean, optimally doped single YBCO crystals. (a) The magnetization curve measured at five different field strengths, ranging from 10–50 kOe. The data was scaled according to the relation $M(H,T)/H^{1/2} = m(t/H^{1/2\nu})$, with $t = (T-T_c)/T_c$. The data measured at all magnetic fields collapses onto the same curve with the critical exponent $\nu = 0.669$. Figure adapted from Ref. [18]. (b) The magnetic penetration depth measured by microwave cavity perturbation. It is seen that $\lambda \propto |t|^{(2-D)\nu/2} = |t|^{-0.33}$, corresponding to $\nu \approx 2/3$, over three orders of magnitude in t. (c) The superfluid density, $\rho_s^{3/2}(T) = \lambda^3(0)/\lambda^3(T)$, of $YBa_2(Cu_{1-x}Zn_x)_3O_{6.95}$ for three different Zn doping levels: $x = 0$ (squares), $x = 0.0015$ (triangles), and $x = 0.0031$ (diamonds). At all three doping levels $\rho_s(T) \propto T^{2/3}$, indicating that *R*BCO remains in the 3D-*XY* universality class even in the presence of disorder. Panels (b) and (c) adapted from Ref. [19].

Accurate measurements of the penetration depth in highly pure single crystals show that $\lambda \propto |T - T_c|^{-1/3}$ as expected for 3D-*XY* scaling over a temperature range as wide as $0.1T_c$ below T_c; inclusion of small amounts of Zn impurities suggest that while T_c is reduced with disorder, the scaling behavior is unchanged in accordance with the Harris criterion [19, 149]. This trend is depicted in Figs. 2.11(b) and (c). Accordingly, detailed studies of the electrical resistance and magnetization both in the *ab* plane and along the *c*-axis show that close to optimal doping the 2D-like properties of single crystal *R*BCO appear only in a very narrow temperature range, with T_{BKT} occurring at most 0.2 K below T_c [156, 157]. In this very narrow temperature range the BKT transition is associated with vortex fluctuations in uncorrelated adjacent CuO_2 bilayers, because the energy of the vortex interactions within a given layer is on the order k_BT_c while the interaction energy between vortices in different layers is a factor λ/d smaller than k_BT_c [158, 159]. At temperatures further than ∼0.2 K below T_c the interlayer coupling becomes strong enough for 3D superconductivity to dominate.

One way, then, to make the BKT transition manifest in cuprates over a larger and more experimentally relevant temperature range is to reduce the coupling between CuO_2 planes by changing the doping level. In the underdoped regime, where *R*BCO is even more highly anisotropic ($\eta \lesssim 1/12$), adjacent CuO_2 bilayer units are only weakly Josephson coupled and superconducting fluctuations are observed to persist over a broader temperature range both above and below T_c. Thermal expansion measurements indicate that as doping is decreased the fluctuation range broadens to wider than 0.75–$1.5T_c$, with the upper temperature limit increasing linearly with decreasing doping [161]. More recent microwave cavity resonance and Nernst effect measurements apply a stronger bound to the temperature range, but still find that fluctua-

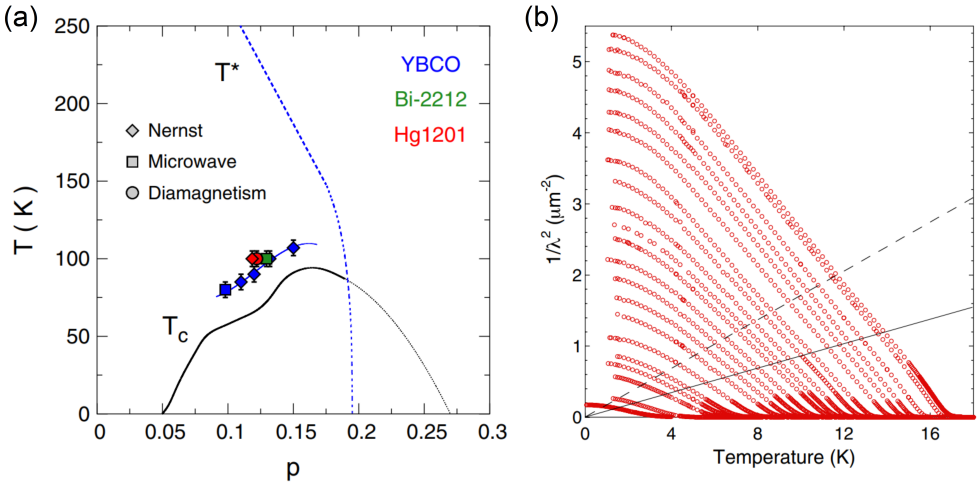

Figure 2.12 (a) The phase diagram for YBCO and other hole doped cuprates depicting the extent of superconducting fluctuations probed by the Nernst effect, microwave cavity resonance, and magnetization measurements. On the underdoped side of the superconducting dome the fluctuations extend at most ∼25 K above T_c. Figure from Ref. [160]. (b) Measurements of the superfluid density by mutual inductance methods in severely underdoped YBCO single crystals. The solid line represents the BKT line (Eq. 2.24) corresponding to one CuO_2 bilayer, while the dashed line denotes the BKT line for a single CuO_2 plane. The superfluid density passes linearly through the intersection points with these two lines, where the T_{BKT} would be expected, indicating the absence of the BKT transition even in strongly underdoped single crystals. As the quantum critical point $p_c \approx 0.054$ is approached the superfluid density $\rho_s(0) \propto (p - p_c)$ and $T_c \propto \sqrt{\rho_s(0)}$, indicating that the quantum critical fluctuations belong to the $(3+1)$D-XY universality class. Figure from Ref. [22].

tions persist up to 20–25 K above T_c and, as shown in Fig. 2.12(a), follow the shape of the superconducting dome on the underdoped side of the phase diagram [160,162]. Measurements of the c-axis optical conductivity by far-IR ellipsometry and reflectivity in underdoped YBCO crystals have also provided evidence that superconducting precursor fluctuations may survive within the CuO_2 bilayer units up to temperatures as high as 180 K [163]. In such data, the anomalous shift of an IR-active phonon near 320 cm^{-1} below an onset temperature $T^{ons} > T_c$ signals the increased concentration of optical conductivity spectral weight into a low-frequency, coherent Drude peak associated with short-lived preformed Cooper pairs within the CuO_2 bilayer units; below T_c this excess spectral weight collapses into the delta-function at $\omega = 0$. Nevertheless, no experimental evidence for the observation of the BKT transition in highly anisotropic, single crystal high-T_c cuprates falling within the 3D-XY universality class has yet been reported. Direct measurements of the superfluid density instead indicate that $\rho_s(T)$ passes linearly through the temperature range where the Nelson-Kosterlitz universal jump is expected from Eq. 2.24 [22], as illustrated in Fig. 2.12(b). Furthermore, the doping (p) dependences of $\rho_s(0)$ and T_c suggest that highly underdoped RBCO falls within the $(3+z)$D-XY universality class upon approaching the quantum critical point p_c, where $z = 1$ is the dynamical critical exponent, and that $\rho_s(0) \propto (p - p_c)$. These results imply that the superconductor-to-insulator transition in the underdoped regime is rather dominated by mean-field behavior with the 3D-XY critical region becoming inaccessibly narrow around T_c [164]. In this case the

characteristic 2D features of the individual superconducting layers are obscured by the complex relationship between 2D and 3D fluctuations caused by Josephson coupling between the CuO_2 planes [165, 166], as well as the variety of competing orders which are known to exist in the pseudogap region of the phase diagram [3, 160].

The second route to approach the crossover from 3D to 2D superconductivity is to increase the transverse penetration depth by reducing the film thickness to less than ξ_c. This reduces the effect of the Josephson coupling between the CuO_2 bilayers and, if near optimal doping, controls for the presence of competing orders on the underdoped side of the phase diagram. Indeed, it was shown that superconductivity is in fact stable in *R*BCO films down to thicknesses of a single unit cell [167–169]. However, early reports of the BKT transition in ultrathin YBCO layers sandwiched in YBCO/PrBCO superlattices based on dc transport measurements are controversial, because the data is either unclear or contradictory [170–175]. Much of the *I*–*V* scaling data shows a smooth rolloff from strongly nonlinear to ohmic behavior upon reducing the current across a wide range of temperatures. Repaci *et al.* [176] argued on the basis of this scaling analysis that the BKT transition is not present in ultrathin YBCO because the smooth rolloff reflects a crossover from vortex-antivortex pair breaking at high currents to a response dominated by free vortices nucleated by finite size effects and disorder at low currents, even significantly below T_c. Furthermore, fits of resistivity data above T_{BKT} to $\ln R \propto (T - T_{BKT})^{-1/2}$ tend to be problematic in a number of works because the fits are applied to a broad range of temperatures, certainly outside the domain of applicability of the Kosterlitz-Thouless and AHNS critical scaling theory [92]. Measurements of the superfluid density by mutual inductance techniques have been made on near optimally doped films thicker than 50 u.c. and appear to show that the BKT transition still only appears very close to T_c, and that optimally doped films thicker than 50 u.c. firmly remain in the 3D-*XY* universality class [177–180]. Vortex diffusion in 1–3 u.c. thick YBCO sandwiched between semiconducting $Pr_{0.6}Y_{0.4}Ba_2Cu_3O_{7-\delta}$ has been studied at microwave frequencies (megahertz to gigahertz) and discussed in terms of the dynamical AHNS theory [181]. However, in such samples the vortex-antivortex interactions appear to be obscured by strong pinning by defects that introduces a strongly temperature dependent vortex diffusion constant $\mathcal{D}(T)$, possibly due to interaction with the PrBCO layers or interdiffusion of Pr ions. It is not clear how the BKT transition or the temperature dependence of $\rho_s(T)$ is affected in this case.

Studies of the superfluid density by two-coil mutual inductance in ultrathin films of *strongly underdoped* Ca-intercalated YBCO have also been carried out. The results of these studies are reproduced and summarized in Fig. 2.13. Curiously, despite the increasing anisotropy with decreasing hole doping, films 20–40 u.c. thick remain in the (3+1)D-*XY* universality class upon approaching the quantum critical point with no indication of a superfluid jump [182], mirroring the situation in strongly underdoped YBCO crystals. In these films, which were also sandwiched between insulating PrBCO layers, 20–30% Ca^{2+} substitution was used to stabilize the YBCO due to the absence of CuO chains in the severely underdoped regime. In similar CaYBCO films with 2 u.c. thickness, on the other hand, the films were observed to fall within the (2+1)D-*XY* universality class [21], indicating the presence of the 3D to 2D crossover somewhere below 20 u.c. The highly underdoped 2 u.c. CaYBCO films showed unmistakable signatures of the Nelson-Kosterlitz superfluid jump at low temperatures (below 30 K). Fitting this superfluid density data with the phenomenology of Ben-

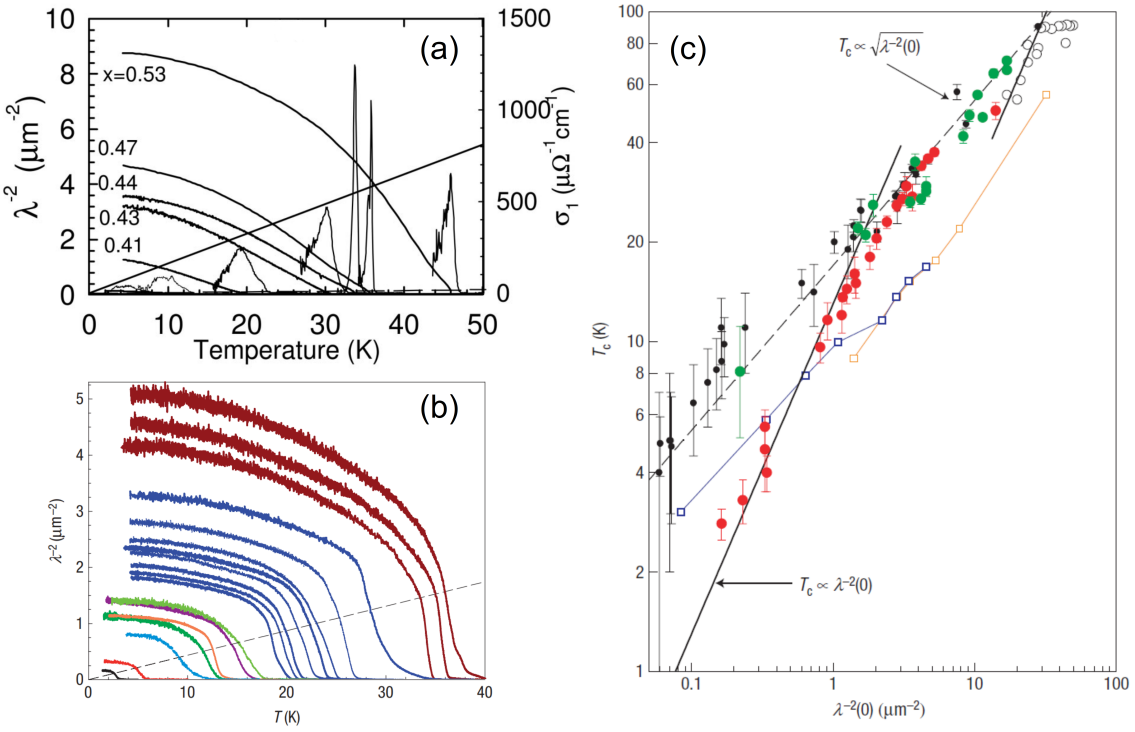

Figure 2.13 The BKT transition in heavily underdoped CaYBCO films. The superfluid density of Ca-intercalated YBCO films, sandwiched between PrBCO layers, was measured as a function of underdoping via a two-coil mutual inductance technique. (a) The superfluid density response in underdoped 40 u.c. thick films does not show a BKT-like jump at the expected T_{BKT} calculated for a single CuO_2 bilayer ($d = 11.7$ Å, solid straight line). On the other hand, a small superfluid density jump may be present for $d = 40 \times 11.7$ Å (dashed line lying close to temperature axis), but the associated T_{BKT} would lie exceedingly close to T_{c0}. The peaks drawn in solid lines correspond to the dissipative response σ_1. The peak position typically marks T_c and the peak width characterizes the level of disorder, with a broader peak denoting a higher level of disorder. Figure adapted from Ref. [182]. (b) The superfluid density measured in similar 2 u.c. thick CaYBCO films. Unlike for the 40 u.c. films, the 2 u.c. films display a distinct downturn of the superfluid density near the expected T_{BKT}, which is depicted as the dashed black line for $d = 2 \times 11.7$ Å. (c) From the data presented in panels (a) and (b), and similar data measured in 20 u.c. CaYBCO films, Hetel *et al.* plotted T_c as a function of the zero-temperature superfluid density $\lambda^{-2}(0)$. The trend established by the 20–40 u.c. thick CaYBCO films (green and black dots) indicate that in samples 20 u.c. and thicker $T_c \propto \sqrt{\lambda^{-2}(0)}$. This implies that in such thick samples the quantum critical fluctuations near the underdoped critical point belong to the (3+1)D-XY universality class. In contrast, for 2 u.c. thick films (red dots) $T_c \propto \lambda^{-2}(0)$. In the ultrathin samples, then, the quantum critical fluctuations belong to the $(2+1)$D-XY universality class, suggesting that a 3D to 2D crossover exists at thicknesses somewhere between 2 and 20 u.c. For comparison Hetel *et al.* included data from lower critical field measurements (open orange squares) and microwave measurements (open blue squares) of clean YBCO bulk crystals as well as Uemura's muon spin relaxation results in YBCO powders (open black circles). Panels (b) and (c) were adapted from Ref. [21].

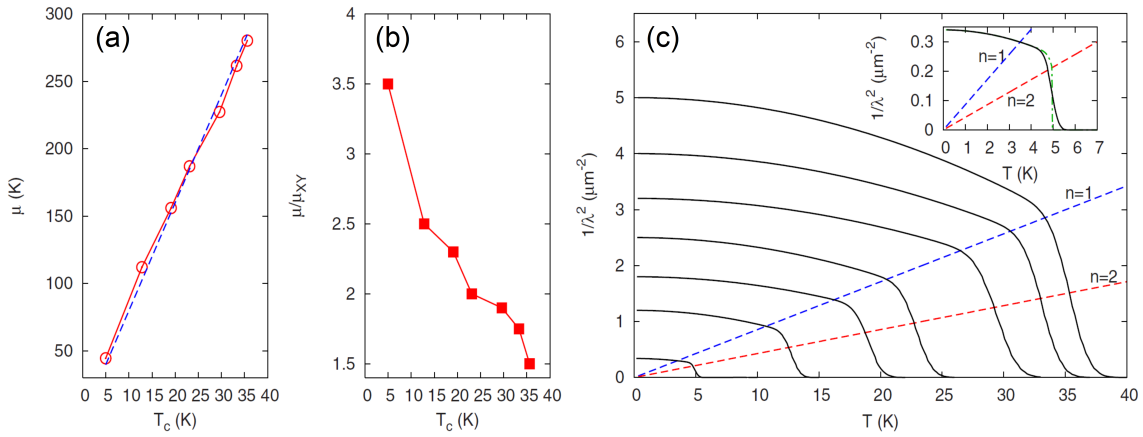

Figure 2.14 The superfluid density data in Fig. 2.13(b) was analyzed using a sine-Gordon renormalization group theory approach [32]. (a) The vortex core energy μ is found to increase proportionally with T_c on the deeply underdoped side of the *R*BCO phase diagram. (b) On the other hand, the ratio μ/μ_{XY} decreases with increasing doping and T_c, and μ/μ_{XY} is significantly larger than the BCS value of $\mu_{\rm BCS}/\mu_{XY} \approx 0.2$ for conventional superconductors like NbN. (c) Theoretical fits of the data in Fig. 2.13(b). Corresponding to the decrease of μ/μ_{XY} with increasing doping, the knee of the downturn in the superfluid density (black lines) shifts towards the BKT line expected for a characteristic length scale of $d = 1$ u.c (blue dashed line) as T_c increases. Inset: at the lowest dopings the knee of the downturn in λ^{-2} is visible near the BKT line for $d = 2$ u.c. (red dashed line). The green dashed-dotted line represents the theoretical fit without integrating over inhomogeneity, demonstrating that some disorder is present in the samples. Figure adapted from Ref. [32].

fatto *et al.* [32] (see Fig. 2.14) reveals that for severely underdoped YBCO the vortex core energy $\mu \propto T_c \propto \rho_s(0)$. At the same time, however, the ratio μ/μ_{XY} *decreases* from ∼3.5 to ∼1.5 upon increasing doping from $T_c \approx 5$ K to $T_c \approx 35$ K. When μ/μ_{XY} is large the Nelson-Kosterlitz jump is observed to occur for the total film thickness, while for small μ/μ_{XY} the jump corresponds to a BKT transition in a single CuO_2 bilayer unit, as in the case when the Josephson coupling is weak. This behavior is puzzling because it appears opposite to the known increase of Josephson coupling with increasing hole doping.

Similar measurements of $\rho_s(T)$ and the BKT transition have not been reported for near optimally doped *R*BCO films at thicknesses less than 20–50 u.c. From the balance of the published evidence it appears clear that only *R*BCO samples thinner than ∼10 u.c. will show BKT physics. Furthermore, the previous studies performed on films as thin as 2 u.c. focused on YBCO that was doped with Ca, patterned into YBCO/PrBCO superlattices, or otherwise sandwiched in semiconducting PrBCO layers. It is not clear how PrBCO alters the superconductivity or electronic structure in adjacent YBCO [168, 183]. In particular, the antiferromagnetic ordering temperature of Pr in PrBCO, at $T_N = 17$ K, is nearly two orders of magnitude larger than what is observed in other *R*BCO materials and this magnetism may reduce superconductivity as expected in the Abrikosov-Gorkov pair-breaking model [184, 185]. It has also been proposed that the hybridization of Pr $4f$ electron states near the Fermi level with the CuO_2 planes contributes to pair breaking, magnetic ordering, and charge localization [39]. Doping of Ca into PrBCO may result in Ca substitution into either the Pr

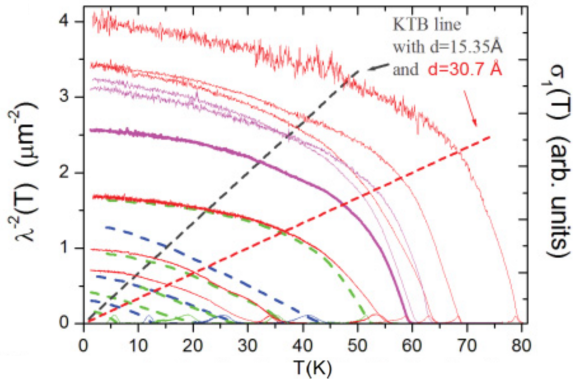

Figure 2.15 The superfluid density $\lambda^{-2}(T)$ of 100 nm thick underdoped $Bi_2Sr_2CaCu_2O_{8+\delta}$ films. At moderate dopings with critical temperatures $T_c \gtrsim 50$ K the Nelson-Kosterlitz universal superfluid jump is clearly visible corresponding to a BKT transition in layers with a characteristic thickness corresponding to two CuO_2 bilayers (red dashed line). However, at very low dopings where $T_c \lesssim 50$ K the superfluid density becomes quite linear in temperature, similar to the underdoped YBCO single crystal data shown in Fig. 2.12(b), and the BKT superfluid jump is no longer visible. Such behavior may indicate the increased role of quantum critical fluctuations in BSCCO. Figure adapted from Ref. [20].

or Ba sites; while Ca substitution of Pr has little effect on the structural properties, $Pr(Ba_{1-x}Ca_x)_2Cu_3O_7$ undergoes an orthorhombic-to-tetragonal transition at $x = 0.1$, and Ca on the Ba sites is expected to more effectively introduce CuO chain disorder [186]. Therefore, the interplay between PrBCO magnetism, orbital hybridization, and disorder produced by interdiffusion of both Ca and Pr ions between CaYBCO and PrBCO layers complicates the interpretation of previous studies. To clarify this issue it will be necessary to carry out measurements of the superfluid density and BKT transition across a wide range of dopings in ultrathin *R*BCO films that are isolated from the influence of Ca or Pr.

The BKT transition has also been probed in other families of cuprates, including $Bi_2Sr_2CaCu_2O_{8+\delta}$ (BSCCO) and $La_{2-x}Sr_xCuO_4$ (LSCO). BSCCO, being one of the most anisotropic cuprates with $\eta_{\mathrm{BSCCO}} = \xi_c/\xi_{ab} \approx 1/60$, provides an important proving ground for the existence of BKT physics in high-T_c superconductors. Early dc transport measurements in BSCCO crystals [187–189] and TlBCCO thick films [190] provided evidence that the BKT universal superfluid jump may be observed in these materials with T_{BKT} lying ~2 K below T_{c0}, corresponding to 2D phase fluctuations and vortex unbinding in single CuO_2 planes. Indeed, studies of the critical scaling of the magnetization, dynamical superfluid response, and dc fluctuation conductivity indicate that the mean-field state in BSCCO falls within the 2D-XY universality class with 3D-XY critical fluctuations appearing only in a narrow range about T_{c0} [191–193]. However, this narrow 3D-XY critical behavior may still obscure the BKT transition in thick samples. RF mutual inductance measurements of the superfluid density in a 1 u.c. thick MBE-grown BSCCO film sandwiched between $Bi_2Sr_2CuO_6$ layers showed that significant phase fluctuations are indeed present in individual CuO_2 planes [194]. The data is very consistent with Minnhagen's dynamical BKT response theory with moderate vortex pinning and thermally activated vortex diffusion. A much more recent study [20] on underdoped BSCCO films across a wide

range of dopings found that, similar to 2 u.c. thick YBCO, BSCCO films as thick as 100 nm also fall within the (2+1)D-XY universality class upon approaching the quantum critical point. As shown in Fig. 2.15, for moderate underdoping ($T_c \gtrsim 50$ K) the Nelson-Kosterlitz superfluid jump is clearly visible, pointing to the dominance of 2D thermal fluctuations. Interestingly, however, for strong underdoping ($T_c \lesssim 50$ K) the superfluid jump *disappears* and $\rho_s(T)$ becomes linear near the expected T_{BKT}, reminiscent of the behavior in strongly underdoped YBCO crystals [22]. This suggests that near the quantum critical point the 2D quantum critical fluctuations become very strong and obscure the 2D thermal fluctuations. Such an effect is not observed in ultrathin YBCO films, where it may be suppressed due to the relatively low degree of anisotropy in YBCO compared to BSCCO.

LSCO has an anisotropy parameter $\eta_{\mathrm{LSCO}} \approx 1/15$, placing it intermediately between YBCO and BSCCO. In keeping with the trend established by these two other cuprate families, thick LSCO films (few hundred nm) fall within the 2D-XY universality class on the underdoped side of the phase diagram, but very close to optimal doping ($x = 0.16$) show a crossover to 3D-XY scaling [197]. Measurements of the magnetoresistance and dc paraconductivity in such thick films point to an absence of the BKT transition even at strong underdoping [198], which suggests that the 3D-XY critical region around T_{c0} is significantly broader than in BSCCO and smears out the superfluid density jump. Similar to the case of YBCO, LSCO films display signatures of the universal superfluid density jump when the film thickness is drastically reduced. Reports of single-coil mutual inductance measurements of the superfluid density in 1 u.c. thick LSCO/La_2CuO_4 heterostructures grown by MBE show a distinct steepening of $\rho_s(T)$ in a temperature range $(T_{c0} - T) \sim 0.25T_{c0}$ below T_{c0}, which is suppressed by a small c-axis applied magnetic field of 0.2 T [199]. The experimental results, analyzed in the dynamical BKT theory, indicate that vortex pinning is present with a pinning energy comparable to the results discussed above on BSCCO/BSCO trilayers. The universal jump has been observed in severely underdoped films as thick as 75 u.c., less than what is seen for BSCCO but certainly thicker than for the RBCO family. In these severely underdoped LSCO films an analysis of magnetoresistance and dc conductivity data shows that the sine-Gordon renormalization group theory of Benfatto *et al.* fits the response very well with vortex core energy $\mu_{\mathrm{LSCO}}/\mu_{XY} \approx 1.4$ [33]. This large vortex core energy (compared to the BCS value of $\mu_{\mathrm{BCS}}/\mu_{XY} \approx 0.2$) implies that in LSCO the relevant length scale that controls the BKT transition is on the order of a few coupled CuO_2 layers; in YBCO, on the other hand, the even larger value $\mu_{\mathrm{YBCO}}/\mu_{XY} \approx 3.5$ at severe underdoping [32] points to an even larger characteristic length scale in the RBCO system. Indeed, the LSCO family appears as an intermediate between BSCCO, where the relevant length scale for the BKT transition is a single CuO_2 plane, and RBCO, where the relevant scale is the total film thickness.

Finally, it is necessary to discuss one of the most classic manifestations of BKT physics in the cuprates, that of the dynamical BKT effect probed in the terahertz range in BSCCO and LSCO, depicted in Fig. 2.16. One conjecture regarding the nature of the pseudogap state on the underdoped side of the cuprate phase diagram is that the observable T_c of the superconducting dome actually reflects a phase disordering temperature that limits superconductivity, and that the temperature scale of the order parameter *amplitude* extends much higher, up to $T^* \sim$ 100–300 K depending on doping level [53]. In this picture the pseudogap state below T^* is formed

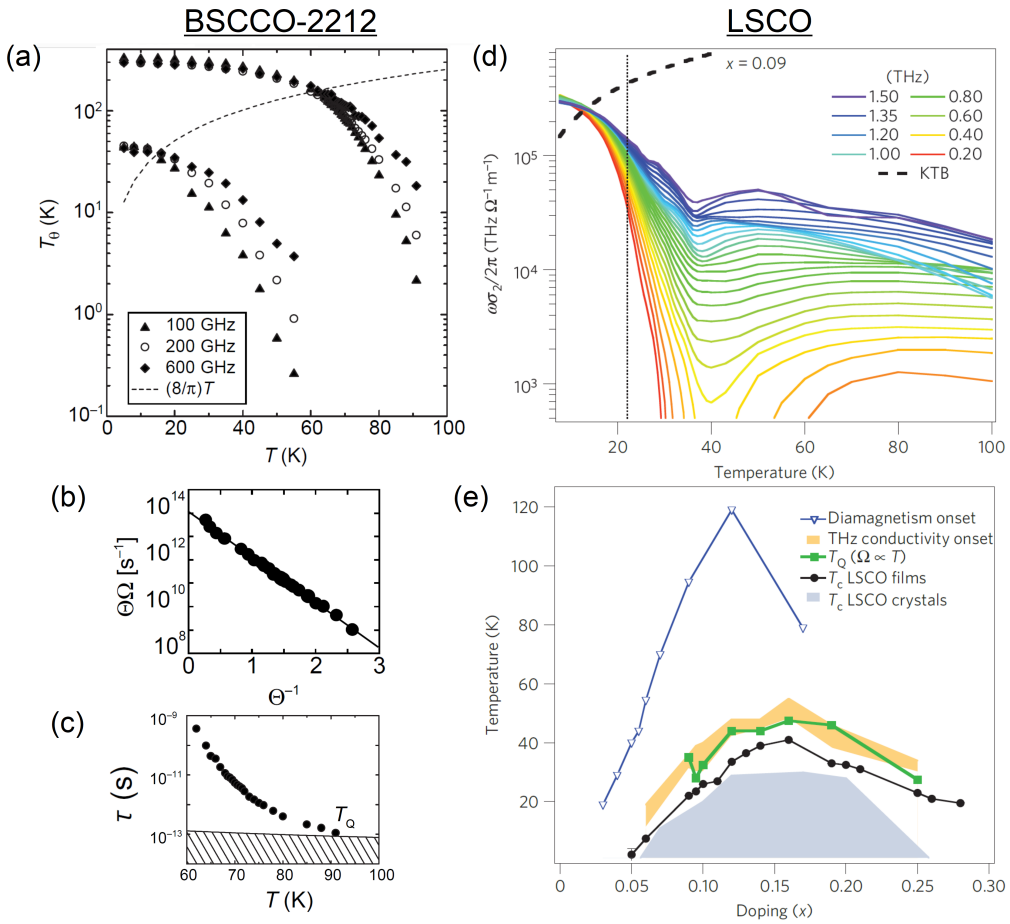

Figure 2.16 Dynamical BKT and phase coherence in BSCCO and LSCO. (a) The superfluid stiffness, parameterized by the phase stiffness energy $T_\theta \approx \rho_s/m^*$, and BKT transition observed in 40–65 nm thick films of underdoped BSCCO by THz time-domain spectroscopy ($T_c = 33$ K, left and $T_c = 74$ K, right) [195]. The dashed curve corresponds to the BKT line. Above the intersection point with the BKT line the data separates, reflecting the frequency dependence of the dynamical BKT superfluid density jump. (b) The frequency $\Omega = 1/\tau$ characterizes the phase-fluctuation time τ of the superconducting correlations. At $\omega > \Omega$, T_θ approaches the bare phase stiffness T_θ^0 of the underlying superconductivity and the complex conductivity $\sigma(\omega) = \sigma_0(k_B T_\theta^0/\hbar\Omega)S(\omega/\Omega)$. Both Ω and S, the scaling function, can be extracted from the real and imaginary parts of $\sigma(\omega)$. Since $\Omega \propto \Omega_0 n_v T_\theta^0/T$, where n_v is the density of free vortices that are expected to be thermally activated, the scattering rate $\Omega \propto (\Omega_0/\Theta)e^{-C/\Theta}$ with $\Theta = T/T_\theta^0$ representing the reduced temperature. The data in (b) show that fluctuations indeed follow this trend, indicating that the proliferation of free vortices suppresses superconductivity above T_c. (c) $\tau(T)$ for the $T_c = 74$ K sample. Phase fluctuations only extend at most to $T_Q \sim 20$ K above T_c, until τ becomes indistinguishable from the mean lifetime of free carriers in the normal state, $\hbar/k_B T$ (shaded area). T_Q from this plot is included in Fig. 2.12(a). (d) Similar THz time-domain spectroscopy measurements of the superfluid stiffness, parameterized as $\omega\sigma_2$, in a 40 nm thick underdoped LSCO film [196]. A similar analysis to the BSCCO film leads to the LSCO phase diagram shown in (e); superconducting phase fluctuations extend at most ~20–25 K above T_c. Yellow area, the onset of THz fluctuation conductivity $\propto \partial^2(\omega\sigma_2)/\partial T^2$; green squares, T_Q defined from the maximum extent of τ as in (c). The phase fluctuations probed by THz measurements are found to lie at temperatures significantly below the onset of fluctuation diamagnetism, shown with blue triangles. Figure adapted from Corson *et al.* [195] and Bilbro *et al.* [196].

from phase-incoherent preformed Cooper pairs. Among many experiments carried out to test this hypothesis, the measurements of Corson *et al.* on BSCCO [195] and Bilbro *et al.* on LSCO [196] stand out. In those works, the dynamical BKT transition was observed in terahertz time-domain spectroscopy measurements of the complex conductivity and the phase correlation time was extracted. For both BSCCO and LSCO it was found that superconducting correlations only persist has high as ∼15 K above T_c, certainly far below the pseudogap temperature T^*. This temperature range appears to agree with Nernst effect measurements [160] and microwave absorption at 15 GHz [162], which show that in YBCO the fluctuations persist as high as ∼23 K above T_c. Given that the *R*BCO family is much less two-dimensional than either BSCCO or LSCO, it would be interesting to explore how the dynamical BKT transition at terahertz frequencies is effected in thin film *R*BCO.

2.3 Optical Sum Rules in the Copper Oxides

As we have seen, the nature of the BKT transition depends upon the details of the critical behavior of the fluctuation conductivity and the superfluid density. However, these quantities are coupled to each other so the nature of the BKT transition in superconductors will also depend strongly on the details of this coupling. The important effect to consider is the relationship between the penetration depth, the density of normal and superconducting charge carriers, and the optical conductivity. This is because the details of the superconducting pairing mechanism and the electronic properties of the normal state strongly influence how changes in the optical conductivity affect changes in the superfluid density, and vice versa. A proper characterization of the BKT transition therefore requires a full understanding of this relationship.

From general considerations of the electrodynamics of solids, it can be shown [200] that the integral of the optical conductivity over all frequencies is a constant, given by

$$\int_0^\infty \sigma_1(\omega)d\omega = \frac{\pi n e^2}{2m},$$

where n is the total density of electrons and m is the electron mass. Notably, this quantity is independent of temperature or the state of the material; as temperature changes or a phase transition is encountered the optical conductivity spectral weight is redistributed to different frequencies but the total value of the integral remains unchanged. When applied to the superconducting transition, the above integral becomes what is known as the *Ferrell-Glover-Tinkham sum rule* [8]:

$$\int_{0^+}^\infty \sigma_1^{T>T_c}(\omega)d\omega = \int_{0^+}^\infty \sigma_1^{T<T_c}(\omega)d\omega + \frac{\pi n_s e^2}{2m} \tag{2.27}$$

Here, $\sigma_1^{T>T_c}(\omega)$ corresponds to the conductivity in the normal state above T_c, while $\sigma_1^{T<T_c}(\omega)$ refers to the conductivity at finite frequencies in the superconducting state below T_c due to the residual response of non-superconducting (or normal) electrons that are not condensed. The second term on the right-hand side of Eq. 2.27 accounts for the density of superconducting electrons, n_s, that have condensed and are found within the δ-function at $\omega = 0$ below the bounds of the integral. This second term is manually added because in a typical optical measurement the integration cannot be taken from truly zero frequency. The FGT sum rule therefore corresponds to the

so-called *two-fluid model* that relates the total density of charge carriers $\rho(T)$ to the "normal fluid" density $\rho_n(T)$ and the superfluid density $\rho_s(T)$:

$$\rho(T) = \rho_n(T) + \rho_s(T). \tag{2.28}$$

Expression 2.28 is ideally valid both above and below T_c; in the BCS case $\rho_s = 0$ above T_c so that $\rho(T > T_c) = \rho_n$, with $\rho(T)$ always constant.

In practice, the integration in Eq. 2.27 also cannot be carried out to $\omega = \infty$ due to experimental limitations. Instead, the integration is typically taken up to a frequency which is large compared to the bandwidth of the energy band that crosses the Fermi level but small compared to the frequency of interband transitions. This procedure introduces additional considerations because the sum is no longer "global." It is possible that in this case the sum becomes both temperature and state dependent, because spectral weight is allowed to transfer into and out of bands lying at higher frequencies. The important questions become, then, to what degree is the FGT sum rule satisfied, and what is the relative importance of the spectral weight transfer to the higher-lying bands? Work has been done by various groups to address these questions but published reports remain contradictory as a result of different experimental restrictions that lead to diverging conclusions [17]. In particular, there is a large gap in the phase-sensitive conductivity measurements that lies in the mid- to far-infrared spectral range, between accurate measurements at microwave and visible frequencies. Based on reflectivity measurements in this gap, it was reported [14,15] that the conductivity spectral weight increases in the superconducting state compared to the normal state in the cuprates. This finding led to discussions of unconventional pairing theories based on kinetic energy saving mechanisms [12,13]. However, infrared reflectivity measurements in the superconducting state can be difficult to interpret because Kramers-Kronig analysis with predetermined assumptions are needed to extract the full complex conductivity. Spectroscopic ellipsometry measurements [16] in the infrared range instead led to the opposite conclusion, that the spectral weight in the superconducting state does not exceed its value in the normal state in cuprates.

Despite the contradictory literature, there are not yet any reports where the spectral weight evolution is measured with the "closed" spectral gap; that is, fully phase-sensitive measurements of the conductivity that smoothly connect the microwave to the visible ranges. Part of the results presented in this thesis seek to address this question of spectral weight recovery as well as the question of whether the FGT sum rule is satisfied in copper oxide superconductors. As will be shown in later chapters, we will present a spectroscopic method wherein quasioptical microwave interferometry, time-domain terahertz spectroscopy, and far-infrared spectroscopic ellipsometry are combined to extract the full complex conductivity and dielectric function in the range 0.1 meV $< \hbar\omega <$ 1 eV without need for Kramers-Kronig relations or model assumptions. Nevertheless, the Kramers-Kronig relations are used to check the consistency of the measured conductivity data. We find that the spectral weight is indeed recovered in the cuprates to within $\pm 0.2\%$, indicating that the FGT sum rule and two-fluid model are obeyed. These results rule out the possibility of a kinetic energy saving mechanism and are consistent with the prior results of Boris *et al.* [16].

Chapter 3

Experimental Methods

3.1 Electrodynamics of Solids

By the middle of the nineteenth century electricity, magnetism, and optics were still considered to be three separate branches of philosophy, and the key principles within each branch were either not unified or existed in a qualitative state. The Scottish mathematician James Clerk Maxwell set out to mathematize and unify all three branches into a single science. In 1861 he succeeded at combining all previous advances in both electricity and magnetism into a set of 20 interdependent equations [201]. In the following year Maxwell used these equations to show that the electromagnetic field propagates as a transverse wave; when he calculated the speed of this wave from constants obtained by electrical measurements he found that the velocity was identical to the optical measurements of the speed of light carried out by Fizeau and Foucault, and he became convinced that light waves were electromagnetic waves [202]. Later, Oliver Heaviside simplified and condensed Maxwell's original 20 equations to the four that are in use today.

The Maxwell equations in the form given by Heaviside are

$$\nabla \cdot \mathbf{E} = \frac{\rho}{\epsilon_0} \tag{3.1}$$

$$\nabla \cdot \mathbf{B} = 0 \tag{3.2}$$

$$\nabla \times \mathbf{E} = -\frac{\partial \mathbf{B}}{\partial t} \tag{3.3}$$

$$\nabla \times \mathbf{B} = \mu_0 \mathbf{J} + \mu_0 \epsilon_0 \frac{\partial \mathbf{E}}{\partial t} \tag{3.4}$$

The first equation follows from Coulomb's force law, the second from Gauss's law applied to the magnetic field, the third from Faraday's law of induction, and the fourth from Ampère's law of magnetic force [203]. Implicit in Maxwell's equations is the continuity equation; by taking the divergence of Eq. 3.4 one obtains $\nabla \cdot \mathbf{J} = -\partial\rho/\partial t$, which is a statement of charge conservation. Also implicit is the wave equation, which formed the basis for Maxwell's conclusion that light waves are electromagnetic waves. By taking the curl of Eq. 3.3 one obtains

$$\nabla^2 \mathbf{E} = \frac{1}{c^2} \frac{\partial^2 \mathbf{E}}{\partial t^2} \tag{3.5}$$

in the absence of free charges or currents, where the wave speed $c = 1/\sqrt{\mu_0\epsilon_0}$. When combined with the Lorentz force $\mathbf{F} = q(\mathbf{E} + \mathbf{v} \times \mathbf{B})$ and Newton's second law of motion, the Maxwell equations give a complete description of the classical dynamics of interacting charged particles and electromagnetic fields.

3.1.1 Fresnel Equations

Starting from Maxwell's equations it is possible to derive Fresnel's equations for transmission and reflection at interfaces. Contained within Eqs. 3.1–3.4 are the boundary conditions for electric and magnetic fields where two different media meet each other. By taking into account the change in the electric and magnetic fields across the interface, the laws of reflection and refraction can be determined and related to the optical properties of each material.

The boundary conditions for field components oriented perpendicular to the interface are obtained from Eqs. 3.1 and 3.2, while those for field components oriented parallel to the interface are obtained from Eqs. 3.3 and 3.4. To begin, we assume that a flat interface separates two semi-infinite media labeled "1" and "2". If we take as a surface an infinitesimally small box straddling the interface and apply the divergence theorem to Eqs. 3.1 and 3.2, where the area of the top and bottom of the box is given by Δa and the total charge enclosed on the interface is $\sigma\Delta a$, then we obtain

$$\epsilon_2\mathbf{E}_{2\perp} - \epsilon_1\mathbf{E}_{1\perp} = \sigma \tag{3.6}$$

$$\mathbf{B}_{2\perp} - \mathbf{B}_{1\perp} = 0 \tag{3.7}$$

Similarly, if we take an infinitesimally small rectangular loop straddling the interface and apply Stokes' theorem to Eqs. 3.3 and 3.4, where the length of the loop elements oriented parallel to the interface is Δl and the current enclosed by the loop is $\mathbf{K}\Delta l$, then we obtain

$$\mathbf{E}_{2\parallel} - \mathbf{E}_{1\parallel} = 0 \tag{3.8}$$

$$\mathbf{B}_{2\parallel} - \mathbf{B}_{1\parallel} = \mu_0\mathbf{K} \tag{3.9}$$

for nonmagnetic materials. As a result, electric fields oriented parallel and magnetic fields oriented perpendicular to the interface are continuous, while electric fields oriented perpendicular and magnetic fields oriented parallel to the interface are discontinuous. The size of the discontinuities are determined by any surface charges and currents present on the interface as well as the difference in the dielectric constant ϵ across the interface.

Next, we assume an electromagnetic wave incident on the interface in the $x = 0$ plane approaches from medium 1 with angle of incidence θ_1 and transmits into medium 2 with angle of refraction θ_2, as illustrated in Fig. 3.1 [204]. There will also be a reflected wave that propagates back through medium 1. Then, the equations for the electric field in medium 1 and medium 2 are given by

$$\mathbf{E}_1(\mathbf{r}, t) = \mathbf{E}_I e^{i(\mathbf{k}_I\cdot\mathbf{r} - \omega_I t)} + \mathbf{E}_R e^{i(\mathbf{k}_R\cdot\mathbf{r} - \omega_R t)}$$

$$\mathbf{E}_2(\mathbf{r}, t) = \mathbf{E}_T e^{i(\mathbf{k}_T\cdot\mathbf{r} - \omega_T t)}$$

Here, ω_I, ω_R, and ω_T are the frequencies of the incident, reflected, and transmitted electromagnetic waves, respectively, while $\mathbf{k}_I$, $\mathbf{k}_R$, and $\mathbf{k}_T$ are their wave vectors. Time

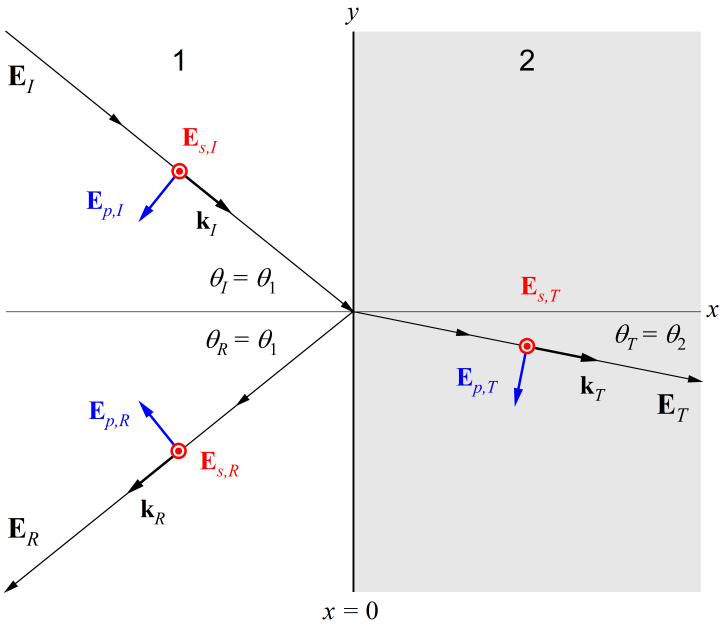

Figure 3.1 An illustration depicting the plane of incidence for an electromagnetic wave incident on the interface at $x = 0$ between medium 1 and medium 2. The p-polarized electric field components (blue vectors) lie within the plane of incidence, in the xy plane. The s-polarized electric field components (red vectors) lie perpendicular to the plane of incidence, in the positive z direction.

invariance requires that $\omega_I = \omega_R = \omega_T = \omega$ and translation invariance on the $x = 0$ plane requires that $\mathbf{k}_I \cdot \mathbf{r} = \mathbf{k}_R \cdot \mathbf{r} = \mathbf{k}_T \cdot \mathbf{r}$. Dependence of the reflected and transmitted waves on the properties of medium 1 and medium 2 enter through the velocity of the waves: $\mathbf{k} = \omega \tilde{n}(\omega)\hat{\mathbf{k}}/c$, where $\tilde{n}(\omega) = n(\omega) + ik(\omega)$ is the *complex* frequency-dependent index of refraction and $c/n(\omega)$ is the speed of light in the medium. The index of refraction is allowed to take complex values in order to account for the possibility that the media absorb energy from the electromagnetic waves. The real-valued parameters $n(\omega)$ and $k(\omega)$ are then termed the *optical constants* of the media. In general, the incident wave can also have an arbitrary polarization about the wave vector $\mathbf{k}_I$, and this polarization will affect the transmission and reflection ratios. The total polarization is therefore written as a linear combination of components with electric field vectors oriented parallel ("p") and perpendicular ("s") to the plane of incidence.

For p-polarized light in the absence of free surface current, Eqs. 3.8 and 3.9 along with the relation $\mathbf{k} \times \mathbf{E} = \omega \mathbf{B}$ give the complex Fresnel reflection and transmission equations for an incident wave passing from medium 1 to medium 2:

$$\tilde{r}_{p,12} = \left[\frac{E_R}{E_I}\right]_{p,12} = \frac{\tilde{n}_2 \cos\theta_1 - \tilde{n}_1 \cos\theta_2}{\tilde{n}_2 \cos\theta_1 + \tilde{n}_1 \cos\theta_2} \tag{3.10}$$

$$\tilde{t}_{p,12} = \left[\frac{E_T}{E_I}\right]_{p,12} = \frac{2\tilde{n}_1 \cos\theta_1}{\tilde{n}_2 \cos\theta_1 + \tilde{n}_1 \cos\theta_2} \tag{3.11}$$

Similarly, for s-polarized light the boundary conditions at the interface lead to the

Fresnel equations

$$\tilde{r}_{s,12} = \left[\frac{E_R}{E_I}\right]_{s,12} = \frac{\tilde{n}_1 \cos\theta_1 - \tilde{n}_2 \cos\theta_2}{\tilde{n}_1 \cos\theta_1 + \tilde{n}_2 \cos\theta_2} \tag{3.12}$$

$$\tilde{t}_{s,12} = \left[\frac{E_T}{E_I}\right]_{s,12} = \frac{2\tilde{n}_1 \cos\theta_1}{\tilde{n}_1 \cos\theta_1 + \tilde{n}_2 \cos\theta_2} \tag{3.13}$$

At first glance it appears as though $\tilde{r}_p$ and $\tilde{r}_s$ lead to contradictory results at normal incidence, where the two polarizations produce reflections which differ by their sign (and hence a phase shift of π). This difference lies in the sign convention of Eqs. 3.8 and 3.9. Because the wave vector $\mathbf{k}$ is inverted upon reflection, the sign convention for the electric field of p-polarized incident waves also experiences a sign inversion, while for s-polarized waves the sign convention remains unchanged. For media with $n_2 > n_1$ the value of $\tilde{r}_p$ is positive while $\tilde{r}_s$ is negative; both equations therefore produce the same result and imply that the reflected electromagnetic wave suffers a phase shift of π when the incident wave impinges upon a more optically dense medium. When $n_1 > n_2$ the signs of $\tilde{r}_p$ and $\tilde{r}_s$ are reversed. Thus, reflection from a medium that is less optically dense than the incident medium produces zero phase shift between incident and reflected waves.

The Fresnel coefficients for the reflected and transmitted intensities, R and T, follow from the definitions of $\tilde{r}$ and $\tilde{t}$ by considering the average power that reflects and transmits at the interface. For s-polarized waves in nonmagnetic media,

$$R_{s,12} = |\tilde{r}_{s,12}|^2 = \left(\frac{\tilde{n}_1 \cos\theta_1 - \tilde{n}_2 \cos\theta_2}{\tilde{n}_1 \cos\theta_1 + \tilde{n}_2 \cos\theta_2}\right)^2 \tag{3.14}$$

$$T_{s,12} = \frac{\tilde{n}_2 \cos\theta_2}{\tilde{n}_1 \cos\theta_1} \left|\tilde{t}_{s,12}\right|^2 = \frac{4\tilde{n}_1\tilde{n}_2 \cos\theta_1 \cos\theta_2}{\left(\tilde{n}_1 \cos\theta_1 + \tilde{n}_2 \cos\theta_2\right)^2} \tag{3.15}$$

In Eqs. 3.10–3.15 the incident and refracted angles θ_1 and θ_2 are related through Snell's law, $\tilde{n}_1 \sin\theta_1 = \tilde{n}_2 \sin\theta_2$, which follows from the condition of translation invariance at the interface, $\mathbf{k}_I \cdot \mathbf{r} = \mathbf{k}_R \cdot \mathbf{r} = \mathbf{k}_T \cdot \mathbf{r}$. Together with Snell's law the Fresnel equations and Fresnel coefficients form a complete set which describes the full behavior of the electromagnetic field at the boundary between two media. Since the electromagnetic field is also linked to the properties of the media through the complex indices $\tilde{n}(\omega)$, all that remains in order to describe the spectroscopic behavior of a medium is to develop a proper model for $\tilde{n}(\omega)$ based on the internal mechanical and quantum mechanical processes which occur in that medium. Alternatively, since the complex $\tilde{n}(\omega)$ consists of a real component $n(\omega)$ and an imaginary component $k(\omega)$, measurement of both R and T, or a measurement of both the amplitude and phase components of $\tilde{r}$ or $\tilde{t}$, will give access to the full complex response function of a material by analytical inversion. Tailored Fresnel equations can also be generated for more complicated or detailed sample geometries by successive application of the basic $\tilde{r}$ and $\tilde{t}$ presented in Eqs. 3.10-3.13 for each structural feature. As a result, the Fresnel equations form the heart of many spectroscopic techniques.

As will be further discussed below, extraction of the full optical constants is most accurately done in a model-independent way by measurement of the amplitude and phase of the transmission function $\tilde{t}(\omega)$. Measurement of the full complex $\tilde{r}(\omega)$ is generally more difficult due to challenges in measuring the amplitude and phase of the incident electric field to high enough precision. Similarly, extraction of material

parameters by measurement of R and T is challenging because in many instances only one of the two measurements is available. Mathematical techniques exist to infer either R or T from the other, such as via the Kramers-Kronig relations, but such techniques require model-dependent assumptions to be made that may introduce artifacts in the extracted material response.

3.1.2 The Drude-Lorentz Model

While the Maxwell equations represented a great leap forward in explaining the relationship between charged matter, electric and magnetic fields, and light waves, the fundamental mechanisms of how electromagnetic radiation interacts with materials remained, for the most part, unknown in the decades following Maxwell's formulation [205]. In particular, it remained a mystery how solids, despite their overall neutral charge, could interact with electromagnetic fields to produce such wildly different phenomena as the spectacular color of crystals, the brilliant luster and high conductivity of metals, the transparency of glass, and the magnetization of lodestones [206]. The first breakthroughs in solving this puzzle came in 1887-1888 when the experiments of Michelson and Morley ruled out the existence of the luminiferous aether and Heinrich Hertz proved the existence of electromagnetic waves and demonstrated their transmission through free space [24, 207]. Second, William Crookes' seminal work on cathode ray tubes, carried out to understand the conduction of electricity in gases, led Hertz and Philipp von Lenard to discover that cathode rays could pass through thin metal foil. Jean Baptiste Perrin was then able to show in 1895 that the cathode rays were actually jets of negatively charged particles and that their trajectories could be deflected with the application of a magnetic field. Third, during the course of his own studies of Crookes and Lenard tubes in late 1895, Wilhelm Conrad Röntgen fortuitously discovered X-rays [208]. Publication of a ghostly image of the bones in his wife's hand stirred great public interest and immediately revolutionized medical science [209]. Shortly thereafter, in 1897, J. J. Thomson discovered the electron and measured its mass-to-charge ratio m/e while working to reproduce Röntgen's results [210]. Taken together, these advances definitively demonstrated that Maxwell's theory was valid, that current was due to the motion of charged particles, that the charged particles carried discrete "quanta" of charge, and that the mass of the electron was 1000 to 2000 times less than the mass of the hydrogen atom. Röntgen, Lenard, Thomson, and Michelson all went on to win the Nobel Prize in physics for this work, with Röntgen becoming the very first recipient in 1901.

The final crucial step in building a first understanding of the electromagnetic properties of solids came in 1900, when Paul Drude combined the key results from these breakthroughs to construct his theory of electrical and thermal conduction in metals [211, 212]. Drude treated metals as a gas of electrons that obey the laws of the classical kinetic theory of gases and which move against a background of heavy, immobile, positively charged ions. His model makes a series of three fundamental assumptions. First, the negatively charged electrons are assumed to be completely free, with all electron-ion interactions neglected except for when the electrons elastically collide with the immobile, positively charged ions. In the absence of any collisions the electrons move according to Newton's equations of motion. In the presence of externally applied electric or magnetic fields the electrons move according to Maxwell's equations. Interactions of the electrons with the edges of the sample are also ne-

glected because the sample dimensions are taken to be quasi-infinite. Second, the electrons are assumed to be independent, with all electron-electron interactions ignored despite the strong Coulomb repulsions which obviously occur between them. The success of the Drude model despite the neglect of electron-electron interactions would prove to be one of the great fundamental questions left unresolved by the theory. Later and with more sophisticated methods, others were able to show that the independent electron assumption can indeed be taken to be true in many important systems, particularly ones in which electronic screening and effects stemming from the Pauli exclusion principle are dominant [206]. Third, Drude assumed that the ensemble of electrons is described by a single constant relaxation time τ, and that in the absence of external forces the system relaxes to thermal equilibrium at a rate $1/\tau$ only through the collisions of the electrons with the immobile, positively charged ions [213]. Immediately after each collision, which is assumed to be an instantaneous event, all information about the electron's prior velocity is destroyed and the electron acquires a new velocity which is randomly directed and given by the local temperature at the site of the collision. In this way the momentum distribution of electrons emerging from collisions is assumed to not depend on the distribution just prior to collisions. In reality, however, the rate at which the ensemble relaxes is strongly dependent upon the total electronic distribution function both before and after collisions because the Pauli exclusion principle forbids electrons from scattering into already occupied states. Drude's concept of the relaxation time is therefore useful if it is possible to describe many complicated, coexisting scattering processes in terms of a single τ that is either constant or a simple function of energy [214]. For generalized systems the relaxation time is a tensor, $\tau_{ij}(\mathbf{k})$. In anisotropic systems $\tau_{ij}(\mathbf{k})$ may contain off-diagonal elements that introduce complicated dependence of τ upon the electron momentum vector $\mathbf{k}$. Strict interpretation of the relaxation time approximation therefore requires isotropic scattering. However, scattering from impurities occurs preferentially in the forward direction and contributes negligibly to the relaxation rate, giving a relaxation time that can be considerably larger than the average time between electron collisions. As a result, the Drude model is most successful where quantities can be derived that do not depend heavily on the details of τ, or where τ can be understood as a generic property rather than as a representation of specific intrinsic processes [206].

Starting from the relaxation time approximation, the probability that a given electron in a metal experiences a collision per unit time is given by $1/\tau$. The equation of motion of the electron under the influence of an electric field at point $\mathbf{r}$ and time t can therefore be expressed as

$$\frac{d}{dt}\mathbf{p}(\mathbf{r},t) = -\frac{1}{\tau}\mathbf{p}(\mathbf{r},t) - e\mathbf{E}_{\mathbf{local}}(\mathbf{r},t), \tag{3.16}$$

where e is the charge of the electron and $\mathbf{E}_{\mathbf{local}}(\mathbf{r},t)$ is the local, microscopic electric field acting on the electron. The electric field is taken to be oscillatory as in Section 3.1.1, with $\mathbf{E}_{\mathbf{local}} \sim e^{i(\mathbf{k}\cdot\mathbf{r}-\omega t)}$. Since the current density $\mathbf{J} = -ne\mathbf{p}/m$, the free current induced by the electric field is given by

$$\mathbf{J}(\mathbf{r},\omega) = \frac{ne^2\tau}{m}\frac{\mathbf{E}_{\mathbf{local}}(\mathbf{r},\omega)}{1-i\omega\tau}.$$

Free electrons probe a spatial volume with dimensions on the order of the mean free path ℓ in a time τ. Therefore, they do not respond simply to $\mathbf{E}_{\mathbf{local}}(\mathbf{r},\omega)$ at a single

point $\mathbf{r}$ but instead to some electric field averaged over a volume $\sim \ell^3$. Provided the wavelength of the electric field $\lambda \gg \ell$, the local electric field strength will not vary appreciably over a distance ℓ and the average local field $\langle \mathbf{E_{local}}(\mathbf{r},\omega)\rangle = \mathbf{E}(\mathbf{r},\omega)$, where $\mathbf{E}(\mathbf{r},\omega)$ represents the macroscopic applied external electric field. The first term on the right hand side of Eq. 3.16 is a viscous damping term so Drude inferred that the energy absorption in a metal results from the same mechanism that gives Joule heating, and that the current is therefore proportional to the applied electric field [215]. Adopting the constitutive relation $\mathbf{J}(\mathbf{r},\omega) = \tilde{\sigma}(\omega)\mathbf{E}(\mathbf{r},\omega)$, Drude found the frequency-dependent complex conductivity to be

$$\tilde{\sigma}(\omega) = \frac{\sigma_0}{1 - i\omega\tau}, \tag{3.17}$$

which reduces to the dc value $\sigma_0 = ne^2\tau/m$ as $\omega \to 0$. With zero total charge density or bound current, Maxwell's equations give

$$-\nabla^2\mathbf{E}(\mathbf{r},\omega) = \frac{\omega^2}{c^2}\left(1 + \frac{4\pi i\tilde{\sigma}(\omega)}{\omega}\right)\mathbf{E}(\mathbf{r},\omega), \tag{3.18}$$

and from comparison with the wave equation, Eq. 3.5, it is evident that the complex dielectric function $\tilde{\epsilon}(\omega) = \epsilon_1(\omega) + i\epsilon_2(\omega)$ is related to the complex conductivity via

$$\tilde{\epsilon}(\omega) = 1 + \frac{4\pi i\tilde{\sigma}(\omega)}{\omega}. \tag{3.19}$$

The real and imaginary parts of the complex conductivity $\sigma_1(\omega)$ and $\sigma_2(\omega)$ can then explicitly be written as

$$\begin{aligned}
\sigma_1(\omega) &= \frac{\omega}{4\pi}\epsilon_2(\omega)\ \text{[Gaussian]} = \frac{\omega}{59.96}\epsilon_2(\omega)\ [\Omega^{-1}\text{cm}^{-1}] \\
\sigma_2(\omega) &= \frac{\omega}{4\pi}\left(1 - \epsilon_1(\omega)\right)\ \text{[Gaussian]} = \frac{\omega}{59.96}\left(1 - \epsilon_1(\omega)\right)\ [\Omega^{-1}\text{cm}^{-1}].
\end{aligned} \tag{3.20}$$

The substitution of the prefactor $1/4\pi$ for $1/59.96$ originates in the conversion from Gaussian units to SI units with frequency ω given in cm^{-1} [203].

Figure 3.2 illustrates the expected Drude model frequency dependence for the real and imaginary parts of the complex conductivity calculated from Eq. 3.17. The response exhibits three main features [200]. First, at low frequencies where $\omega\tau < 1$ the metal falls within the classical skin effect regime. Here $\sigma_1(\omega)$ is close to constant, $\sigma_2(\omega) \sim \omega$, and $k \approx n$. This regime is therefore defined by an electronic mean free path ℓ which is significantly less than the skin depth δ to which the electromagnetic wave penetrates, and electrons in the skin layer suffer many collisions during one oscillation period of the wave. As a result, the relationship between the free current and the applied electric field is local and instantaneous, and the relation $\mathbf{J}(\mathbf{r},t) = \tilde{\sigma}\mathbf{E}(\mathbf{r},t)$ holds. Second, near $\omega\tau \approx 1$ the metal enters the relaxation regime where $\sigma_1 = \sigma_2 = \sigma_0/2$. At this frequency the distance the electrons travel in one oscillation period, v/ω, falls in the limit $v/\omega < \ell < \delta$ and the inertial effects of the electrons become important. The constitutive relation

$$\mathbf{J}(\mathbf{r},t) = \tilde{\sigma}\int \mathbf{E}(\mathbf{r},t')e^{(t-t')/\tau}dt'$$

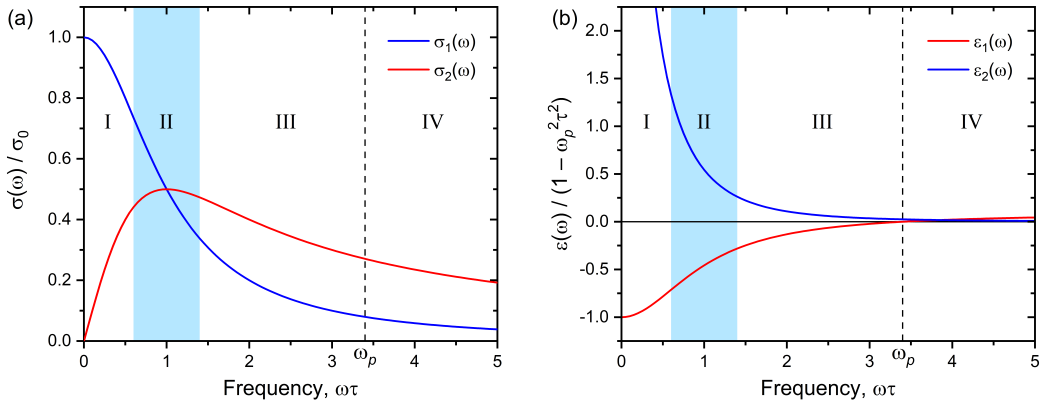

Figure 3.2 (a) The real (blue) and imaginary (red) parts of the complex conductivity $\tilde{\sigma}(\omega)$ in the Drude model, normalized to the value σ_0. (b) The correspondiing real (red) and imaginary (blue) parts of the complex dielectric function. Region I includes the classical skin effect regime at $\omega\tau \ll 1$, where $\epsilon_1(\omega)$ approaches its limiting value of $1-\omega_p^2\tau^2$ and $\epsilon_2(\omega)$ diverges as $1/\omega$. Region II corresponds to the relaxation regime; screening and absorption are approximately matched with $\epsilon_1(\omega) \propto 1/\omega$ and $\epsilon_2(\omega) \propto 1/\omega^2$. In Region III the screening of the electromagnetic wave by free electrons dominates over the absorption so that $\epsilon_1(\omega) \propto 1/\omega^2$ and $\epsilon_2(\omega) \propto 1/\omega^3$. Region IV is the region of transparency above $\omega > \omega_p$.

is no longer Ohmic, instead becoming nonlocal in time, and the free current lags the applied electric field by an increasing amount as frequency increases. With increasing frequency $\sigma_2(\omega)$ becomes increasingly greater than $\sigma_1(\omega)$ and the phase shift approaches $\pi/2$. Third, at high frequencies where $\omega\tau > 1$ the electrons respond to the oscillating electric field as free electrons and the effect of collisions becomes much less dominant. In this regime $\ell \gtrsim \delta$ so the electrons act to screen the applied external electric field and $k > n$. Consequently, $\sigma_1(\omega) \sim 1/\omega^2$ and $\sigma_2(\omega) \sim 1/\omega$ (or equivalently, $\epsilon_1(\omega) \sim -1/\omega^2$) so the reflection is high, while the $\pi/2$ phase shift of the response implies that absorption in the skin layer is negligible.

As $\omega\tau$ is increased further the complex dielectric function passes through a point where $\epsilon_1(\omega) = 0$. From Eq. 3.18 it is evident that the wave equation is satisfied with a phase velocity $v_{ph} = c/\sqrt{\epsilon_1}$. Therefore, at this point both v_{ph} and the wavelength of the electromagnetic wave in the metal become infinite; the electrons all oscillate in phase and the frequency at which this occurs is referred to as the plasma frequency ω_p. Following Eq. 3.19 with $\omega\tau \gg 1$ it is found that

$$\omega_p^2 = 4\pi\frac{ne^2}{m}\ [\text{Gaussian}] = 59.96\frac{ne^2}{m}\ [\text{cm}^{-2}], \tag{3.21}$$

where once again the prefactor of 59.96 in the second equality originates from the frequency being given in units of cm^{-1}. However, there is no oscillation of the total polarization charge density as with a true plasma. The plasma oscillation is only a normal mode of the system if it can sustain itself in the absence of an external field, $\tilde{\epsilon}(\omega)\mathbf{E}(\omega) = 0$. With $\epsilon_1 = n^2 - k^2 = 0$ the condition $n = k$ will support a resonantly driven plasma oscillation, but if $k \neq 0$ there will be dissipation and the oscillation will not be a normal mode. Since the separation of charges in the electron gas produces a restoring field $\mathbf{E}$, the true plasma oscillation requires the complex $\tilde{\epsilon}(\omega) = 0$ because then $n = k = 0$. Finally, at $\omega > \omega_p$ the metal becomes transparent and both $\epsilon_1(\omega)$ and $\epsilon_2(\omega)$ are nonzero and positive.

Despite the simplicity and widespread use of the Drude model by the scientific community, more than 100 years passed after the publication of Drude's seminal papers before the model was finally experimentally verified. Typically, verification of the Drude model is challenging because standard infrared spectroscopy techniques are only sensitive in the frequency range corresponding to the Drude tail, and infrared reflectivity measurements suffer from the need to make an extrapolation of the data to high and low frequencies in order to apply the Kramers-Kronig transformations. By utilizing high quality thin films of the heavy fermion metal UPd_2Al_3 and phase sensitive microwave spectroscopy techniques, Martin Dressel and Marc Scheffler *et al.* were able to show that the simple Drude model is indeed valid with a single temperature dependent scattering rate to within an accuracy of better than 1% [216, 217]. They were successful due to the particular mix of electronic conditions and disorder in the films. The strong electron correlations in the UPd_2Al_3 give rise to an electronic mass enhancement of ∼1000, which in turn leads to an extremely slow relaxation rate of just a few GHz, while the impurity level in the films lies in just the right range to create a single Drude relaxation time that is not too large to be observed by low frequency techniques. These results showed that, if the right material conditions are present, the Drude scattering rate is indeed independent of frequency.

Aside from the Drude model's success at describing the ac electrical conductivity of metals, especially in the limit where the wavelength of the applied electric field $\lambda \gg \ell$, the model was able to provide a reasonable explanation of the classical Hall magnetoresistance, the magnitude of the Hall coefficient $R_H = -1/nec$, the thermal conductivity, and the classical Seebeck effect. Later, Arnold Sommerfeld expanded on the Drude model to make use of Fermi statistics and take into account the fact that the classical ideal gas laws cannot be applied to an electron gas. The resulting Sommerfeld and Drude models describe the magnitude of the Hall coefficient and the thermal conductivity of a metal reasonably well because these quantities do not rely on specific details of the relaxation time. Similarly, the Drude model successfully describes the ac electrical conductivity of metals because the identity of the scattering mechanisms that constitute τ are unimportant for the macroscopic response and the Pauli exclusion principle strongly limits electron-electron interactions at the Fermi level. However, significant problems with the Drude theory lie in its three primary assumptions: that the electrons are free and independent and can be described by a single relaxation time. For example, the oversimplification of the relaxation time approximation leads the Drude model to fail to properly explain the Wiedemann-Franz law and the τ-dependence of the magnetoresistance, while the free electron approximation leads to a failure to predict the magnetic field dependence of the magnetoresistance or the correct sign of the Hall coefficient in some metals. Even the greatest success of Drude's theory, the ac electrical conductivity, suffers from a failure to predict the detailed frequency and temperature dependence of the conductivity due to a neglect of electron-ion interactions (and in some cases, electron-electron interactions). In fact, relaxing the free electron approximation serves as an important first step in improving the theoretical description of metals.

Hendrik Antoon Lorentz improved upon the Drude model in 1905 by taking into account the binding force between electrons and the ionic cores in a solid [214]. The so-called Drude-Lorentz or extended Drude model departs from the simple Drude model by modifying Eq. 3.16 to take into account a Hooke's law restoring force on

the electrons,

$$m\frac{d^2\mathbf{r}'}{dt^2} = -e\mathbf{E}_{\mathbf{local}}(\mathbf{r},t) - \frac{m}{\tau}\frac{d\mathbf{r}'}{dt} - m\omega_0^2\mathbf{r}', \tag{3.22}$$

where $m\omega_0^2$ is the Lorentz oscillator and represents the strength of the restoring force, $\mathbf{r}$ is the local position of an electron, and $\mathbf{r}'$ is the displacement of the electron about $\mathbf{r}$. The solution to this new equation of motion is found by once again looking for an oscillatory solution of the form $e^{i(\mathbf{k}\cdot\mathbf{r}-\omega t)}$. Since the dipole moment induced by the action of the local electric field on an electron is $\mathbf{P}_{\mathbf{local}} = -e\mathbf{r}'$, the local dipole moment is given by

$$\mathbf{P}_{\mathbf{local}}(\mathbf{r},\omega) = \frac{e^2}{m}\frac{\mathbf{E}_{\mathbf{local}}(\mathbf{r},\omega)}{(\omega_0^2-\omega^2)-i\omega/\tau}.$$

Assuming a linear relationship between the applied electric field and the induced dipole moment, $\mathbf{P}_{\mathbf{local}}(\mathbf{r},\omega) = \tilde{\alpha}(\omega)\mathbf{E}_{\mathbf{local}}(\mathbf{r},\omega)$ where $\tilde{\alpha}(\omega)$ is the complex electronic polarizability. If there are n electrons per unit volume then the macroscopic polarization is

$$\mathbf{P}(\mathbf{r},\omega) = n\tilde{\alpha}(\omega)\langle\mathbf{E}_{\mathbf{local}}(\mathbf{r},\omega)\rangle. \tag{3.23}$$

In general, $\langle\mathbf{E}_{\mathbf{local}}(\mathbf{r},\omega)\rangle \neq \mathbf{E}(\mathbf{r},\omega)$ because $\langle\mathbf{E}_{\mathbf{local}}(\mathbf{r},\omega)\rangle$ is an average over lattice sites, not over the region between the lattice sites. For localized electrons, Lorentz calculated the average field acting at a point $\mathbf{r}$ in a polarized isotropic medium and found that $\langle\mathbf{E}_{\mathbf{local}}\rangle = \mathbf{E} + 4\pi\mathbf{P}/3$ [214]. However, in a realistic material there can be considerable overlap between electric fields produced by ions at different lattice sites in the vicinity of $\mathbf{r}$. As a result, $\langle\mathbf{E}_{\mathbf{local}}\rangle$ actually lies between $\mathbf{E}$ and $\mathbf{E} + 4\pi\mathbf{P}/3$, tending instead to $\mathbf{E}$ [218,219]. For nonlocalized or free electrons, as discussed above in the context of the simple Drude model, the average electric field is calculated by taking a weighted average of the microscopic electric field throughout the unit cell, where the weighting factor is the position-dependent polarizability $\tilde{\alpha}(\mathbf{r})$. For free electrons, however, the spatial charge distribution is uniform and the weighting factor is constant in space, resulting in an average field which is just $\mathbf{E}$. Therefore, $\langle\mathbf{E}_{\mathbf{local}}(\mathbf{r},\omega)\rangle$ can justifiably be replaced by $\mathbf{E}(\mathbf{r},\omega)$ in Eq. 3.23, and the displacement field $\tilde{\epsilon}(\omega)\mathbf{E}(\mathbf{r},\omega) = \mathbf{E}(\mathbf{r},\omega) + 4\pi\mathbf{P}(\mathbf{r},\omega)$ yields the complex dielectric function

$$\tilde{\epsilon}(\omega) = 1 + \frac{4\pi ne^2}{m}\frac{1}{(\omega_0^2-\omega^2)-i\omega/\tau}.$$

If the system contains N bound levels and therefore N Lorentz oscillators, the displacement field can be generalized by adding N contributions to the polarization as $\tilde{\epsilon}(\omega)\mathbf{E}(\mathbf{r},\omega) = \mathbf{E}(\mathbf{r},\omega) + 4\pi\sum_{j=1}^{N}\mathbf{P}_j(\mathbf{r},\omega)$ and the complex dielectric function becomes

$$\tilde{\epsilon}(\omega) = 1 + \frac{4\pi ne^2}{m}\sum_{j=1}^{N}\frac{f_j}{\left(\omega_j^2-\omega^2\right)-i\omega/\tau_j}. \tag{3.24}$$

Here, f_j represents the oscillator strength while ω_j and $1/\tau_j$ are the resonant frequency and relaxation rate of the jth oscillator, respectively. This result contains the response of both bound and free charges. If the simplest case is taken where $\omega_0 = 0$ then the original Drude result is obtained. Then, the general Drude-Lorentz formalism is expressed as

$$\tilde{\epsilon}(\omega) = \tilde{\epsilon}_{\mathrm{Drude}}(\omega) + \tilde{\epsilon}_{\mathrm{Lorentz}}(\omega) + \epsilon_\infty, \tag{3.25}$$

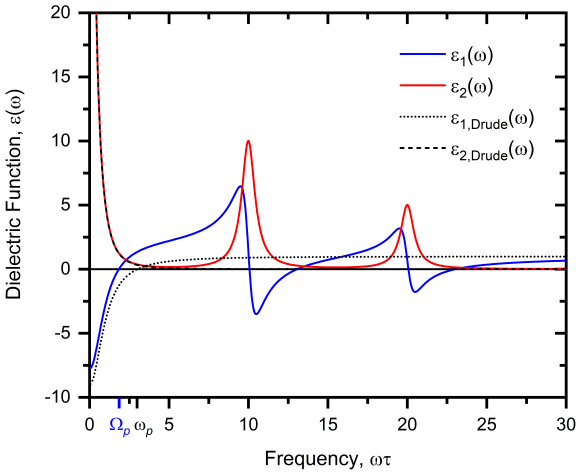

Figure 3.3 The real (blue) and imaginary (red) parts of the complex dielectric function $\tilde{\epsilon}(\omega)$ in the Drude-Lorentz model calculated for a Drude response with two Lorentz oscillators. The response was calculated with parameters $\epsilon_\infty = 1$, $\omega_p^2\tau^2 = 10$, $\Delta\epsilon_{j=1} = 1$, $\omega_{j=1} = 10/\tau$, $\Delta\epsilon_{j=2} = 0.25$, $\omega_{j=2} = 20/\tau$, and $\tau_1 = \tau_2 = \tau$. For reference, the black dotted and dashed curves represent the real and imaginary parts of $\tilde{\epsilon}_{\text{Drude}} + \epsilon_\infty$, respectively. Comparison of $\epsilon_{1,\text{Drude}}(\omega)$ with $\epsilon_1(\omega)$ reveals the shift of the screened plasma frequency Ω_p from its unscreened value ω_p due to the presence of the Lorentz oscillators.

where

$$\begin{aligned}\tilde{\epsilon}_{\text{Drude}}(\omega) &= -\frac{\omega_p^2}{\omega^2 + i\omega/\tau} \\ \tilde{\epsilon}_{\text{Lorentz}}(\omega) &= \sum_{j=1}^{N} \frac{\Delta\epsilon_j\omega_j^2}{\left(\omega_j^2 - \omega^2\right) - i\omega/\tau_j}\end{aligned} \tag{3.26}$$

with $\Delta\epsilon_j\omega_j^2$ replacing f_j as the oscillator strength through $\Delta\epsilon_j = 4\pi ne^2 f_j/m\omega_j$. In this notation, the total contribution to the dc dielectric constant from the Lorentz oscillators is $\Delta\epsilon_{\text{Lorentz}} = \sum \Delta\epsilon_j$. The term ϵ_∞ in Eq. 3.25 represents the contribution to the dielectric function from free space as well as all absorptions at high frequencies not captured by the Lorentz term. In the Drude-Lorentz formalism, the Drude term represents all contributions to the dielectric function from intraband transitions while the Lorentz term represents all interband transitions and phononic contributions. If the sum in $\tilde{\epsilon}_{\text{Lorentz}}(\omega)$ includes all phonons, interband transitions, and absorptions, then $\epsilon_\infty = 1$ as in vacuum. The frequency dependence of the real and imaginary parts of the complex dielectric function $\tilde{\epsilon}(\omega)$ in the Drude-Lorentz formalism are illustrated in Fig. 3.3.

In addition to explaining the more complicated frequency-dependent absorption spectrum of real solids, the Drude-Lorentz model also takes into account the important consequences of screening due to bound currents. The primary effect of the interband transitions lying at higher frequencies is to shift ϵ_1 at lower frequencies by approximately $\Delta\epsilon_{\text{Lorentz}}$, so the screening most clearly manifests in the infrared and optical portions of the spectrum as a shift of the plasma frequency from its bare value in a free electron metal. This effect is illustrated in Fig. 3.3 by the shift of the zero crossing of ϵ_1 to lower frequencies from the black dashed curve to the blue

curve, which represent the simple Drude and full Drude-Lorentz response, respectively. If the Drude scattering rate is not negligible and the frequency is not in the limit $\omega\tau \gg 1$ then the finite electronic lifetime will also contribute to a shift of the plasma frequency. In this case, the screened plasma frequency becomes

$$\Omega_p^2 = \frac{\omega_p^2}{\epsilon_\infty + \Delta\epsilon_{\text{Lorentz}}}\left(1 - \frac{\epsilon_\infty + \Delta\epsilon_{\text{Lorentz}}}{\omega_p^2\tau^2}\right) = \frac{4\pi ne^2}{m^*}.$$

As indicated by the second equality, the screened plasma frequency can be expressed as the bare plasma frequency renormalized with the effective electronic mass m^*. Then, at sufficiently low frequencies where $\tilde{\epsilon}_{\text{Lorentz}}(\omega)$ is approximately given by $\Delta\epsilon_{\text{Lorentz}}$, the complex dielectric function can be expressed as

$$\tilde{\epsilon}(\omega) = \epsilon_\infty - \frac{\Omega_p^2}{\omega^2 + i\omega/\tau^*}. \tag{3.27}$$

The plasma frequency is a measure of the density of electrons and is therefore an important quantity that is deeply connected to the fundamental properties of a metal. In general, the fundamental symmetries of a physical system manifest themselves through Noether's theorem as the invariance of the Lagrangian action S under continuous transformations of the quantum mechanical basis and field configurations [220]. An associated observable quantity is then globally conserved if it produces zero change of S under such a symmetry transformation. For a non-interacting electron gas, the system is invariant under a constant phase transformation and the components of the conserved quantity are the charge density ρ and current density $\mathbf{J}$. The conserved quantity therefore represents particle current, and for an isolated system with a suitable choice of representation the particle (electron) number is fixed [221]. All electrons participate in the electrodynamic response of the metal; the polarizability appearing in Eq. 3.24 sums up all contributions. The oscillator strength f_j then represents the probability of the jth transition taking place with characteristic frequency ω_j [200]. Quantum mechanically, this probability is represented as $f_j \to f_{kj} = -2\left|\langle k|\hat{p}|j\rangle\right|^2/m\hbar\omega_{kj}$, where $\hat{p}$ is the momentum operator. Following commutator algebra the transition obeys the Thomas-Reiche-Kuhn sum rule $\sum_j f_{kj} = 1$, also known as the f-sum rule, which serves as a normalization condition for f_j [214]. With this constraint, it is seen that the frequency integral of $\omega\epsilon_2(\omega)/4\pi = \sigma_1(\omega)$ is a conserved quantity,

$$\int_0^\infty \sigma_1(\omega)d\omega = \frac{\omega_p^2}{8} = \frac{\pi ne^2}{2m}, \tag{3.28}$$

where m is again the bare electron mass. In units where frequency is given in cm^{-1} the 8 is replaced with 38. The area under the $\sigma_1(\omega)$ curve therefore also represents the total density of electrons and is referred to as the optical conductivity *spectral weight*.

While dispensing with the free electron picture of solids the Drude-Lorentz formalism continues to assume the validity of the relaxation time and independent electron approximations. However, as pointed out above, both of these assumptions do not always hold and considerable care must be taken in applying the Drude-Lorentz model to real systems. The relaxation time approximation overlooks the fact that the scattering time $\tau(\mathbf{k})$ depends in general on the nonequilibrium electronic distribution function $g(\mathbf{k})$, which varies across different experimental conditions [206]. Impurities

and crystal defects such as missing or misplaced ions, stacking faults, grain boundaries, thermal deviations from perfect lattice periodicity, and other extrinsic effects impact the details of $g(\mathbf{k})$. At the same time, crystallographic symmetry and the shape of the Fermi surface must be taken into account because anisotropy can introduce significant $\mathbf{k}$ dependence in τ.

Electron-electron interactions also impact the form of $g(\mathbf{k})$ and the entangled quantum many-body electronic states can change the fundamental symmetries of the system, resulting in a change of the conserved observables. In the simplest case the electron-electron interactions can justifiably be neglected even in the presence of strong interactions due to reasoning set forth by Landau in his theory of the Fermi liquid. Starting from a non-interacting electron gas, the strength of electron-electron interactions in a Fermi liquid is adiabatically increased such that the electronic energy spectrum $\varepsilon_e(\mathbf{k})$ evolves smoothly into a *quasiparticle* energy spectrum $\varepsilon_{qp}(\mathbf{k})$, where there is a one-to-one correspondence between electronic and quasiparticle excitations [222]. The quasiparticles simply represent collective excitations from the many-body quantum ground state and the charge, current, and spin remain conserved quantities because their operators continue to commute with the non-interacting Hamiltonian of the system. The Pauli exclusion principle limits electron scattering and only electrons with energy within $\varepsilon \sim k_B T$ of ε_F participate in the transport processes. As a result, the scattering rate $1/\tau \propto T^2$ and the quasiparticle system behaves macroscopically according to the Drude picture, with the bare electron mass m replaced by the renormalized effective mass m^* to reflect the change to quasiparticles. More specifically, the imaginary part of the single-particle self-energy vanishes as $\mathrm{Im}\Sigma(k_f, \varepsilon) \propto \max(\varepsilon^2, T^2)$ near the Fermi surface, so the single-particle Green's function becomes identical to that of a free particle [222]. Fermi liquid theory is valid when perturbation theory is valid; it is not valid when there is not a one-to-one correspondence between $\varepsilon_e(\mathbf{k})$ and $\varepsilon_{qp}(\mathbf{k})$, such as in the case of a phase transition induced by electron-electron interactions. When this occurs the simple f-sum rule presented in Eq. 3.28 must be reevaluated as was done by Ferrell, Glover, and Tinkham for the normal state to superconductor transition [7, 223]. Consideration of screened potentials also characteristically reduces the importance of electron-electron interactions [206]. For example, in the Hartree-Fock approximation screening of the exchange term in the Hamiltonian by the dielectric function $1/\epsilon(k - k')$ removes singularities in the electron velocities at $k = k_F$, and the screened result approaches that for free electrons. When the screening has time dependence $e^{-i\omega t}$, as in the RPA or Lindhard approximations, $\epsilon(\omega)$ similarly reduces to the Drude result. However, because the energy spectrum $\varepsilon_e(\mathbf{k})$ depends on $g(\mathbf{k})$, nonequilibrium processes modify $\varepsilon_{qp}(\mathbf{k})$ and the nonequilibrium quasiparticle properties are affected. Thus for time-dependent, dynamical, and nonlinear processes the electron-electron interactions have a more complicated effect than simply modifiying the scattering rate, and the details of the nonequilibrium distribution function must be explicitly considered.

3.1.3 Kramers-Kronig Consistency Analysis

The complex dielectric function $\tilde{\epsilon}(\omega)$ and the complex conductivity $\tilde{\sigma}(\omega)$ represent basic response functions of a material system to an applied electric field. This means they must obey the fundamental principle of causality, which states that the physical response of a system to an impulse must only occur in time after the impulse is applied;

future behavior cannot influence past behavior. A very important consequence follows from this requirement: the real and imaginary parts of a response function are related to each other and can be derived from one another, which is significant because it means that if only one part of the response function is experimentally available, then the other part can be obtained through a simple mathematical analysis. For some experimental techniques, such as reflectivity measurements, this kind of procedure is necessary in order to obtain both $\epsilon_1(\omega)$ and $\epsilon_2(\omega)$ because only the relative intensity is experimentally accessible.

The mathematical relations were discovered by H. A. Kramers and R. de L. Kronig nearly a century ago and are derived by applying Cauchy's theorem to the response functions in the upper half-plane of the complex frequency $\omega + i\delta$ [200, 203]. For the complex dielectric function $\tilde{\epsilon}(\omega)$ the *Kramers-Kronig* (KK) *relations* are

$$\epsilon_1(\omega) - 1 = \frac{2}{\pi}\mathcal{P}\int_0^\infty \frac{\Omega\epsilon_2(\Omega)}{\Omega^2 - \omega^2}d\Omega \tag{3.29}$$

$$\epsilon_2(\omega) = -\frac{2\omega}{\pi}\mathcal{P}\int_0^\infty \frac{\epsilon_1(\Omega) - 1}{\Omega^2 - \omega^2}d\Omega \tag{3.30}$$

where $\mathcal{P}$ denotes the principal part. A second consequence of causality and response functions is the existence of sum rules: the optical conductivity sum rule given by Eq. 3.28 follows directly by combining the KK relations with the definition of the plasma frequency ω_p at energies far above the highest absorption [200]. It is important to note that the integration bounds in Eqs. 3.29 and 3.30 run over all frequencies from 0 to ∞. This means that the KK relations and the optical conductivity sum rule represent a self-consistent set of expressions that describe the global response of a material across all frequencies. Therefore, in order to properly obtain one part of the optical response from the other it is necessary to measure across a sufficiently wide spectral range, because the real response at any one frequency is determined by the weighted sum total of the imaginary response at all frequencies (and vice versa).

This property enables the use of the KK relations to test for consistency of a measured data set if both the real and imaginary parts of the response spectrum have been measured independently. Such independent measurements can be made, for example, by interferometric, time domain, and spectroscopic ellipsometry techniques. The KK transform of one part of the response is calculated and the result is compared to the experiment. In practice, however, it is not possible to carry out the integrations in Eqs. 3.28, 3.29, and 3.30 to truly infinite frequency, as is required by Cauchy's theorem and causality, because the experimental equipment cannot measure infinitely high. To accommodate this limitation in the consistency analysis, the measured $\tilde{\epsilon}(\omega)$ and $\tilde{\sigma}(\omega)$ are *extrapolated* to infinite frequency. Since optical experiments also cannot measure to exactly zero frequency, the measured data is also extrapolated to $\omega = 0$ from the lowest measured point. The KK consistency check is then performed with the fully extrapolated data sets. Therefore, one of the key strengths of the KK consistency analysis is that it extends the sensitivity of the experiment to beyond the measured spectral range. While the exact frequency dependence of the extrapolations cannot be uniquely determined by the KK procedure, the distribution of spectral weight *can*, which allows for questions of spectral weight transfer at electronic transitions to be investigated. Such questions are especially pertinent, for example, in the physics of high-T_c superconductors, where the nature of spectral weight transfer has important implications for different proposed pairing mechanisms [12, 14, 16].

It must be mentioned that the necessity to extrapolate the measured data to properly obtain the KK transform has profound implications for reflectivity experiments (where a KK consistency check is not possible). Errors of just a few percent in the assumed spectral weight located in the extrapolated regions, particularly at low frequencies, can dramatically alter the frequency dependence of the KK transform across a very broad spectral range. This is especially perilous for reflectivity studies of superconductors because the relative reflected intensity at low frequencies is extremely close to 1. Small deviations of the extrapolation from the true reflectivity values in this region can therefore cause incorrect assignment of a significant amount of spectral weight even in the measured spectral range. This type of situation underscores the need to obtain simultaneous and independent measurements of both the real and imaginary parts of the electromagnetic response.

In some cases the integration of the sum rule in Eq. 3.28 does not have to be taken to infinite frequency, but rather a high frequency cutoff ω_{cutoff} may be used, if absorptions do not extend above a certain frequency range. This high frequency integration cutoff must be significantly higher than the highest frequency absorption to ensure that all spectral weight is accounted for. In a material system such as a superconductor it is expected that the relevant energy scale upon transition into the superconducting state lies at the level of intraband transitions [16], so it is sufficient to place ω_{cutoff} intermediately between the intra- and interband energy scales. To avoid unnecessary errors resulting from the neglect of the interband transitions (since transitions to higher-lying bands are still present in the total response) the *difference conductivity* $\Delta\sigma_1(T,\omega) = \sigma_1(T,\omega) - \sigma_1(T_c,\omega)$ is used; as long as there is no appreciable transfer of spectral weight at interband energies then $\Delta\sigma_1(T,\omega)$ is only nonzero at energies comparable to twice the superconducting gap $2\Delta(T)$. This step is further justified because in the optical analysis of superconductors the *changes* in the electrodynamic response across the transition are sought.

From Eqs. 3.28 and 3.29 the resulting KK consistency relations for a superconductor are obtained, where $\Delta\sigma_1^{\text{extr}}(\omega)$ is the extrapolated difference conductivity:

$$SW_1 = \int_{0^+}^{\omega_{\text{cutoff}}} \Delta\sigma_1^{\text{extr}}(\omega)d\omega \tag{3.31}$$

$$\Delta\epsilon_1^{\text{KK}}(\omega) - 1 = 38\mathcal{P}\int_{0^+}^{\infty} \frac{\Delta\sigma_1^{\text{extr}}(\Omega)}{\Omega^2 - \omega^2}d\Omega + \frac{SW_2}{\omega^2} \tag{3.32}$$

The constant 38 appears in Eq. 3.32 when $\Delta\sigma_1^{\text{extr}}$ is in units of $\Omega^{-1}\text{cm}^{-1}$ and frequency is in units of cm^{-1}. Here, the spectral weight shift SW_1 corresponds to the difference in the normal charge carrier density $\Delta\rho_n$ between the superconducting and normal states. On the other hand, SW_2 is the spectral weight that has accumulated into a δ-function at $\omega = 0$ and corresponds to the difference in the superconducting charge carrier density $\Delta\rho_s$. The term SW_2/ω^2 necessarily appears in Eq. 3.32 as a consequence of the FGT sum rule (see the discussion in Section 2.3). The FGT sum rule states that the total σ_1 response of a superconductor consists of a sum response of the superconduting electrons at $\omega = 0$ (representative of dissipationless transport and the Meissner effect) and a residual quasiparticle response at finite frequencies, $\sigma_1(\omega) = SW_2\delta(\omega) + \sigma_1^{qp}(\omega \neq 0)$. Since it is impossible to directly observe the δ-function response at $\omega = 0$ in the measured conductivity, the response of the superconducting spectral weight must be manually added in. By performing the integral in Eq. 3.32 the mathematical KK transform $\Delta\epsilon_1^{\text{KK}}$ of the measured and extrapolated

difference conductivity is obtained. To test for KK consistency of the measured data $\Delta\epsilon_1^{\mathrm{KK}}(\omega)$ is compared to the experimentally measured $\Delta\epsilon_1(\omega)$.

By virtue of the FGT sum rule, in the simple two-fluid model of superconductivity the total charge carrier density is given by the sum of superconducting and normal charge carriers, $\rho = \rho_s + \rho_n$. The total charge carrier density remains constant at all temperatures such that $\Delta\rho = 0$, while $\rho_s = 0$ above T_c. If the FGT sum rule and two-fluid model hold then it is expected that $SW_1 = SW_2$ because charge carriers that are no longer in the normal state below T_c have condensed to form the superconducting condensate. However, if $SW_1 \neq SW_2$ then the KK consistency analysis implies that spectral weight either shifts into or out of high energy bands that lie above ω_{cutoff} (depending on which of SW_1 or SW_2 is greater). In that case, additional components must be introduced into the model corresponding to additional processes and energy bands that affect superconductivity.

3.2 Submillimeter Quasioptical Interferometry

Since the 1980's much research work has focused on closing the terahertz gap by applying optical methods to conventional electronic sources in novel ways. From the microwave side, developments in high-frequency circuits, diodes, multiplexers, and vacuum electronics have enabled submillimeter sources to be scaled up into the low terahertz range. By incorporating these sources into interferometers it has become possible to perform phase-sensitive spectroscopy at wavelengths $\lambda \gtrsim 1$ mm. These so-called *quasioptical* techniques do not truly operate in the far-field limit but nevertheless provide powerful tools to access the full complex dielectric response of materials.

The ancestor of submillimeter quasioptical spectroscopy is the Fourier transform infrared spectrometer (FTIR). Based on the Michelson interferometer, the FTIR obtains the complex response of a sample via Fourier transformation of an interferogram acquired by recombining radiation from a polychromatic infrared source [224]. By adjusting the length of the reference arm the interferogram is produced and then subsequently modulated by the absorption spectrum of the sample, which is placed outside the interferometer. The Fourier transform procedure allows the complex sample spectrum to be extracted from the observed modulations because the total measured signal is a convolution of the sample spectrum and the interferogram of the empty interferometer. The bandwidth and resolution of the FTIR are therefore related to the bandwidth of the polychromatic source radiation and the size of the maximum displacement of the reference arm; to obtain high resolution and broad bandwidth the reference arm is scanned over as large a distance as possible such that all the lobes of the interferogram are captured by the scan.

In the infrared spectral range the FTIR enjoys significant advantages over frequency-domain dispersive spectroscopy. In particular, the FTIR is characterized by the multiplex advantage, because all frequencies are measured simultaneously, and the throughput advantage, because the radiation is collimated by a circular aperture as opposed to a linear grating. However, if the bandwidth of the polychromatic radiation is too narrow, the interferogram is broad and, if it extends beyond the scanning range of the interferometer, leads to the appearance of artifacts and loss of resolution. The limited availability of broadband radiation sources within the terahertz gap

therefore requires the FTIR technique to be modified at submillimeter frequencies. Many sources in the submillimeter frequency range have the advantage of producing intense monocromatic or continuous wave (CW) radiation, but this comes with the disadvantage that they are not suitable for FTIR spectroscopy. To adapt monochromatic sources of submillimeter radiation to phase-sensitive quasioptical spectroscopic measurements it is necessary to utilize interferometric techniques which incorporate the sample directly into the arms of the interferometer. In this way the material response is directly incorporated into the measured interference pattern. To obtain the optical constants $n(\omega)$ and $k(\omega)$ it is then necessary to measure both the magnitude and phase response of the interferometer, as the signal observed at the detector can no longer be described as a convolution of the sample spectrum and interference spectrum of the empty interferometer. With a monochromatic source this measurement is performed directly in the frequency domain by tuning the frequency output of the source. The optical constants are then extracted by inverting the Fresnel equations appropriate for the geometry and structure of the sample. While the multiplex advantage of the FTIR is thus lost, the axial beam symmetry of the interferometer implies that the throughput advantage is retained, giving quasioptical interferometry an advantage in signal-to-noise ratio compared to other spectroscopic techniques.

In this work, the optical constants $n(\omega)$ and $k(\omega)$ in the submillimeter spectral range are measured by employing a CW technique with independent measurements of the electric field magnitude and phase. A backward-wave oscillator is chosen as the submillimeter radiation source for its versatility, high power output, and frequency tunability. This source is then coupled to a Mach-Zehnder interferometer, which provides access to the complex dielectric response of a sample through tunability of the interferometer reference arm. The independent measurement of the transmission coefficient $T(\omega)$ and phase $\phi(\omega)$ allows $n(\omega)$ and $k(\omega)$ to be calculated independently of each other without the need for a Kramers-Kronig analysis.

3.2.1 The Backward Wave Oscillator

The backward wave oscillator (BWO) was invented independently in 1948 by Loshakov in Russia and in 1951 by Epsztein in France and Kompfner in Great Britain [225–227]. It was developed following a series of advances in research on klystrons, cavity magnetrons, and traveling-wave tubes as part of broader progress in military radar technology during and immediately following World War II [205, 228, 229]. Pioneered by the British on the eve of the war, radar was applied to devastating effect by all participant nations and its use significantly impacted both tactical and strategic choices as well as the war's final outcome. In particular, the inability of aircraft to evade radar detection was an important factor which led to the use of large bomber fleets to overwhelm the defensive capabilities of an adversary. Later, as the battle lines of the Cold War were drawn it became clear that a technology was needed which could defeat the extensive radar screens employed by both sides. Such a technology needed to provide high power, be rapidly tunable, and be portable enough to operate aboard a wide variety of aircraft. Furthermore, it needed to operate at frequencies above radio and microwaves in order to overwhelm and scramble the electronics of radar detection systems [230, 231].

These practical engineering requirements led to the defining characteristics of the BWO: (1) high intensity radiation greater than 10 mW; (2) high monochromaticity

with $\Delta\omega/\omega \approx 10^{-5}$; (3) high degree of polarization (>99.99%); (4) frequency emission up to 1.5 THz; and (5) rapidly electronically tunable to produce frequencies ±30% of the central value [232]. The BWO is a type of vacuum electronic device which reaches the terahertz frequency range by combining elements of microwave electronics technology with infrared optical techniques. In general, vacuum electronic devices fall within one of two types of classification [233]. The first type, which includes large accelerator-based instruments such as free electron lasers, produces electromagnetic radiation by bremsstrahlung, or transverse modulation of an electron beam. The second type, to which the BWO belongs, produces microwave radiation by slow-wave modulation of a longitudinal current via the Cerenkov effect.

BWO Operational Principles

The primary components of the BWO include a slow-wave circuit structure, electron gun, electron beam, voltage-biased collector, focusing magnet, and radiation output coupling, as depicted in Fig. 3.4 [233, 234]. The slow-wave structure is a micropatterned circuit or folded waveguide that is designed to support harmonics of a traveling spatial wave. As the electron beam passes across the slow-wave structure the electrons encounter the spatially varying field and velocity distribution produced by the periodic shape of the structure, and the electrons in the beam become gathered into bunches. The ∼1 T magnet improves the efficiency of the device by tightly focusing the electron beam into a thin filament. Like any oscillating cavity, the closed BWO tube-and-circuit system requires an amplitude and phase matching condition to always be satisfied to produce radiation emission. The fundamental $n = 0$ cavity mode corresponds to a traveling wave which runs in the same direction as the electron beam velocity. Interaction of the forward traveling electron beam with the $n = -1$ cavity spatial mode, however, produces a traveling wave with a forward phase velocity and backward group velocity. By matching the electron beam velocity with the forward phase velocity via the synchronization condition $v_e = v_{ph}$, the electron bunches only encounter a decelerating field and beam kinetic energy is transferred into backward traveling electromagnetic energy [235]. This backward electromagnetic wave further bunches electrons and provides a cavity feedback mechanism. If the input and output loads are matched, then there is zero flow of circuit energy in the slow wave structure and the radiated energy comes entirely from conversion of the electron beam kinetic energy. The feedback process produces a very stable, coherent CW wavefront which is coupled out of the tube at 90° via a waveguide.

At low beam currents regenerative amplification occurs, but above a threshold at higher currents space-charge oscillations appear and the cavity produces spurious backward waves at other frequencies [234]. In addition to the synchronization condition for electron beam and phase velocities, the slow-wave structure must be dispersive to allow the output frequency to be tuned by varying the electron beam acceleration voltage [236]. Furthermore, the cavity must be fixed to operate in the $n = -1$ spatial harmonic mode independent of frequency. This is possible if the slow-wave structure is designed to provide negative dispersion such that the total dispersion of the circuit exactly cancels. However, due to engineering limitations, the dispersion in the slow-wave structure eventually becomes either too little or too great to maintain this condition as the electon beam velocity and output frequency are varied across wide ranges. The bandwidth of output frequencies the BWO can

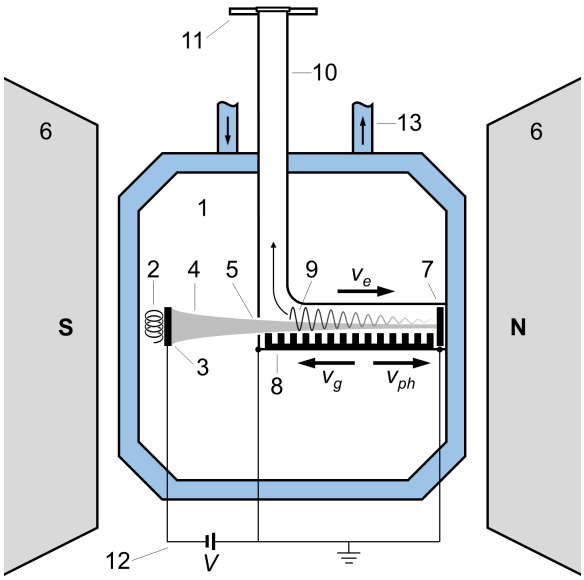

Figure 3.4 Cutaway schematic of the BWO device used in this work [232, 233, 236]. (1) Sealed vacuum cavity; (2) heater coil; (3) cathode; (4) electron beam; (5) aperture; (6) permanent focusing magnet; (7) collector and anode; (8) slow-wave structure; (9) traveling electromagnetic wave; (10) waveguide power output; (11) output coupling to free space; (12) external electronics control system; and (13) water coolant inlet and outlet.

produce is therefore related to the range of frequencies over which the $n = -1$ spatial mode and velocity matching conditions remain fulfilled.

Advantages and Disadvantages of BWO Sources

The disadvantages of the BWO and other vacuum electronic sources of microwave and terahertz radiation largely stem from the complex engineering requirements which need to be fulfilled to ensure their operation [237]. Most notably, BWOs and other traveling wave tubes suffer greatly from physical scaling problems. As power output and emission frequency are increased the necessary electron beam current densities also rapidly increase and become relativistic while the characteristic dimensions of the slow-wave structures rapidly decrease. Enormous acceleration voltages are required and space-charge buildup becomes significant, leading to formidable engineering challenges in developing circuitry, electronics control systems, and device cooling. High frequency BWO sources also suffer from increased metallic losses and the need for extremely high magnetic fields to focus the electron beam; at frequencies above 1.5 THz electromagnets are needed which can produce fields in excess of 1-2 T. Source operational lifetimes are only on the order of a few thousand hours and decrease with increasing output frequency. As such, in recent decades cheaper and more compact solid state sources of microwave and terahertz radiation have nearly completely pushed BWOs out of scientific and commercial use. With the last commercial developments coming in Russia in the late 1980's and early 1990's, functional BWO sources have become difficult to obtain [232, 237].

The main alternatives to the BWO include the Gunn diode, IMPATT (avalanche) diode, far-infrared CO_2 gas lasers, quantum cascade lasers, free electron lasers, and synchrotron facilities [238, 239]. Gunn and IMPATT diodes are solid state oscillator

devices which produce CW radiation at room temperature with a narrow linewidth of $\Delta\omega/\omega \approx 10^{-6}$, an order of magnitude narrower than for commercially available BWO sources. They can emit at powers >100 mW at 100 GHz but lack rapid tunability and are limited to operating over a restricted frequency band as determined by the physical dimensions and bandstructure of the semiconductor junctions. Furthermore, the emitted power falls off with frequency as $1/f^3$ above 100 GHz due to the transit time of carriers and dissipation in the diodes, and frequency multipliers are needed to reach frequencies above 200 GHz. Far-infrared CO_2 gas lasers provide increased power of 1-100 mW near 1 THz and can be designed to operate at CW in the range 0.3-5 THz, but are also poorly tunable and require an exchange of gas and laser line in order to change the laser frequency. Recent advances in terahertz gas lasers utilizing rotational modes of organic molecules have attempted to resolve this tunability problem up to an operating frequency of ∼2.5 THz but output powers in these systems remain below 1 mW [240]. Quantum cascade lasers suffer from similar operational problems. Despite emitting at powers up to ∼100 mW and frequencies up to ∼5 THz, they operate at single fixed frequencies determined by device dimensions and require the use of cryogenic cooling in order to achieve appreciable output power [241]. The final category of alternative terahertz radiation sources to BWOs, the accelerator based vacuum electronic sources, are primarily only available at a select few user facilities around the world and constitute very large, expensive, and complicated instruments. Free electron lasers, such as those at ELBE in Dresden-Rossendorf and at NovoFEL in Novosibirsk, are capable of providing pulsed terahertz radiation spanning from ∼1 THz to the far-infrared spectral region with large average powers in excess of 500 W and peak powers up to 1 MW [233]. Electron synchrotron facilities operating bending magnets, such as BESSY and KARA in Germany and NSLS and Jefferson Lab in the United States, produce coherent radiation in the mid- and far-infrared spectral ranges down to frequencies as low as 0.3-1 THz.

Despite the impressive advances in alternative terahertz radiation sources over the past three decades, the BWO remains the only radiation source in the submillimeter range which simultaneously offers high output powers, rapid and broad tunability, CW operation, and narrow linewidth with a very stable and coherent wavefront in a relatively compact package. These advantages make the BWO an ideal radiation source for applications where high power and phase stability are needed, such as in terahertz spectroscopic measurements of superconductors, metals, magnetic materials, and samples with high attenuation [242]. Furthermore, some spectroscopic techniques, such as quasioptical interferometry, are only compatible with BWO radiation sources in the microwave and terahertz range due to the need for coherent and highly collimated radiation which can be coupled into free space [232]. The next section discusses such submillimeter quasioptical interferometry in more detail.

3.2.2 Mach-Zehnder Interferometry

The Mach-Zehnder interferometer is a modified version of the Michelson interferometer. It is characterized by two arms which are separated and recombined at different points in space, in contrast to the single central beamsplitter characteristic of the Michelson interferometer. A basic illustration of the geometry of the Mach-Zehnder interferometer is shown in Figure 3.5. The interferometer consists of an incoming beam which is polarized by an adjustable polarizer and then split into two arms by a

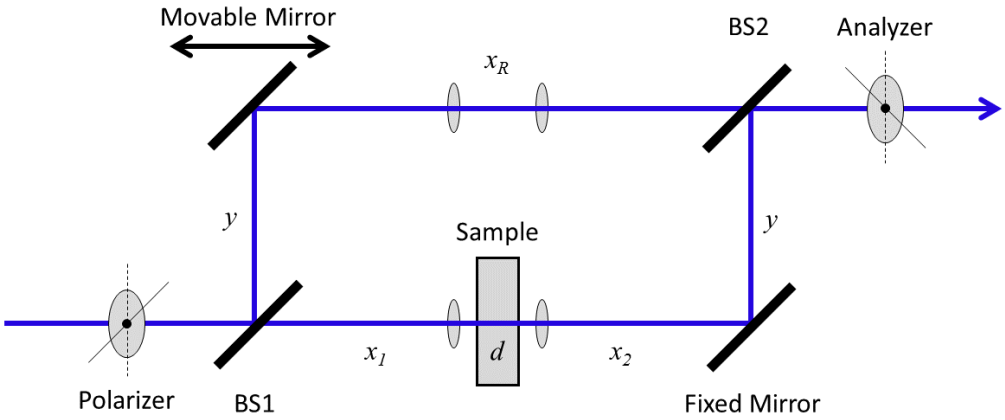

Figure 3.5 A schematic layout of the quasioptical Mach-Zehnder interferometer used to carry out phase sensitive measurements in the submillimeter spectral range. The BWO source is placed before the polarizer while the detector (bolometer or golay cell) is placed after the analyzer position.

beamsplitter, marked BS1. Radiation transmitted through BS1 enters the measurement arm of the interferometer and passes through the sample, while the radiation reflected by BS1 travels along the reference arm. The two beams are then recombined by a second beam splitter, marked BS2. For the case of microwave radiation the two beamsplitters are wire-grid polarizers with their axes oriented perpendicular to each other. BS1 is oriented horizontally while BS2 is oriented vertically, so that radiation of horizontal polarization passes through the sample while radiation polarized vertically passes through the reference arm.

Since the BWO source does not produce perfectly polarized radiation, the angle of the initial polarizer is chosen to balance the intensity of microwave radiation in each arm of the interferometer. The angle of the analyzer after BS2 is then chosen such that the microwave radiation exiting the interferometer is maximally extinguished in the zeroth-order mode of interference when an empty aperture is placed in the sample space (BS2 $\sim 90^\circ$ relative to BS1). That is, in the case of the "empty channel" when the sample is removed and the optical path lengths of the measurement and reference arms are equal, the radiation passing through the two arms will recombine at BS2 to produce maximum constructive interference with the same polarization as the initial polarizer. If either of the optical path lengths changes slightly as compared to the other (for example, by adding the sample), then the resulting combined wave will possess a small degree of elliptical polarization and a detector placed after the analyzer will detect the appearance of a small orthogonal polarization component. This component is measured as an increase in signal power above the background noise level when the analyzer and initial polarizer are orthogonal to each other.

A set of microwave lenses is intalled on either side of the sample space in order to focus radiation onto the sample. An identical set of lenses is installed in the reference arm in order to equalize the optical path lengths. Due to the relatively long wavelengths of microwave radiation compared to typical sample film thicknesses, the radiation cannot be assumed to focus at a single point in space. Instead, the focus will have a finite beam waist as determined by Gaussian optics and the wavefronts

on either side of the focus will be curved while the wavefront at the focus will be flat. Therefore the sample should ideally be placed as close to the focus as possible in order to minimize beam distortion.

Prior to the measurement of the phase the position of a movable mirror on the reference arm is calibrated in order to ensure that the interferometer operates at the zeroth-order interference minimum. The zeroth-order interference position is technically an interference maximum but the presence of the analyzer ensures that this maximum is interpreted as a minimum by the detector. The correct zeroth-order optical path length is found by adjusting the position of the movable mirror to maintain a minimum signal at the detector while the microwave frequency is scanned. If the mirror is located at the zeroth-order position then its position will be independent of the frequency. However, if the mirror is initially located at a higher-order interference minimum then the position of the mirror will depend linearly on frequency. Thus the initial position of the movable mirror is adjusted until a frequency-independent position is found. The calibration procedure is carried out twice in order to determine the zeroth-order position for both the empty channel and the sample.

Experimentally Obtaining $T(\omega)$

Transmission measurements are carried out by first blocking the path of the reference arm. The intensity of transmitted submillimeter radiation is then measured separately with the sample in place and with the sample removed, leaving an empty reference aperture, and the transmission coefficient $T(\omega)$ is obtained:

$$T(\omega) = \frac{I_{sample}(\omega)}{I_{ref}(\omega)}. \tag{3.33}$$

Intensity I is measured using either a 1.6 K bolometer or Golay cell. Because the wavelength of the of the radiation ($\sim$1 mm at 300 GHz) is significant compared to the aperture sizes used ($\sim$8 mm), it is imperative to ensure that variances in diffraction effects caused by the aperture edges do not occur or the Fabry-Pérot interference pattern of the sample could be destroyed. Samples which are highly reflective or poorly transmissive are much more susceptible to errors of this kind. This issue is resolved by mounting the sample on a stick which has a fixed aperture and then sliding the sample in and out of the aperture window instead of moving the aperture itself.

Experimentally Obtaining $\phi(\omega)$

After the transmission coefficient $T(\omega)$ is obtained the phase $\phi(\omega)$ of the transmitted electric field is measured. The experimental setup is converted into a Mach-Zehnder interferometer by unblocking the path of the reference arm which has been split off the main microwave beam before it passes through the sample. The two beams are then recombined after some distance and the phase is determined by comparing the difference in the optical path lengths of the two interferometer arms.

To measure the phase $\phi(\omega)$, a calibration scan is carried out in the empty channel configuration and the zero-signal position of the movable mirror is recorded as a function of frequency. Afterwards, a measurement scan is carried out with the sample in place and the zero-signal position of the mirror is recorded at the same frequencies. The phase is then extracted from the difference in the two mirror positions.

In the empty channel configuration the phase difference between the measurement and reference beams is given by

$$\Delta\Phi_E = \frac{\omega}{c}L_E - \frac{\omega}{c}L_{R1},$$

where L_E is the optical path length of the measurement arm with the empty channel, L_{R1} is the optical path length of the reference arm, and c is the speed of light in vacuum. Without a sample in place, the wave in the sample arm travels a distance $x_1 + d + x_2 + y$ while the wave in the reference arm travel a distance $y + x_{R1}$ (see Figure 3.5), so the optical path lengths are

$$L_E = x_1 + d + x_2 + y,$$

$$L_{R1} = y + x_{R1}.$$

Since the instrument maintains the position of the adjustable mirror at the zeroth-order interference minimum, $\Delta\Phi_E = 0$ and

$$x_1 + x_2 = x_{R1} - d. \tag{3.34}$$

Similarly, with the sample in place the phase difference between the two arms of the interferometer is

$$\Delta\Phi_S = \frac{\omega}{c}L_S - \frac{\omega}{c}L_{R2},$$

where L_S is the optical path length of the measurement arm with the sample and L_{R2} is the optical path length of the reference arm, which has changed from L_{R1} due to the addition of the sample. The sample has an index of refraction $n(\omega)$, so

$$L_S = x_1 + dn(\omega) + x_2 + y,$$

$$L_{R2} = y + x_{R2}.$$

Again, we take $\Delta\Phi_S = 0$ in zeroth-order interference which gives

$$x_1 + dn(\omega) + x_2 + y = x_{R2} + y,$$

and substitution with Equation 3.34 gives

$$x_{R2} - x_{R1} = dn(\omega) - d.$$

Here, x_{R1} and x_{R2} represent absolute distances between the movable mirror and beam-splitter BS2 during the calibration and measurement scans, respectively. However, since the above expression depends only on the difference in the reference arm length between the two scans, the length of the arm may be measured from any arbitrary position as long as that position remains the same for both scans. Thus, we may substitute for x_{R1} and x_{R2} the variables C and M, respectively, which represent the calibration and measurement position readings of a micrometer on the movable mirror that are read out by a data acquisition unit:

$$M - C = d\left[n(\omega) - 1\right]. \tag{3.35}$$

Finally, we may define the phase $\phi(\omega)$ of the sample as

$$\phi(\omega) = \frac{\omega}{c}dn(\omega),$$

which leads to the relation

$$\phi(\omega) = \frac{\omega}{c}(M - C + d) \tag{3.36}$$

between the experimentally measured parameters and the phase.

Relating Measured Quantities to $n(\omega)$ and $k(\omega)$

To properly extract the optical constants $n(\omega)$ and $k(\omega)$, the experimentally measured values of $T(\omega)$ and $\phi(\omega)$ must be analytically related to the complex transmission of the system. Planar layered systems are categorized into three separate groups according to their number of layers: single layer slabs, double layer film-on-substrate systems, and multilayers with 3 or more layers. The parallel planar structure and normal incidence of the incoming electromagnetic wave greatly simplify the analytical treatment of the complex transmission by removing the angular and thickness dependences of the Fresnel equations. In this work the response of multilayer films is not explored and so only the transmission and phase of single layer slabs and film-on-substrate systems are treated here.

Single layer systems. The transmission coefficient $T(\omega)$ is given by the square of the complex transfer function, $T(\omega) = \left|\tilde{t}(\omega)\right|^2$, where

$$\tilde{t}(\omega) \equiv \frac{\tilde{t}_{sample}(\omega)}{\tilde{t}_{ref}(\omega)} = \frac{\tilde{E}_{sample}(\omega)}{\tilde{E}_{ref}(\omega)}. \tag{3.37}$$

An electromagnetic wave passing through a slab of thickness L must transmit through both the front and back interface of the sample in addition to accumulating a phase shift proportional to L. The electric field transmitted by the sample is therefore expressed as

$$\tilde{E}_{sample}(\omega) = \tilde{t}_{01}\tilde{P}_1\tilde{F}_1\tilde{t}_{10}\tilde{E}_0(\omega),$$

where $\tilde{t}_{01}$ is the complex Fresnel transmission coefficient for a wave passing from vacuum into the slab, $\tilde{P}_1$ is the accumulated phase as the wave traverses the slab, $\tilde{F}_1$ is the Fabry-Pérot coefficient, and $\tilde{t}_{10}$ is the complex transmission coefficient of the wave passing from the slab back into vacuum [207]. Following Eq. 3.11 in the discussion of the Fresnel equations in Section 3.1.1, the complex Fresnel coefficients are frequency dependent and are given by

$$\tilde{t}_{01}(\omega) = \frac{2\tilde{n}_0(\omega)}{\tilde{n}_0(\omega) + \tilde{n}_1(\omega)}, \qquad \tilde{t}_{10}(\omega) = \frac{2\tilde{n}_1(\omega)}{\tilde{n}_1(\omega) + \tilde{n}_0(\omega)} \tag{3.38}$$

$$\tilde{P}_1(\omega) = e^{i\omega\tilde{n}_1(\omega)L/c}. \tag{3.39}$$

The Fabry-Pérot coefficient represents the infinite set of reflections and standing waves which occur in the cavity formed by the two slab interfaces. Each reflection interferes with the incoming wave, so the Fabry-Pérot contribution is expressed as the complex sum

$$\tilde{F}_1(\omega) = \sum_{j=0}^{\infty} \left[\tilde{r}_{10}^2(\omega)e^{2i\omega\tilde{n}_1(\omega)L/c}\right]^j,$$

where each term includes reflection from both the front and back interfaces and the phase accumulated by round-trip transit of the wave through the slab. By comparison with the geometric series, this sum is customarily written in closed form as

$$\tilde{F}_1(\omega) = \frac{1}{1 - \tilde{r}_{10}^2(\omega)e^{2i\omega\tilde{n}_1(\omega)L/c}} \tag{3.40}$$

with the complex reflection coefficient

$$\tilde{r}_{10}(\omega) = \frac{\tilde{n}_0(\omega) - \tilde{n}_1(\omega)}{\tilde{n}_0(\omega) + \tilde{n}_1(\omega)}.$$

When the sample is removed the electromagnetic wave accumulates a relative phase shift equivalent to passing through a volume of vacuum of thickness L. The reference electric field is therefore given by

$$\tilde{E}_{ref}(\omega) = e^{i\omega\tilde{n}_0(\omega)L/c}\tilde{E}_0(\omega).$$

Combining the above equations and omitting the explicit frequency dependence of the Fresnel coefficients, the complex transmission transfer function for a single layer slab can be written as

$$\tilde{t}_1(\omega) = \tilde{t}_{01}\tilde{F}_1\tilde{t}_{10}e^{i\omega(\tilde{n}_1(\omega)-\tilde{n}_0(\omega))L/c} \tag{3.41}$$

and the measured transmission and phase are related to the complex optical constants $\tilde{n}_1(\omega) = n_1(\omega) + ik_1(\omega)$ of the sample by combining Equations 3.33, 3.36, and 3.41:

$$\frac{I_{sample}(\omega)}{I_{ref}(\omega)} = \left|\tilde{t}_{01}\tilde{F}_1\tilde{t}_{10}\right|^2 \tag{3.42}$$

$$M(\omega) - C(\omega) = \frac{c}{\omega}\left[\arg\left(\tilde{t}_{01}\tilde{F}_1\tilde{t}_{10}\right) + 2\pi m\right] + \left[\tilde{n}_1(\omega) - \tilde{n}_0(\omega)\right]L. \tag{3.43}$$

Here, m is an integer and represents the numerical correction that is required if the phase of either the measurement or calibration scans were not performed in the zeroth-order mode. If both scans were performed in the same order mode, then $m = 0$.

Double layer systems. In a double layer system, an electromagnetic field first enters a top layer of thickness d before transmitting across an interface and then out through a second layer of thickness L. The electric fields transmitted through the sample and reference aperture are expressed as

$$\tilde{E}_{sample}(\omega) = \tilde{t}_{01}\tilde{P}_1\tilde{F}_1\tilde{t}_{12}\tilde{P}_2\tilde{F}_2\tilde{t}_{20}\tilde{E}_0(\omega)$$

$$\tilde{E}_{ref}(\omega) = e^{i\omega\tilde{n}_0(\omega)(d+L)/c}\tilde{E}_0(\omega),$$

with explicit frequency dependence of the Fresnel coefficients omitted for clarity [243]. As in the single layer case, the first four coefficients of the sample correspond to the transmission of the first layer only, with the transmission, phase, and Fabry-Pérot coefficients

$$\tilde{t}_{01}(\omega) = \frac{2\tilde{n}_0(\omega)}{\tilde{n}_0(\omega)+\tilde{n}_1(\omega)}, \qquad \tilde{t}_{12}(\omega) = \frac{2\tilde{n}_1(\omega)}{\tilde{n}_1(\omega)+\tilde{n}_2(\omega)}$$

$$\tilde{P}_1(\omega) = e^{i\omega\tilde{n}_1(\omega)d/c}, \qquad \tilde{F}_1(\omega) = \frac{1}{1-\tilde{r}_{10}(\omega)\tilde{r}_{12}(\omega)e^{2i\omega\tilde{n}_1(\omega)d/c}}.$$

The final three coefficients of the sample correspond to Fabry-Pérot oscillation and transmission in the second layer. In contrast to the single layer case, however, $\tilde{F}_2$ carries a reflection contribution from both interfaces of the first layer. Thus the second Fabry-Pérot coefficient is written as

$$\tilde{F}_2(\omega) = \frac{1}{1-\tilde{r}_{20}(\omega)\tilde{r}_{210}(\omega)e^{2i\omega\tilde{n}_2(\omega)L/c}},$$

where

$$\tilde{r}_{210}(\omega) = \tilde{r}_{21}(\omega) + \tilde{r}_{10}(\omega)\tilde{t}_{21}(\omega)\tilde{P}_1^2(\omega)\tilde{t}_{12}(\omega)\tilde{F}_1(\omega)$$

is the composite reflection coefficient of the first layer. From Eqs. 3.10 and 3.11, the Fresnel reflection, transmission, and phase coefficients for the second layer are given by

$$\tilde{r}_{10(20)}(\omega) = \frac{\tilde{n}_{0(0)}(\omega) - \tilde{n}_{1(2)}(\omega)}{\tilde{n}_{0(0)}(\omega) + \tilde{n}_{1(2)}(\omega)}, \qquad \tilde{r}_{12(21)}(\omega) = \frac{\tilde{n}_{2(1)}(\omega) - \tilde{n}_{1(2)}(\omega)}{\tilde{n}_{2(1)}(\omega) + \tilde{n}_{1(2)}(\omega)}$$

$$\tilde{t}_{20(21)}(\omega) = \frac{2\tilde{n}_{2(2)}(\omega)}{\tilde{n}_{2(2)}(\omega) + \tilde{n}_{0(1)}(\omega)}, \qquad \tilde{P}_2 = e^{i\omega\tilde{n}_2(\omega)L/c}.$$

With Eq. 3.37 and combining the above Fresnel coefficients, the complex transmission transfer function for a double layer system is therefore given by

$$\tilde{t}_{\mathrm{II}}(\omega) = \tilde{t}_{01}\tilde{F}_1\tilde{t}_{12}\tilde{F}_2\tilde{t}_{20}e^{i\omega(\tilde{n}_1(\omega)-\tilde{n}_0(\omega))d/c}e^{i\omega(\tilde{n}_2(\omega)-\tilde{n}_0(\omega))L/c}, \tag{3.44}$$

and the measured transmission and phase are related to $\tilde{n}_1(\omega) = n_1(\omega) + ik_1(\omega)$ and $\tilde{n}_2(\omega) = n_2(\omega) + ik_2(\omega)$ of the two layers through

$$\frac{I_{sample}(\omega)}{I_{ref}(\omega)} = \left|\tilde{t}_{01}\tilde{F}_1\tilde{t}_{12}\tilde{F}_2\tilde{t}_{20}\right|^2 \tag{3.45}$$

$$M(\omega) - C(\omega) = \frac{c}{\omega}\left[\arg\left(\tilde{t}_{01}\tilde{F}_1\tilde{t}_{12}\tilde{F}_2\tilde{t}_{20}\right) + 2\pi m\right] + \left[\tilde{n}_1(\omega) - \tilde{n}_0(\omega)\right]d + \left[\tilde{n}_2(\omega) - \tilde{n}_0(\omega)\right]L. \tag{3.46}$$

The transmission spectrum takes the form of an infinite set of equally spaced fringes whose magnitudes approach $T = 1$ and which are damped by the absorption of the material. The spacing and sharpness of the fringes are simultaneously determined by the layer thicknesses and the magnitude of the discontinuities in the index of refraction at the interfaces. If the layered sample is measured in either vacuum or a low density gaseous atmosphere that does not have infrared active modes near the measurement frequency, such as nitrogen or helium exchange gas in a bath cryostat, then $\tilde{n}_0(\omega) = 1$. The expected transmission and phase response for a single layer dielectric slab in such a medium is shown in Fig. 3.6(a) and (b), calculated from Eqs. 3.42 and 3.43 for $L = 1$ mm of $(LaAlO_3)_{0.3}(Sr_2AlTaO_6)_{0.7}$ (LSAT), a common substrate material. The gradual reduction in magnitude of the transmission peaks with increasing frequency reflects the small value of $k(\omega)$. Oscillatory behavior of the phase results from the Fabry-Pérot interference in the slab, with an offset from zero given by Eq. 3.35. The spacing of the transmission fringes and the period of oscillation of the phase are given by $\Delta f = \Delta\omega/2\pi = c/2nL$, as highlighted by the vertical dashed lines in Fig. 3.6; since the velocity of light in the material is c/n, this quantity corresponds to the inverse of the round-trip transit time of a photon in the slab. Therefore, the transmission fringes are due to resonant enhancement in the cavity: transmission approaches $T = 1$ when the frequency of the electromagnetic wave is equivalent to an integer multiple of the round-trip transit frequency in the slab. When a second layer is added to the system the transmission pattern becomes further attenuated and experiences a phase shift. If both layers have thicknesses larger than $c/2nf$, then the transmission pattern of the first layer is modulated by the Fabry-Pérot interference pattern of the second layer and the phase shifts by a small amount due to the complex Fresnel transmission and reflection coefficients at the shared interface. However, if the additional layer is very thin, with $d \ll c/2nf$,

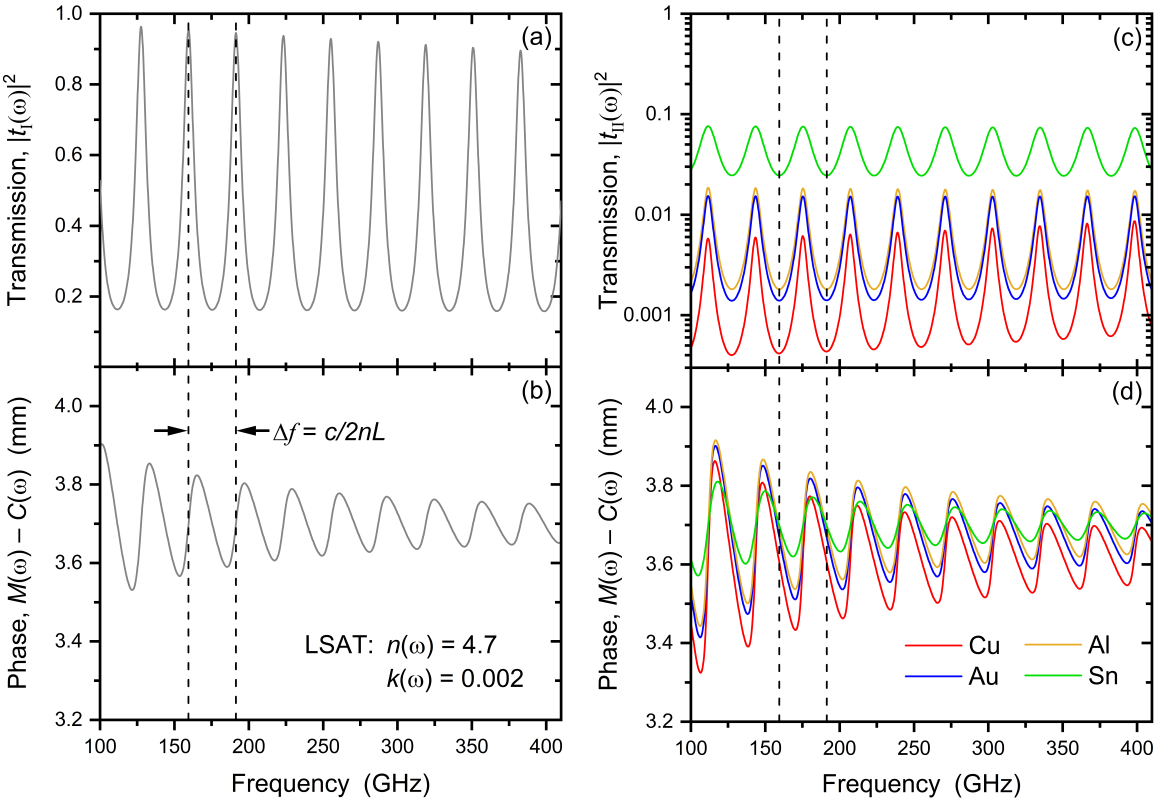

Figure 3.6 (a, b) The transmission and phase of a single layer in a Mach-Zehnder interferometer, calculated by Eqs. 3.42 and 3.43 for $L = 1$ mm of LSAT. (c, d) The transmission and phase of a double layer, calculated by Eqs. 3.45 and 3.46 using Drude model parameters for $d = 100$ nm of Cu, Au, Al, and Sn on $L = 1$ mm of LSAT at 295 K [206, 244]. Vertical dashed lines correspond to the fifth and sixth transmission fringes of a single LSAT layer, with a frequency spacing of $\Delta f = 31.9$ GHz.

then the Fabry-Pérot interference pattern of the thicker layer is not modulated but instead attenuated by the reflectivity of the thin layer. Furthermore, the transmission pattern undergoes an abrupt π phase shift when the complex reflection coefficient at the shared interface, $\tilde{r}_{210}(\omega)$, changes sign. This occurs due to a large discontinuity in $k(\omega)$ at the interface and indicates the presence of strong screening in the thin layer. Figure 3.6(c) and (d) depict the expected transmission and phase for a double layer film-on-substrate system, calculated from Eqs. 3.45 and 3.46 for $d = 100$ nm of four common metals (Cu, Al, Au, and Sn) on $L = 1$ mm of LSAT using Drude model parameters σ_0 and τ at 295 K [206, 244]. The vertical dashed lines correspond to the fifth and sixth transmission maxima of the single layer LSAT as in (a) and (b). By comparison of the dashed lines in panels (a) and (b) to those in (c) and (d), it is clear that the transmission patterns of the metallic thin films are shifted by half a period compared to the transmission spectrum of the bare LSAT substrate. Thus a phase shift of π in the Fabry-Pérot interference spectrum can be regarded as a key feature of a thin metallic film on a substrate, and the π jump is interpreted as the onset of diamagnetic screening.

Finally, it is apparent from Fig. 3.6(c) that 100 nm of highly reflective metal (the noble metals Cu and Au, with $\sigma_0 \approx$ 450-600 $\mathrm{m\Omega^{-1}cm^{-1}}$ and $\tau \approx 2\text{-}3 \times 10^{-14}$ s) is enough to attenuate the transmission signal to $\lesssim$1% of the intensity of the incoming

radiation. By using filters and a 1.6 K bolometer as a detector it is possible to resolve transmission fractions as low as 10^{-4} to 10^{-5}. Therefore, despite these metals having Drude (unscreened) plasma frequencies as high as ∼8-10 eV, the Mach-Zehnder interferometer is capable of differentiating the Drude parameters σ_0 and τ with measurement frequencies in the sub-THz range. Also notable is the response of the poor metal conventional superconductors Al and Sn, which have *dc* conductivities less than those of the noble metals at 295 K. The transmissions of Al and Sn lie in the range of 1-10%, indicating that quasioptical Mach-Zehnder interferometry is well suited to the study of the sub-THz response of thin film superconductors.

3.3 Terahertz Time-Domain Spectroscopy

Compared to submillimeter quasioptical interferometry and Fourier transform infrared spectroscopy, terahertz time-domain spectroscopy (TTDS) is a complementary technique used to measure the phase sensitive response of materials in the frequency range 0.1–10 THz. TTDS was developed in the late 1980's and early 1990's following advances in ultrafast pulsed laser technology, in particular the development of the Ti:Sapphire femtosecond laser [10]. Since its initial development, the technique has seen much use and success in the study of gases, condensed matter systems (notably dielectrics, semiconductors, metals, and correlated electron materials), high-speed electronics, atmospheric science, pharmaceuticals, biology, medicine, and defense and security applications.

The basic operational principle of TTDS consists of four primary elements: (1) an emitter which couples pulsed terahertz radiation into free space, (2) a sample chamber optimized for interaction of a sample with the freely propagating terahertz waves, (3) a detector unit for time-resolved detection of the terahertz electric field components, and (4) a time delay mechanism between the generation and detection elements to vary the relative arrival time of the terahertz pulse and probe pulse at the detector [245]. Since the frequency range 0.1–10 THz generally falls above the highest frequencies achievable from electronic sources but below the lowest frequencies obtainable from most optical techniques, the pulsed terahertz sources used in TTDS usually combine key elements of both electronic and optical sources. As will be discussed further in Appendix A, such *optoelectronic* devices most often used to generate and detect pulsed terahertz radiation include gated photoconductive antennas and the electrooptic effect via second-order frequency conversion processes in a noncentrosymmetric crystal. Photoconductive antennas take advantage of picosecond polarization currents in patterned microstructures (commonly called *Auston switches* after their inventor) to rectify a femtosecond near-IR laser pulse. Terahertz generation by the electrooptic effect in materials such as poled polymers, $LiNbO_3$, $LiTaO_3$, CdTe, ZnTe, and GaP produces terahertz pulses with bandwidths determined by the width of the frequency envelope of the near-IR femtosecond laser pulse. The reversibility of the second-order processes allow the same devices that are used for terahertz generation to also be used for terahertz detection. The sample vessels most often used in TTDS experiments are the same types of optical cryostats used in submillimeter quasioptical interferometry and infrared spectroscopy, notably liquid helium bath and compact cold finger cryostats; however, it is also possible to perform TTDS experiments with samples mounted in the ambient laboratory atmosphere. The time delay mechanism

most commonly employed in a traditional TTDS setup involves a retroreflective mirror mounted on a motorized linear track, but rotating mirrors and oscillating optical elements are also used. As ultrafast laser technology continues to progress to include new achievements in ultrahigh repetition rates and pulse stabilization, it has become possible to construct time delay mechanisms based on asynchronous sampling of optical pulses without need for physical moving delay stages. This latter type of time delay mechanism provides a marked improvement in data acquisition rates and time resolution, and opens the door to applying TTDS to the study of physical phenomena in a wider range of experimental conditions.

TTDS shares many significant features with FTIR spectroscopy, but the two techniques also differ in key ways. Irrespective of the details of the detection mechanism, the signal $S(t)$ that is obtained in TTDS is described by the convolution

$$S(t) \propto I_{\text{opt}}(t - t') \otimes E_{\text{THz}}(t),$$

where $I_{\text{opt}}(t - t')$ is the intensity of the near-IR detector laser pulse and t' is the relative time delay between the terahertz pulse and the detector pulse. If the width of $I_{\text{opt}}(t-t')$ in the time domain is much smaller than the duration of the terahertz pulse, then $I_{\text{opt}}(t - t')$ can be approximated as a Dirac delta function and $S(t) \propto E_{\text{THz}}(t)$. Importantly, $S(t)$ is sensitive to the sign of the terahertz field. The terahertz spectrum is then found by Fourier transform of $E_{\text{THz}}(t)$,

$$\tilde{E}_{\text{THz}}(\omega) = \frac{1}{\sqrt{2\pi}} \int_{-\infty}^{\infty} E_{\text{THz}}(t) e^{i\omega t} dt \tag{3.47}$$

The Fourier transform takes the real-valued function $E_{\text{THz}}(t)$ and outputs a complex-valued function $\tilde{E}_{\text{THz}}(\omega)$. The complex spectrum can therefore be written as

$$\tilde{E}_{\text{THz}}(\omega) = A(\omega) e^{i\phi(\omega)}$$

with an amplitude component $A(\omega)$ and phase component $\phi(\omega)$. TTDS thus has access to the full complex response of the terahertz field (both amplitude and phase information) through a single measurement of $E_{\text{THz}}(t)$ compared to FTIR, which measures only the intensity $|E_{\text{THz}}(t)|^2$ of the terahertz field as a function of time delay and does not directly measure the phase. Despite this difference, both techniques possess the so-called Fellgett, or multiplex, advantage and the Jacquinot advantage [224,246]. The Fellgett advantage describes the property of the Fourier technique where many wavelengths contribute to the measurement simultaneously, as compared to spectroscopic measurements performed in the frequency domain. The Jacquinot advantage describes the increased power throughput of a circular diaphragm characteristic of a spectrometer with axial symmetry, as compared to a slit or grating spectrometer.

As a result of its design, the TTDS technique enjoys several advantages over FTIR in the spectral range below ∼5 THz. First, TTDS has ∼5 orders of magnitude higher signal-to-nose ratio than FTIR with typical dynamic ratios of 60–70 dB, and coherent detection of terahertz pulses by the electrooptic sampling technique has ∼4 orders better noise equivalent power than a helium cooled bolometer. The reason for this is because of the use of gated detection in TTDS; the detector is almost always off except for when the ultrafast detector pulse is impingent, so the Johnson noise is negligible [247]. Second, the terahertz sources used in both TTDS and FTIR have typical average powers of ∼0.1 μW. FTIR typically uses a mercury lamp as a

radiation source, which functions as an incoherent blackbody. In TTDS, on the other hand, the source (either a photoconductive antenna or electrooptic generation in a nonlinear crystal) has a duty cycle of $\sim 10^{-4}$, so the peak power of the individual terahertz pulses is on the order of 1 mW [246]. Third, the Bose-Einstein occupation factor, which measures the number of photons present in a unit coherence volume, is proportional to $1/(e^{\hbar\omega/kT} - 1)$ and is approximately equal to 1 for a blackbody at room temperature near terahertz frequencies. In contrast, the number of photons in a single terahertz pulse in TTDS is $\sim 10^5$, so the fluctuation rate is $1/\sqrt{N} \sim 300$ times smaller for TTDS than for FTIR. However, at frequencies above ~5–7 THz, difficulties in TTDS pulse generation and detection emerge due to limitations on the rate of electronic response in photoconductive antennas and the breakdown of electrooptic efficiency in nonlinear crystals from the presence of phonon bands. These difficulties dramatically reduce the signal-to-noise ratio of TTDS, so at frequencies above ~5–7 THz FTIR is typically a superior technique.

3.3.1 The TTDS Spectrometer

The TTDS setup used in this work is schematically illustrated in Fig. 3.7. The system is based on the high speed asynchronous optical sampling technique, which replaces the traditional time delay stage with two coupled 1 GHz repetition rate lasers with central wavelength near 800 nm. The repetition rates of the two lasers are offset by just 2000 Hz such that the beat frequency between the two lasers serves as the physical mechanism of scanning in the time domain. The faster slave laser pumps the photoconductive antenna while the slower master laser probes the transient terahertz electric field in a 200 μm thick (110)-oriented GaP electrooptic detector crystal optically contacted onto a 3 mm thick (100)-oriented GaP substrate. The terahertz pulse source is a LaserQuantum GmbH TeraSED interdigitated finger antenna unit, a type of large-area antenna that is capable of producing terahertz pulses with bandwidths of 0.1–7 THz and dynamic ratios of ~70 dB [248]. Negative dispersion mirror pairs are used to achieve transform limited laser pulses with the miniumum possible laser pulse duration of 40–45 fs. A set of off-axis gold-coated parabolic mirrors are used to focus the emitted terahertz radiation onto a sample, which is contained within a liquid helium bath cryostat. An identical set of off-axis parabolic mirrors then focuses the terahertz radiation onto the GaP electrooptic detector crystal. All terahertz optics are contained within a dry nitrogen purge box in order to reduce terahertz absorption by atmospheric humidity. The details of each of these spectrometer elements are discussed in Appendix A.

Asynchronous Optical Sampling

Conventional TTDS systems generally employ various mechanical elements to achieve a variable time delay between the arrival of the terahertz pulse and probe pulse at the detector [10, 245]. The most common scheme is to use a retroreflecting mirror mounted on a motorized linear translation stage that is controlled electronically by data acquisition software in tandem with a mechanical or electrooptic chopping scheme to enable synchronous detection. With step sizes on the order of 10 μm this allows for time resolutions of 50–100 fs. Other mechanical detection schemes include rotating mirrors and oscillating optical elements. However, these time-delay schemes

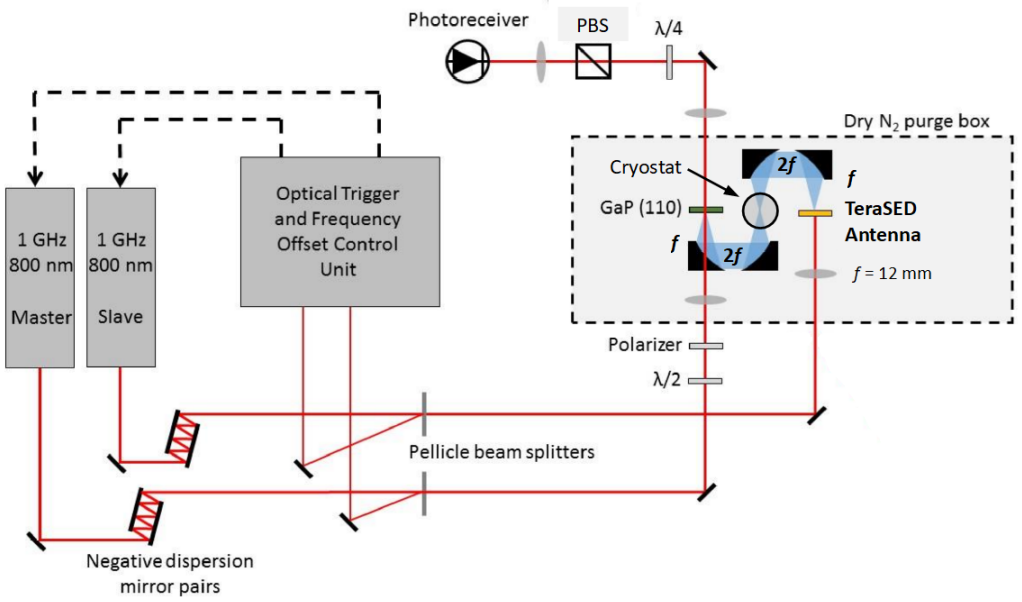

Figure 3.7 A schematic outline of the TTDS system used in this work. The time delay mechanism and detection scheme are based on the asynchronous optical sampling technique, which uses two 1 GHz repetition rate lasers with a repetition frequency offset of just 2 kHz. Terahertz radiation is generated with an interdigitated finger photoconductive antenna patterned on GaAs. Terahertz radiation is detected electrooptically in a 200 μm thick (110)-oriented GaP detector crystal pressed onto a 3 mm thick (100)-oriented GaP substrate.

come with the disadvantage that the moving mechanical elements introduce appreciable mechanical noise into the experiment and often have restricted ranges of motion that limit the duration of the time delay window, resulting in reduced frequency resolution and bandwidth. Furthermore, moving optical elements can give rise to position-dependent beam alignment errors that introduce amplitude and phase errors into the measurement.

The asynchronous optical sampling (ASOPS) technique is an all-optical time delay scheme that provides an alternative to mechanical time delay setups. The ASOPS method utilizes two modelocked pulsed lasers operating with their frequencies f offset by a few kilohertz [249]. The few-kilohertz beat frequency $\Delta f = f_{\text{pump}} - f_{\text{probe}}$ produces a repetitive time delay between the pump and probe laser pulses that progressively increases in steps of $1/f_{\text{probe}} - 1/f_{\text{pump}}$ with each successive laser period so that the repetition rate of the full time trace is the frequency Δf. With each repetition of the pump laser, the probe samples a slightly later point in the decay curve of the pump pulse such that the time axis measured in real (laboratory) time is scaled from the time axis of the true pump response by the factor $f_{\text{pump}}/\Delta f$. Therefore, the defining feature of the ASOPS technique is that it enables time-resolved measurement of ultrafast processes by dramatically expanding the time axis of the measurement to allow such processes to be resoloved by much slower conventional electronic methods [250]. To increase the time resolution of the ASOPS detection f_{pump} must be large and Δf must be small.

ASOPS used in TTDS setups enjoys a distinct advantage over conventional mechanical time delay stages in that full time traces spanning 1 ns can be completed

in milliseconds [251]. Conventional mechanical time delay stages, on the other hand, require translation distances of 15 cm to obtain a 1 ns time trace. With step sizes of 10–100 μm, the time required to position the translation stage at each point and average out noise can lead to acquisition times on the order of tens of minutes, in which time long-period laboratory fluctuations can have a significant effect (such as fluctuations of the cryostat temperature, air humidity, or beam alignment). As a result, ASOPS is well suited to measurements that must be performed in dynamic or unstable environments, such as in pulsed magnetic fields or with transient applied currents.

The TTDS setup employed in this work utilizes a high speed ASOPS detection scheme based on two coupled Ti:Sapphire lasers from LaserQuantum GmbH with a frequency offset of $\Delta f = 2$ kHz [252]. Terahertz transients are detected by a master laser with repetition frequency $f \approx 1$ GHz and generated with a frequency-locked slave laser of frequency $f + \Delta f$. The throughput electronics with 14-bit analog-to-digital converter provide a data sampling rate of $f_{\text{sampling}} = 100$ MHz. As a result, the time resolution $\tau_{\text{res}} = \Delta f / f_{\text{pump}} f_{\text{sampling}}$ is just 20 fs, comparable to most conventional TTDS setups, giving a spectral bandwidth of ~1 GHz to ~20 THz. The timing trigger signal is provided by using pellicle beamsplitters to direct a small fraction of both the master and slave laser powers onto an ultrafast photodiode, with the trigger signal occuring when both laser pulses arrive simultaneously at the photodiode. Timing jitter between the pump and probe lasers serves as the limiting factor on the time resolution. To reduce the timing jitter, the ASOPS electronic control unit (HASSP-THz, LaserQuantum GmbH) takes advantage of the 10th harmonic of the laser repetition rates and a direct-digital-synthesis integrated circuit to to define the repetition rate offset [253]. This novel ASOPS control scheme eliminates sidebands in the phase-locked feedback control loop (which link the master and slave repetition frequencies) that are separated by Δf and higher harmonics of Δf. These sidebands can cause signifcant miscalibration of the measurement time axis if the bandwidth of the phase-locked feedback loop approaches Δf. The effective time resolution afforded by this control scheme is ≈45 fs with scan rates up to 5 kHz. At such fast scan rates, measurements can typically be completed before mechanical noise takes effect and measurements can be made at the shot noise limit.

3.3.2 Experimental Measurements in TTDS

For measurements of a bulk sample, such as a substrate or thick piece of material, an empty aperture is used as a reference. For measurements of a thin film on a thick substrate, an identical bare substrate is used as the reference. After the sample and reference have been mounted on the sample insert and placed inside the cryostat the terahertz transmission through the reference is maximized by making minor x, y, and z adjustments of the cryostat position. It is also necessary to inspect the position of any reflections in the time-domain trace of the terahertz transient. In addition to the series of reflections originating in the photoconductive antenna, sample substrate, and detector crystal, as discussed above, reflections may arise from cavities formed between the surfaces of optical elements and cryostat windows. Reflections occuring between the inner and outer cryostat windows, as well as between the sample surface and the inner cryostat windows, are especially problematic because the distances between these components are only a few millimeters, so reflections may become

embedded in the tail of the main terahertz pulse as it disperses in the sample. The best way to remove these problematic reflections is to rotate either the sample or the cryostat itself by up to $\sim 5^\circ$ to eliminate the cavity resonance.

Sample and reference measurements are performed several times each and in alternating order to reduce systematic error, with short individual scan times no longer than a few minutes. In this way the effects of slow drift of the laser power, repetition rates, temperature variations, air currents in the laboratory, etc. are reduced because the sample and reference can be compared before any significant drift has occured, and this type of systematic error can be effectively averaged out [254]. In principle, the drift effects are most easily eliminated if the sample and reference measurements are averaged in the time domain before the Fourier transform is calculated. However, if the spectrometer alignment is adjusted between measurement sets, or measurements performed hours or more apart need to be combined, it is necessary to perform the averaging of the complex transmission in the frequency domain because small changes in the absolute phase of the terahertz transient will become embedded as interferences if the measurements are averaged in the time domain. The procedure of calculating the complex transmission for each individual sample-reference pair eliminates the absolute phase shift of the signal and only considers the relative phase difference between the sample and reference transients.

3.3.3 Data Analysis in TTDS

Analysis of raw data in TTDS proceeds similarly to data analysis in submillimeter quasioptical interferometery. However, because data is collected in the time domain rather than in the frequency domain, Fourier transformation of the measured terahertz transients is needed. This provides TTDS with the distinct advantage over submillimeter quasioptical interferometry that the full complex response can be obtained from a single measurement of a sample and a reference, rather than needing to separately measure the phase. The data analysis proceeds in three key steps. First, the time domain terahertz transient is windowed with a suitable window function to remove reflections and increase the signal-to-noise ratio. Second, the Fourier transform of the windowed time domain data is calculated to obtain the complex-valued spectrums of the sample and reference. Third, the complex transmission transfer function is described by the Fresnel equations and the expression is numerically inverted to obtain the values of $n(\omega)$ and $k(\omega)$ of the sample.

Window Functions

Windowing of the time domain data must be done to eliminate unnecessary reflections, which introduce oscillations in the extracted spectrum. The window function therefore serves as a high-pass filter. Mathematically, the windowed signal calculated prior to the Fourier transform and is given by

$$E_{\text{windowed}}(t) = E_{\text{THz}}(t)W(t). \tag{3.48}$$

The window function $W(t)$ must go to zero as $t \to \pm\infty$. There are many possible choices of $W(t)$ that satisfy this condition, with the correct choice depending on the purpose of the measurement and whether maximum signal-to-noise ratio, maximum spectral resolution, or minimum spectrum distortions are desired. Usually, a $W(t)$

that has a simple Fourier transform is chosen in order to control its effects on the extracted spectrum $\tilde{E}_{\mathrm{THz}}(\omega)$. The same window function is typically used for both the sample and reference measurements to reduce distortions of the extracted response functions. Some common window functions used in TTDS include [255]:

- *Rectangular window.* The simple rectangular window provides minimal distortion of the time-domain transient and offers a straightforward method of simply cutting unwanted reflections from the terahertz transient. However, the sharp steps at the edges of the rectangular window can introduce appreciable artifacts at high frequencies. Thus, while the quality of the extracted response function increases somewhat from the case of using no window function, the rectangular window generally provides only marginal improvement in the dynamic range and usable bandwidth of the terahertz signal.

- *Gaussian window.* The Gaussian window is often a good choice in TTDS because its Fourier transform is another Gaussian. The smoothly decaying wings of the Gaussian damp out oscillations and noise present in both the low and high frequency portions of the spectrum. As a result, the Gaussian window provides moderate improvement in both the dynamic ratio and the usable spectral bandwidth.

- *Force-exponential window.* The force-exponential window is similar to the rectangular window, with a step function defining the leading edge just before the start of the terahertz transient. Instead of a second step function on the trailing edge, however, the force window has a steep cosine taper to zero and the entire window function is damped with a decaying exponential [256]. The cosine taper eliminates aliasing and improves the signal-to-noise ratio by also removing the noise in the trailing parts of the terahertz transient, which may have energy of the same order as the main pulse. The decay rate of the exponential is typically matched to the decay rate of the main pulse in the terahertz transient and attenuates the noise present in the main pulse. Use of the force-exponential window can provide a large improvement in both the dynamic range and usable spectral bandwidth, but due to the shift property of the Fourier transform the measured absorption coefficient must be corrected by an amount equal to the damping constant of the decaying exponential [257].

Fourier Transform

Prior to calculating the Fourier transform of the windowed time-domain data it may be necessary to zero-pad the data, which is to append zeros at times before and after the windowed terahertz pulse. This step increases the extracted bandwidth of the spectrum and resoultion. However, this increased resolution is purely mathematical and not true experimental resolution, because the actual experimental bandwidth and resolution is limited by the width of the window function. Nevertheless, zero padding may be necessary as a method for filling out the spectral data and interpolating between experimental data points. The Fourier transform of a time-domain trace containing n data points is then given by

$$\tilde{E}_{\mathrm{THz}}(\omega) = \frac{1}{\sqrt{n}} \sum_{j=1}^{n} E_{\mathrm{THz}}(t_j) W(t_j) e^{i(\omega - 2\pi)(j-1)\Delta t}, \tag{3.49}$$

where Δt is the time increment between measured data points.

Extraction of $n(\omega)$ and $k(\omega)$

After the Fourier transforms of the windowed sample and reference transients are calculated, the resulting spectrums are used to obtain the complex transmission $\tilde{t}(\omega) = \tilde{E}_{\text{sample}}(\omega)/\tilde{E}_{\text{ref}}(\omega)$. The complex transmission must be converted from the complex-valued form $\tilde{t}(\omega) = t_1(\omega) + it_2(\omega)$ into an amplitude and phase as $\tilde{t}(\omega) = A(\omega)e^{i\phi(\omega)}$. This is because the FFT procedure returns values sitting on a circle in the complex plane, where the phase is defined as lying in the range $0 \leq \phi(\omega) < 2\pi$. However, the actual phase may contain integer multiples of 2π, and in this case the phase function $\phi(\omega)$ will appear as a sawtooth with discontinuities of magnitude 2π where $\phi(\omega)$ wraps around the complex unit circle. The phase of the transmission function must therefore be unwrapped by adding an integer multiple of 2π at every discontinuity so that $\phi(\omega)$ is smooth and everywhere differentiable [258]. The phase-unwrapped complex transmission of the sample is then used to extract $n(\omega)$ and $k(\omega)$ and calculate any additional quantities, such as the conductivity $\tilde{\sigma}(\omega)$ or dielectric function $\tilde{\epsilon}(\omega)$. Experimentally measured values of $\tilde{t}(\omega)$ are set equal to the appropriate Fresnel transmission transfer function for the sample and $n(\omega)$ and $k(\omega)$ are determined by numerical inversion.

Single layer systems. For a single layer system of thickness L such as a substrate, the Fresnel transmission function is given by

$$\tilde{t}_{\text{sample}} = \tilde{t}_{0\text{s}}\tilde{P}_{\text{s}}\tilde{t}_{\text{s}0} \tag{3.50}$$

with $\tilde{t}_{jk}$ given by Eq. 3.38 and the phase $\tilde{P}_j$ given by Eq. 3.39, while the transmission through the empty reference aperture is described simply by the phase $\tilde{t}_{\text{ref}} = \tilde{P}_0$. It is not necessary to include the Fabry-Pérot coefficient because the time duration of the terahertz transient is less than $2n_{\text{s}}L/c$, the round-trip time for a photon in the substrate. The complex transmission transfer function is then

$$\tilde{t}(\omega) = \frac{\tilde{t}_{\text{sample}}}{\tilde{t}_{\text{ref}}} = \frac{4\tilde{n}_{\text{s}}}{(1+\tilde{n}_{\text{s}})^2}e^{i\omega(\tilde{n}_{\text{s}}-1)L/c}. \tag{3.51}$$

The actual numerical inversion is done by taking the logarithm of the complex transmission function to preserve the phase unwrapping. Extracted values of $\tilde{n}_{\text{s}}(\omega) = n_{\text{s}}(\omega) + ik_{\text{s}}(\omega)$ are then obtained from

$$\ln\left[A(\omega)\right] + i\phi(\omega) = \ln\left[\frac{4\tilde{n}_{\text{s}}}{(1+\tilde{n}_{\text{s}})^2}\right] + i\frac{\omega}{c}(\tilde{n}_{\text{s}}-1)L. \tag{3.52}$$

Thin film on a thick substrate. For a thin film of thickness d on a substrate of thickness L, the Fresnel transmission function of the sample is given by

$$\tilde{t}_{\text{sample}} = \tilde{t}_{0\text{f}}\tilde{P}_{\text{f}}\tilde{F}_{\text{f}}\tilde{t}_{\text{fs}}\tilde{P}_{\text{s}}\tilde{t}_{\text{s}0}\tilde{P}_0^{(\Delta L)}, \tag{3.53}$$

where $\tilde{F}_{\text{f}}$ is the Fabry-Pérot coefficient of the film, and the Fresnel transmission function of the reference is

$$\tilde{t}_{\text{ref}} = \tilde{P}_0^{(d)}\tilde{t}_{0\text{s}}\tilde{P}_{\text{s}}\tilde{t}_{\text{s}0}. \tag{3.54}$$

The coefficient $\tilde{P}_0^{(d)}$ appearing in Eq. 3.54 corresponds to the phase difference acquired by the terahertz transient in the reference because it does not pass through a thin

film, while $\tilde{P}_0^{(\Delta L)}$ in Eq. 3.53 accounts for the possible difference in thickness of the sample and reference substrates. The complex transmission transfer function is then given by [259]

$$\tilde{t}(\omega) = \frac{2\tilde{n}_\mathrm{f}(1+\tilde{n}_\mathrm{s})}{(1+\tilde{n}_\mathrm{f})(\tilde{n}_\mathrm{f}+\tilde{n}_\mathrm{s})}\tilde{F}_\mathrm{f} e^{i\omega(1+\tilde{n}_\mathrm{s})\Delta L/c} e^{i\omega(\tilde{n}_\mathrm{f}-1)d/c} \tag{3.55}$$

and the complex index of the film $\tilde{n}_\mathrm{f}(\omega) = n_\mathrm{f}(\omega) + ik_\mathrm{f}(\omega)$ is found by numerically inverting the expression $\ln \tilde{t}(\omega) = \ln A(\omega) + i\phi(\omega)$.

Substrate Thickness Mismatch

The substrate thickness mismatch parameter ΔL in Eqs. 3.53 and 3.55 arises because, even if two substrates from the same manufacturing batch are used for the sample and reference, small thickness differences on the order of a few micrometers to a few tens of micrometers are usually present due to miscuts of the substrate crystals. This mismatch can cause phase shifts of the measured signal comparable to that induced by a ∼100 nm thick film. ΔL is therefore used as a free fitting parameter. To obtain the correct values of $\sigma_1(\omega)$ and $\epsilon_1(\omega)$ of the film, ΔL is adjusted until σ_1 and ϵ_1 match values obtained by other methods, such as dc transport measurements above T_c. In the work presented here, TTDS measurements are compared with submillimeter interferometry and far-IR ellipsometry measurements obtained at the same temperature.

3.3.4 Resolution Limits

Both upper and lower limits on the resolvable values of n and k exist in TTDS. The lower limit follows as usual from the minimum error bar or standard deviation of measurements, while the upper limit is a consequence of the maximum dynamic ratio available in the reference spectrum. Since the complex transmission can be expressed as $\tilde{t}(\omega) = A(\omega)e^{i\phi(\omega)}$, the maximum measurable absorption coefficent α_max for a thin film on a thick substrate is [259]

$$\alpha_\mathrm{max} = \frac{\omega k_\mathrm{max}}{2\pi c} = \frac{1}{2\pi d}\ln\left(R\frac{\tilde{t}_{0\mathrm{f}}\tilde{t}_{\mathrm{fs}}\tilde{F}_\mathrm{f}}{\tilde{t}_{0\mathrm{s}}}\right), \tag{3.56}$$

where the maximum value of $A(\omega)$ is the dynamic ratio R. For a film of thickness $d = 80$ nm this corresponds to $\alpha_\mathrm{max} \approx 32\ \mu\mathrm{m}^{-1}$. Absorption values larger than this will be measured as exactly α_max rather than the true value. As a result, samples with strong absorption lines may have their resonances truncated and extraction of the correct resonance lineshapes becomes difficult. It is therefore necessary to perform TTDS measurements with as large a dynamic ratio as possible and to use thinner samples when the material under study is strongly absorbent.

The lower limit of resolvability of the absorption coefficient is given by [254]

$$\Delta\alpha_\mathrm{min} = \frac{\omega\Delta k_\mathrm{min}}{2\pi c} > \frac{\xi s}{2\pi d}\sqrt{\frac{2}{N}}, \tag{3.57}$$

where s is the standard deviation of the measurement, N is the number of times the measurement is repeated, and $\xi \geq 1$ is an integer corresponding to the desired confidence interval of the measurement, with $\xi = 3$ corresponding to 99.7% confidence in

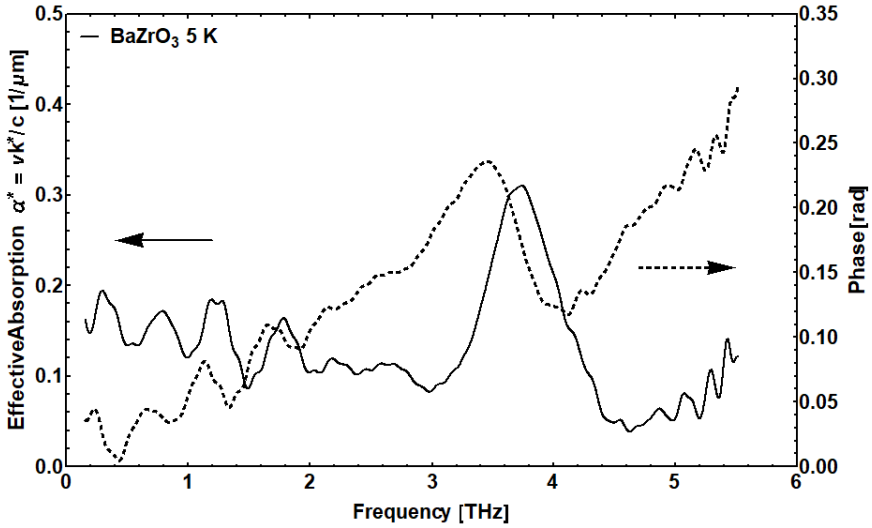

Figure 3.8 High-speed ASOPS TTDS measurements of the absorption coefficient (solid line) and phase shift (dashed line) of a $d = 80$ nm thick film of the incipient ferroelectric $BaZrO_3$ on an MgO substrate at 5 K. The TO2 phonon mode at 3.7 THz is just visibile with an amplitude of $\alpha \approx 0.3\ \mu m^{-1}$. The TO1 phonon at 1.9 THz, which is ∼100 times weaker than the TO2 phonon, is buried in the noise.

the detection of the thin film. To illustrate the sensitivity of the TTDS measurement, Fig. 3.8 shows the measured absorption coefficient and phase shift of a $d = 80$ nm thick film of $BaZrO_3$, a cubic perovskite, on an MgO substrate at a temperature of 5 K. Classified as an incipient ferroelectric, $BaZrO_3$ has two infrared active phonon modes near 1.9 THz (TO1) and 3.7 THz (TO2) [260]. Both modes exhibit significant softening with decreasing temperature. The mode softening is accompanied by a concomitant increase in ϵ_1 with a saturation plateau below 20 K, which results from quantum fluctuations that stabilize the paraelectric phase. As shown by the solid line in Fig. 3.8, the TO2 phonon resonance of the thin $BaZrO_3$ film observed near 3.7 THz has an amplitude of $\alpha \approx 0.3\ \mu m^{-1}$. The calculated value of the minimum resolvable absorption coefficient by TTDS is $\Delta\alpha_{min} = 0.1$–$0.2\ \mu m^{-1}$ based on the noise present in the measurement. The extracted absorption coefficient therefore lies only just above the minimum resolvable limit, rendering the TO1 mode, which is a factor of ∼100 weaker than the TO2 mode, unobservable.

There is also a lower limit on the measured index of refraction, or phase shift, that is resolvable by a TTDS spectrometer. This minimum phase shift is related to the error bar or standard deviation of the measurement as

$$\frac{\omega}{c}\Delta n_{min} d > \xi s\sqrt{\frac{2}{N}} + 2\frac{\omega}{c} n_f d \frac{\mathrm{Re}\,(\tilde{r}_{f0}\tilde{r}_{fs})}{\mathrm{Re}\,(\tilde{r}_{f0}\tilde{r}_{fs}) - 1}, \tag{3.58}$$

where $\tilde{r}_{f0}$ and $\tilde{r}_{fs}$ are the Fresnel reflection coefficients from film to vacuum and film to substrate, respectively. For the 80 nm thick $BaZrO_3$ film $\omega\Delta n_{min} d/c \approx 0.05$ rad with $\xi = 3$; the observed feature in the frequency dependence of the phase, depicted by the dashed line in Fig. 3.8, has a magnitude of ∼0.12 rad. Thus, the extracted absorption coefficent and phase shift of the TO2 mode both lie just above the minimum resolvable limits, demonstrating that the TTDS system used in this work is capable of resolving the presence of multiferroic films as thin or thinner than

80 nm. In comparison, the minimum resolvable thicknesses of various dielectric films measured by conventional TTDS spectrometers have been reported to lie in the range 200–1400 nm [254]. The TTDS system based on high-speed ASOPS presented here therefore provides remarkable sensitivity in thin film sensing without need for more complicated mechanical techniques, such as difference-signal extraction.

3.4 Spectroscopic Ellipsometry

The final experimental technique that we make use of is spectroscopic ellipsometry, which is a very powerful tool for characterizing thin film systems because it provides access to information regarding optical properties and interface layers to sub-Angstrom resolution [261]. Like submillimeter quasioptical interferometry and terahertz time-domain spectroscopy, spectroscopic ellipsometry is a method capable of simultaneously obtaining both the real and imaginary parts of the complex dielectric response, $\tilde{\epsilon}(\omega) = \epsilon_1(\omega) + i\epsilon_2(\omega)$, without need for Kramers-Kronig relations. This is accomplished by measuring the full polarization state of light as a function of frequency after it reflects from the surface of a sample. As we have seen from the discussion of the Fresnel equations in Section 3.1.1, light encounters different complex reflection and transmission coefficients at an interface depending on whether it is polarized parallel (p) or perpendicular (s) to the optical plane of incidence. If the incident light is polarized such that it has both p and s components, then each component will suffer different amplitude and phase shifts at the interface and the reflected light becomes elliptically polarized. A complete and very detailed description of the spectroscopic ellipsometry technique is given in Ref. [261].

For the case of Fabry-Pérot reflection and transmission through a slab at normal incidence, it is enough to define the electric field polarization in terms of the p and s components and use the Fresnel equations to obtain $\tilde{\epsilon}(\omega)$. In ellipsometry, on the other hand, it is more convenient to define the polarization in terms of the angles Ψ and Δ by the Jones vector,

$$\hat{E} = \begin{pmatrix} \sin\Psi e^{i\Delta} \\ \cos\Psi \end{pmatrix} \tag{3.59}$$

Here, the angle Ψ is determined by the relative attenuation of the reflected light and Δ is the relative phase shift of the two polarization components with respect to each other,

$$\tan\Psi = \frac{|\tilde{r}_p|}{|\tilde{r}_s|}, \quad \Delta = \delta_p - \delta_s \tag{3.60}$$

The full complex dielectric function can therefore be obtained by measuring Ψ and Δ. The experimental setup is illustrated in Fig. 3.9 and consists of an initial polarizer at angle P, a sample at angle of incidence θ, a second polarizer (the analyzer) at angle A, and a detector. In the IR and far-IR spectral ranges a bolometer is used to detect the intensity of the reflected light as a function of P and A. The angle of incidence is chosen such that it lies near the Brewster angle to increase the sensitivity of the experiment to changes in $\tilde{\epsilon}(\omega)$; at this angle $r_p \approx 0$ when $\epsilon_2(\omega) \approx 0$, but small changes in ϵ_2 produce large changes in Δ. This is because Δ changes rapidly from 0° to 180° in the vicinity of the Brewster angle, with Δ changing more rapidly when ϵ_2 is smaller.

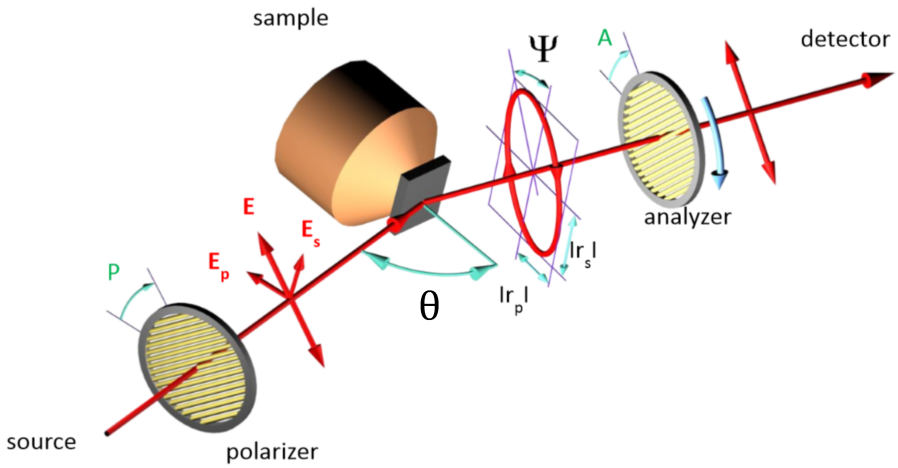

Figure 3.9 An illustration of the spectroscopic ellipsometry measurement technique. Radiation enters the instrument (left side) and is polarized by an initial polarizer at angle P. The polarized beam then reflects from the sample at angle of incidence θ and becomes elliptically polarized according to the Fresnel equations for s and p polarized light. The polarization state of the beam is characterized by the ellipsometric angles Ψ (relative attenuation) and Δ (relative phase shift). The elliptical beam then passes through a second polarizer (analyzer) at angle A and reaches the detector. The full polarization state of the measured light is obtained by measuring the intensity profile $I(A)/I_0$ of the elliptical beam as a function of analyzer angle. Frequency dependence is obtained by placing an interferometer (not shown) between the radiation source and initial polarizer.

Typical measurements are performed by fixing the angle P and then rotating the analyzer through 360°. This procedure produces an angular intensity profile $I(A)$ that has a sinusoidal form,

$$\frac{I(A)}{I_0} = 1 + \alpha \sin(2A) + \beta \cos(2A), \tag{3.61}$$

which is then fit by a computer program to extract the coefficients α and β. These two coefficients are related to the ellipsometric angles Ψ and Δ through

$$\tan\Psi = |\tan P| \sqrt{\frac{1+\alpha}{1-\alpha}}, \quad \cos\Delta = \mathrm{sgn}(P) \frac{\beta}{\sqrt{1-\alpha^2}} \tag{3.62}$$

Frequency dependence is introduced by inserting a Michelson interferometer between the radiation source and initial polarizer. This interferometer functions much in the same way as an FTIR spectrometer; an oscillator constantly modulates the length of a reference arm, and the detector measures an interferogram. Therefore, for each analyzer angle A, an interferogram (and hence a spectrum) is obtained. As a result, for each frequency ω there is a separate A-dependent sinusoid that corresponds to a separate pair of angles $\Psi(\omega)$ and $\Delta(\omega)$. This spectrum of ellipsometric angles is then used to solve for $\epsilon_1(\omega)$ and $\epsilon_2(\omega)$ by equating the complex relative reflectivity to the Fresnel reflection coefficients for the sample,

$$\tan\Psi(\omega)\, e^{i\Delta(\omega)} = \frac{\tilde{r}_p(\omega)}{\tilde{r}_s(\omega)}, \tag{3.63}$$

where $r_p(\omega)$ and $r_s(\omega)$ are given in Section 3.1.1 in terms of n and k. The alignment of the ellipsometer and the experimental resolution is improved by repeating the measurements at several values of $\pm P$.

Three ellipsometer setups are used to measure across the full spectrum from far-IR to deep UV (10 meV to 6.5 eV). First, a home-built ellipsometer attached to a Bruker IFS 66v/s interferometer, on the IR-1 beamline of the KARA synchrotron at the Karlsruhe Institute of Technology, is used to measure at frequencies from 80 cm^{-1} to approximately 700 cm^{-1}. This setup utilizes coherent far-IR radiation from the 110 m diameter electron storage ring, which operates at beam energies of 0.5–2.5 GeV. Second, an identical home-built ellipsometer attached to a Bruker Vertex 80v interferometer at our lab in the Max Planck Institute for Solid State Research is used to reach frequencies in the range 700–10000 cm^{-1}. Two different radiation sources with overlapping spectral outputs are employed to cover this range. In the mid-IR portion of the spectrum a SiC globar is used and in the near-IR a tungsten lamp is used. Third, a visible-to-UV VASE (variable angle spectroscopic ellipsometer) purchased from J. A. Woollam Co. covers the frequency range above approximately 4000 cm^{-1}. After measuring the response of a sample on all three instruments, $\epsilon_1(\omega)$ and $\epsilon_2(\omega)$ are extracted across the full spectral range from 10 meV to 6.5 eV by first combining the raw data for $\Psi(\omega)$ and $\Delta(\omega)$ from all instruments using custom Mathematica code developed by other members of our research group [262]. The complex dielectric function is then obtained from the composite data set using commercial Woollam WVASE software.

Chapter 4

Approaching 2D Superconductivity in Ultrathin $DyBa_2Cu_3O_{7-\delta}$

4.1 $DyBa_2Cu_3O_{7-\delta}$ Thin Films

The understanding of the physics of cuprates in the 2D limit has progressed hand-in-hand with technological developments in epitaxial oxide film growth techniques, notably with the advancement of molecular beam epitaxy (MBE) [263]. A significant challenge for the fabrication of complex oxide films has been the difficulty of reproducibly obtaining pure single-phase samples. Defects such as dislocations, stacking faults, twin boundaries, and the formation of undesired secondary impurity compounds commonly occur due to the thermodynamic details of the film deposition process and conditions of the substrate surfaces. These defects drastically impact the electronic properties of the samples and so it is necessary to achieve minimal defect density in order to approach the intrinsic properties of complex oxides. Recent advances in oxide MBE [11], particularly atomic layer-by-layer MBE, have provided a route to reliably achieve highly pure, atomically smooth copper oxide films thinner than 1 nm. Atomic layer-by-layer MBE differs from conventional MBE in that, instead of employing co-deposition of all atomic species simultaneously, vacuum shutters are used to open individual elemental effusion cells in a predefined order to obtain greater stoichiometry control [264]. Oxide MBE takes advantage of low deposition energies of the atomic species and so, compared to pulsed laser deposition and reactive magnetron sputtering, achieves uniquely low densities of defects and high electron mobilities.

Many prior studies of ultrathin YBCO films focused on the properties of samples grown by pulsed laser deposition, sputtering, and reactive evaporation techniques rather than oxide MBE. Early work found that superconductivity in YBCO can be observed in individual CuO_2 bilayers [167–169] but that a 4–6 u.c. thick interfacial layer is necessary to epitaxially adapt the film to the underlying substrate [265–267]. The nature of this few-u.c. layer was attributed to the formation of a strain-induced defect distribution that creates a rapidly diminishing zone of high defect density and inhomogeneously distributed oxygen vacancies due to the lattice matching requirements [268]. As a result, a significant number of studies employ few-u.c. thick PrBCO buffer layers because the orthorhombic structure of PrBCO has a maximum lattice mismatch of only ∼1.5% with YBCO [21, 175, 269, 270]. However, as discussed in

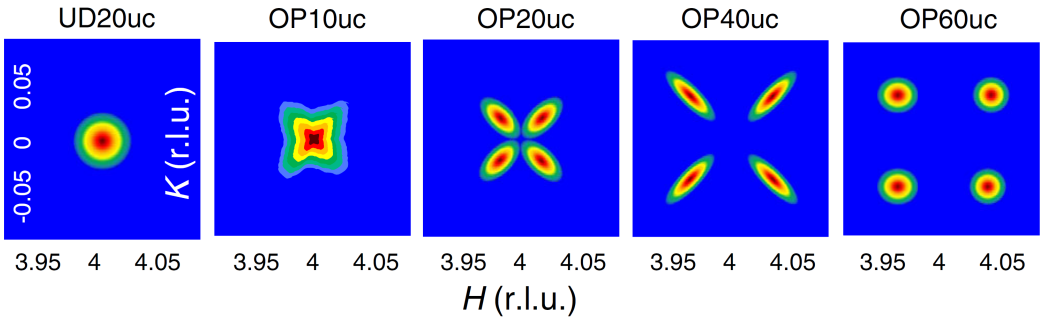

Figure 4.1 Illustrations of high-resolution XRD reciprocal space maps for the HK plane centered about the (4 0 10) reflection, adapted from Ref. [273]. The X-ray results show that for all near optimally doped films the structure is dominated by four-fold orthorhombic twin domains, as indicated by four diffraction subpeaks observed for OP60uc, OP40uc, and OP20uc. These subpeaks merge together with decreasing thickness until a single, distorted diffraction spot is observed for OP10uc. By contrast, an underdoped 20 u.c. thick film displays a single circular diffraction spot, indicative of tetragonal symmetry.

Section 2.2.4, inclusion of PrBCO in thin film heterostructures introduces additional disorder because the Pr ion contributes to pair breaking, magnetic ordering, and charge localization [39]. The presence of PrBCO buffer layers in RBCO thin film structures therefore complicates the interpretation of the nature of the superconducting state and, in order to assess the intrinsic superconducting properties of RBCO, it is necessary to investigate RBCO films grown in the absence of influence from extrinsic compounds.

For the studies presented in this thesis, DyBCO films with thicknesses ranging from 7 to 60 u.c. (8–70 nm) were grown on (100)-oriented $(LaAlO_3)_{0.3}(Sr_2AlTaO_6)_{0.7}$ (LSAT) substrates of dimensions 10×10 mm^2 by ozone-assisted atomic-layer-by-layer oxide MBE. In this technique [271] Dy, Ba, and Cu metals were evaporated in oxygen atmosphere one atomic layer at a time from separate evaporation sources in a predefined manner to achieve highly pristine superconducting films with T_c as high as 90 K. DyBCO films were chosen rather than YBCO because the higher vapor pressure of Dy as compared to Y allows for higher quality films to be achieved at typical MBE growth temperatures [272]. A series of DyBCO films with a range of thicknesses were selected in order to avoid effects caused by modification of the sample Fermiology due to strain and doping differences. LSAT substrates, as opposed to LAO, LSAO, or STO, were used because the a and b lattice parameters of LSAT ($a = b = 3.87$ Å) lie between the a and b parameters of DyBCO, resulting in minimized strain effects. The high crystal structure quality of the films was confirmed by X-ray diffraction (XRD) and transmission electron microscopy measurements and reported elsewhere by Putzky *et al.* [273]. The DyBCO films were further characterized by visible-to-UV spectroscopic ellipsometry and mutual inductance measurements to ascertain their doping level and transport properties prior to investigating the submillimeter, terahertz, and infrared response of the superconducting condensate.

Due to the epitaxial contact of the films with the substrates, on approaching the 2D limit effects stemming from the film thickness, strain, doping level, and disorder become intertwined. To disentangle and control for these effects we begin by investigating the thickness dependence of the film lattice structure and strain. Fig. 4.1

depicts illustrations of high-resolution XRD measurements of the HK plane centered about the (4 0 10) reflection for DyBCO films ranging from 10–60 u.c. thick grown near optimal doping, adapted from data measured on the same films reported in Ref. [273]. In thick near optimally doped films (right hand side of the figure) the orthorhombic lattice structure is observed as indicated by four nearly circular diffraction subpeaks. The four subpeaks appear due to sample twinning, which results in an effective macroscopic four-fold rotational symmetry. The circular shape of the subpeaks implies that the strain in the orthorhombic structure is close to fully relaxed. As the film thickness is reduced below 60 u.c. (moving left) the diffraction subpeaks enlongate and migrate towards the (4 0 10) point. Below a thickness of 10 u.c. the diffraction subpeaks merge into a single distorted diffraction peak at (4 0 10). This propeller-like diffraction pattern indicates that the thinnest films adapt to the square structure of the underlying substrate lattice while also retaining CuO chains. In a vacuum annealed, underdoped 20 u.c. thick control film, on the other hand, a single circular diffraction spot at (4 0 10) is observed as a result of the tetragonal symmetry of its epitaxial lattice. This trend implies that in near optimally doped films the lattice strain relaxation decreases with decreasing film thickness and the films become increasingly less orthorhombic below 60 u.c.

Such a dependence of the strain on decreasing film thickness suggests the possibility that thickness-induced changes in the doping level may be present, which could alter the observed T_c of the films. This is because compressive strain along the DyBCO b-axis has the tendency to release O atoms from the CuO chains. To check the doping level of the films we performed spectroscopic ellipsometry measurements of the ab-plane complex dielectric function in the visible spectral range. If the films are indeed becoming increasingly underdoped with decreasing thickness then it is expected that spectral features corresponding to optical transitions related to the CuO chain layers that evolve with thickness will be observed. In particular, an absorption peak in ϵ_2 centered near 4 eV in the in-plane optical response is unique to the RBCO family of cuprates and is attributed to Cu $3d_{3z^2-1}$ to Cu $4p_x$ transitions of the dumbbell O(IV)-Cu(I)-O(IV) units in the absence of CuO chains [274, 275]. At severe underdoping $R\mathrm{Ba_2Cu_3O_6}$ is tetragonal so the a and b axes are equivalent, and the 4 eV feature is observed in both polarizations along with an absorption gap below 1.5 eV and an additional peak at 1.75 eV (corresponding to O $2p$ to Cu $3d$ charge-transfer excitations). As the CuO chains are filled with increasing doping, however, the Cu $4p_{x,y}$ degeneracy is broken and the optical response becomes polarized, with a 4.1 eV peak remaining in the b-axis and a 4.7 eV peak appearing in the a-axis response [276]. At intermediate dopings this change is accompanied by a transfer of optical conductivity spectral weight from high photon energies to energies below the charge-transfer gap and a low-frequency metallic feature appears. Finally, as the doping level approaches $R\mathrm{Ba_2Cu_3O_7}$, the characteristic 4.1 and 4.7 eV features disappear and both the a and b axis responses are dominated only by a conductivity upturn below approximately 1 eV.

As can be seen in Fig. 4.2(a), for near optimally doped 60 u.c. thick films, which were shown by XRD measurements to possess intact CuO chains, the response of ϵ_2 shows a strong upturn at low photon energies along with the absence of any other sharp spectral features. At the same time, the corresponding measured ϵ_1 plotted in Fig. 4.2(b) indicates a screened plasma frequency in excess of 1 eV. As the thickness of the near optimally doped films is decreased down to 7 uc this qualitative trend

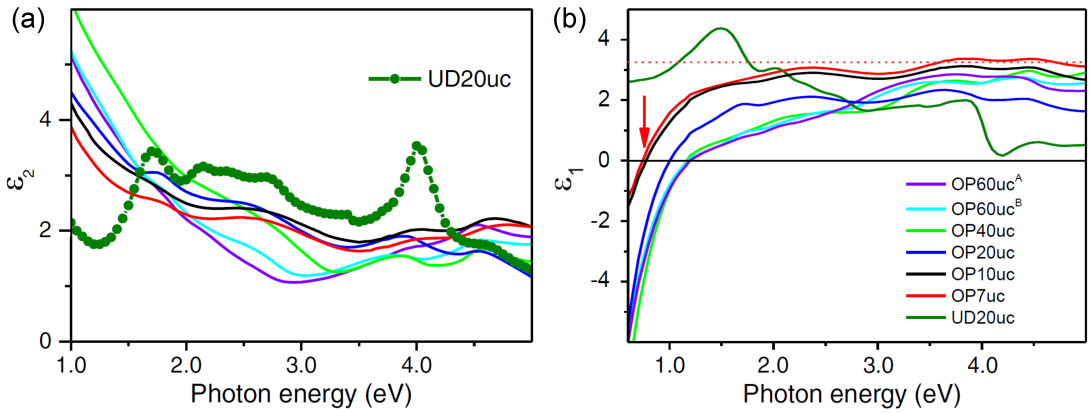

Figure 4.2 The complex dielectric function as measured at $T = 293$ K by spectroscopic ellipsometry in the visible-near-UV range for a series of DyBCO thin films. (a) The imaginary part of the dielectric function. All films designated as "OP" display an upturn in the conductivity at low photon energies and absence of a peak near 4 eV. A vacuum annealed, underdoped 20 u.c. film, on the other hand, shows a clear 4 eV peak (dark green points) that is attributed to dumbbell Cu $3d_{3z^2-1}$ to $4p_x$ transitions and indicates the absence of intact CuO chains [274, 276]. Additionally, the measured ϵ_1 in (b) for the UD20uc sample (dark green line) does not show a screened plasma frequency in the visible spectral range. These results indicate that all "OP" films possess intact CuO chains and are indeed near optimal doping down to a thickness of 7 u.c. (b) The real part of the dielectric function. The screened plasma frequency for OP7uc is marked by the red arrow while ϵ_∞ is indicated by the red dashed line.

in ϵ_1 and ϵ_2 is observed to hold, with only the screened plasma frequency decreasing with decreasing thickness. Given the twinned nature of all films the observation of peaks near both 4.1 and 4.7 eV is expected if the films are becoming increasingly underdoped, but importantly, no sharp spectral absorption features in ϵ_2 are observed above 4 eV even in the 7 u.c. thick optimally doped sample. In the vacuum annealed, underdoped reference sample UD20uc, on the other hand, a clear 4 eV peak is observed in ϵ_2 along with a 1.75 eV feature and drastically reduced optical weight below ~1.5 eV. Together, these results imply that all films 7–60 u.c. thick that were grown as optimally doped are indeed near optimal doping. Despite the presence of unrelaxed epitaxial strain in the thinnest films the CuO chains remain largely intact.

Disorder is also intrinsically related to film thickness because epitaxial effects and strain from the substrate interface affect the quality of the CuO chains, grain boundaries, stacking faults, and other defects despite the carefully controlled atomic-layer-by-layer growth process. Previous studies of the effect of disorder on T_c, transport properties, and the quasiparticle scattering rate in radiation damaged YBCO [277] have shown that at high defect densities quantum phase fluctuations become dominant and have the effect of strongly reducing T_c. In this case the strong dependence of T_c on defect density arises from the very small coherence lengths ξ in the cuprates, which prevent the Cooper pairs from uniformly averaging over the disorder and thereby making them highly susceptible to rapid variations in the local potential. At low and moderate defect densities, on the other hand, the width of the superconducting transition is described by the Abrikosov-Gorkov pair-breaking model, where the critical temperature and width of the transition scale linearly with small amounts

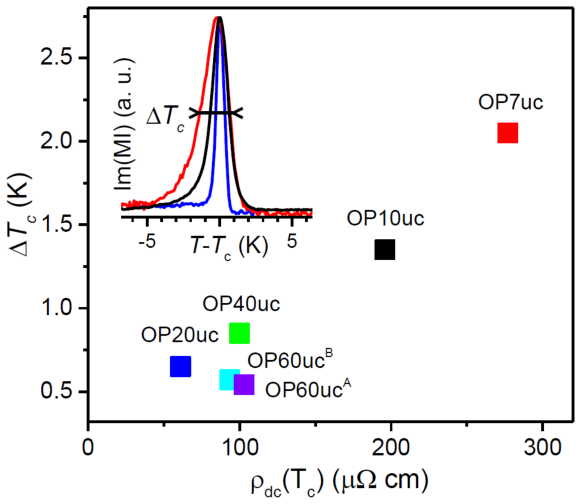

Figure 4.3 The FWHM of the peak in the imaginary part of MI(T), measured at 1 kHz and drive current of 50 μA (inset), as a function of the dc resistivity $\varrho_{\rm dc} = 1/\sigma_{\rm dc}$. The nearly linear dependence of ΔT_c vs. $\varrho_{\rm dc}$ suggests moderate disorder in our films, well below the highly damaged regime characterized by critical scattering where T_c is considered in Ref. [277] to be determined by quantum phase fluctuations of the order parameter.

of pair breaking. To investigate the effects of disorder and film thickness on the superconducting transition in our samples we examine the normal state scattering rate and dc transport properties extracted from visible-to-UV spectroscopic ellipsometry and terahertz conductivity measurements. For the thinnest samples, the screened plasma frequency (red arrow) and ϵ_∞ (red dashed line) obtained from the ϵ_1 data in Fig. 4.2(b) give the unscreened $\omega_{pl} = 1.27(1.37) \pm 0.03$ eV for OP7uc (OP10uc), which corresponds to a quasiparticle scattering rate $\gamma = 60(50) \pm 3$ meV. Taking the Fermi velocity as 2.5×10^7 cm/s [278], this allows us to estimate the mean free path $\ell = 28(34) \pm 2$ Å at T_c for OP7uc (OP10uc), which is significantly larger than the in-plane coherence length $\xi_{ab} = 13$ Å [279]. This result implies the effect of disorder is not dominant and that T_c inhomogeneity in the film has a larger effect than scattering or pair breaking on the width of the transition ΔT_c.

Accordingly, we consider the relationship between the width ΔT_c of the transition as defined by the FWHM of the peak in the imaginary part of the mutual inductance and the dc resistivity $\varrho_{\rm dc}$ at T_c, extrapolated at zero frequency from terahertz conductivity measurements, which is proportional to the disorder level. Fig. 4.3 reports the observed dependence of the superconducting transition width on $\varrho_{\rm dc}(T_c)$. It is apparent that in these near optimally doped films, upon reducing the thickness from 60 u.c. to 7 u.c. the transition width ΔT_c increases by only ∼1.5 K, from 0.5 K to 2.0 K. At the same time the transition temperatures of the films are more than an order of magnitude larger than ΔT_c and range from $T_c \approx$ 72–90 K. Especially notable is the difference in ΔT_c of just 0.6 K between OP10uc and OP7uc, despite a difference in T_c of ∼13 K. Furthermore, the linear dependence of ΔT_c on $\varrho_{\rm dc}(T_c)$ is in accordance with the presence of moderate disorder in our films that lies well below the highly disordered regime where T_c becomes dominated by quantum phase fluctuations of the order parameter [277]. Taken together, this behavior indicates that factors aside from either T_c inhomogeneity or disorder are primarily responsible

for differences in the superconducting properties between the various DyBCO films. Despite the presence of mild T_c inhomogeneity the *superconducting state* in the films remains predominantly homogeneous.

The XRD, spectroscopic ellipsometry, mutual inductance, and extrapolated dc transport data presented in this section demonstrate that the MBE-grown DyBCO films used in this study are indeed of high quality with reduced extrinsic disorder and relatively uniform doping and superconductivity. While the presence of the substrate interface ensures that some degree of disorder is inescapable, it is possible to proceed with investigations of these films with the understanding that the disorder and doping variations do not have dominant effects on the superconducting properties of interest here. Figs. 4.1 and 4.2 provide evidence that the near optimally doped films retain their doping level and CuO chains down to thicknesses of 7 u.c. while simultaneously accommodating the epitaxial strain of the underlying LSAT substrate, but the effect of the unrelaxed strain in the thinnest samples is not yet clear. This strain issue will be directly addressed later in this chapter in Section 4.6, where it will be discussed in terms of the formation of a ∼4 u.c. non-superconducting layer in contact with the substrate interface. We will argue that the epitaxial strain fully relaxes across this ∼4 u.c. layer and that the unit cells lying above are relaxed and retain their superconducting properties.

4.2 Terahertz Conductivity of $DyBa_2Cu_3O_{7-\delta}$ Thin Films

As discussed extensively in Chapter 2, previous studies of the superfluid density and BKT transition in ultrathin YBCO films have primarily focused on results obtained from inductance measurements carried out at single frequencies. Gasparov *et al.* [181] probed the kinetic impedance of superconducting 1–3 u.c. thick YBCO films sandwiched between non-superconducting (Pr,Y)BCO buffer layers at frequencies (megahertz to gigahertz) close to the vortex-antivortex resonance frequency $\omega \sim 14\mathcal{D}(T)/\xi_+^2(T)$ and claimed that their results were in agreement with the AHNS dynamical BKT theory with vortex-antivortex pinning. The authors reported a frequency dependent critical temperature near the resonance condition in the films studied, whose doping levels were not specified but whose dc T_{BKT}^{ω} values were as high as 56 K, and found a temperature dependent vortex diffusion constant $\mathcal{D}(T)$ that was strongly exponential in T. However, strong pinning of vortices by defects obscures the vortex-antivortex interaction. While the films in Gasparov *et al.* were reported to have a single domain, the effects of twinning or the presence of interfacial magnetic Pr ions, oxygen vacancies, inhomogeneity, and other defects greatly complicate the analysis and create ambiguity around the interpretation of the experimental results. As was shown in the previous section, the films studied in this thesis are in the moderate disorder regime far below the disorder level where quantum critical fluctuations become important. Nevertheless, to obtain the true value of the superfluid density it is necessary to treat the full superconducting response rather than an indirect value such as the inverse of the kinetic inductance.

Another important issue that must be addressed in order to properly treat the suppression of the mean field transition temperature due to 2D fluctuations is to compare the full temperature dependence of the superfluid density with the "universal"

dependence that occurs in the absence of 2D fluctuations. In Gasparov *et al.* [181] this suppression of T_c was estimated by comparing the extracted $\rho_s(T)$ to a mean field dependence $\rho_s^{MF} \propto T^2$. However, in the cuprates $\rho_s(T)$ does not follow a T^2 temperature dependence; in the clean limit $\rho_s(T)$ is linear as $T \to 0$ and in the presence of moderate disorder $\rho_s(T) \propto T^2$ only at low temperatures [19, 280]. Instead, the full temperature dependence of $\rho_s(T)$ is defined by a combination of defect scattering, doping level, and topology of the Fermi surface [281]. To obtain the proper "universal" temperature dependence of $\rho_s(T)$ we adopt a different experimental approach based on systematic and accurate measurements of the full superconducting response under thickness, strain, and doping control. Specifically, we obtain the full complex conductivity response in the frequency range 0.1 meV $< \hbar\omega <$ 1.1 eV using amplitude- and phase-sensitive techniques, which allows us to simultaneously track the complete evolution of both the superconducting state and the conductivity spectral weight. From these measurements the model independent superfluid density and penetration depth are obtained.

The measured complex conductivity in the terahertz and far-IR spectral range, obtained from submillimeter quasioptical interferometry, TTDS, and spectroscopic ellipsometry, is shown in Fig. 4.4 for two representative near optimally doped 60 u.c. and 20 u.c. thick DyBCO films. As can be seen from $\sigma_1(\omega, T)$, below T_c (thick black lines) a large amount of conductivity spectral weight is observed to shift from frequencies below 27–28 THz in both samples. This spectral weight shift is accompanied by a dramatic upturn in $\sigma_2(\omega, T)$ below T_c that is proportional to $1/\omega$, which is indicative of the accumulation of spectral weight into a δ-function in $\sigma_1(\omega)$ at $\omega = 0$ (and the formation of the superconducting condensate). Despite this, a significant amount of residual spectral weight remains below the optical gap at the lowest measured temperatures ($T = 5$ K). At frequencies far below the optical gap ($\omega \ll$ 27–28 THz) the response is therefore determined by the superconducting contribution to σ_2 and the residual normal carrier contribution to σ_1. At the lowest measured frequencies ($\omega < 0.3$ THz) σ_2 is an order of magnitude greater than σ_1 at $T = 5$ K. Since the lowest measured frequency is two orders of magnitude smaller than the optical gap it is expected that the behavior of σ_2 will dominate the low frequency conductivity response up to just a few K below T_c.

Below a frequency of $\omega \sim$ 1–2 THz a strongly temperature dependent peak in σ_1 is observed in Fig. 4.4(a, c) just below T_c. This peak, present in all measured samples both optimally doped and underdoped, is more easily apparent in the plot of $\sigma_1(T)$ at $\omega = 280$ GHz shown in Fig. 4.5(a). Here, the different widths and magnitudes of the peaks corresponding to different films reflect the differences in growth conditions, dc resistivities, and disorder details from one sample to the next. Each peak in $\sigma_1(T)$ is associated with the onset of $\sigma_2(T)$ (Meissner screening) at T_c, as seen in Fig. 4.5(b), in a manner that is reminiscent of the "coherence peak" observed in conventional BCS superconductors. In BCS superconductors, T_c is much less than the Debye temperature so in disordered samples scattering from defects dominates over phonon effects and the scattering rate γ (or $1/\tau$ where τ is the quasiparticle Drude lifetime) is temperature independent below T_c. The conductivity is therefore dominated by coherence factors that arise from temperature dependent constructive interference between the wavefunctions of the occupied quasiparticle states [8]. A peak occurs in the low frequency conductivity $\sigma_1(T)$ just below T_c due to the combination of the

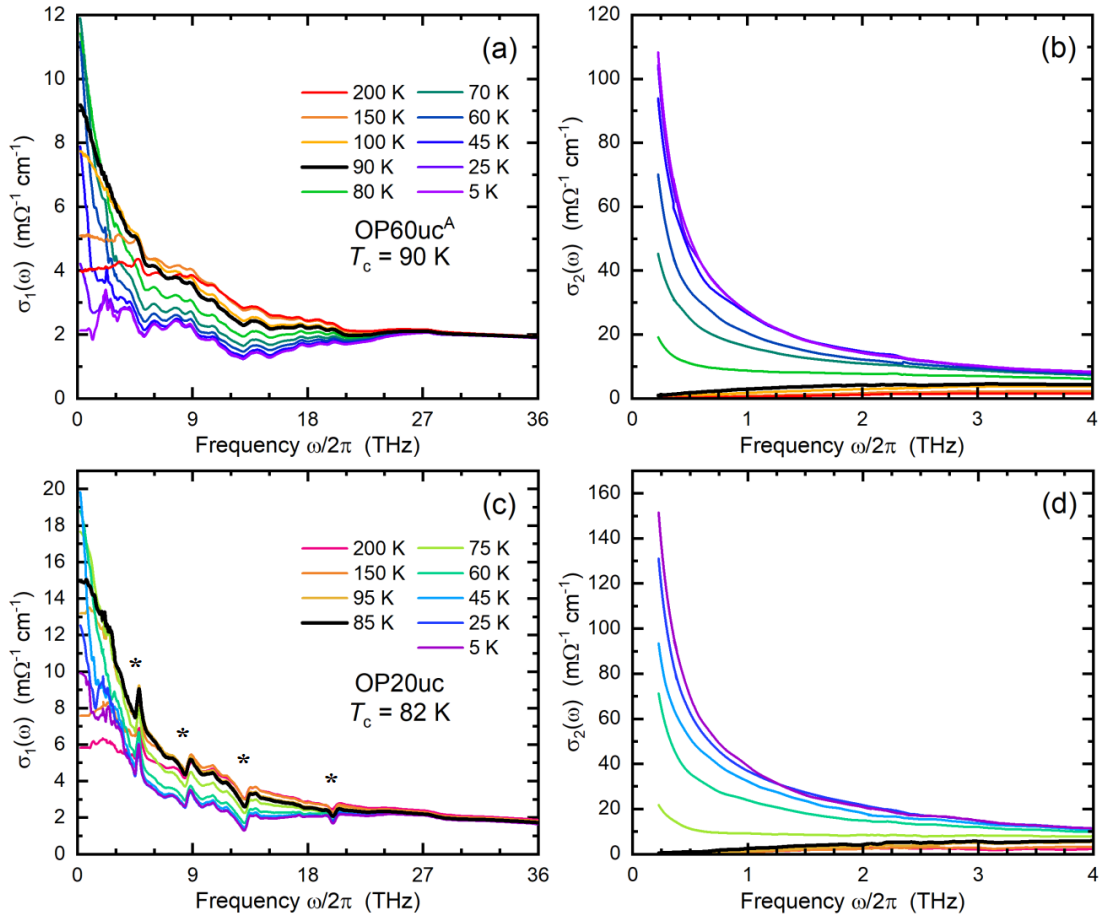

Figure 4.4 The real and imaginary parts of the complex conductivity for two representative near optimally doped DyBCO films, as measured by quasioptical microwave interferometry, TTDS, and nar-IR spectroscopic ellipsometry. (a, b) The conductivity spectra for a 60 uc thick DyBCO film. The shift of significant optical conductivity spectral weight below $\omega/2\pi \sim 27$ THz is accompanied by an upturn in $\sigma_2(\omega)$ proportional to $1/\omega$, marking the emergence of the superconducting condensate below T_c. (c, d) The conductivity spectra measured for a 20 uc thick DyBCO film. The asterisks in (c) mark the positions of residual LSAT substrate phonons.

type II coherence factor,

$$F(\Delta, E, E+\hbar\omega) = \frac{1}{2}\left(1 + \frac{\Delta^2}{E(E+\hbar\omega)}\right),$$

and the superconducting density of states,

$$N_s(E) = N_n(E)\,\mathrm{Re}\,\frac{|E|}{\sqrt{E^2-\Delta^2}}.$$

$N_s(E)$ diverges as $E \to \Delta$ from above, so as the temperature is reduced below T_c and the superconducting gap opens a peak in $\sigma_1(T)$ appears for sufficiently low probe frequencies. This conductivity peak is accompanied by the Hebel-Slichter peak in the nuclear-spin-lattice relaxation rate $1/T_1$, as observed by NMR measurements, which tracks the relaxation of the nuclear spins in the lattice due to interaction with the

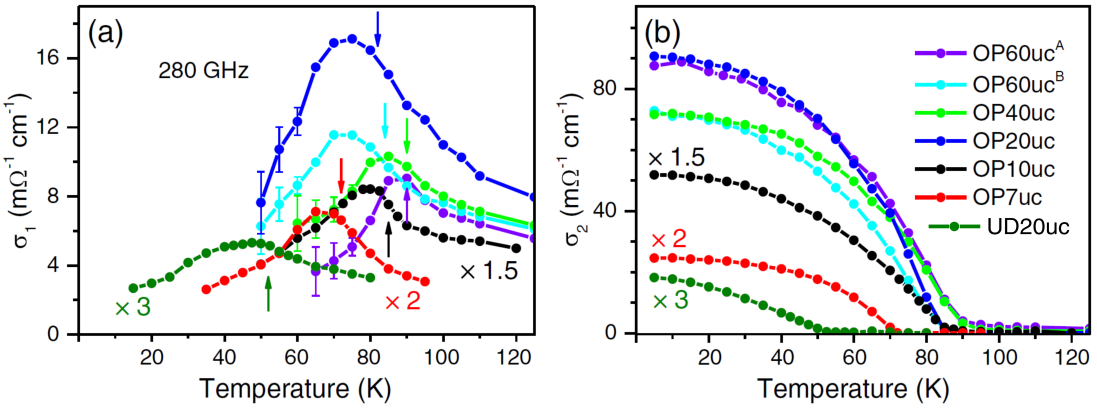

Figure 4.5 The temperature dependence of the real (a) and imaginary (b) parts of the complex conductivity, $\tilde{\sigma} = \sigma_1 + i\sigma_2$, measured at 280 GHz for all samples studied. The arrows indicate the values of T_c. The σ_1 peak observed in all samples below T_c arises due to the sudden reduction of the quasiparticle scattering rate γ below T_c, and the sharpness of this peak indicates sample homogeneity.

quasiparticles [282]. Like the conductivity peak, the Hebel-Slichter peak also occurs just below T_c as a consequence of type II coherence factors.

In copper oxide high-T_c superconductors, on the other hand, the Hebel-Slichter peak is not observed in NMR data [283], which implies that the conductivity peak present in Figs. 4.4 and 4.5 cannot be due to coherence effects. In fact, the coherence peaks in both NMR and conductivity measurements are expected to be completely suppressed in superconductors with the presence of strong coupling [284]. Several studies [285–287] have instead reported evidence that the cuprates display a sharp temperature dependent drop in the quasiparticle scattering rate γ below T_c as a universal feature. When the conductivity peak is analyzed at low frequencies in the two-fluid model the temperature dependent scattering rate implies that the conductivity peak occurs as the result of competition between a decreasing γ (or increasing quasiparticle τ) and decreasing normal carrier density ρ_n as temperature is reduced below T_c [287, 288]. This is because at low frequencies the σ_1 response is dominated by the residual normal carrier conductivity $\sigma_1 \approx \rho_n e^2\tau/m^*$, while the response of the superconducting carriers only dominates in σ_2. The presence of the "γ-conductivity peak" in the cuprates therefore suggests that the dominant scattering mechanism is electronic rather than phononic or from defects, because the strong reduction of the scattering channel at T_c indicates that the quasiparticles are coupled to an excitation spectrum that is modified in the superconducting state. If this is indeed the case, and the γ-conductivity peak can be properly described by the two-fluid model at low frequencies, then the superfluid density and penetration depth $\rho_s(T) = 1/\lambda^2(T) = \lim_{\omega\to 0} \mu_0\omega\sigma_2(T)$ can be obtained directly from Fig. 4.5(b) because ω is within the London limit.

In the next section we check the validity of the two-fluid model by performing a Kramers-Kronig consistency and spectral weight analysis of the measured complex conductivity data presented in Fig. 4.4. By ensuring that the two-fluid model holds it is then possible to obtain the correct non-mean field $\rho_s(T)$ and universal temperature dependence of the superfluid density in the DyBCO films.

4.3 Optical Sum Rule and Penetration Depth

In the two-fluid model and FGT sum rule, defined by Eq. 2.27, the electrodynamic response of a superconductor is separated into a normal charge, or quasiparticle, component and a superconducting component. The total density of charges, $\rho_s + \rho_n$, is considered to be constant at all temperatures; this assumption is a consequence of the principle of conservation of charge. Below T_c electrons in the normal charge fluid may bind together to form Cooper pairs and join the superconducting condensate, but, as long as the material is isolated, total charge cannot enter or exit the system. Since the superconducting charge density "resides" within a δ-function at $\omega = 0$, which is experimentally inaccessible in optical measurements, the superconducting response is only directly detected in $\sigma_2(\omega)$ in the form of a $1/\omega$ dependence, as observed above in Section 4.2. This behavior in σ_2 is equivalent to $\epsilon_1(\omega) \propto -1/\omega^2$ in the dielectric permittivity. The FGT sum rule therefore appears in the KK consistency analysis equations (Eqs. 3.31 and 3.32) through the terms SW_1 and SW_2:

$$SW_1 = \int_{0^+}^{1.5\,\mathrm{eV}} \Delta\sigma_1^{\mathrm{extr}}(\omega)d\omega$$

$$\Delta\epsilon_1^{\mathrm{KK}}(\omega) - 1 = 38\mathcal{P}\int_{0^+}^{\infty} \frac{\Delta\sigma_1^{\mathrm{extr}}(\Omega)}{\Omega^2 - \omega^2}d\Omega + \frac{SW_2}{\omega^2}$$

The loss of spectral weight SW_1 below T_c in the frequency dependence of $\sigma_1(\omega)$ is, by itself, only an indirect probe of the superconducting state. If the FGT sum rule holds and the sum rule integral is taken over the full range $\omega \in (0, \infty)$ then SW_1 can indeed be attributed to the formation of the superconducting condensate. In this case $SW_1 = SW_2$ and the calculated $\Delta\epsilon_1^{\mathrm{KK}}(\omega)$ matches the experimentally measured $\Delta\epsilon_1(\omega)$. However, in actual experiments the integration cannot be taken to infinity due to the reasons outlined in Section 3.1.3. Instead, a high frequency cutoff is used that is chosen to lie above the highest absorptions in the system, which are typically related to intraband transitions. If high energy bands are involved in the superconducting transition, on the other hand, then spectral weight may transfer to energies above the cutoff frequency and it may appear that $SW_1 \neq SW_2$. We therefore seek to analyze the degree to which the FGT sum rule is satisfied in the cuprates because this will allow us to accurately determine the full temperature dependence of the superconducting condensate density.

The results presented in Fig. 4.6 illustrate the outcome of the KK consistency analysis of the optical conductivity data shown in Fig. 4.4(a, b) for a near optimally doped 60 u.c. thick DyBCO film with $T_c = 90$ K. Panels (a) and (b) of Fig. 4.6 show the analysis at $T = 7$ K, deep in the superconducting state and close to the lowest measured temperature, while panels (c) and (d) show the same analysis closer to T_c at the intermediate temperature of $T = 70$ K. In both analyses the low temperature conductivity data was compared to the conductivity at T_c by calculating $\Delta\sigma_1(\omega, T) = \sigma_1(\omega, T) - \sigma_1(\omega, T_c)$. By defining the difference conductivity in this way the negative values of $\Delta\sigma_1$ in Fig. 4.6(a, c) represent spectral weight that has shifted *out* of the measured spectral range, while the sharp positive upturn at low frequencies in (c) represents the conductivity peak that occurs just below T_c. The KK consistency analysis then proceeded in two steps. First, $\Delta\sigma_1(\omega, T)$ was extrapolated to $\omega \to 0$ with Drude functions designed to match the low frequency ($\omega < 2$ THz) data, and to

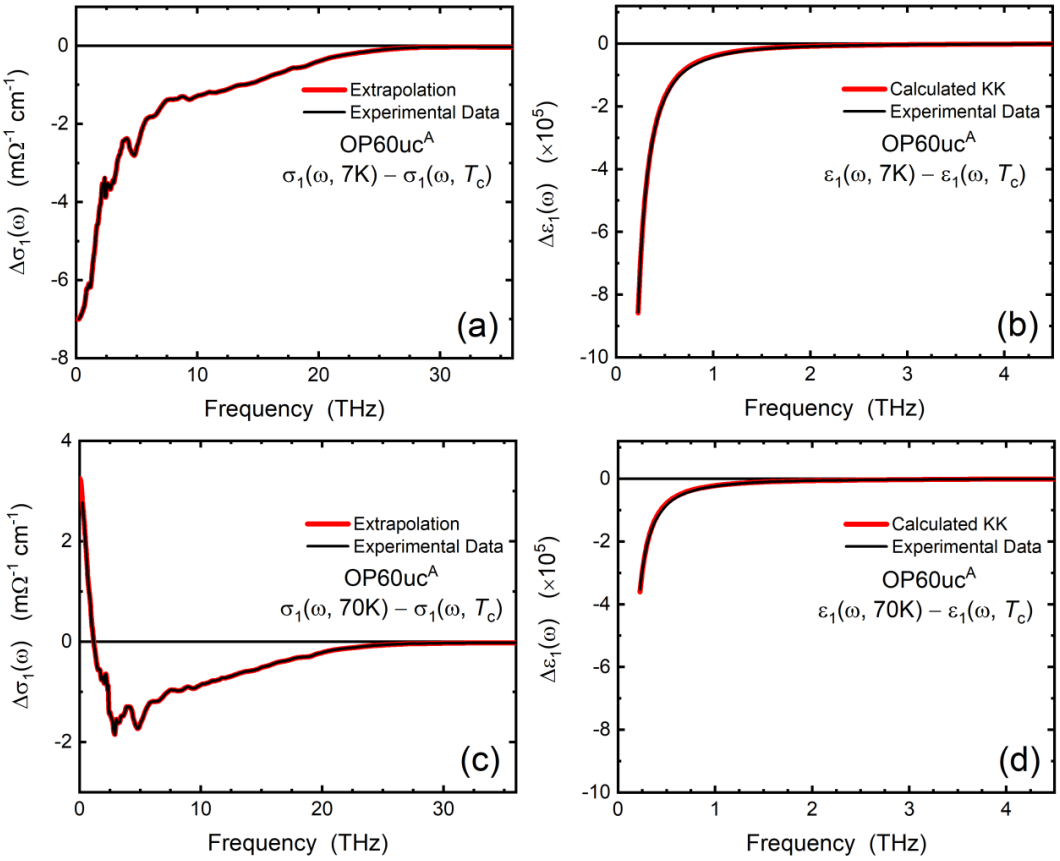

Figure 4.6 The Kramers-Kronig consistency analysis of the 60 u.c. thick DyBCO film below T_c at 7 K (a, b) and 70 K (c, d). In all panels the black curves correspond to the experimentally measured data. In (a, c) the red curves correspond to the extrapolated values $\Delta\sigma_1^{\text{extr}}(\omega, T)$, while in (b, d) the red curves represent the calculated Kramers-Kronig transformation of the extrapolated conductivity difference spectra by Eq. 3.32. At both 7 K and 70 K the calculated Kramers-Kronig values $\Delta\epsilon_1^{\text{KK}}(\omega, T)$ match the experimentally obtained values $\Delta\epsilon_1(\omega, T)$, indicating that the two-fluid model and FGT sum rule remain valid at the lowest and intermediate temperatures. The positive $\Delta\sigma_1(\omega, T)$ at low frequencies in (c) corresponds to the γ-conductivity peak in Fig. 4.5(a)

$\omega \to \infty$ with $\Delta\sigma_1 = 0$ because the difference conductivity values are indistinguishable from zero above 1 eV. The spectral weight shift SW_1 at each temperature was then calculated by integrating the resulting $\Delta\sigma_1^{\text{extr}}(\omega, T)$ to a frequency cutoff of $\hbar\omega = 1.5$ eV, which is significantly higher than the bandwidth of the energy band that crosses the Fermi level but below the energy of interband transitions. Second, the mathematical KK transform $\Delta\epsilon_1^{\text{KK}}(\omega, T)$ was calculated from $\Delta\sigma_1^{\text{extr}}(\omega, T)$ using the value of SW_1 in place of SW_2 and compared to the measured data $\Delta\epsilon_1(\omega, T) = \epsilon_1(\omega, T) - \epsilon_1(\omega, T_c)$. The resulting transforms, shown in Fig. 4.6(b, d) as red lines, were found to agree with the measured data for $SW_1 = SW_2$ at both $T = 7$ K and $T = 70$ K. An equivalent KK consistency analysis at $T = 7$ K and $T = 60$ K is presented in Fig. 4.7 for a near optimally doped 20 u.c. thick DyBCO film with $T_c = 82$ K. The results are both qualitatively and quantitatively similar to the near optimally doped 60 u.c. sample. Near the lowest measured temperatures $\Delta\sigma_1$ is

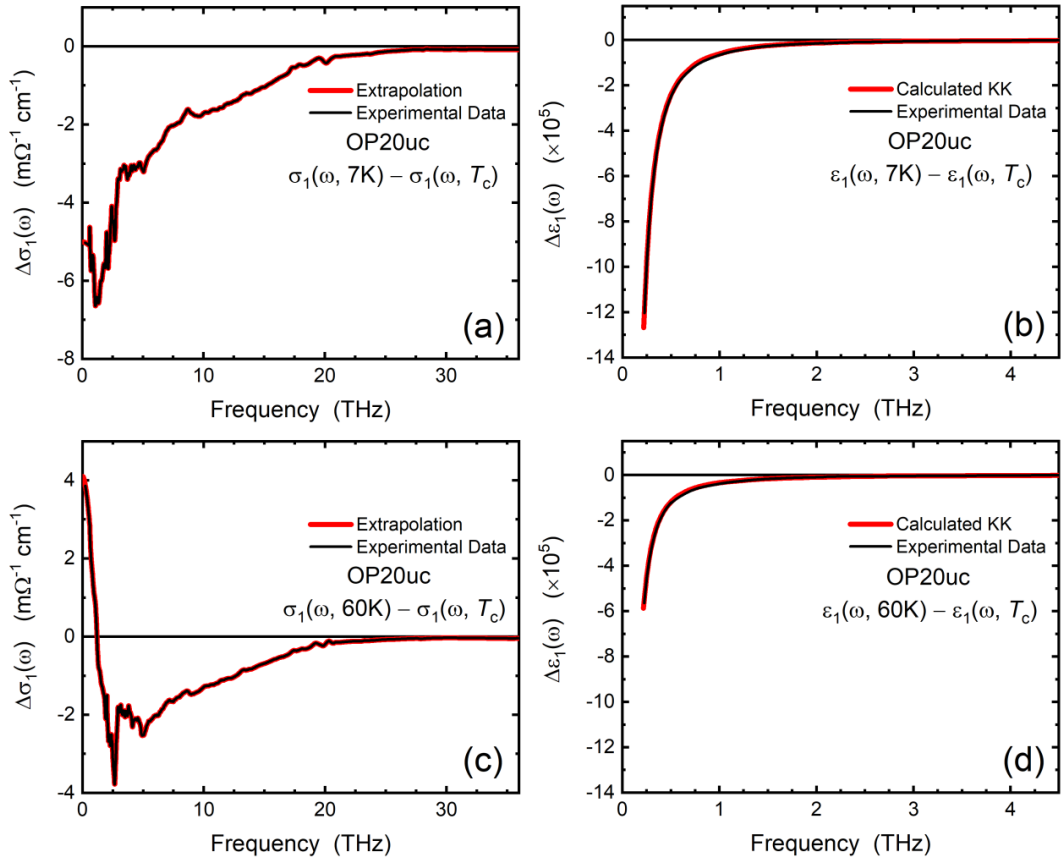

Figure 4.7 The Kramers-Kronig consistency analysis of the 20 u.c. thick DyBCO film below T_c at 7 K (a, b) and 60 K (c, d). (d) Like in the 60 u.c. thick film, the calculated Kramers-Kronig values $\Delta\epsilon_1^{\mathrm{KK}}(\omega, T)$ match the experimentally obtained values $\Delta\epsilon_1(\omega, T)$ at both 7 K and 60 K, indicating that the two-fluid model and FGT sum rule remain valid at the lowest and intermediate temperatures.

entirely negative, indicating that spectral weight has only shifted out from frequencies below the optical gap, while a sharp positive upturn at low frequencies just below T_c corresponds to an accumulation of quasiparticle spectral weight due to the previously discussed conductivity peak. For both $T = 7$ K and $T = 60$ K, as in the case of the 60 u.c. thick sample, the calculated $\Delta\epsilon_1^{\mathrm{KK}}(\omega, T)$ was found to match the measured $\Delta\epsilon_1(\omega, T)$ for $SW_1 = SW_2$.

To quantify the degree of agreement between SW_1 and SW_2 we perform a reanalysis of the KK consistency check by manually unbalancing the spectral weight and recalculating $\Delta\epsilon_1^{\mathrm{KK}}(\omega, T)$. An example of this reanalysis is shown in Fig. 4.8 for the near optimally doped 60 u.c. thick film at $T = 7$ K. Here, as a guide, we make use of the experimental uncertainty of the submillimeter Mach-Zehnder interferometer of $\pm 2\%$ below 1 THz. Our experimental error in this spectral range is actually even lower than 2% because the procedure by which we extract the optical constants, i.e., by combining submillimeter interferometry with TTDS and far-IR spectroscopic ellipsometry, is well controlled and the data combination procedure further bounds the extracted values of $\epsilon_1(\omega)$. By calculating $\Delta\epsilon_1^{\mathrm{KK}}(\omega, T)$ for $SW_1 = SW_2 \pm 2\%$ (blue dash-

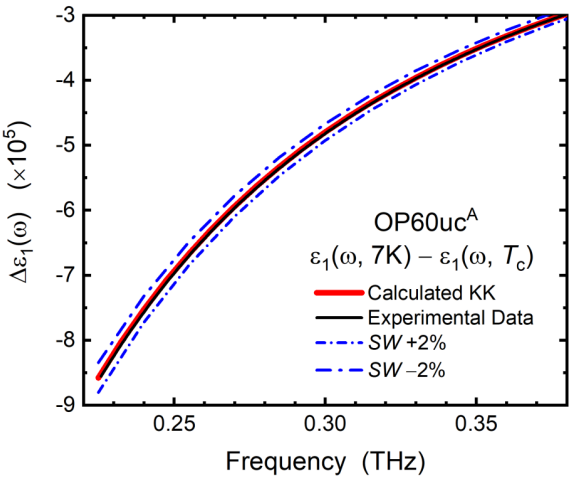

Figure 4.8 To illustrate the accuracy of the data analysis procedure and extraction of $\rho_s(T)$, the Kramers-Kronig transformation $\Delta\epsilon_1^{\rm KK}(\omega)$ of the difference conductivity spectra for sample OP60uc$^{\rm A}$ at 7 K was calculated by unbalancing the integrated spectral weight SW_1 in Eq. 3.31 and superfluid density SW_2 in Eq. 3.32 by +2% (lower blue curve) and −2% (upper blue curve). The experimentally measured $\Delta\epsilon_1(\omega)$ falls neatly within these bounds, showing that the two-fluid model and FGT sum rule is satisfied to within $|SW_1 - SW_2|/SW(7\ {\rm K}) = 0.2\%$.

dotted curves in Fig. 4.8) we see that the calculated KK transform with $SW_1 = SW_2$ (red curve) matches the experimental data to much better than 2%. In fact, if we quantify the actual experimental error as $|SW_1 - SW_2|/SW_0$ in order to compare the uncertainty to the total spectral weight in the superconducting state (where SW_0 is the total spectral weight at 7 K, not the difference spectral weight), then we find that $|SW_1 - SW_2|/SW_0 = 0.2\%$. We therefore conclude that the KK consistency analysis is only limited by the experimental error of the spectra combination procedure and that the total spectral weight at T_c is equivalent to the total spectral weight in the superconducting state to within 0.2%.

It is important to note that the KK consistency analysis results are the *same* for the near optimally doped 20 u.c. and 60 u.c. thick DyBCO films despite the differences in their disorder levels and dc normal-state resistivities (see Fig. 4.3). Additionally, it was found that the agreement between $\Delta\epsilon_1^{\rm KK}(\omega, T)$ and the measured $\Delta\epsilon_1(\omega, T)$ was not affected by the shape of the conductivity extrapolation at low frequencies; different extrapolation forms were tried (Drude, linear, and square) but only the total spectral weight at low frequencies appreciably affects the calculation of $\Delta\epsilon_1^{\rm KK}(\omega, T)$. This analysis shows that changes in $\sigma_2(\omega)$ are quantitatively consistent with the opening of the superconducting gap in $\sigma_1(\omega)$ and its spectral weight transfer into the δ-function at $\omega = 0$. The consistency of the measured conductivity data up to near-IR frequencies (∼1.5 eV) implies that the FGT sum rule and two-fluid model are obeyed in DyBCO to within 0.2% error. Our finding confirms that the conductivity peak observed just below T_c and at frequencies below $\omega \sim$ 1–2 THz is indeed due to the competition between increasing quasiparticle lifetime $\tau(T)$ and decreasing $\rho_n(T)$ as temperature is decreased, rather than BCS-like coherence effects [287, 289, 290]. As a result, our low frequency measurements of the complex conductivity give direct access to the true superfluid density $\rho_s(T)$.

A further consequence of our analysis is that our results agree with the findings of Boris *et al.* [16] that superconductivity in the cuprates cannot be due to a kinetic energy saving mechanism, as has been proposed for certain theories of high-T_c superconductivity [12, 13], and that the interband transitions do not contribute to any transfer of spectral weight in the superconducting state. This is because we find that the total spectral weight shift below T_c is conserved when integrating $\Delta\sigma_1$ up to 1.5 eV, which lies below the interband transition energy. To see that this rules out any kinetic energy saving mechanism we recall what kind of scenario *could* lead to such a mechanism where the kinetic energy changes between the normal and superconducting states. For a simple noninteracting single band tight-binding model, with $\nabla_k^2\varepsilon_k \sim -\varepsilon_k$, the "band sum rule" [13, 291] is given by

$$SW = \int_0^{\omega_{\text{cutoff}}} \sigma_1(\omega)d\omega = \frac{\pi e^2}{2N}\sum_k \nabla_k^2\varepsilon_k n_k = \frac{\pi e^2 a^2}{2\hbar^2 V_u}\langle -K\rangle, \tag{4.1}$$

where n_k is the electronic distribution function, a is the in-plane lattice constant, V_u is the unit cell volume, and $\langle -K\rangle$ is the (negative) kinetic energy. For a nearly full band, hopping between neighbors leads to optical transitions that lie above the intraband energies. Considering just the nearest-neighbor interactions, the FGT sum rule in this case becomes

$$\int_0^{\infty} \Delta\sigma_1(\omega)d\omega = \int_0^{\omega_{\text{cutoff}}} \Delta\sigma_1^{\text{intraband}}(\omega)d\omega + \frac{\pi e^2 a^2}{2\hbar^2 V_u}\Delta\langle K\rangle. \tag{4.2}$$

If the intraband spectral weight decreases in the superconducting state, as it does in BCS superconductors, then this simple model would imply that the kinetic energy can increase and superconductivity must be related to a reduction of the potential energy. On the other hand, if the intraband spectral weight *increases*, then the superconductivity must be due to a kinetic energy saving mechanism. This latter possibility could arise from the situation where fermions become more mobile in the superconducting state as a result of smaller self-energy, which can occur for strong coupling [17]. However, in our analysis we observe that the full spectral weight in the superconducting δ-function is completely accounted for by the change in the intraband spectral weight, which is inconsistent with pictures wherein superconductivity is driven by mechanisms based on the decrease of kinetic energy.

For $T > T_c$, on the other hand, different behavior of the spectral weight shift may be observed. The spectral weight included in the band sum rule in Eq. 4.1 is temperature dependent because the electronic distribution function n_k is temperature dependent. Over a broad temperature range the total intraband spectral weight changes due to the smearing of the Fermi occupation function with increasing temperature. This change can be analyzed by using the Sommerfeld expansion to approximate the temperature dependence of n_k. Carrying the expansion to first order for a flat density of states gives

$$SW(T) = SW(0) - BT^2 \tag{4.3}$$

where the coefficient $B = \pi^2/12D$ and D is the half-bandwidth (related to the hopping t in the tight-binding model as $D = 4t$). The total intraband spectral weight is therefore expected to increase with decreasing temperature as the smearing of the Fermi function decreases and less of its tail lies at high energies corresponding to interband transitions. Indeed, for several families of underdoped, optimally doped,

and overdoped LSCO and BSCCO a total increase of the intraband spectral weight of $\Delta SW/SW_0 = [SW(7\text{ K}) - SW(300\text{ K})]/SW(7\text{ K}) \approx 3$–$5$ % has been observed when the integral in Eq. 4.1 is taken up to $\omega_{\text{cutoff}} \approx \omega_p \approx 1$ eV [292]. However, this change of intraband spectral weight is quite large compared to that seen in conventional metals such as gold, and calculations based on noninteracting nearest-neighbor tight-binding and flat band models produce values of $\Delta SW/SW_0$ that are much too small to reconcile with cuprate experimental data. Furthermore, the values of SW_0 and B extracted from the temperature dependence of the spectral weight in LSCO and BSCCO lead to different values of t, with t extracted from SW_0 being one order of magnitude larger than t extracted from B, which points to the presence of two different energy scales and the importance of strong correlations. Dynamical mean-field theory calculations taking into account strong correlation effects by including the Hubbard on-site repulsion U in the tight-binding model have reconciled the difference between theory and experiment and shown that the presence of strong correlations leads to the large temperature dependence of $\Delta SW/SW_0$ (i.e., the large value of B) in the cuprates [293].

To analyze the behavior of the spectral weight transfer above T_c in the DyBCO films, we have performed a KK consistency analysis on the 60 u.c. thick and 20 u.c. thick near optimally doped samples for difference spectra $\Delta\sigma_1(\omega, T)$ and $\Delta\epsilon_1(\omega, T)$ between T_c and 200 K. The results of this analysis are summarized in Fig. 4.9. For the 60 u.c. thick sample we find that the value of the integrated difference spectral weight $\Delta SW = \int[\sigma_1(\omega, 90\text{ K}) - \sigma_1(\omega, 200\text{ K})]d\omega$ is positive and the KK transform matches the experimentally measured $\Delta\epsilon_1$, as shown in panels (a) and (b). We find the value of SW_0 by integrating the total spectral weight at 90 K, $SW_0 = \int \sigma_1(\omega, 90\text{ K})d\omega$, up to $\omega_{\text{cutoff}} = 1.5$ eV, which leads to a relative spectral weight shift above T_c of $\Delta SW/SW_0 = 1.9\%$. Similarly, for the 20 u.c. thick sample we find that the integrated difference spectral weight above T_c is also positive with $\Delta SW/SW_0 = 2.2\%$, as shown in panels (c) and (d). For comparison, the values of $\Delta SW/SW_0$ for crystals of several different cuprate families, including LSCO, BSCCO, and YBCO, are shown in Fig. 4.10 as a function of hole doping level p. Our results for the near optimally doped DyBCO films are in agreement with these prior reported results. In particular, the values of $\Delta SW/SW_0$ for the DyBCO films (red and blue stars) agree very well with values obtained for YBCO and BSCCO single crystals measured between 100 K and 200 K (green diamond and octagon). These four data points lie somewhat below other values for LSCO, BSCCO, and dynamical mean-field theory calculations, because the latter values were obtained by comparing the spectral weight at the lowest measured temperatures to the spectral weight at 300 K rather than 200 K. These results imply that the intraband spectral weight in the DyBCO thin films indeed increases with decreasing temperature above T_c, but that once the superconducting state is entered below T_c the total spectral weight remains constant, with any changes in the intraband spectral weight compensated by the appearance of the superconducting δ-function.

The change in the kinetic energy above T_c is therefore unrelated to the FGT sum rule, as any changes in $\langle K \rangle$ are due to the smearing of the Fermi occupation function around the Fermi level with temperature rather than a redistribution of spectral weight. Below T_c the opening of the superconducting gap on the Fermi surface causes the total spectral weight to remain constant in the superconducting state and the FGT sum rule is governed only by changes of the intraband (Drude) spectral weight, ruling out any kinetic energy saving mechanism in the cuprates. This means that

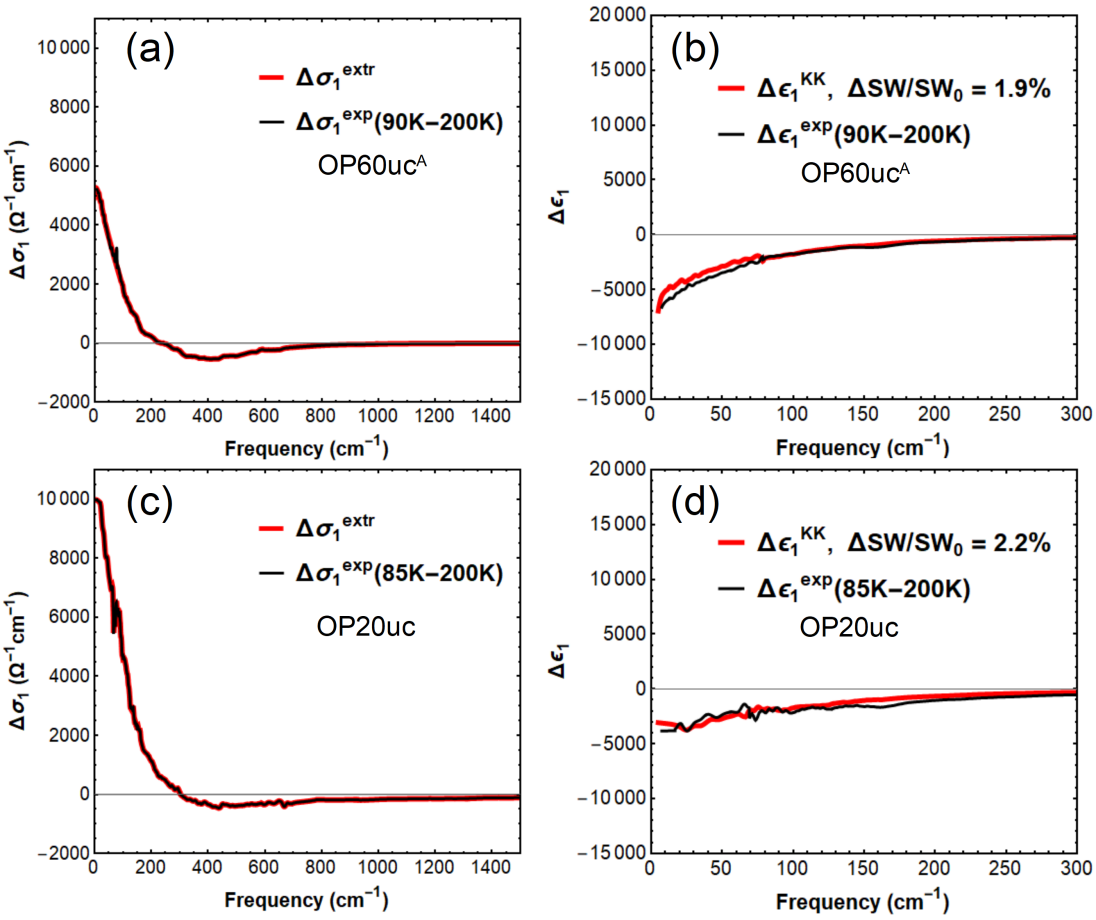

Figure 4.9 The Kramers-Kronig consistency analysis above T_c for the near optimally doped 60 u.c. thick (a, b) and 20 u.c. thick (c, d) DyBCO films, where $\Delta\sigma_1(\omega) = \sigma_1(\omega, T_c) - \sigma_1(\omega, 200\text{ K})$. For both films the integrated difference spectral weight $\Delta SW = \int \Delta\sigma_1(\omega)d\omega$ is positive, implying that the intraband spectral weight increases as temperature decreases from 200 K to T_c. Based on the values of the total spectral weight SW_0 at T_c it is found that $\Delta SW/SW_0 = 1.9\%$ for $OP60uc^A$ and $\Delta SW/SW_0 = 2.2\%$ for OP20uc.

high energy interband excitations are not involved in the opening of the superconducting optical gap; spectral weight may be rearranged at high energies but does not become redistributed to low energies with the opening of Δ. However, while the total spectral weight of the *superconducting state* remains constant at $T < T_c$, the intraband spectral weight of the *normal state* continues to increase below T_c because of the T^2 dependence of $SW(T)$ in Eq. 4.3. By extrapolating the measured $SW(T)$ from above T_c to $T = 0$ using Eq. 4.3 it is possible to determine the expected normal state spectral weight, $SW_n(T)$, that would be found below T_c in the absence of a transition. We find that the relative change of the intraband spectral weight between superconducting and normal states at the lowest measured temperature is $[SW_s(7\text{ K}) - SW_n(7\text{ K})]/SW_n(7\text{ K}) \approx -0.5\%$ for both the near optimally doped 20 u.c. and 60 u.c. thick DyBCO films. This result confirms that the superconducting state in the cuprates is related to a slight reduction of the intraband spectral weight (or slight increase in $\langle K \rangle$) compared to the normal state at the same temperature. The result is consistent with collective boson models of superconductivity where fermions interact with collective spin fluctuations [16, 17]. In such models the

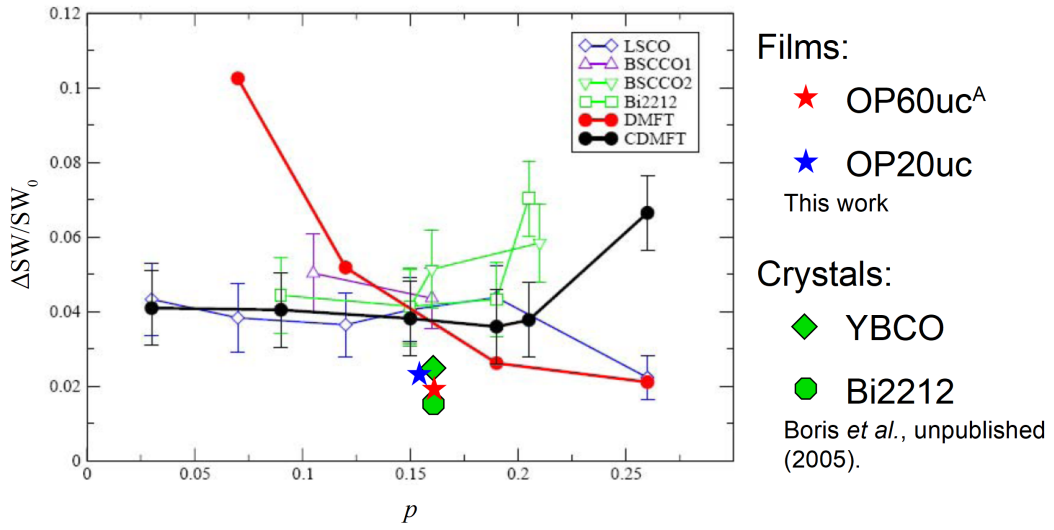

Figure 4.10 The measured values of $\Delta SW/SW_0$ for the near optimally doped 60 and 20 u.c. thick DyBCO films (red and blue stars, respectively) are compared to values for LSCO, BSCCO, and YBCO single crystals as well as single-site and cluster dynamical mean-field theory calculations as a function of hole doping p [293,294]. The data points for the DyBCO films and the optimally doped YBCO and BSCCO crystals measured by Boris *et al.* lie at roughly half the value of the other data points because for these four samples $\Delta SW = SW(T_c) - SW(200\text{ K})$. For all other data points the change in intraband spectral weight is defined as $\Delta SW = SW(0) - SW(300\text{ K})$, a temperature range that is twice as large above T_c. The behavior of the intraband spectral weight shift above T_c in the DyBCO films is therefore consistent with the behavior observed in the other cuprate families.

continuum of collective excitations becomes gapped in the superconducting state, causing a reduction of fermionic damping and a decrease in fermion self-energy, but the fixing of the intraband spectral weight due to the opening of the superconducting gap overcompensates and gives rise to the negative value of $SW_s(0) - SW_n(0)$. In this picture the nearest-neighbor-only, single band tight-binding description contained in Eqs. 4.1 and 4.2 becomes inadequate, and spectral weight transfer between higher lying Hubbard bands must be considered.

The sum rule and spectral weight analysis we have presented here also allows us to avoid the issues related to measurement of the superfluid density at single frequencies, as are present in studies of the penetration depth by mutual inductance methods in the megahertz to gigahertz spectral range. Measurements of the kinetic inductance are highly susceptible to the details of disorder and vortex pinning. In particular, the vortex-antivortex interactions are dependent upon the vortex diffusion length $\ell_\omega = \sqrt{14\mathcal{D}/\omega}$, so that the response at ω is dominated by vortex-antivortex pairs that have separation $r \sim \ell_\omega$. In the clean limit or where disorder is not significant, ℓ_ω is equivalent to the vortex coherence length ξ_+ and measurement at ω in effect probes the temperature dependence of this parameter. Taking the Bardeen-Stephen expression for the diffusion constant of free vortices [111], $\mathcal{D} = 2e^2\xi_{\rm GL}k_BT/\pi\hbar^2\sigma^n_{dc}$ (where σ^n_{dc} is the normal state dc conductivity), we find that for frequencies in the range 10 MHz to 10 GHz the vortex diffusion length is approximately 30 nm $< \ell_\omega <$ 1 μm. This length scale and dependence on σ^n_{dc} suggests that defect-induced disorder

(vacancies, stacking faults, impurity compounds, twin boundaries, domain walls, etc.) will dramatically affect ℓ_ω. Indeed, at strong vortex pinning, $\mathcal{D}$ can acquire exponential dependence on temperature with a large pinning energy that obscures the true temperature dependence of the vortex-antivortex interactions [181]. By measuring the full spectral weight evolution across a very broad range of frequencies we instead probe the global superfluid response in our samples independently of the vortex diffusion dynamics.

4.4 Superfluid Density and BKT Transition in $DyBa_2Cu_3O_{7-\delta}$

Having carefully investigated and controlled for disorder, strain, and spectral weight transfer in our DyBCO films, we now turn to the details of the evolution of the superfluid density ρ_s with temperature and sample thickness. In Section 4.3 we established the KK consistency of the measured $\sigma_1(\omega)$ and $\sigma_2(\omega)$ along with the validity of the FGT sum rule in DyBCO. We are therefore able to obtain the true temperature dependence of the penetration depth from $\lambda^{-2}(T) = \lim_{\omega\to 0} \mu_0\omega\sigma_2(\omega, T)$, because the fact that our lowest measured frequencies ($\omega < 0.3$ THz) lie in the London limit, where $\sigma_2 \propto \omega^{-1}$, means that σ_2 provides a very close estimate of the superfluid response. Following Section 4.3, we accurately extract the in-plane superfluid density $\rho_s(T)$ by fitting the complex conductivity spectra with the two-fluid model,

$$\tilde{\sigma}(\omega, T) = \frac{i\rho_n(T)}{\omega + i/\tau} + \frac{i\rho_s(T)}{\omega},$$

with $\rho_n + \rho_s$ remaining constant.

The evolution of $\rho_s(T)$ with temperature for near optimally doped DyBCO films with thicknesses ranging from 10 u.c. to 60 u.c. are shown in Fig. 4.11(a). To facilitate comparison between samples we plot the normalized superfluid density, $\rho_s(T)/\rho_{s0}$, where ρ_{s0} is the superfluid density at $T = 0$. The first striking feature we find is that $\rho_s(T)/\rho_{s0}$ is identical for all samples, regardless of film thickness, impurity details, strain, or normal state dc resistivity. This result implies that our observed $\rho_s(T)/\rho_{s0}$ is the *universal* superfluid density temperature dependence for the DyBCO thin films. Such an effect is initially surprising because one would expect that the different details of disorder and strain relaxation will lead to different pair breaking behavior and, as a result, different curvature of the various data sets. Instead, the fact that the superfluid density evolution is the same for all samples is a testament to the high quality of our MBE-grown films and an additional indication that disorder effects are not dominant. The lack of dependence of $\rho_s(T)/\rho_{s0}$ on strain relaxation is also notable because our previously discussed XRD measurements (see Fig. 4.1) imply that the structure of the near optimally doped films smoothly evolves from completely orthorhombic at 60 u.c. thickness to almost fully tetragonal at 10 u.c. This may suggest that the shape of $\rho_s(T)/\rho_{s0}$ is more related to the presence of CuO chains than the orthorhombicity of the unit cell.

The universality of $\rho_s(T)/\rho_{s0}$ further implies that the limiting behavior and functional form of the temperature dependence are related to intrinsic details of the superconducting state. Also shown in Fig. 4.11(a) is $\rho_s(T)/\rho_{s0}$ for an ultraclean, detwinned single crystal of near optimally doped YBCO averaged over the a and b

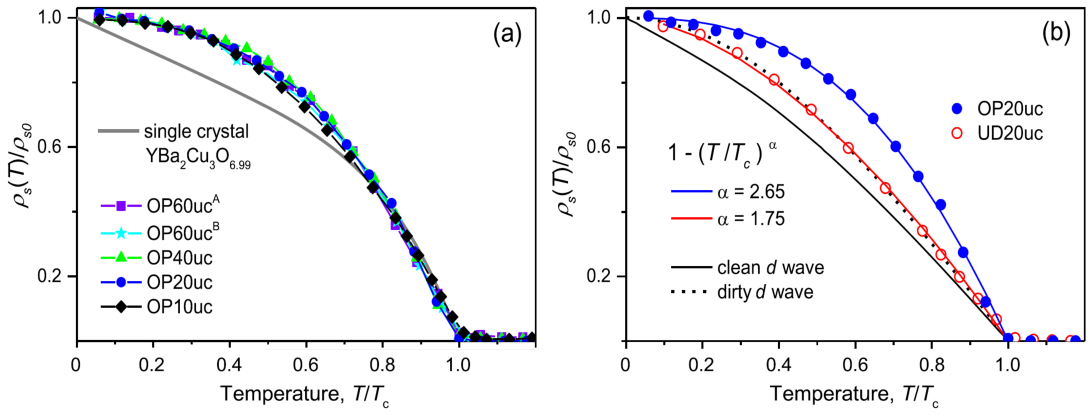

Figure 4.11 (a) The temperature dependence of the normalized superfluid density for five near optimally doped DyBCO films with thicknesses 10–60 u.c. The solid gray line shows $\rho_s(T)/\rho_{s0}$ averaged over a and b crystallographic directions for pure $YBa_2Cu_3O_{6.99}$ single crystals [280]. Agreement between the single crystal curve and the experimental data implies that the films share 3D-XY critical behavior near T_c. (b) The normalized superfluid density for an annealed underdoped 20 u.c. DyBCO film (red open circles) compared with a near optimally doped 20 u.c. film (blue dots). $\rho_s(T)/\rho_{s0}$ for the underdoped film agrees well with calculations for a dirty d-wave superconductor with a circular Fermi surface [281] (black dotted line), but is significantly different than the temperature dependence for the near optimally doped film.

crystallographic directions [280]. Close to T_c our data for each of the near optimally doped DyBCO films is consistent with the temperature dependence for the YBCO single crystal, with all curves displaying the same critical behavior. This constitutes evidence that the DyBCO films 10 u.c. and thicker belong to the 3D-XY universality class over a broad temperature range down to $T \sim 0.8T_c$ [19]. As such, our results agree with prior work [182] that indicates the superconducting state in RBCO remains three-dimensional down to thicknesses even less than 20 u.c. Below $T \sim 0.8T_c$ our data deviate from that of the single crystal. Linear dependence of $\rho_s(T)$ as $T \to 0$ is a key piece of evidence for nodes in the energy gap in high-T_c superconductors [295] because the normal charge carrier density reduces to $\rho_n \propto k_B T/\Delta_{\max}$ for all singlet pairing states other than s-wave when the Fermi surface is cylindrical. While such linear dependence of $\rho_s(T)$ is clearly observed in the intrinsic single crystal YBCO data, $\rho_s(T)$ for the DyBCO films instead displays a characteristic T^2 dependence at low temperatures. It is well known that nodal pair breaking by strong scattering from unitarity-limit impurities, which include defects residing within the CuO_2 planes, can rapidly induce a crossover to T^2 behavior in $\rho_s(T)$ as $T \to 0$, with accompanying suppression of superfluid density [281,296]. On the other hand, the lack of significant reduction of T_c in our 60 u.c. thick films ($T_c = 90$ K) implies that the concentration of strong scatterers must be small. The observation of $\rho_s(T) \propto T^2$ at low temperatures in our DyBCO films, independent of thickness, is therefore in agreement with our assignment that the films are within the moderate disorder regime.

To draw a comparison to the effects of underdoping, we plot $\rho_s(T)/\rho_{s0}$ for both a near optimally doped 20 u.c. thick film and an underdoped (annealed) 20 u.c. thick film in Fig. 4.11(b). It is apparent that the temperature dependence for the underdoped film is much more linear than our universal temperature dependence,

which is represented by the data for the near optimally doped sample, especially near T_c. To quantify this difference we use a phenomenological fit to the data, $\rho_s(T)/\rho_{s0} = 1 - (T/T_c)^\alpha$, and find that the scaling factor α decreases from $\alpha = 2.65$ to $\alpha = 1.75$ upon crossing over from near optimal doping to underdoping. This trend is consistent with previous observations for highly underdoped YBCO [22], where $\rho_s(T)$ follows a distinct linear T dependence over a broad temperature range up to very close to T_c (see panel (b) in Fig. 2.12). The clear deviation from 3D-XY critical behavior in such strongly underdoped samples was found to be due to quantum critical fluctuations that place the system into the $(3+1)$D-XY universality class upon approaching the quantum critical point at $p = p_c$ [182]. These fluctuations reduce the 3D-XY critical region to an inaccessibly narrow range around T_c so that the critical behavior crosses over from a $\rho_s \propto T^{2/3}$ to $\rho_s \propto T$ dependence. Since the superfluid density scales with T_c as $\rho_s \propto T_c$ on the underdoped side of the phase diagram, this implies that changes in the critical behavior due to quantum critical fluctuations must change the slope of the full temperature dependence of $\rho_s(T)$. Therefore, from considering the behavior of $\rho_s(T)$ just below T_c, we find that one effect of deliberate underdoping is to necessarily *reduce* the steepness with which $\rho_s(T)/\rho_{s0}$ drops to zero. As a result, we find that underdoping in the cuprates has the opposite effect on $\rho_s(T)/\rho_{s0}$ than what one expects to observe for the Nelson-Kosterlitz superfluid jump at a BKT transition.

The temperature dependence of $\rho_s(T)/\rho_{s0}$ for the underdoped 20 u.c. thick DyBCO film also bears striking resemblance to the results of recent calculations of the superfluid density in a dirty d-wave superconductor of tetragonal symmetry with cylindrical Fermi surface [281]. These calculations, based on a realistic model of the Fermi surface of LSCO obtained from ARPES spectra, determined the changes to $\rho_s(T)/\rho_{s0}$ due to the inclusion of both strong- and weak-limit scattering impurities. While both types of scatterers reduce $\rho_s(0)$ and T_c, only scattering in the strong (unitarity) limit gives rise to a crossover to T^2 dependence in $\rho_s(T)$ at low temperatures; weak (Born limit) scattering instead preserves the $\rho_s(T) \propto T$ dependence as $T \to 0$. Furthermore, the details of the topology of the Fermi surface determine the exact shape of the full temperature dependence of $\rho_s(T)/\rho_{s0}$. Examples of these calculations performed in the clean and dirty limits are plotted together with the DyBCO experimental data in Fig. 4.11(b) as solid and dotted lines, respectively. The clean limit calculation, which includes zero scattering by definition, represents the temperature evolution of the superfluid density under the influence of only the Fermi surface topology. On the other hand, the dirty limit calculation, with the unitarity-limit scattering rate $\Gamma_N = 0.1T_{c0}$, agrees particularly well with the measured data for the underdoped 20 u.c. thick film. There, the disorder causes the clear crossover to T^2 behavior at low temperatures, whereas the particular choice of the Fermi surface determines the critical behavior as T approaches T_c. The agreement between our data and the calculations is also consistent with a change of the Fermi surface topology from orthorhombic to tetragonal symmetry upon crossing over from near optimal doping to underdoping. This change is not completely surprising because our XRD measurements show that there is indeed a structural change to tetragonal symmetry with underdoping. However, as we recall from our discussion above of Fig. 4.11(a), the change of the unit cell shape from rectangular to square is not sufficient by itself to produce a change in the temperature dependence of $\rho_s(T)/\rho_{s0}$, as the data for the near optimally doped 10 u.c. film follows the universal dependence despite the

unit cell being predominantly tetragonal. Rather, the role of the CuO chains is key, as their presence will cause a change in the topology of the Fermi surface even for a square lattice. Comparison of calculations to the entire temperature dependence of $\rho_s(T)/\rho_{s0}$ for the near optimally doped films remains difficult because the details of such Fermi surface distortions are not yet fully quantified. Further calculations based on the realistic Fermi surface of near optimally doped DyBCO are required to explain the temperature dependence of our universal behavior in Fig. 4.11(a). Very recent reports of *in situ* ARPES measurements of similar MBE-grown DyBCO films indicate that these calculations may be possible [297]. Nevertheless, we find that in addition to the rise of quantum critical fluctuations on the underdoped side of the phase diagram, the change of the Fermi surface topology is also an important factor that can act to obscure 3D-XY critical behavior near T_c.

When the thickness of the DyBCO film is further reduced below 10 u.c. a very different result is obtained than for underdoping. The temperature dependence of the superfluid density $\rho_s(T) = \lambda^{-2}(T)$ for the near optimally doped 10 u.c. thick film is compared with that for a near optimally doped 7 u.c. thick film in Fig. 4.12(a). The striking result we find is that $\rho_s(T)$ for the 7 u.c. thick sample is much steeper as $T \to T_c$ than the universal temperature dependence observed for all other optimally doped samples, as indicated by the difference between the red squares and the black dotted curve in the figure. When $\rho_s(T)$ for the 7 u.c. thick sample is compared with the (scaled) superfluid density of the 10 u.c. thick film it becomes evident that the two follow the same temperature dependence below $T \approx 50$ K. Remarkably, however, above 50 K the superfluid density temperature dependence of the two films deviates, with the data for the 7 u.c. thick film falling rapidly to zero and showing a suppression of T_c from the 10 u.c. value by approximately 13 K. This change is accompanied by only a minor broadening of the T_c, from $\Delta T_c = 1.4$ K at 10 u.c. thickness to $\Delta T_c = 2$ K for 7 u.c. The fact that ΔT_c remains small compared to the ∼13 K T_c suppression, and that the absolute T_c remains high (72 K for OP7uc), is evidence that this behavior is not due to significantly increased disorder effects in the 7 u.c. thick film compared to the 10 u.c. sample (that is, the superconducting transition remains sharp). This kind of T_c reduction is expected as a consequence of enhanced 2D *thermal* fluctuations, as opposed to increased quantum critical fluctuations. Whereas quantum critical fluctuations cause a reduction of the slope in $\rho_s(T)$, thermal fluctuations in 2D systems belonging to the 2D-XY universality class lead instead to a BKT transition at a temperature $T_{BKT} < T_c$ that is characterized by the Nelson-Kosterlitz superfluid jump. The magnitude of this jump is given by $\rho_s(T_{BKT}) = 8\pi\mu_0 k_B T_{BKT}/L\Phi_0^2$, where L is the thickness of the ultrathin film, so the temperature at which the jump occurs can be estimated by finding where $\rho_s(T)$ intersects the line $\rho_s(T_{BKT})$.

Figure 4.12(a) compares the measured data for the two thinnest DyBCO films to two such BKT lines, shown as the black ($L = 10$ u.c.) and red ($L = 7$ u.c.) solid lines. For a 10 u.c. thick superconducting layer the predicted T_{BKT} is expected to occur very close to T_c. Accordingly, no superfluid density jump is evident in the measured $\rho_s(T)$ data for the near optimally doped 10 u.c. thick DyBCO film, in keeping with this sample displaying critical behavior belonging to the 3D-XY universality class as discussed previously. On the other hand, the BKT transition for an $L = 7$ u.c. thick film is predicted to occur at a significantly lower temperature that is consistent with the temperature range in which $\rho_s(T)$ for our 7 u.c. sample exhibits a steeper drop. However, instead of a distinct jump (i.e., a near-discontinuity) in $\rho_s(T)$ at T_{BKT},

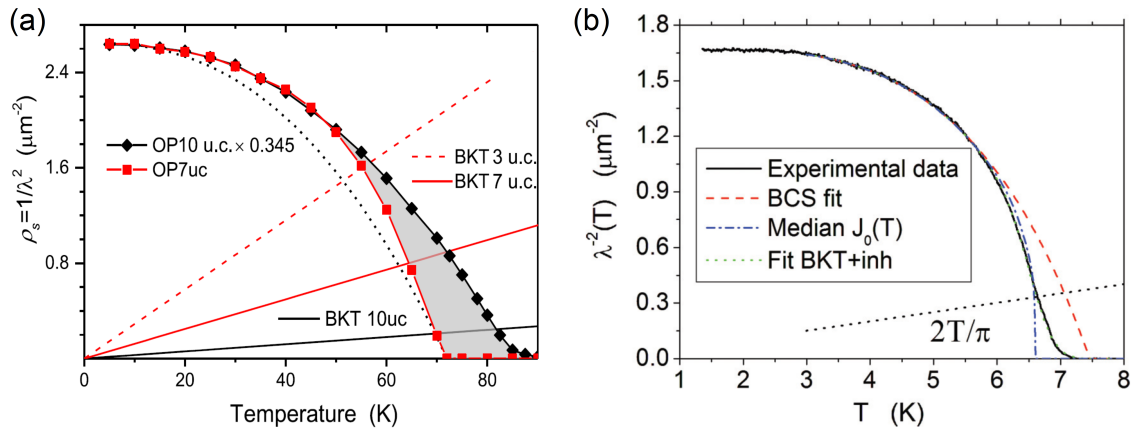

Figure 4.12 Superfluid density jump in DyBCO. (a) The superfluid density for near optimally doped 10 u.c. (black diamonds) and 7 u.c. (red squares) DyBCO films, with $\rho_s(T)$ for the 10 u.c. film scaled by 0.345. The linear dashed red, solid red, and solid black lines correspond to the expected BKT superfluid density for a 3, 7, and 10 u.c. thick superconducting layer, respectively. The black dotted curve represents the universal temperature dependence observed in Fig. 4.11(a). A superfluid jump is not observed in the OP10uc data near the intersection with the 10 u.c. BKT line, which occurs very close to T_c. On the other hand, the data for OP7uc deviates from that of OP10uc above $T \approx 50$ K, near the expected T_{BKT} for a 3 u.c. thick layer, consistent with behavior expected for enhanced thermal fluctuations in 2D. However, instead of a sharp jump, the drop of $\rho_s(T \to T_c)$ is smeared out about the intersection point with the BKT line for a 7 u.c. thick layer. This smearing behavior implies the existence of a moderate amount of T_c inhomogeneity in the film. (b) Theoretical calculations [32, 128] incorporating the effects of disorder have found that T_c inhomogeneity does indeed broaden the BKT jump near the expected average T_{BKT}, in very good agreement with our results for 7 u.c. thick DyBCO. Here, the measured superfluid density of a 2 nm thick NbN film (black line) deviates from the expected BCS response (red dashes) near T_c. A sample with a uniform superfluid stiffness energy J_0 (blue dashed-dotted line) would indeed be expected to produce a sharp jump at T_{BKT} (dotted black line). If T_c inhomogeneity is included such that the local superfluid stiffnesses J_i vary according to a Gaussian distribution about the median value J_0, then the BKT jump is smeared out above the mean T_{BKT} (indicated by the green dotted fit, which coincides with the experimental data). The superfluid density deviates from the expected BCS curve below T_{BKT} due to the vortex core energy μ (with $\mu/\mu_{XY} \approx 0.35$), as discussed in Chapter 2. Panel (b) adapted from Ref. [128].

Film ID	L (u.c./nm)	T_c (K)	σ_{dc} ($m\Omega^{-1}cm^{-1}$)	ρ_{s0} (μm^{-2})
$OP60uc^A$	60/69.6	90	10.7	19.1
$OP60uc^B$	60/69.6	84	9.7	15.6
OP40uc	40/46.4	90	10.0	16.0
OP20uc	20/23.3	82	16.4	19.9
OP10uc	10/11.7	85	5.1	7.67
OP7uc	7/8.3	72	3.6	2.65
UD20uc	20/23.6	52	1.7	1.33

Table 4.1 Nominal thicknesses L and values of T_c, zero-frequency limit of the real part of the optical conductivity at T_c, $\sigma_{\rm dc} = \sigma_1(\omega \to 0, T_c)$, and zero-temperature superfluid density $\rho_{s0} \equiv 1/\lambda^2$ obtained from the data in Fig. 4.5.

the decrease in superfluid density is rounded or smeared around the intersection point with the BKT line. This feature also cannot be due to strong disorder effects; we recall that our visible-to-UV spectroscopic ellipsometry measurements and disorder analysis imply that the electronic mean free path significantly exceeds the in-plane coherence length, $\ell/\xi_{ab} > 1$ (see the discussion around Fig. 4.3 in Section 4.1). The distribution of T_c values has a more dominant effect on the width of the superconducting transition than the distribution of defects and impurities.

Smearing or broadening of the superfluid density jump around T_{BKT} due to T_c inhomogeneity is consistent with recent theoretical calculations of Benfatto *et al.* [32,128]. These calculations treat vortex unbinding in both conventional and high-T_c superconducting thin films by mapping the BKT problem into the quantum 1D sine-Gordon model, where the vortex core energy μ is an adjustable parameter. It is found that the broadening of the superfluid density jump around T_{BKT} is determined by the width of a Gaussian distribution of T_c values that is uniformly distributed in the sample (every point in the sample is described by the same Gaussian T_c distribution). Distribution widths of just $\Delta T_c/T_c \approx 2$–8% are sufficient to fit the measured $\rho_s(T)$ data for both NbN and severely underdoped CaYBCO thin films. At the same time, the temperature at which the BKT jump occurs is determined in the theoretical model by the relative value of the vortex core energy compared to its value in the pure 2D-XY model, μ/μ_{XY}. As μ/μ_{XY} decreases the BKT transition shifts to lower temperatures than what is expected for the pure 2D-XY value of T_{BKT}. To facilitate comparison of the model with our DyBCO data we show the measured $\rho_s(T)$ for a 2 nm thick NbN film along with its theoretical fits in Fig. 4.12(b). It is apparent that the superfluid density drop in the NbN film is broadened about the intersection point of $\rho_s(T)$ with the BKT line to a very similar degree as is observed for our 7 u.c. thick DyBCO film. The data can be fit very accurately by including a small T_c distribution of just $\Delta T_c/T_c \approx 4\%$, as indicated by the coincidence of the solid black and dotted green curves. In comparison, the observed width of the superconducting transition in our near optimally doped 7 u.c. thick DyBCO film from mutual inductance measurements is $\Delta T_c/T_c \approx 3\%$. The fit of the NbN data also incorporates a vortex core energy of $\mu/\mu_{XY} \approx 0.35$, which explains the observation of the broadened superfluid density jump at a lower temperature than the intersection point of the BKT line with the usual BCS temperature dependence of $\rho_s(T)$ (red dashed curve). Similar fits of $\rho_s(T)$ in severely underdoped 2 u.c. thick CaYBCO films imply that

$\mu/\mu_{XY} \sim 2$–3 is significantly larger in the cuprates than in BCS superconductors, which indicates that the superfluid density jump should appear at a *higher* temperature than T_{BKT} expected from the 2D-XY model [32]. However, μ/μ_{XY} decreases rapidly with increasing hole doping, as shown in Fig. 2.14(b), so it is possible that near optimal doping $\mu/\mu_{XY} < 1$ in RBCO, consistent with our observation that the superfluid jump in 7 u.c. thick DyBCO is at a lower temperature than where the red BKT line intersects the black 10 u.c. data in Fig. 4.12(a). To obtain a more quantitative understanding of the role of the T_c distribution and vortex core energy in near optimally doped DyBCO it will be necessary to carry out a more detailed analysis of our data of the kind that appears in Benfatto *et al.*

4.5 BKT Transition in a Transverse Applied Magnetic Field

An important test of the presence of BKT physics in a quasi-2D system is to investigate the vortex unbinding behavior under the influence of generic perturbations in addition to temperature, such as different interlayer coupling or an applied magnetic field. These perturbations play the role of changing the effective dimensionality of the system; reducing interlayer coupling isolates individual layers while an externally applied magnetic field confines charge carriers to motion in planar orbits, thereby rendering the system more 2D-like. Since the DyBCO films investigated in this work are already in the ultrathin limit where only a few superconducting CuO_2 planes are present, we probe the effect of a magnetic field applied parallel to the c-axis on the temperature dependence of the superfluid density in the thinnest samples.

As in the case of the field-free BKT transition discussed in Chapter 2, the simple 2D-XY model can be taken as a starting point to understand the expected magnetic field dependence of vortex unbinding. The Hamiltonian of the 2D-XY model (Eq. 2.5) is easily modified to take into account the interaction between vortex excitations in the system and a transverse external magnetic field by incorporating a magnetic frustration term F_{ij},

$$\mathcal{H} = -J \sum_{\langle ij \rangle} \cos\left(\varphi_i - \varphi_j - F_{ij}\right). \tag{4.4}$$

We recall from the discussion in Section 2.2.2 that the total phase difference must be an integer multiple of 2π when the sum in Eq. 4.4 is taken over an arbitrary closed loop containing any number of lattice sites $\langle ij \rangle$. As a result, the magnetic frustration term can be defined by a sum over a single plaquette of lattice sites (the smallest possible closed loop) such that for a square lattice $F_{ij} + F_{jk} + F_{kl} + F_{li} = 2\pi H a^2/\Phi_0$, where H is the externally applied magnetic field and a is the lattice dimension of the system. Monte Carlo simulations have indicated that the stiffness modulus ρ of this system becomes suppressed as $Ha^2/\Phi_0 \to 1/2$ with an accompanying decrease of T_{BKT} [298]. Furthermore, the value of the Nelson-Kosterlitz jump becomes nonuniversal, $\rho/k_B T_{BKT} > 2m^2/\pi\hbar^2$, with increasing H. At a field strength of $Ha^2/\Phi_0 = 1/2$ it is evident that the problem of the 2D-XY model in a transverse magnetic field is formally equivalent to the problem of the long-range Ising antiferromagnet. The shift of the superfluid density jump can then be considered to be due to Ising-like excitations of the vortices in the magnetic field. However, the periodicity of the total phase and the discrete nature of the system implies that the

degeneracy of the ground state changes discontinuously with continuous variation of F_{ij}, leading to a situation where T_{BKT} is *nonmonotonic* with increasing H. Signatures of the periodic dependence of the vortex unbinding transition on H have indeed been observed in patterned arrays of Nb Josephson junctions, with a periodicity in H equivalent to Φ_0/a^2 [299]. In such micropatterned superconducting arrays the nonmonotonic behavior with H is observable because for an array with characteristic dimension $a = 1$ μm the periodicity is on the order $\Phi_0/a^2 \approx 20$ Gauss. For a cuprate thin film, on the other hand, the characteristic dimension is on the order of the in-plane lattice parameters, leading to a periodicity in H at inaccessibly high fields of $\Phi_0/ab \approx 14000$ T. This simple analysis suggests that, contrary to what is seen in patterned superconducting arrays, the magnetic field dependence in cuprate thin films should remain monotonic and proportional to H at experimentally accessible fields.

In the 2D Coulomb gas description of the BKT transition the population of free vortices is described by the Poisson-Boltzmann equation (Eq. 2.10), which takes into account the densities of vortices with right and left handed helicity, n_f^+ and n_f^-, respectively. When $H = 0$ the two densities are the same and the system is overall neutral, so $n_f^+ = n_f^- = n_f/2$ and the model is simplified to produce the results discussed in Section 2.2.2. In the presence of an externally applied magnetic field, on the other hand, $n_f^+ \neq n_f^-$ and the 2D Coulomb gas carries an effective "charge." The magnetic field dependence of the vortex interactions is therefore determined by performing a statistical analysis of the populations n_f^+ and n_f^- as a function of H. This procedure leads to the result [134]

$$\frac{\rho_s(B,T)}{\rho_s(0,T)} = \left(1 + \frac{14c}{\epsilon_{\text{eff}}\omega_0}\frac{1}{\Phi_0\kappa\sigma_{dc}^n}\frac{T_c^0 - T}{T_c^0}B\right)^{-1} \tag{4.5}$$

just below T_c, where ϵ_{eff} is the 2D Coulomb gas effective dielectric constant, ω_0 is the frequency of the probing electromagnetic field, T_c^0 is the GL mean-field transition temperature, $\Phi_0 = h/2e$ is the flux quantum, and $\kappa = \lambda/\xi_{\text{GL}}$ is the GL parameter at $T = 0$. Here, the superfluid density $\rho_s(B,T)$ is given in terms of the flux density B rather than the field H because the vortices interact with the flux that penetrates into the sample rather than the external magnetic field. In principle this would allow the critical magnetic fields of the sample to be determined but in practice the variations in sample details and disorder make the true flux penetration difficult to estimate. Nevertheless, for type-II superconductors that have a very large GL parameter κ, such as the high-T_c cuprates, the average magnetization induced in the sample by the external field is very small even for films that are only a few unit cells thick [300] and to a first approximation it is possible to take $B \approx \mu_0 H$.

In Fig. 4.13 we compare the predicted magnetic field dependence of the superfluid density in the 2D Coulomb gas model with measured values for both the near optimally doped 7 u.c. thick and 10 u.c. thick DyBCO films at two temperatures just below T_c. The solid blue line in Fig. 4.13 corresponds to Eq. 4.5 at $T = 67$ K with an effective dielectric constant $\epsilon_{\text{eff}} = 20$ estimated from the data in Fig. 4.12(a). We find that in the 10 u.c. thick sample ($T_c = 85$ K), which does not show signatures of the BKT transition, $\rho_s(H)/\rho_s(0)$ gradually decays with increasing field at $T = 78$ K but is not completely suppressed to zero at a field strength of 7 T, as shown by the open black diamonds in panel (a). At the lower temperature of 67 K, where $\rho_s(0)$ is approximately a factor of 3 larger than at 78 K, $\rho_s(H)/\rho_s(0)$ displays a similar form

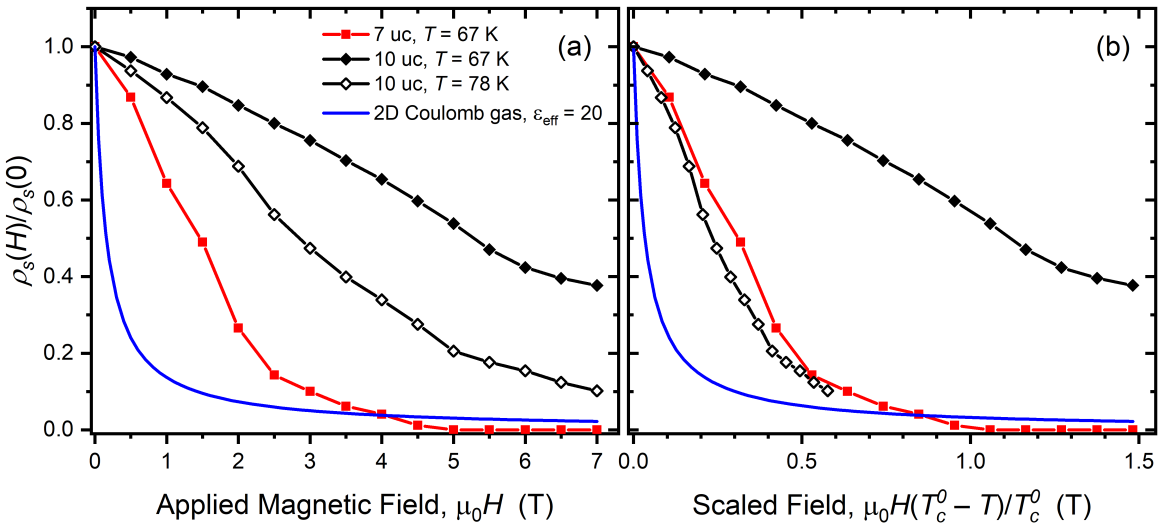

Figure 4.13 A plot of the magnetic field dependence of the superfluid density, measured at two temperatures in the vicinity of T_c for a near optimally doped 7 u.c. thick DyBCO film (red points) and 10 u.c. thick DyBCO film (black points). Panel (a) shows $\rho_s(H)/\rho_s(0)$ as a function of magnetic field applied parallel to the c-axis with $\rho_s(H)$ normalized to its zero-field value. The solid blue line corresponds to the theoretical magnetic field dependence in the 2D Coulomb gas model, Eq. 4.5, with the effective dielectric constant $\epsilon_{\text{eff}} = 20$ estimated from the data in Fig. 4.12(a). Panel (b) depicts the same data presented in panel (a), but plotted as a function of the scaled magnetic field $\mu_0 H(T_c^0 - T)/T_c^0$ in order to compare the magnetic field dependence of the two samples measured immediately below their respective T_c values.

of decay that persists to higher applied fields (filled black diamonds). In the near optimally doped 7 u.c. thick film ($T_c = 72$ K), on the other hand, $\rho_s(H)/\rho_s(0)$ decays more quickly with increasing field and is completely suppressed above $H = 5$ T. Still, the decay of $\rho_s(H)/\rho_s(0)$ occurs more weakly with increasing H than expected from the 2D Coulomb gas model despite the 7 u.c. thick film showing signatures of a smeared superfluid density jump below T_c. At $T = 67$ K the pure 2D Coulomb gas model predicts a steep drop of $\rho_s(H)/\rho_s(0)$ below ~0.5 T, whereas the measured data shows a comparable decrease over the much larger range of ~2.5 T.

To better compare the magnetic field dependence of the superfluid density in the 7 u.c. and 10 u.c. thick films just below their respective T_c values, we plot $\rho_s(H)/\rho_s(0)$ as a function of the scaled magnetic field, $H(T_c^0 - T)/T_c^0$, in Fig. 4.13(b). It is evident that the 7 u.c. sample at 67 K and the 10 u.c. sample at 78 K have the same field dependence in this case. Since at these temperatures the two samples both have an effective vortex dielectric constant of $\epsilon_{\text{eff}} \approx 20$, this implies that the quantity $\Phi_0 \kappa \sigma_{dc}^n$ is the same for both films, despite the large difference in their normal state dc conductivities (see Table 4.1). In contrast, the dependence of $\rho_s(H)/\rho_s(0)$ on the scaled field is much less steep for the 10 u.c. thick film at 67 K and is indicative of mean field behavior in the 10 u.c. sample at temperatures far below T_c. The analysis of the sample quality presented in Section 4.1 has shown that the disorder in the DyBCO films lies well below the highly disordered regime where phase fluctuations of the superconducting order parameter and vortex pinning effects are dominant. As a result, the agreement between $\rho_s(H)/\rho_s(0)$ in the 7 u.c. thick film at 67 K and the 10

u.c. thick film at 78 K suggests that the magnetic field dependence of the superfluid density just below T_c is dominated by the response of the Abrikosov vortex lattice in the mixed state, which obscures any signatures of vortex-antivortex pair unbinding. If any magnetic field signatures of the BKT transition are indeed present in ultrathin DyBCO films they are likely to lie at temperatures much further below T_c^0 where the GL phenomenology is of questionable validity.

Upon further inspection additional issues come to light regarding the comparison of the experimental data in Fig. 4.13 to the conventional 2D Coulomb gas model. First, as mentioned above, the 2D Coulomb gas model gives $\rho_s(B)/\rho_s(0)$ in Eq. 4.5 in terms of the magnetic induction B rather than the field H. This is not convenient because the Meissner screening as well as details of the sample make B difficult to determine. In fact, by computing the magnetization from the functional derivative of the free energy it is found [301] that the magnetization more properly depends upon both the vortex core energy μ and the superfluid density $\rho_s(T)$, resulting in a relationship between H and $\rho_s(H)$ that is not straightforward. Second, smearing of the BKT transition due to T_c inhomogeneity is not treated in the usual 2D Coulomb gas model, as has been discussed at length in Section 2.2. It is not clear *a priori* how the broadening of the BKT superfluid density jump will affect $\rho_s(H)/\rho_s(0)$. The sine-Gordon approach to extend the 2D-XY model, on the other hand, allows the effects of vortex core energy, T_c inhomogeneity, and coupling to external perturbations to be incorporated into the BKT physics in a clear way [138]. In the mapping of the 2D-XY model onto the 1D sine-Gordon problem, the interaction with the magnetic field is introduced into the Hamiltonian (Eq. 4.4) via the minimal coupling prescription

$$F_{ij} = \frac{2\pi}{\Phi_0}\int_i^j \mathbf{A}\cdot d\ell \approx \frac{2\pi a}{\Phi_0}\mathbf{A}_{(\hat{x},\hat{y})}(\mathbf{r}). \tag{4.6}$$

The partition function of the vortices is defined by the functional integral over a scalar field ϕ as

$$Z = \int \mathcal{D}\phi e^{-S}, \tag{4.7}$$

where ϕ depends on $\mathbf{r}$ only and the action S is given by [301]

$$S = \int \frac{d^2\mathbf{k}}{(2\pi)^2}\frac{k^2 + 2k\lambda^2/L}{2\pi K}|\phi(\mathbf{k})|^2 - \frac{g}{\pi a^2}\int d\mathbf{r}\cos(2\phi) + \frac{2i}{\Phi_0}\int d\mathbf{r}\phi\hat{z}\cdot\mathbf{H} - \int d\mathbf{r}dz\frac{\mathbf{H}^2}{8\pi k_B T}. \tag{4.8}$$

Here, the Nelson-Kosterlitz jump is represented by the superfluid density $K^{-1} = 16\pi^2 k_B T/L\Phi_0^2$ and the vortex fugacity is $g = 2\pi e^{-\mu/k_B T}$. When the action is expressed in this way we see that the effect of the transverse applied magnetic field is to shift the superfluid density and vortex core energy to "effective" values. It is expected, then, that the effect of the magnetic field on the BKT transition should be more readily visible by investigating the shape of the superfluid density jump as a function of temperature in constant field. Not only will ρ_{s0} and T_{BKT} decrease with increasing H, but the magnitude of the superfluid density jump at T_{BKT} will become nonuniversal.

The measured temperature dependence of the superfluid density for the near optimally doped 10 u.c. and 7 u.c. thick films are shown for $\mu_0 H = 0$ T and 5 T in Fig. 4.14. Panels (a) and (b) depict the absolute superfluid density measured for

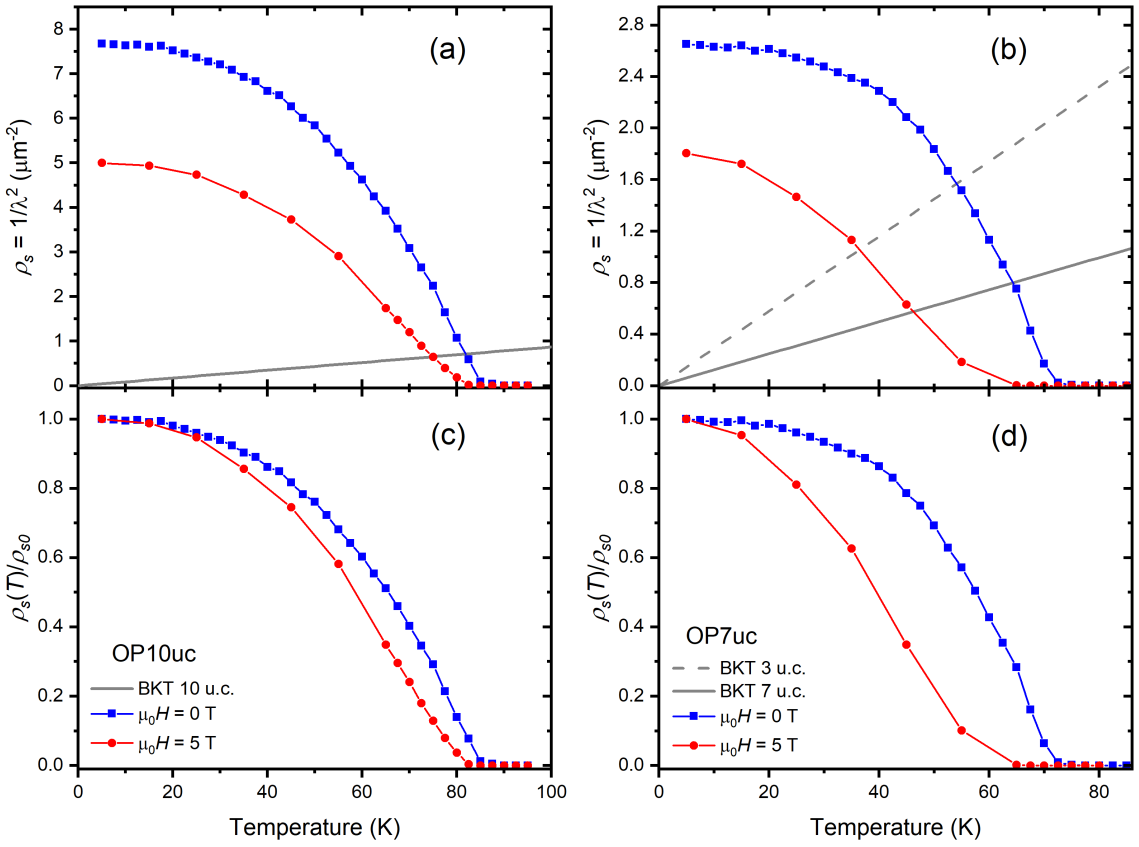

Figure 4.14 The temperature dependence of the superfluid density for the near optimally doped 10 u.c. thick DyBCO film (a, c) and 7 u.c. thick DyBCO film (b, d) with $\mu_0 H = 0$ T (blue squares) and $\mu_0 H = 5$ T (red dots). Panels (a) and (b) depict the absolute values of the measured superfluid density for both samples compared to the theoretical BKT lines for (a) 10 u.c., (b) 7 u.c., and 3 u.c. thick superconducting layers, represented by the gray solid and dashed lines. Panels (c) and (d) contain the same data as shown in panels (a) and (b), plotted as the normalized superfluid density $\rho_s(T)/\rho_{s0}$.

the two samples, respectively, and compare the measured data with the theoretical BKT lines for 10, 7, and 3 u.c. thick superconducting layers (shown in gray). Under the influence of the 5 T external transverse magnetic field the value of $\rho_s(0)$ is reduced by a similar fraction for both films compared to the 0 T value. For the 10 u.c. thick DyBCO film the BKT line crosses $\rho_s(T)$ very close to T_c, so if a BKT vortex unbinding transition exists in this sample T_{BKT} would be very near T_c and the superfluid response would be dominated by mean field behavior. Accordingly, the value of T_c is only observed to reduce by ∼2–3 K with the application of a 5 T magnetic field. In the 7 u.c. thick DyBCO film, on the other hand, the BKT lines for a 7 u.c. thick and 3 u.c. thick superconducting layer cross $\rho_s(T)$ significantly further below T_c, and T_c is observed to reduce by ∼12 K at $\mu_0 H = 5$ T. The changes in $\rho_s(T)$ with increasing H are more effectively visible by comparing the normalized superfluid density, $\rho_s(T)/\rho_{s0}$, at different magnetic field strengths as shown in panels (c) and (d). Whereas the changes in $\rho_s(T)/\rho_{s0}$ for the 10 u.c. film are minimal with the shape of the temperature dependence remaining largely unchanged, $\rho_s(T)/\rho_{s0}$ for the 7 u.c. thick film experiences a dramatic shift to lower temperatures when the transverse

magnetic field is applied. At $\mu_0 H = 5$ T the cusp of the superfluid density jump in the 7 u.c. thick film appears to occur at temperatures below 20 K.

The behavior of $\rho_s(T)/\rho_{s0}$ in the 7 u.c. thick DyBCO film is consistent with the BKT vortex unbinding transition shifting to lower temperatures as a result of a shift of the relative vortex core energy μ/μ_{XY} with increasing H. Work by Benfatto and coworkers [30–32, 137] has shown that while the width of the BKT superfluid density jump is determined by the amount of T_c inhomogeneity in a film, the temperature at which the jump occurs is set by the value of μ/μ_{XY}. A shift of the superfluid density jump to lower temperatures accompanies a reduction of the relative vortex core energy. Furthermore, in BCS superconductors the value of μ scales with the value of the energy gap Δ [137], suggesting that the strength of Cooper pair coupling governs the position of T_{BKT}. The data presented in Fig. 4.14(c, d) is in agreement with a picture based on this analysis; the transverse applied magnetic field acts to break Cooper pairs and reduce Δ, leading to a reduction of μ/μ_{XY} and downward shift of T_{BKT} with increasing H. The strong shift of $\rho_s(T)/\rho_{s0}$ in the 7 u.c. thick film, but not the 10 u.c. thick film, provides additional evidence that the BKT vortex unbinding transition is indeed present in 7 u.c. thick DyBCO. As in the case of the field-free BKT transition discussed in Section 4.4, a theoretical analysis and treatment of our data with the model of Benfatto *et al.* is necessary to determine the quantitative value of μ/μ_{XY}. Additionally, future work is needed to obtain $\rho_s(T)/\rho_{s0}$ at other magnetic field strengths in order to obtain the full magnetic field dependence of the vortex core energy. Such measurements would help to further validate the sine-Gordon extension of the 2D-XY model and shed additional light on the nature of Cooper pair coupling in the cuprates.

4.6 Role of the Substrate Interface Layer

From our analysis of the complex conductivity and superfluid density in the DyBCO films we have obtained very accurate measurements of the dc conductivity, $\sigma_{\rm dc} = \sigma_1(\omega \to 0, T_c)$, and zero-temperature superfluid density, ρ_{s0}, in the full set of both near optimally doped and underdoped (annealed) samples. The results of these measurements are summarized in Table 4.1 along with the nominal DyBCO layer thickness L and critical temperature T_c. With these values in hand, it is possible to explore different scaling laws or correlations between the physical quantities. One of these scaling relations, $\rho_{s0} \propto \sigma_{\rm dc} T_c$, points to the presence of a non-superconducting 4 u.c. thick layer that persists at the interface of the film with the substrate.

Early after the discovery of high-temperature superconductivity in the cuprates, it was found from muon spin relaxation experiments that in underdoped cuprates the muon spin relaxation rate, which is proportional to the superfluid density n_s/m^*, was proportional to T_c [302]. It is now well known that this scaling law, $\rho_{s0} \propto T_c$, is not valid at all near optimal doping or in overdoped cuprates even though it works well on the underdoped side of the phase diagram. On the other hand, Homes *et al.* showed [27] from measurements of the infrared reflectivity that the scaling relation $\rho_{s0} \propto \sigma_{\rm dc} T_c$ is obeyed in all cuprate families, including underdoped, overdoped, highly disordered, and electron doped samples, across more than four orders of magnitude in both ρ_{s0} and $\sigma_{\rm dc} T_c$. This empirical relationship makes intuitive sense in optical experiments because the spectral weight shift that participates in the formation of the

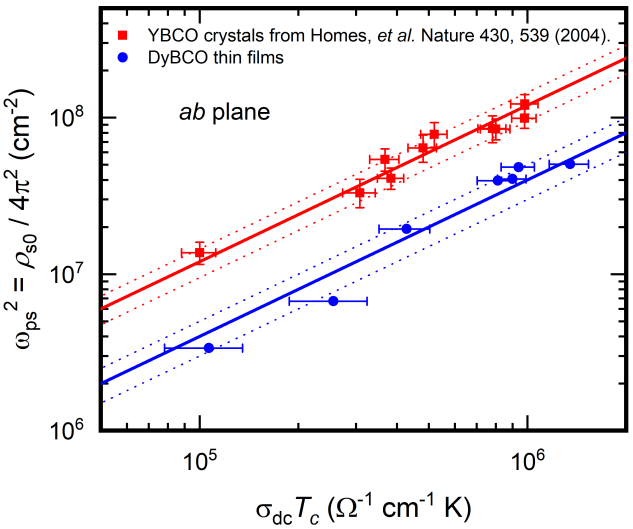

Figure 4.15 A log-log plot of Homes' scaling law, $\rho_{s0} \propto \sigma_{\rm dc} T_c$, for several YBCO single crystals from Homes *et al.* [27] (red squares) and the DyBCO thin films studied in this thesis (blue circles). All data points shown correspond to measurements in the *ab* crystallographic plane. The YBCO single crystal data (which includes underdoped, optimally doped, and overdoped samples in addition to (Pr,Y)BCO crystals and radiation damaged crystals) falls on the line $\omega_{ps}^2 = (120 \pm 25)\sigma_{\rm dc} T_c$ (red solid and dashed lines). The DyBCO thin films are also observed to obey a Homes scaling law but fall on the line $\omega_{ps}^2 = (40 \pm 10)\sigma_{\rm dc} T_c$, significantly below the single crystal data. The superfluid density is plotted as $\omega_{ps}^2 = \rho_{s0}/4\pi^2$ since $\rho_{s0} \equiv \lambda^{-2}$.

superconducting state comes mostly from frequencies below 2Δ, and $\Delta \propto T_c$. In this way $\rho_{s0} \propto \sigma_{\rm dc} T_c$ is a consequence of the statement that the FGT sum rule is obeyed. However, Homes' scaling law has interesting implications. From simple dimensional analysis considerations [28] the law implies that the T_c in cuprates is high because the normal state just above T_c is characterized by large "Planckian" dissipation, where the scattering rate approaches $1/\tau(T_c) \sim k_B T_c/\hbar$. Furthermore, the original report of Homes' law [27] only contained information about the scaling behavior in single crystal samples. It is not yet clear if the scaling relation should hold in thin film samples due to effects such as interfacial scattering or reduced dimensionality.

Figure 4.15 shows a log-log plot of the square of the superconducting plasma frequency, $\omega_{ps}^2 = \rho_{s0}/4\pi^2$, versus $\sigma_{\rm dc} T_c$ for all DyBCO films studied in this thesis in addition to data for several YBCO crystals taken from Homes *et al.* [27]. The YBCO samples include pristine optimally doped crystals, underdoped and overdoped crystals, radiation damaged crystals, and (Pr,Y)BCO crystals. Each of the YBCO data points (red squares) are observed to lie along the line $\omega_{ps}^2 = (120 \pm 25)\sigma_{\rm dc} T_c$. The constant $120 \pm 25\ \Omega\,{\rm cm}^{-1}{\rm K}^{-1}$ is considered to be universal for single crystals; *c*-axis superfluid density, iron pnictide superconductors, and the BCS superconductors Nb and Pb also lie on this line [9] (not shown). Our data for the DyBCO thin films, including both near optimally doped and underdoped samples, are likewise observed to obey Homes scaling $\rho_{s0} \propto \sigma_{\rm dc} T_c$, a result that is expected because we have shown in Section 4.3 that the FGT sum rule is satisfied in our samples to within $\pm 0.2\%$. However, the DyBCO thin films lie along the line $\omega_{ps}^2 = (40 \pm 10)\sigma_{\rm dc} T_c$, significantly below the data for the single crystals. The "universal" scaling constant is a factor of

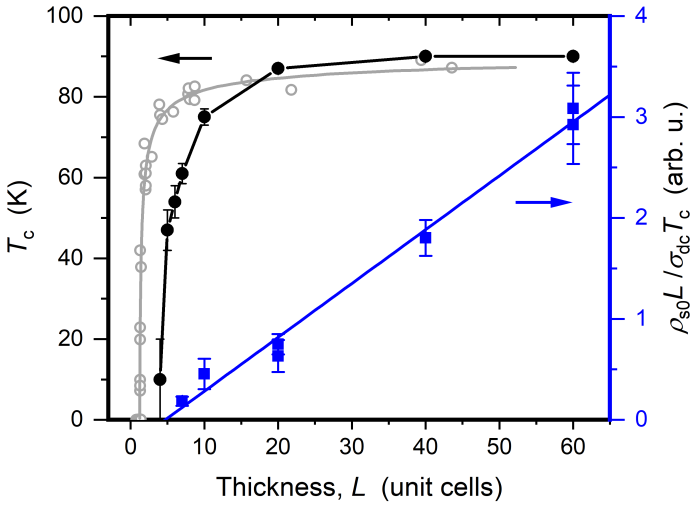

Figure 4.16 The thickness dependence of T_c of the DyBCO films (solid black circles, left axis) as determined by MI measurements [273]. Samples thinner than 5 u.c. were unstable and displayed a broad $\mathrm{Im}\,\mathrm{MI}(T)$ peak close to $T = 0$. The open gray circles represent the T_c of YBCO layers of thickness L sandwiched between a 1000 Å buffer layer and 200 Å capping layer of PrBCO on yttria stabilized zirconia and MgO substrates from Chan *et al.* [270]. The trend line of the PrBCO/YBCO/PrBCO data (solid gray curve) drops to $T_c = 0$ at $L = 1$ u.c. Also plotted as a function of thickness is the quantity $\rho_{s0}L/\sigma_{\mathrm{dc}}T_c$, which represents a measure of the effective superconducting layer thickness (blue squares, right axis). This trend of this quantity intersects 0 at $L \approx 4$ u.c.

3 smaller than what is observed in single crystals, which implies that the fraction of electrons that condense into the superconducting state in the films is fully one third less than the fraction that condense in crystals.

It remains plausible that our DyBCO films are not uniformly superconducting throughout their entire thickness and that up to two thirds of the total sample volume remains in the normal state far below T_c. To investigate this possibility we examine the dependence of the critical temperature on thickness L of the films, as illustrated in Fig. 4.16, and find that T_c drops rapidly to zero near $L = 4$ u.c. (solid black circles) [273]. We also plot the quantity $\rho_{s0}L/\sigma_{\mathrm{dc}}T_c$ versus L because the variation in interfacial and impurity scattering exhibited by the films (demonstrated by the variety of conductivity peak widths and amplitudes in Fig. 4.5(a)) means that we cannot directly draw a comparison between ρ_{s0} and L. Here, $\rho_{s0}L/\sigma_{\mathrm{dc}}T_c$ is a measure of the effective superconducting layer thickness (a universal Homes constant doesn't appear in the ratio so it is *proportional* to the effective layer thickness). As can be seen from the blue squares in Fig. 4.16, the effective superconducting layer thickness extrapolates to zero at $L \approx 4$ u.c., in agreement with the film thickness where T_c drops precipitously to zero. This behavior suggests that a 4 u.c. thick non-superconducting layer persists at the film-to-substrate interface in all our DyBCO samples. In the near optimally doped 7 u.c. thick film a 3 u.c. superconducting layer remains, which approaches the threshold for 2D superconducting fluctuations to emerge. Accordingly, we plot a BKT line corresponding to a 3 u.c. thick layer (red dashed line) in Fig. 4.12(a). Assuming that ρ_{s0} also needs to be renormalized to take into account the effective thickness of the superconducting layer, this BKT line serves as a lower bound on the value of T_{BKT} for the vortex unbinding transition in 7 u.c. thick DyBCO.

The 4 u.c. thick non-superconducting interfacial layer plays the role of the semiconducting (Pr,Y)BCO buffer layers used in previous studies of ultrathin superconducting YBCO films to adapt the orthorhombic film structure to the square lattice of the underlying substrate [21, 175, 176, 181, 270, 303]. A minimum (Pr,Y)BCO buffer layer thickness of 4–5 u.c. has been observed to be required to relax the epitaxial strain that is caused by the substrate in order to observe superconductivity in a 1 u.c. thick YBCO layer that lies on top [169, 265, 303]. Fig. 4.16 illustrates that the DyBCO interfacial layer plays this role by comparing $T_c(L)$ for our films with $T_c(L)$ for YBCO films grown epitaxially on top of 1000 Å thick PrBCO buffer layers (open gray circles) [270]. Due to the presence of the thick PrBCO buffer the YBCO films are fully relaxed and their T_c drops to zero only below $L = 1$ u.c. The functional dependence of the two data sets match, but $T_c(L)$ for the DyBCO films is shifted to higher thicknesses from the YBCO data by $L \approx 4$ u.c. The XRD data summarized in Fig. 4.1 likewise shows that the structure of the DyBCO films smoothly becomes less orthorhombic as thickness is reduced but that an appreciable tetragonal component only appears below ∼10 u.c. As a result, we find that it is possible to achieve strain relaxation in an ultrathin DyBCO film while leaving the layers above superconducting with CuO chains intact and a high T_c without the need for PrBCO buffers. This is advantageous because it allows extraneous impurities such as magnetic Pr ions to be eliminated from the system.

Previous studies characterizing the MBE growth of ultrathin DyBCO films [273] reported that the interfacial layer is non-superconducting because the substrate-induced strain effects lead to CuO chain disorder and an oxygen vacancy distribution that relaxes to the bulk properties within ∼5–7 u.c. However, in all our near optimally doped samples independent of thickness, including the 7 u.c. thick film, the 4 eV absorption peak associated with CuO chain vacancies is entirely absent from the visible-to-UV spectroscopic ellipsometry data (see Fig. 4.2(a)). This suggests that the films are uniformly oxygenated. While it is possible that macroscopically tetragonal films accommodate excess oxygen in chain segments comprising only a few atomic sites, a nonuniform oxygen vacancy distribution would instead give rise to a partially developed 4 eV peak in the effective medium response, which is not seen. The large values of T_c and small values of ΔT_c further indicate that T_c is relatively uniform because a thickness dependent oxygen vacancy distribution would lead to a broad range of T_c values extending to very low temperatures and a large value of ΔT_c. This result therefore implies that an epitaxially induced oxygen vacancy distribution cannot be primarily responsible for the origin of the non-superconducting layer. Instead, the spectroscopic ellipsometry data and small ΔT_c values imply that the non-superconducting interfacial layer shares a sharp boundary with the superconducting portion of the films, which points to a scenario of phase separation and an alternate origin for the lack of superconductivity in the 4 u.c. thick layer.

One possibility is that epitaxially stabilized competing order, such as charge density wave correlations (which universally exist in cuprate high-temperature superconductors [3]), may be present and suppress superconductivity. Recent resonant X-ray scattering measurements on underdoped YBCO films grown epitaxially on $SrTiO_3$ substrates indicate that epitaxial strain can stabilize 3D charge order, with the Cu sites in the CuO chain layers participating in the charge ordered state [61]. In that work, the apparent lack of competition between 3D charge order and superconductivity was interpreted as possible evidence of mesoscopic phase separation between

regions hosting the charge ordered and superconducting states. It is therefore possible that the 4 u.c. thick interfacial layer in DyBCO films represents an intrinsic charge ordered but non-superconducting region. However, the YBCO films in which the 3D charge order was observed were in the more moderately underdoped regime with $T_c \sim 50$ K, whereas our DyBCO films are closer to optimal doping (the 7 u.c. film shows $T_c = 72$ K). Charge ordering in the cuprates is also typically associated with insulating rather than metallic behavior.

The presence of the 4 u.c. thick non-superconducting interfacial layer is consistent with the discrepancy of the 7 u.c. thick DyBCO film from the universal Homes scaling shown by the solid red line in Fig. 4.15, where the density of superconducting electrons in the DyBCO films appears to be one-third of its value in cuprate single crystals. By rescaling the superfluid density to take into account the reduction in superconducting volume of the film, the data point for the 7 u.c. thick sample can be made to roughly agree with the red universal Homes scaling line. However, for thicker DyBCO films this procedure does not completely hold. In the near optimally doped 60 u.c. thick films, for example, the 4 u.c. thick interfacial layer comprises only $\sim$7% of the total sample volume, implying that the superfluid density would need to correspond to a London penetration depth of $\lambda \sim 130$ nm to agree with the red line. Such a low value of λ is comparable to the smallest values reported for ultraclean YBCO single crystals from muon spin rotation and infrared techniques [304, 305], and therefore, given that all our films lie in the moderate disorder regime, is not likely to be the true value. Instead, for the DyBCO thin film data to agree with the universal Homes scaling, the blue DyBCO data points need to shift left to lower values of $\sigma_{\rm dc}T_c$, which implies that the non-superconducting portion of the films is *metallic* rather than insulating. As a result, our findings may be related to recent reports of an anomalous bosonic metal state in 10 u.c. thick superconducting YBCO films [306]. In this exotic state Cooper pairs are observed to exhibit 2D metallic behavior in a narrow range at the transition between superconducting and insulating states due to fluctuations near a disorder-induced quantum critical point. While the disorder level in our films is far from the regime where strong disorder-induced fluctuations become dominant (see the discussion in Section 4.1), it may be the case that epitaxially induced disorder is enough to place only the first 4 u.c. of DyBCO into the quantum critical regime, leaving the rest of the unit cells lying above at moderate disorder levels. In any case, the discrepancy of the observed Homes scaling between the DyBCO films and cuprate single crystals by a factor of 3 is puzzling, especially because films 10 u.c. and thicker have been shown to lie in the 3D-XY universality class. Further studies of epitaxial RBCO thin films are needed to clarify whether the different Homes scaling is indeed a general feature of thin film cuprates, as well as to elucidate the full nature of the non-superconducting interfacial layer.

Chapter 5

Summary and Conclusion

Our contemporary understanding of high-temperature superconductivity paints a remarkably detailed and colorful picture of the physics of copper oxides. The scientific progress of the past 35 years has made it clear that a complete elucidation of high-T_c superconductivity must extend far beyond a description of the superconducting state itself to include a firm understanding of strongly correlated electron materials as a whole. It is now widely accepted that superconductivity in the copper oxides is only one of many forms of intertwined order, with crystal structure, dimensionality, and various electron interactions conspiring to produce a rich phase diagram [3]. Nevertheless, despite the existence of a vast body of published literature, there is not yet any generally agreed-upon microscopic explanation of the mechanism of high-T_c superconductivity that is on par with the BCS theory for conventional superconductors. The scientific literature instead presents a multitude of clues that point in often contradictory directions.

The study of empirical scaling laws between various observable parameters offers an intuitive route toward mapping out the interplay of the many interactions in strongly correlated electron materials. One such scaling law for superconductors, known as Homes' law, states that the density of superconducting electrons is proportional to the product of a material's normal-state dc conductivity and its T_c [27]. By simple dimensional analysis considerations this implies that the critical temperature is high in the cuprates as a consequence of "Planckian" dissipation, where the quasiparticle damping is of the order $k_B T/\hbar$ [28]. Furthermore, the validity of Homes' law for a wide variety of superconducting materials, including both conventional and unconventional superconductors, points to the importance of optical conductivity sum rules, and in particular implies that the Ferrell-Glover-Tinkham sum rule is obeyed in the cuprates. However, optical data and spectral weight analyses from various groups based on infrared reflectivity and spectroscopic ellipsometry measurements allow conflicting conclusions to be drawn, which leaves open the possibility that the FGT sum rule and two-fluid model are instead violated [14, 16]. A gap in phase resolved conductivity data in the terahertz portion of the spectrum has contributed to this experimental uncertainty by leading to ambiguity in the interpretation of the low frequency optical data, where a significant fraction of the spectral weight is understood to shift in the superconducting transition. This uncertainty has led to an influential class of theories of high-T_c superconductivity based on a kinetic energy saving pairing mechanism [12, 13]. In this thesis, we address the question of the validity of the FGT sum rule in the cuprates by combining several fully phase-resolved

spectroscopy techniques in order to precisely follow the evolution of the intraband spectral weight across the superconducting transition. The results presented here avoid the ambiguities contained in previously reported studies by accessing the full spectrum from submillimeter to visible without need for Kramers-Kronig relations or model-dependent assumptions.

As a first step, we present a detailed analysis of the film quality and disorder in a series of near optimally doped and underdoped $DyBa_2Cu_3O_{7-\delta}$ thin films, which were grown with varying thicknesses by atomic layer-by-layer oxide MBE. Many prior studies of cuprate thin films in the *R*BCO family utilized (Pr,Y)BCO buffer layers to stabilize and adapt the crystal structure of the thin films to the underlying substrate lattice. However, the Pr ion contributes to pair breaking, magnetic ordering, and charge localization [39], and so complicates the interpretation of the nature of the superconducting state. By contrast, the DyBCO films studied in this work were grown epitaxially on LSAT without any kind of Pr buffer layer. High resolution XRD measurements show that near optimal doping the films become increasingly tetragonal in structure as a function of decreasing thickness below 60 u.c. to adapt to the square lattice of the LSAT. At a thickness ∼10 u.c. and below the structure of the optimally doped films is nearly fully tetragonal and comparable to the structure of an annealed (underdoped) 20 u.c. thick film. Despite this similarity, spectroscopic ellipsometry measurements in the visible-to-UV range for the full series of films reveal that the 4 eV peak in $\epsilon_2(\omega)$, which is observed in the underdoped 20 u.c. film and corresponds to empty CuO chains, is entirely absent in near optimally doped DyBCO films even in the thinnest samples studied. This result indicates that near optimal doping films as thin as 7 u.c. retain their CuO chains, and rules out a scenario where the epitaxially induced strain produces an oxygen vacancy distribution along the *c*-axis that strongly reduces T_c. Furthermore, the mean free path $\ell \approx 30$ Å in the thinnest films is significantly larger than the in-plane coherence length $\xi_{ab} \approx 13$ Å, implying that the effect of disorder and scattering is not dominant and that T_c inhomogeneity has a larger effect on the superconducting properties. Our analysis of ΔT_c and the dc resistivity in the films finds that the T_c inhomogeneity remains in the linear regime where $\Delta T_c \propto \varrho_{\mathrm{dc}}$. On this basis we conclude that the DyBCO thin films studied in this work remain only moderately disordered, well below the strong disorder regime where T_c becomes dominated by quantum phase fluctuations of the superconducting order parameter.

Second, we turn to phase sensitive measurements of the complex conductivity to address the issue of spectral weight transfer in the cuprates. Specifically, we combine measurements from submillimeter quasioptical interferometry, time-domain terahertz spectroscopy, and spectroscopic ellipsometry to obtain the full complex response of the DyBCO films in the spectral range 0.1 meV $< \hbar\omega <$ 1 eV without need for Kramers-Kronig transforms. Still, a Kramers-Kronig consistency analysis of the independently extracted data is employed in order to precisely follow the spectral weight shift across the superconducting transition. With this technique we show that both the FGT sum rule and two-fluid model are obeyed in the cuprates to within ±0.2% error. This result implies that the peak in $\sigma_1(\omega)$ that occurs just below T_c and at frequencies below 1–2 THz cannot be due to coherence effects, as is the case in conventional BCS superconductors. Instead, the conductivity peak arises from competition between a decreasing normal charge carrier density and increasing quasiparticle lifetime below T_c. Our observation of this so-called "γ-conductivity" peak is further evidence that the dominant

scattering mechanism in the DyBCO films at low temperatures is electronic rather than phononic or from disorder effects, and implies that the quasiparticles are coupled to an excitation spectrum that is modified in the superconducting state.

Our study of the spectral weight shift both above and below T_c indicates that superconductivity in the copper oxides cannot be due to a kinetic energy saving mechanism. At $T < T_c$ we find that the total intraband spectral weight is constant as a function of temperature, with any changes in the normal state (Drude) spectral weight precisely compensated by changes in the superconducting δ-function at $\omega = 0$. This means that interband transitions lying at $\hbar\omega > 1.5$ eV do not contribute to any transfer of spectral weight in the superconducting state; the FGT sum rule and two-fluid model are governed by changes in the intraband spectral weight only. Above T_c, on the other hand, the Kramers-Kronig consistency analysis shows that the spectral weight below 1.5 eV increases by $\sim$2% between 200 K and T_c. Since any changes in spectral weight above T_c are due to smearing of the Fermi occupation function around the Fermi level with temperature, the constant intraband spectral weight below T_c implies that there is a slight reduction in spectral weight of the superconducting state compared to the $T = 0$ spectral weight of the normal state. As a result, we conclude that scenarios of high-T_c superconductivity based on the reduction of kinetic energy are untenable, in agreement with the prior reported results of Boris *et al.* [16]. Our findings are instead consistent with collective boson models of superconductivity where fermions interact with collective spin fluctuations [17].

The remainder of the results reported in this thesis focus on an expanded view of high-T_c superconductivity in the cuprates to include some more general aspects of the physics of strong correlations. Various models of strong correlations in 1D and quasi-1D have largely been solved, but so far solutions in higher dimensions have not been found. Nevertheless, the solutions of the quasi-1D strong correlation problem are well understood where an array of intertwined ordered phases emerges from non-Fermi liquids [4]. Results of these models in 1D can give insight into the behavior of 2D and 3D strongly correlated electron systems. There is evidence that the variety of intertwined orders emerge as "daughter" phases of a more fundamental parent phase in the cuprates, which spontaneously breaks a large number of symmetries. Such evidence, however, is not yet definitive and still widely debated. It is expected that a larger variety of intertwined orders will exist in 2D rather than 3D because topological effects allow a multitude of phases to emerge that would otherwise be energetically prohibited in higher dimensions. Developing a more complete experimental description of the cuprates in 2D, therefore, is key to a better understanding of this interplay. In particular, knowledge of the Berezinskii-Kosterlitz-Thouless transition and phase excitations across the full superconducting dome is needed in order to understand how superconductivity interacts with the various types of fluctuations that occur throughout the phase diagram. Until recently, experimental studies of the superconducting BKT transition in cuprates primarily focused on the underdoped side of the phase diagram where the pseudogap and quantum critical fluctuations approaching the underdoped quantum critical point (p_{min}) play a dominant role.

In this thesis we report studies of the BKT vortex unbinding transition near optimal doping in ultrathin DyBCO films upon approaching the 2D limit. Because we have shown that the FGT sum rule and two-fluid model are obeyed in the cuprates, we take advantage of our wide band spectroscopy data to obtain highly accurate measurements of the superfluid density as a function of temperature and magnetic

field. This approach allows us to avoid the vortex pinning effects that are a general feature of mutual inductance experiments and which obscure the underlying vortex-antivortex unbinding behavior. We find that near optimal doping, DyBCO films 10 u.c. and thicker display a "universal" temperature dependence of the superfluid density that is consistent with 3D-XY scaling behavior across a wide temperature range down to $\sim 0.8T_c$. As $T \to 0$ the superfluid density rolls over to a characteristic T^2 dependence that is consistent with the presence of only moderate disorder in the films. In underdoped (annealed) samples, the superfluid density is instead linear with temperature just below T_c, which is in agreement with a crossover from 3D-XY to $(3+1)$D-XY critical behavior as the critical doping p_{min} is approached on the underdoped side of the phase diagram.

The exact shape of the superfluid density temperature dependence depends on the specifics of the Fermi surface topology in addition to the details of the disorder. The data for an underdoped 20 u.c. thick film agrees well with calculations based on the realistic tetragonal Fermi surface of LSCO obtained from ARPES measurements [281]. The superfluid density of the near optimally doped 10 u.c. thick film, on the other hand, follows the temperature dependence of the orthorhombic Fermi surface shape despite XRD measurements which indicate that the structure of the 10 u.c. film has adapted to the tetragonal structure of the LSAT substrate. This is further evidence for the presence of intact CuO chains in the thinnest near optimally doped samples. Theoretical calculations based on the realistic Fermi surface of DyBCO are needed to quantify this difference.

Below a thickness of 10 u.c. we observe signatures of the BKT superfluid density jump in the data for the near optimally doped films. Specifically, we observe a steepening of the normalized superfluid density $\rho_s(T)/\rho_{s0}$ above $\sim$50 K as T approaches T_c in a 7 u.c. thick film. This steepening is consistent with a broadened superfluid density jump due to the presence of T_c inhomogeneity. Furthermore, the cusp of the superfluid density jump near 50 K occurs at temperatures well below the crossing point of $\rho_s(T)$ and the BKT line for a 7 u.c. thick layer, which suggests that the relative vortex core energy $\mu/\mu_{XY} \lesssim 1$ in optimally doped DyBCO. For comparison, the value of the relative vortex core energy is $\sim$3 on the strongly underdoped side of the phase diagram in (Ca,Y)BCO [32]. The presence of a BKT vortex pair unbinding transition in the thinnest sample was further probed in a c-axis (transverse) magnetic field. Our data for the magnetic field dependence of the superfluid density $\rho_s(H)/\rho_s(0)$ suggests that the conventional 2D Coulomb gas model is insufficient to properly capture the full BKT physics in the cuprates because it does not provide a straightforward way to treat the flux penetration of the externally applied magnetic field or the effects of T_c inhomogeneity. Instead, the temperature dependences $\rho_s(T)/\rho_{s0}$ of the two thinnest films (10 u.c. and 7 u.c.) in a constant applied transverse magnetic field are qualitatively consistent with the mapping of the 2D-XY model to the 1D sine-Gordon problem by Benfatto *et al.* [30, 31, 301], where the applied magnetic field modifies the relative vortex core energy. Further magnetic field measurements and model calculations are needed to provide a more quantitative analysis.

With the values of T_c, $\sigma_{\rm dc}(T_c)$, ρ_{s0}, and thickness L in hand from our various analyses, we finally circle back and once again address the empirical scaling laws in ultrathin DyBCO films. While the universal Homes' scaling $\rho_{s0} \propto \sigma_{\rm dc} T_c$ is well known for single crystals, it remains largely unexplored in copper oxide thin films. We report

here that ultrathin DyBCO films also obey a Homes' scaling relationship, which is expected because our Kramers-Kronig consistency analysis shows that the FGT sum rule is valid, but that the scaling constant is smaller by a factor of 3 compared to single crystals. By following the thickness dependence of both T_c and a measure of the effective superconducting fraction, we find that both quantities reach zero together at $L \sim 4$ u.c. Our results suggest that there is a $\sim$4 u.c. thick non-superconducting layer at the interface between film and substrate. This interface layer plays the role of the (Pr,Y)BCO buffer layers used in previous studies to adapt the *R*BCO structure to the underlying substrate. We therefore find that it is possible to achieve strain relaxation in ultrathin *R*BCO without need for PrBCO layers. However, as we pointed out above, an epitaxial strain-induced oxygen vacancy distribution cannot be the cause of the non-superconducting layer, because visible-to-UV spectroscopic ellipsometry data indicates the presence of intact CuO chains in film thicknesses down to 7 u.c. with no detectable admixture of empty chain structures. Instead, the ellipsometry results and small ΔT_c values point to the existence of a sharp interface between superconducting and non-superconducting regions of the films and a scenario of electronic phase separation. The nature of this non-superconducting layer remains unidentified, but we propose that it may be consistent with a picture in which moderate epitaxially induced disorder places only the first few unit cells of a film into a disorder-induced quantum critical regime, where Cooper pairs exhibit 2D metallic ("bosonic metal") behavior at the transition between superconducting and insulating states.

Appendices

Appendix A

Terahertz Time-Domain Spectrometer Components

This Appendix contains detailed discussion of the main components of the TTDS spectrometer apparatus utilized in this work. Sections are included that focus on the principles of terahertz generation by photoconductive antennas, spherical antenna lenses, the fundamentals of the electrooptic effect, negative dispersion mirror pairs used for laser pulse compression, dry nitrogen purgebox, and the liquid helium bath cryostat for low temperature measurements.

A.1 Photoconductive Antennas

Photoconductive antennas consist of metallic dipole structures micropatterned onto a doped semiconducting wafer that has a band gap chosen to match the energy $\hbar\omega$ of the near-IR femtosecond excitation laser [307]. They generate terahertz pulses by taking advantage of second-order nonlinear processes to rectify the femtosecond optical pulse train. The most common wafer type is low-temperature grown GaAs because its optical band gap of $E_g \approx 1.42$ eV lies just below $\hbar\omega \approx 1.55$ eV of 800 nm laser light, and its index of refraction in the far-IR makes it mosly transparent to terahertz radiation [308, 309]. Additionally, it has a lower carrier relaxation time and higher carrier mobility than other common wafer types, such as radiation-damaged silicon on sapphire [245, 310]. The metallic microstructure is usually patterned from gold with a small gap of $d = 5$–20 μm separating the positive and negative bias terminals. The near-IR femtosecond laser is focused into a small spot of diameter $\sim$5 μm at the center of the gap; when the near-IR laser pulses impinge upon the dipole structure they excite charge carriers across the semiconductor band gap and the electrical circuit formed by the antenna and an external power source is closed. The power source is set to supply a dc bias of 10–20 V so the creation of the charge carriers creates a sudden burst of current that persists for timescales on the order of tens of picoseconds. Since the electric field radiated by the dipole is proportional to the time derivative of the current burst, the emitted terahertz pulse persists for just 100 fs to a few picoseconds, often including only a single or sometimes even half an oscillation period. The shape of the dipole and bias terminal leads also affects the shape of the emitted terahertz pulse. For this reason the shape of the patterned antenna is calculated in order to minimize spatial or frequency distortions or even

amplify the emission in certain portions of the spectrum. The most common antenna shapes include H-shaped, bowtie, or spiral leads, but large area patterns such as interdigitated finger antennas and micro-dipole arrays are also utilized in order to make more complete use of the full semiconducting wafer surface to obtain higher output powers.

The output spectrum of a simple dipole antenna can be modeled with Maxwell's equations and a simple description of the photoexcited carriers in the semiconductor using the Drude model. The electric field radiated by an oscillating dipole with dimensions $d \ll \lambda$ is given by [203]

$$\mathbf{E_{rad}}(\omega) = \left[\frac{\omega^2}{c^2}(\hat{r} \times \mathbf{p}) \times \hat{r}\frac{e^{i\omega r/c}}{r} + (3\hat{r}[\hat{r} \cdot \mathbf{p}] - \mathbf{p})\left(\frac{1}{r^3} - \frac{i\omega}{cr^2}\right)e^{i\omega r/c}\right], \tag{A.1}$$

where $\hat{r}$ is the unit vector in the direction of observation, $\mathbf{p}$ is the electric dipole moment vector, and r is the distance from the dipole. If we take the electric field to be a purely transverse wave and utilize the property that the field can be written as a sum of its Fourier components, then the vector component of $\mathbf{E_{rad}}$ perpendicular to the direction of propagation $\hat{r}$ in the time domain is

$$\tilde{E}_{\mathrm{rad}}(r, \theta, t) = \left(\frac{1}{r^3} + \frac{1}{cr^2}\frac{d}{dt} + \frac{1}{c^2 r}\frac{d^2}{dt^2}\right)\tilde{p}(t_r)\sin\theta, \tag{A.2}$$

where θ is the angle between $\mathbf{p}$ and $\hat{r}$, and $t_r = t - r/c$ is the retarded time. Since the dipole dimensions are in the far-field limit, where $d \ll \lambda \ll r$, the radiated electric field reduces to

$$\tilde{E}_{\mathrm{rad}}(r, \theta, t) = \frac{1}{c^2 r}\frac{d^2}{dt^2}\tilde{p}(t_r)\sin\theta. \tag{A.3}$$

The dipole moment is $\mathbf{p} = \int \rho(\mathbf{r})\mathbf{r}d^3\mathbf{r}$, where $\rho(\mathbf{r})$ is the charge density, so by comparison with the continuity equation the radiated electric field is proportional to the first time derivative of the free current density $J(t)$. The free current in the dipole is itself given by [311]

$$J(t) = qn(t)v(t) \tag{A.4}$$

where q is the charge of the carriers, $n(t)$ is the density of free carriers, and $v(t)$ is their velocity. The number of free carriers is determined by the generation rate $G(t)$ of carriers excited across the semiconductor band gap by the femtosecond near-IR laser pulse, and the trapping time τ_T of carriers becoming trapped by mid-gap impurity states,

$$\frac{d}{dt}n(t) = -\frac{n(t)}{\tau_T} + G(t). \tag{A.5}$$

The generation rate is proportional to the intensity of the femtosecond laser pulse envelope, which can be approximated by a transform-limited Gaussian as

$$G(t) \propto I_0 e^{-4\ln 2(t/\tau_L)^2}, \tag{A.6}$$

where τ_L is the full-width at half-maximum and I_0 is the peak intensity of the laser pulse. As discussed above in Section 3.1.2, in the Drude model the velocity of the free charge carriers is determined by the scattering time τ_S and the value of the local electric field in the antenna,

$$\frac{d}{dt}v(t) = -\frac{v(t)}{\tau_S} + \frac{qE_{\mathrm{local}}(t)}{m^*}. \tag{A.7}$$

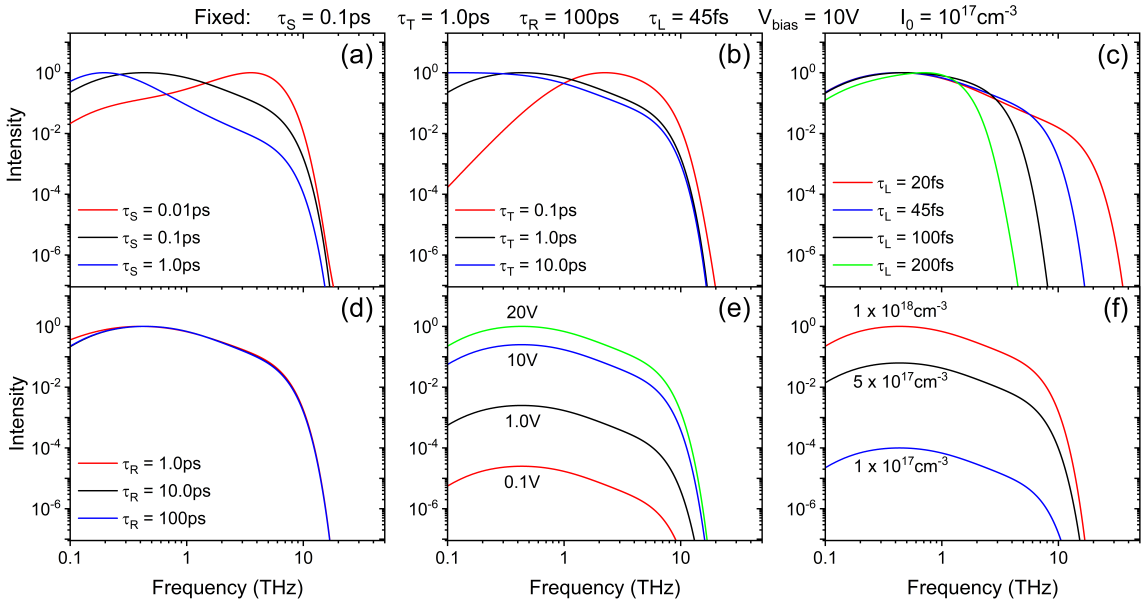

Figure A.1 The calculated emission spectrum of a biased photoconductive dipole antenna for a variety of values of (a) the Drude scattering time τ_S, (b) the trapping time τ_T of photoexcited carriers in mid-gap states, (c) the near-IR excitation laser pulse duration τ_L, (d) the carrier recombination time τ_R, (e) the antenna bias voltage V_{bias}, and (f) the near-IR excitation laser intensity in units of carriers excited per unit volume. The dispersion of the GaAs substrate in the terahertz regime was not included in the calculation.

The local field in the antenna is different from the applied bias field $E_{\text{bias}} = -V_{\text{bias}}/d$, which is screened by the buildup of screening polarization p_{sc}. This screening of the applied bias field is given by

$$E_{\text{local}}(t) = E_{\text{bias}}(t) - \frac{p_{\text{sc}}(t)}{\eta\epsilon}, \tag{A.8}$$

where $\eta\epsilon$ is a screening factor determined by the relative permittivity of the semiconductor. Thus, a rapid buildup of screening polarization extinguishes the local accelerating field and produces faster current transients, which in turn give higher frequency terahertz radiation. The dynamics of the polarization screening are determined by

$$\frac{d}{dt}p_{\text{sc}}(t) = -\frac{p_{\text{sc}}(t)}{\tau_R} + J(t). \tag{A.9}$$

Here τ_R is the recombination time for electron-hole pairs. The emitted terahertz electric field is then determined by solving this system of differential equations for $E_{\text{THz}}(t) \propto dJ(t)/dt$.

Figure A.1 illustrates the calculated emitted power spectrum of a simple dipole antenna for a series of values of τ_S, τ_T, τ_L, τ_R, V_{bias}, and I_0. The calculation was done assuming the charge carriers are primarily electrons excited into the bottom of the conduction band in GaAs with $m^* = 0.067m_e$ and $\eta\epsilon \approx 1$, with a dipole length of $d = 5$ μm. From the calculation several properties of photoconductive antennas are evident. First, as the scattering time τ_S increases the emitted spectrum shifts to lower frequencies with only a small decrease in bandwidth. This implies that a higher transient photoconductivity produces lower frequency emission because the

photoexcited current is decelerated over a longer period of time. Second, as the trapping time τ_T decreases the spectrum shifts to higher frequencies, ultimately giving rise to peaked emission at high frequencies. This effect can be understood in terms of the increase in the transition rate with decreasing capture time for electrons excited between the conduction band and deep lying trapping states. The increase in the transition rate reflects a larger energy difference between the conduction band and the trapping state, and the peak in the terahertz spectrum near the resonance frequency arises from stimulated emission between these energy levels. Third, as the excitation laser pulse duration τ_L decreases the bandwidth of the spectrum increases as $\sim 1/\tau_L$. Thus to achieve as broad of a bandwidth as possible it is important to use as narrow of a femtosecond pulse as possible. Since the spectral bandwidth of a pulse is related to its temporal width, the condition of the shortest possible pulse is achieved when the pulse is *transform limited*, that is, when the time-bandwidth product $\tau_L \Delta\omega$ is equal to its minimum possible value. For this reason, optical beam compressors utilizing negative dispersion mirrors or optics are usually placed in the beam path just before the generation and detection apparatus. Fourth, the spectrum is roughly independent of the electron-hole recombination time τ_R, because τ_R merely sets the length of the decay tail of the current transient. Since the amplitude of the emitted terahertz electric field is determined by the first time derivative of the transient current, $dJ(t)/dt$, the terahertz pulse is primarily generated by the initial steep onset of current following excitation by the femtosecond laser. A long decay tail of $J(t)$ is instead characterized by a slow rate of decay and so contributes negiligibly to the terahertz pulse shape. However, for recombination times significantly less than 1 ps terahertz emission at high frequencies can be obtained due to rapid extinguishing of the transient current [312]. Fifth, the intensity of the emitted terahertz spectrum is proportional to the square of the applied bias voltage and so it is advantageous to operate the photoconductive antennas at the highest voltage possible. The maximum voltage and thus the maximum obtainable radiation power, however, is limited by dielectric breakdown in the semiconductor material [313]. As a result, most photoconductive antennas operate with applied voltages up to ± 30 V. Lastly, the total power emitted can depend on the fourth power of the excitation laser intensity ($I_0{}^4$) because $J(t)$ is quadratic in I_0. This behavior arises because both the screening polarization and the density of photoexcited carriers are dependent on I_0. Therefore, terahertz generation in a photoconductive antenna is a second-order nonlinear process and the polarization current in the antenna effectively rectifies the excitation laser pulse.

Terahertz transients can be detected by optical gating of a second photoconductive antenna identical to that used to generate the terahertz pulses [314]. In this case the terahertz electric field itself provides the accelerating force for free carriers in the dipole structure and the transient electric current is detected. The current in the detection antenna at a time delay t' is given by [315]

$$J(t') = \frac{q^2 \tau_{\text{eff}}}{m^*} \int_{-\infty}^{\infty} n(t - t') E_{\text{THz}}(t) dt,$$

where τ_{eff} is the effective carrier lifetime. If the transient photoexcited charge $qn(t)$ and the duration of the near-IR femtosecond laser pulse are much faster than $E_{\text{THz}}(t)$ such that the response approximates a Dirac delta function, then $J(\omega) \propto E_{\text{THz}}(\omega)$. In practice, however, the near-IR femtosecond probe pulse and response of the detector

have a finite time duration compared to the terahertz pulse and so the transient photocurrent response in the detector is given by

$$J(\omega) \propto [I(\omega)R(\omega)]\, E_{\mathrm{THz}}(\omega), \tag{A.10}$$

where $I(\omega)$ and $R(\omega)$ are the Fourier transforms of the mid-IR femtosecond laser pulse and the time-dependent response function of the photoexcited carriers, respectively. The product $I(\omega)R(\omega)$ corresponds to the spectral sensitivity of the photoconductive detector antenna and the transient response of the free carriers in the detector functions as a low-pass filter that is dependent upon the effective carrier lifetime τ_{eff}. Therefore, in contrast to the case of the photoconductive antenna used as a terahertz source, the performance and bandwidth of the photoconductive detector antenna can be dramatically improved by decreasing the scattering time τ_S, trapping time τ_T, recombination time τ_R, and the near-IR femtosecond laser pulse duration τ_L. Indeed, terahertz pulse detection in photoconductive antennas at frequencies up to several tens of THz have been reported, but these devices tend to suffer from low signal-to-noise ratios at high frequencies due to the practical limitations on the minimum achievable values of τ_S, τ_T, and τ_R in semiconducting materials [316–318]. As a result, electrooptic detection in thin nonlinear crystals provides a more practical alternative for ultrabroadband terahertz pulse detection.

A.2 Spherical Antenna Lenses

Since a dipole antenna radiates electromagnetic waves in all directions (see Eq. A.3), collimating optics are necessary in order to utilize the full efficiency of the terahertz emitter. Furthermore, the series of Fabry-Pérot reflections of the terahertz pulse within the GaAs antenna substrate can limit the usable time-domain window and interfere with the tail of the main pulse, introducing artifacts in the frequency spectrum particularly for samples with significant dispersion. However, it is possible to obtain diffraction limited terahertz beams by locating the dipole source at the focal point of a truncated spherical collimating lens, provided the dipole size is much smaller than the terahertz wavelength [319]. The emitted terahertz pulses can then be well described by a Gaussian beam with a waist defined by the lens diameter [320]. Such lenses are several millimeters in radius and are most commonly fabricated from high resistivity silicon that is index matched to the GaAs substrate. The increased optical thickness of the lens-coupled antenna therefore also has the effect of temporally separating the Fabry-Pérot reflections of the antenna substrate.

There are generally two types of truncated spherical antenna lenses [321]. The first kind, collimating lenses, are defined by the condition

$$d_{\mathrm{collimating}} = R\left(\frac{n}{n-1}\right),$$

where $d_{\mathrm{collimating}}$ is the distance from the dipole to the tip of the lens, R is the radius of the lens, and n is the index of refraction of the lens. This distance is derived following the requirement that the dipole structure is located at the focus of the spherical lens. The second kind, hyperhemispherical lenses, are defined by the condition

$$d_{\mathrm{hyper}} = R\left(\frac{n+1}{n}\right),$$

derived by the requirement that the dipole is located such that the amount of radiation lost to total internal reflection is minimized. For both types of lenses the beam divergence is frequency dependent with the lower frequencies having larger divergence angles, while the high frequencies are concentrated toward the beam propagation axis. However, the two lens types have different advantages and disadvantages. Collimating lenses typically have abberations due to rays propagating close to the critical angle for total internal reflection, but the intensity of high frequency components propagating along the beam propagation axis is higher than for hyperhemispherical lenses. Hyperhemispherical lenses, on the other hand, are free from spherical abberations and coma and the total radiated power integrated over all divergence angles is ∼80% higher than for collimating lenses due to the fact that some of the generated terahertz rays are trapped within the collimating lens by total internal reflection. This higher efficiency comes at the cost of a large divergence cone angle of ∼30°, which requires the use of low f-number optics that are more difficult to align. Furthermore, the collimating lens places no limitations on the bandwidth of the lens-coupled antenna. In contrast, the hyperhemispherical lens introduces interference fringes even along the beam propagation axis, with the effect that the hyperhemispherical lens limits the measurable bandwidth of the emitter. Hyperhemispherical lenses typically have better Gaussian coupling efficiency while collimating lenses have better directivity. At high frequencies collimating lenses can have 2–3 orders of magnitude higher beam intensity along the axis of propagation. As a result, the choice of lens is typically made depending on the needs of the application, such as whether higher emitter intensity or a higher degree of collimation is more important.

A.3 The Electrooptic Effect

In addition to terahertz generation and detection by rectification of near-IR laser pulses by ultrafast currents in photoconductive antennas, it is possible to generate and detect terahertz pulses by the electrooptic effect in a noncentrosymmetric crystal. The electrooptic effect is a second-order nonlinear optical process that generates terahertz pulses through optical rectification by difference-frequency mixing of all the frequency components in an ultrafast laser pulse [322]. The resultant transient terahertz electric field has a shape similar to the envelope of the pump laser pulse. The two primary factors that influence the bandwidth and temporal shape of the terahertz pulse are therefore the bandwidth of the excitation laser pulse and the quality of the phase matching between the near-IR pump laser and the generated terahertz electric field.

Since the electrooptic effect is a second-order nonlinear optical effect, it requires a medium that has noncentrosymmetric symmetry in order to allow for matrix elements of the dielectric susceptibility that are quadratic in the field strength. Terahertz generation in such materials was first demonstrated in $LiNbO_3$, $LiTaO_3$, and the (110)-oriented zincblende crystals GaAs, CdTe, and InP [323, 324]. Coherent electrooptic detection of terahertz transients was demonstrated later in a 500 μm thick $LiTaO_3$ crystal [325]. However, (110)-oriented ZnTe and GaP have become the most common crystals for both generation and detection of terahertz pulses by electrooptic sampling because they have the best phase matching between the terahertz and near-IR electric fields, expecially for laser wavelengths near 800 nm [326, 327]. ZnTe is the optimum material for generation and detection of terahertz pulses with frequencies

below ∼4 THz due to its higher conversion efficiency. Unfortunately, the bandwidth of ZnTe is limited due to its strong optical phonon at 5.3 THz, which destroys the phase matching and absorbs terahertz radiation. GaP, on the other hand, has its optical phonon close to 11 THz [328], enabling it to have a wider usable bandwidth that extends to 7–8 THz at the cost of a slightly reduced conversion efficiency. To generate and detect high frequencies the thickness of the nonlinear electrooptic crystal must be quite thin in order to maintain the phase matching condition over as large a bandwidth as possible. Generally, the crystal thicknesses used are 0.5 mm or thinner. The resulting small interaction distance between the nonlinear medium and the near-IR laser pulse comes with the expense of a reduced signal intensity because the electrooptic signal is proportional to the crystal thickness. Furthermore, complications due to multiple reflections of the terahertz pulse in the electrooptic crystal can lead to artifacts in the extracted signal due to interference. These reflections can be avoided by the use of an additional index-matched medium attached to the back of the electrooptic crystal that temporally separates out the reflections. In zincblende crystals, there is no second-order dielectric response with the crystal oriented along the (100) axis, so by optically contacting a sub-0.5 mm thick (110)-oriented slice to a (100)-oriented plate with a thickness of several millimeters, it is possible to obtain a broad reflection-free time window [327].

As mentioned above, the second-order nonlinear process responsible for electrooptic generation of terahertz pulses is the difference-frequency generation effect. Since the frequency of the terahertz electric field Ω is several orders of magnitude less than the frequency ω of the near-IR pump pulse, the interaction of the terahertz and near-IR photons are in the slowly varying amplitude limit, where $\partial\tilde{E}(\omega,z)/\partial z \ll k\tilde{E}(\omega,z)$ assuming wave propagation in the z direction. Here, k denotes the phase $k(\omega) = \omega n(\omega)/c$. The ultrafast near-IR pump pulse can also be assumed to satisfy the group velocity approximation, where the bandwith of the near-IR pulse $\Delta\omega$ is much smaller than the central frequency ω_0. Solving the nonlinear wave equation for difference-frequency generation in these limits gives the generated terahertz electric field [329],

$$\tilde{E}_{\mathrm{THz}}(\Omega,z) = \frac{\Omega^2 e^{ik(\omega)z}}{k(\Omega)c^2}\chi^{(2)}_{\mathrm{eff}}\frac{e^{i\Delta k(\omega,\Omega)z}-1}{\Delta k(\omega,\Omega)}\int_{-\infty}^{\infty} E^*_{\mathrm{IR}}(\omega+\Omega)E_{\mathrm{IR}}(\omega)d\omega, \tag{A.11}$$

where $\chi^{(2)}_{\mathrm{eff}}$ is the effective second-order susceptibility and $\Delta k(\omega,\Omega)$ is the total phase mismatch between Ω, ω, and $\omega+\Omega$. The phase mismatch in the group velocity approximation is given by

$$\Delta k(\omega,\Omega) = \frac{1}{c}\left[n(\omega+\Omega)(\omega+\Omega) - n(\omega)\omega - n(\Omega)\Omega\right] \approx \frac{\Omega}{c}\left[n_g(\omega_0) - n(\Omega)\right],$$

where n_g and n are the group and phase indices of refraction, respectively. Thus, the amplitude of the generated terahertz electric field is determined by the autocorrelation of the near-IR pump electric field and a correction factor that depends on the phase mismatch. For a noncentrosymmetric crystal of length L, the intensity of the generated terahertz pulse is then

$$I_{\mathrm{THz}}(\Omega,L) = \left|\tilde{E}_{\mathrm{THz}}(\Omega,L)\right|^2 \propto L^2\,\mathrm{sinc}^2\left(\frac{\Delta k(\omega_0,\Omega)L}{2}\right)$$

Approaching $\Delta kL/2 \approx \pi$ the intensity of the generated radiation thus falls rapidly to zero as the output wave becomes out of phase with the driving polarization. Beyond $\Delta kL/2 \approx \pi$, the rate $\partial \tilde{E}_{\mathrm{THz}}(\Omega, z)/\partial z$ can become negative as energy is converted from $\tilde{E}_{\mathrm{THz}}(\Omega, z)$ back into $\tilde{E}_{\mathrm{IR}}(\omega, z)$ and $\tilde{E}_{\mathrm{IR}}(\omega+\Omega, z)$ in the reverse of the difference-frequency generation process. As a result, there is a coherence length

$$L_c = \frac{2}{\Delta k(\omega_0, \Omega)} \approx \frac{2c}{\Omega(n_g - n)} \tag{A.12}$$

for the maximum length of the coherent difference-frequency generation process. For GaP, which has an index of $n_g = 3.19$ near 800 nm and $n = 3.34$ at 1 THz, this corresponds to a coherence length of $L_c = 0.6$ mm [330,331]. The presence of dispersion near 800 nm, however, can have the effect of significantly modifying the coherence length and introducing strong frequency dependence in the terahertz range [332].

In contrast to the difference-frequency process that is responsible for terahertz generation, terahertz pulse detection by the electrooptic effect is a second-order nonlinear process caused by sum-frequency mixing of terahertz and near-IR photons. In essence, the sum-frequency process is the difference-frequency generation process run in reverse; the electrooptic effect leads to phase retardation between the two polarization components of a near-IR probe beam by an amount proportional to the incident terahertz electric field. For zincblende crystals, the phase retardation between orthognally polarized near-IR electric field components is given by [329]

$$\Delta\phi = \frac{\omega {n_0}^3 r_{\mathrm{eff}} L}{c} E_{\mathrm{THz}}, \tag{A.13}$$

where n_0 is the static index of refraction of the noncentrosymmetric crystal at the near-IR probe wavelength ω and r_{eff} is the effective electrooptic coefficient. Therefore, an optical setup that is able to detect the phase retardation between the two polarization components of the near-IR probe pulse can be used for detection of the field strength of the terahertz beam. The electrooptic signal detected in a noncentrosymmetric crystal is given by [322]

$$S(\tau) \propto \frac{1}{c} \int_{-\infty}^{\infty} \tilde{E}_{\mathrm{THz}}(\Omega) f(\Omega) e^{-i\Omega\tau} d\Omega \tag{A.14}$$

for a time delay τ between the terahertz field and the near-IR probe pulse. This is simply the inverse Fourier transform of the terahertz electric field and the filter function $f(\Omega)$. If $f(\Omega)$ is frequency independent then $S(\tau)$ is given exactly by the terahertz field entering the crystal. In general, the filter function is given by [10]

$$f(\Omega) = \int_{-\infty}^{\infty} \frac{\omega^2}{|\omega n(\omega)/c|} e^{-2\omega\kappa(\omega)z/c} \chi^{(2)}_{\mathrm{eff}}(\omega) \frac{e^{i\Delta k(\omega,\Omega)z} - 1}{i\Delta k(\omega, \Omega)} E^*_{\mathrm{IR}}(\omega) E_{\mathrm{IR}}(\omega - \Omega) d\omega$$

where in this case $\kappa(\omega)$ denotes the imaginary part of the complex index of refraction in order to differentiate it from the phase (or wavenumber) $k(\omega)$.

From this filter function it is evident that several factors impact the fidelity of the measured pulse $\tilde{E}_{\mathrm{THz}}(\Omega)$. First, the frequency dependent coherence length $L_c(\omega)$, given by the term dependent upon Δk, can strongly limit the efficiency of terahertz detection. Second, if the near-IR probe laser pulse is too broad in the time domain then the probe spectrum $E_{\mathrm{IR}}(\omega)$ will be narrow and the autocorrelation

$\int E^*_{\mathrm{IR}}(\omega)E_{\mathrm{IR}}(\omega-\Omega)d\omega$ will be strongly frequency dependent. Third, the signal $S(\tau)$ can be distorted by the frequency dependent nonlinearity $\chi^{(2)}_{\mathrm{eff}}(\omega)$ and strong terahertz absorption in the crystal, which is especially strong near resonance frequencies of the noncentrosymmetric crystal in the terahertz region. Since the slowly varying envelope approximation $\Delta\omega \ll \omega_0$ is valid, $S(\tau)$ simplifies to

$$S(\tau) \propto \frac{1}{c}\int_{-\infty}^{\infty} \tilde{E}_{\mathrm{THz}}(\Omega)P(\Omega,\omega_0)C(\Omega)e^{-i\Omega\tau}d\Omega, \tag{A.15}$$

where $C(\Omega) = \int E^*_{\mathrm{IR}}(\omega)E_{\mathrm{IR}}(\omega-\Omega)d\omega$ is the autocorrelation of the near-IR probe pulse and $P(\Omega,\omega_0)$ is a phase mismatch function. In the limit $\Omega \ll \Delta\omega$ the autocorrelation $C(\Omega)$ has little effect and $P(\Omega,\omega_0)$ contains all experimental sources of phase mismatch and distortions. Thus, in order to optimize the filter function, a noncentrosymmetric crystal with dimensions close to L_c, as short of a near-IR pulse as possible, and a crystal with optical phonons at as high as frequency as possible are necessary.

The frequency spectrum $\tilde{E}_{\mathrm{THz}}(\Omega)$ appearing in the function $S(\tau)$ is the terahertz field incident on the crystal and is affected by the Fresnel transmission coefficient at the front interface of the crystal,

$$\tilde{E}_{\mathrm{THz}}(\Omega) = \tilde{t}_{12}\tilde{E}_{0,\mathrm{THz}}(\Omega).$$

The effect of the Fresnel coefficients of the crystal are eliminated by considering the transfer function $\tilde{t}(\Omega)$ between a sample and reference measurement,

$$\tilde{t}(\Omega) = \frac{\tilde{t}_{12}\tilde{E}^{sample}_{0,\mathrm{THz}}(\Omega)}{\tilde{t}_{12}\tilde{E}^{ref}_{0,\mathrm{THz}}(\Omega)} = \frac{\tilde{E}^{sample}_{\mathrm{THz}}(\Omega)}{\tilde{E}^{ref}_{\mathrm{THz}}(\Omega)} \tag{A.16}$$

A photodiode converts the optical signal $S(\tau)$ into an electronic signal that is read out by a data acquisition unit. Since the electrooptic effect results in the phase retardation given by Eq. A.13 between orthogonal polarization components of the near-IR probe beam, a linearly polarized probe pulse becomes elliptically polarized by an amount proportional to the amplitude of the terahertz electric field. As depicted by the experimental schematic shown in Fig. 3.7, after the electrooptic crystal the probe pulse passes through a $\lambda/4$ wave plate and a polarizing beam splitter before illuminating the photodiode. The $\lambda/4$ wave plate rotates the polarization of the probe beam such that it is nearly circularly polarized; in the absence of a terahertz electric field in the electrooptic crystal the probe pulse illuminating the photodiode is exactly circularly polarized, while the presence of a terahertz electric field results in a small perturbation from circular polarization whose sign is given by the sign of the terahertz field. Thus, the signal is read out electronically as the intensity change of the orthogonal polarization component of the probe laser on the photodiode.

Equation A.15 for electrooptic detection of terahertz pulses in noncentrosymmetric crystals corresponds to Eq. A.10 for terahertz detection in photoconductive antennas. Ultimately, the more optimum detection scheme depends on the relative difference between the efficiency of the phase mismatch $P(\Omega,\omega_0)$ for electrooptic detection and the spectral sensitivity $I(\Omega)R(\Omega)$ for photoconductive antennas. Given the advantages of second-order nonlinear effects in GaP (ie, good phase matching in the terahertz regime and the lowest optical phonon at 11 THz), electrooptic detection is usually a better

option for terahertz detection at frequencies below ∼7-8 THz than photoconductive antennas. Indeed, most TTDS setups utilize electrooptic detection irrespective of the chosen generation scheme.

A.4 Negative Dispersion Mirror Pairs

As illustrated in Fig. A.1, one of the most effective methods to increase the terahertz spectral bandwidth and power output of a photoconductive antenna is to reduce the full-width at half-maximum τ_L of the pump laser pulse. A short τ_L also gives a probe pulse that better approximates a Dirac delta function in electrooptic detection, which results in an electrooptic signal $S(\tau)$ with a finer time resolution. The TTDS spectrometer therefore operates at optimum efficiency when τ_L is at its minimum possible value and the pump and probe laser pulses are transform limited. When this occurs the time-bandwidth product $\tau_L \Delta\omega$ is also at its minumum value. This condition in turn requires a frequency-independent spectral phase—meaning that there is no dispersion of the laser pulses and all frequency components in the pulse trains travel together and arrive at the same time. Unfortunately, dispersion present in the optical elements, atmosphere, and laser cavity itself gives rise to time-dependent spectral phase that creates complicated temporal structure in the pulse electric field profiles. The details of the femtosecond laser pulse propagation in the spectrometer therefore must be taken into consideration and accounted for in the spectrometer design.

The electric field of a femtosecond laser pulse is a complex quantity and so can be expressed as [333]

$$\tilde{E}(t) = E(t)e^{i\phi(t)}e^{i\omega_l t}, \tag{A.17}$$

where ω_l is the carrier frequency (central laser frequency) and $E(t)e^{i\phi(t)}$ is a complex envelope function with a time-dependent phase $\phi(t)$. At any given time, the instantaneous carrier frequency is then

$$\omega_l'(t) = \omega_l + \frac{d}{dt}\phi(t). \tag{A.18}$$

For constant $d\phi/dt$ the carrier frequency is simply shifted by a constant value, but for $d\phi/dt = f(t)$ the carrier frequency is time dependent and the pulse is said to be *chirped*. The simplest case of chirp, then, is for constant $d^2\phi/dt^2$. When $d^2\phi/dt^2 < 0$ the carrier frequency decreases along the pulse and the pulse is "down chirped." Similarly, $d^2\phi/dt^2 > 0$ implies that the carrier frequency increases along the pulse and the pulse is "up chirped."

According to Huygens' principle, every point on a wavefront is itself a source of spherical wavelets and the propagation of a light beam can be described by considering the constructive and destructive interference of all wavelets. A spherical wavefront is approximated by a quadratic phase $\phi(x) \propto x^2$, where x is the direction orthogonal to any arbitrary propagation axis. A quadratic phase modulation therefore implies focusing or defocusing of the light ray and vice versa. The analog in the temporal coordinate is also true: $\phi(t) \propto t^2$, and imparting a quadratic phase modulation in time leads to either pulse compression or broadening in time. Thus, pulse propagation through a dispersive medium inherently leads to pulse broadening. The wavevector

of the pulse in such a medium can be approximated by

$$k(\omega) = \frac{\omega}{c} n(\omega) \approx k(\omega_l) + (\omega - \omega_l) \left.\frac{dk}{d\omega}\right|_{\omega_l} + \frac{1}{2}(\omega - \omega_l)^2 \left.\frac{d^2k}{d\omega^2}\right|_{\omega_l}, \tag{A.19}$$

where $k(\omega_l)$ is the wavevector of the carrier frequency. The term proportional to the first frequency derivative of k gives the group velocity v_g, defined as

$$v_g = \left(\left.\frac{dk}{d\omega}\right|_{\omega_l} \right)^{-1}, \tag{A.20}$$

and corresponds to the propagation velocity of the wave packet. The third term on the right-hand side of Eq. A.19 is the correction to the wavevector caused by the group velocity dispersion (GVD). GVD is defined simply as $d^2k/d\omega^2|_{\omega_l}$ and characterizes the amount of chirp present in the pulse, usually given in units of with units fs^2/m. A second convenient way to express GVD is in terms of the group velocity and wavelength λ as

$$\frac{dv_g}{d\lambda} = \frac{\omega^2 {v_g}^2}{2\pi c} \frac{d^2k}{d\omega^2}. \tag{A.21}$$

In this form it is evident that positive GVD gives rise to up chirp while negative GVD gives down chirp.

A closely related quantity to GVD is the group delay dispersion (GDD). Following from the Fourier transform of Eq. A.17, the spectral phase of the wave packet can be expressed as

$$\phi(\omega) \approx \phi(\omega_l) + (\omega - \omega_l) \left.\frac{d\phi}{d\omega}\right|_{\omega_l} + \frac{1}{2}(\omega - \omega_l)^2 \left.\frac{d^2\phi}{d\omega^2}\right|_{\omega_l}. \tag{A.22}$$

Here, $d\phi/d\omega|_{\omega_l}$ is the group delay, which describes how phases of different frequencies are delayed differently in time. The GDD is given by $d^2\phi/d\omega^2|_{\omega_l}$ and is equivalent to the GVD of the pulse after propagation over a distance L. Since the units of GDD are fs^2, GVD is the GDD per unit length.

Most common materials have positive GVD at optical wavelengths so femtosecond laser pulses naturally tend to broaden and chirp as they propagate through a spectrometer aparatus. The GVD of air at 1 bar of pressure, for example, is 20 fs^2/m [334]. As a result, compensators or pulse compressors that introduce negative GDD are required to maintain transform limited pulse shapes. The most convenient way to do this is by using chirped mirrors: positive GDD acquired in the spectrometer elements is compensated by bouncing the laser pulses on multilayer mirrors that have been designed with predefined reflection and phase behavior, $\tilde{r}(\omega) = R(\omega)e^{i\psi(\omega)}$. This is accomplished by optimizing the thicknesses and orders of various layers with different indices of refraction. Typically, stacks of alternating high and low index quarter-wave layers are used and reflect a very narrow band of frequencies with a very high reflectivity; a series of stacks corresponding to a series of narrow frequency bands are used together to obtain high reflectivity over a broader frequency range. Stacks are placed at different depths underneath the surface of the mirror to allow different frequencies to reflect with different phase accumulations. To achieve negative GDD, the different stacks are ordered such that layers corresponding to lower frequencies are located deeper underneath the mirror surface, while thinner layers that reflect higher

frequencies are located at shallower depths. Subresonances between the various layers and the air-film interface produce modulations of the GDD as a function of frequency. Smoother dispersion curves are therefore obtained by employing chirped mirror pairs, with the GDD of each mirror designed to modulate in antiphase to the other.

Diagnostics are performed using pulse analyzers in order to optimize the GDD of the pulse compressor and monitor the spatial, temporal, spectral, and phase distributions of the resulting femtosecond laser pulses. Autocorrelators are often used for this purpose. However, autocorrelators are generally not frequency or phase resolved and the autocorrelation procedure averages out fine structure in the pulse—the time resolution is comparable to the laser pulse duration τ_L. As a result, the extracted temporal and spectral widths may be significantly different from their true values and even sometimes smaller than allowed by the minimum value of the time-bandwidth product. A more robust method of femtosecond pulse analysis is provided by the frequency resolved optical gating (FROG) technique, which is simultaneously spectrally, temporally, spatially, and phase resolved [335]. A very simple modern implementation of the FROG technique with only four fixed optical elements is known as the GRENOUILLE; it uses a cylindrical lens and a Fresnel biprism (a triangluar prism with apex angle $\sim 180°$) to first focus the femtosecond laser pulse into a horizontal line, and then optically gate the pulse with itself by crossing the left and right halves onto each other. The Fresnel biprism crosses the two halves of the pulse in a nonlinear second-harmonic generation crystal. The relative arrival times of the left and right halves of the pulse depend on the transverse horizontal position in the crystal, so after imaging the second harmonic signal onto a camera the horizontal axis corresponds to the temporally resolved measurement of the laser pulse. Since the cylindrical lens focuses the laser beam in the transverse vertical direction with a large focusing angle (low f-number) and the second-harmonic generation crystal is thick, the second harmonic signal is emitted in a vertical fan with the frequency of the second harmonic being a near-linear function of emission angle. Thus, the vertical dimension of the image on the camera corresponds to the spectrally resolved measurement of the pulse. The strength of the GRENOUILLE is that the Fresnel biprism allows each laser pulse to measure itself with a temporal and spectral resolution much higher than is possible in an autocorrelator, and it can be set up in a single-shot configuration to obtain time and frequency resolved traces of individual pulses. Furthermore, the simultaneous measurement of the time and frequency dependence allows the temporal and spectral phase to be extracted and the spatial profile of the pulses to be retrieved.

The negative dispersion chirped mirror pairs used in the TTDS setup employed in this work were Laser Quantum DCM11 mirrors with reflectivity $R \approx 99.8\%$ and dimensions $35 \times 20 \times 10$ mm, designed to provide -150 fs^2 GDD per pair of bounces at $\lambda = 796$ nm with an angle of incidence of $\sim 7°$. It was found that 9 bounce pairs were necessary for both the pump (slave) and probe (master) lasers to achieve optimum terahertz pulse generation and electrooptic detection. Figure A.2 displays typical time, frequency, and position resolved traces of the laser pulses both with and without use of the negative GDD mirror pairs, obtained from pulse diagnostics performed with a Swamp Optics GRENOUILLE pulse analyzer. Due to the symmetry of the pulse analyzer the time axes of the traces run such that positive time values coorrespond to earlier arrival times while negative values correspond to later arrival times. It is evident that without the negative GDD mirror pairs the laser pulse is broad ($\tau_L = 157$ fs) and significantly chirped, with longer wavelengths arriving earlier

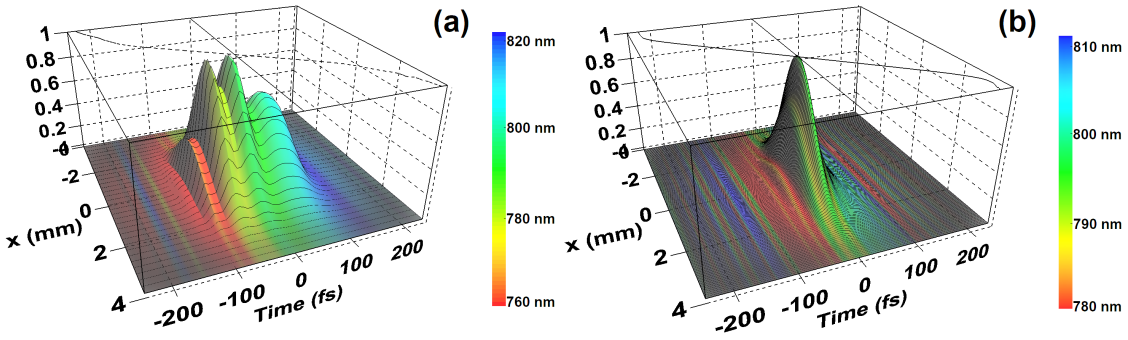

Figure A.2 Time and position resolved FROG intensity traces of a femtosecond laser pulse (a) without pulse compression and (b) with pulse compression after 9 round trips in a negative dispersion mirror pair with -150 fs^2 GDD per round trip. The color coding corresponds to the time-dependent wavelength of the femtosecond pulse, with red corresponding to short wavelengths and blue corresponding to long wavelengths. The central wavelength of the laser pulse is 796 nm with $\Delta\lambda = 24$ nm. It is evident that without pulse compression the laser pulse exhibits a broad temporal profile ($\tau_L = 157$ fs), significant time-dependent structure, and chirping, with high frequences appearing at earlier times and low frequences at later times. After pulse compression $\tau_L = 43$ fs with all wavelengths in phase.

and shorter wavelengths arriving later, as in Fig. A.2(a). Furthermore, the pulse displays complicated temporal structure and modulations of intensity. Such a laser pulse is generally too broad with too low peak intensity to excite usable terahertz transients in the TeraSED photoconductive antenna. With the negative GDD mirror pairs, on the other hand, a nearly transform limited pulse is obtained with $\tau_L = 43$ fs and all spectral components in phase, as illustrated in Fig. A.2(b). In both traces the spectral bandwidth was measured to be $\Delta\lambda = 24$ nm. The above values of τ_L can be contrasted with the pulse durations τ_{AC} obtained by autocorrelation of the same pulses. The pulse in Fig. A.2(a) has an autocorrelation width $\tau_{\mathrm{AC}} = 196$ fs and the pulse in Fig. A.2(b) has $\tau_{\mathrm{AC}} = 73$ fs, illustrating the large degree of uncertainty present in autocorrelator measurements of femtosecond laser pulses.

A.5 Off-Axis Parabolic Mirrors

Special terahertz optics are used to focus the terahertz transients onto the sample and detector element. Focusing mirrors are used rather than dispersive optics such as lenses because mirrors are free from chromatic abberation and pulse broadening (chirp), and they can be designed to have high reflectivity across a very wide spectral bandwidth. It is therefore possible to align mirrors with a different wavelength of light than is used for measurements—a distinct advantage when working in spectral ranges far outside the visible range. Parabolic mirrors are the most common mirror type employed in TTDS setups in order to avoid errors caused by sperical abberations. When collimated light is incident on a parabolic mirror the parabolic surface focuses the light into a single point without phase distortion of the spatial components. The converse is also true. Light reflected from a point source located at the focal point of a parabolic mirror is collimated into a beam with flat wavefronts.

An off-axis parabolic mirror is a segment of a parent parabola that shares the

main optical axis with the parent, but which is offset from the axis by a distance such that the collimated light is focused along a predefined angle with respect to the main optical axis. Since the off-axis parabola does not form a full surface of revolution about the main optical axis, the reflected wavefront is not symmetric. The asymmetry is compensated by utilizing pairs of identical off-axis parabolic mirrors arranged in a symmetric geometry. As depicted in Fig. 3.7, four 90° off-axis parabolic mirrors were used in the TTDS setup employed in this work, with the first and last mirrors having an effective focal length of 50.8 mm and the two middle mirrors (which focus the terahertz beam onto the sample) having a longer effective focal length of 101.6 mm to accommodate the dimensions of the optical cryostat. All four mirrors had a circular cross-section perpendicular to the main optical axis with a diameter of 2 in.

The propagation of terahertz waves in the spectrometer is described in the paraxial approximation by Gaussian beam dynamics, where the transverse width $w(z)$ of a beam propagating in the z direction is given by [333]

$$w(z) = w_0 \sqrt{1 + \left(\frac{\lambda z}{n \pi {w_0}^2} \right)^2}. \tag{A.23}$$

Here, w_0 is the transverse radius of the beam at the focus, n is the index of refraction of the medium, and $2n\pi {w_0}^2/\lambda$ is the confocal parameter (or depth of focus). As a result of Eq. A.23, the Gaussian terahertz beam spreads hyperbolically in the transverse direction with increasing propagation distance z with the cone opening angle asymptotically approaching $\theta = 4\lambda/2\pi w_0$. The cone can be re-collimated with a focusing element of f-number f/D, where f is the focal length and D is the diameter of the element. For such an optical element the full focusing angle is given by $\theta = D/f$, so the diameter of the beam waist is

$$2w_0 = \frac{4\lambda}{n\pi} \frac{f}{D} \tag{A.24}$$

with depth of focus

$$\mathrm{DOF} = \frac{8\lambda}{n\pi} \left(\frac{f}{D} \right)^2. \tag{A.25}$$

This gives a beam diameter of ∼0.8 mm at the focal point with a depth of focus of ∼3 mm at 1 THz for a beam propagating in air, focused by optics with an f-number of 2. For 0.3 THz, the beam diameter is ∼2.5 mm at the focus with a depth of focus of ∼10 mm. The f-number of the focusing optics and the diameter of the aperture used to mount the sample therefore act to limit the lower bound on the spectral bandwidth of the TTDS system. If the f-number of the focusing optics is not low enough or the diameter of the aperture not large enough then significant distortions in both the time-domain and frequency-domain signals can occur due to diffraction at the aperture edges. Furthermore, the tendency of a Gaussian beam to spread in the transverse direction as it propagates implies that an "8f" optical geometry is needed to achieve a frequency independent focal spot [336]. The 8f geometry is constructed so that the distance between the antenna and first off-axis parabolic mirror is f, the distance between the first and second mirrors is $2f$, the distance between the second mirror and the sample is f, and the geometry is exactly inverted after the sample as illustrated in Fig. 3.7. The $2f$ spacing in the portions of the spectrometer where the terahertz beam is collimated is particularly important, as it exactly compensates for the spatial Gaussian beam distortion that is acquired during propagation.

The wide emission angle of the photoconductive antenna and the need for a small focal spot require the f-number of the spectrometer to be minimized to the lowest possible value. For TTDS systems that incorporate optical cryostats this can pose a challenge, especially for systems that are built around magneto-optical cryostats, because the dimensions of the optical windows and magnets can strongly limit the maximum focusing cone angle θ. For a full description of the alignment procedure of off-axis parabolic mirrors, see Appendix B.

A.6 Dry Nitrogen Purge Box

An additional consideration related to the detection of terahertz pulses is the absorption of terahertz radiation by water vapor in the atmosphere. There are 9 distinct absorption lines of water below 1.5 THz with a very strong absorption line at 1.7 THz [337]. Furthermore, water vapor in the atmosphere can reduce transmission by 30–50% in the spectral range 0.1–3 THz, with transmission decreasing more sharply above 1 THz [338]. Considerable absorption begins to appear at relative humidity values of just 10% and beam path lengths of 2 meters.

To compensate for these atmospheric effects it is necessary to perform terahertz generation, measurement, and detection in a closed box that is purged of water vapor by the use of an inert gas. Dry nitrogen is often the best choice because its use does not significantly alter the index of refraction of the measurement environment while also being easily available from either a laboratory pressurized gas network or as boil-off from liquid nitrogen dewars. The most common setup is a plexiglas box of horizontal dimensions $\sim 1 \times 1$ m^2 with walls and a top that clip into place or are otherwise easily removable to allow for unrestricted access to the optical components inside. Dry nitrogen gas is then fed into the box through a hose and a humidity sensor is placed inside to monitor the water vapor levels. Small holes are drilled into the walls of the plexiglas box to allow the pump and detection laser beams to pass through. Small glass windows with antireflection coatings may be used to seal the laser holes, but if the nitrogen pressure inside the box is kept slightly higher than the ambient laboratory pressure then this is usually not necessary.

A.7 Liquid Helium Bath Cryostat and Sample Insert

A CryoVac Konti Type Spektro 4 liquid helium bath optical cryostat is used for low temperature measurements. The cryostat is capable of reaching temperatures of 4.2 K without and 2.6 K with vacuum pumping on the sample chamber. Optical measurements along two perpendicular axes are possible via a set of four windows at the sample chamber; one pair of these windows on the outer cryostat wall was replaced with 125 μm thick Mylar to optimize terahertz transmission and minimize internal reflections within the window material. All four windows on the inner cryostat wall were similarly replaced with 100 μm thick polypropylene (PP) foil. The cryostat itself was mounted on a traveling nonmagnetic scaffold on the optical table to allow translation in the xy plane. Motion in the z (vertical) direction was enabled by a manual mechanical corkscrew elevator. Rotation about the z axis was also possible

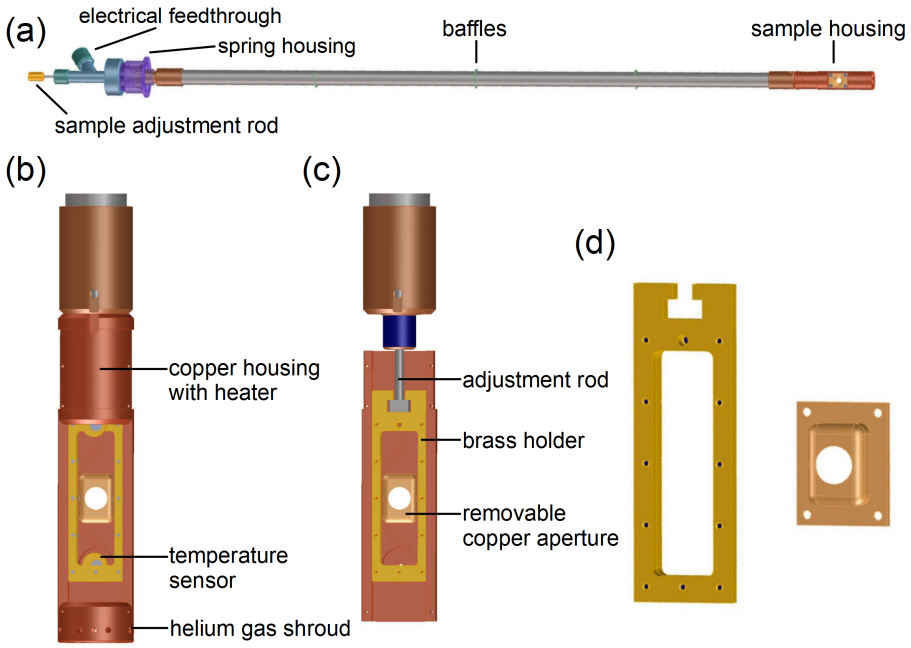

Figure A.3 A schematic of the custom-built cryostat insert used in this work. (a) An overview of the full sample stick. A spring at the top of the stick is used to ensure contact between the bottom of the stick and bottom of the cryostat sample chamber at all temperatures. (b) A view of the sample housing. The housing was machined from large pieces of copper in order to provide temperature stability. A temperature sensor was mounted in a small grove on this housing beneath the brass sample frame. (c) A cutaway schematic of the movement mechanism for the brass sample holder. (d) The brass frame and interchangeable brass aperture.

by mounting the cryostat on a large ring bearing.

The sample insert was custom-built in house based on previous designs used for submillimeter quasioptical interferometry. We discovered that the previously used sample stick setup, which employed three separate aperatures to which samples could be mounted, was highly susceptible to systematic errors in the TTDS data. The old sample stick was operated by changing the vertical position of the entire stick between sample and reference measurements, but this procedure led to interference problems due to inequivalent diffraction patterns of the individual apertures caused by small differences in their shapes. We resolved this problem by designing the sample insert depicted in Fig. A.3. This sample insert features a single fixed aperture with a movable frame to which the samples are mounted. A spring located at the top of the insert stick ensures that the bottom of the stick remains firmly in contact with the bottom of the cryostat sample chamber at all temperatures to avoid inadvertent motion of the aperture position as the length of the insert expands and contracts. The samples are mounted onto a thin sheet of Mylar with GE varnish, which is held tightly in place by the brass frame. This frame can be moved vertically with a narrow adjustment rod in order to alternate between sample and reference measurements. The aperture is machined into an interchangeable piece of copper and is designed to make contact with the back side of the Mylar sheet. Several apertures with diameters ranging from 1–10 mm mere made.

Appendix B

How to Align Off-Axis Parabolic Mirrors

Proper alignment of the off-axis parabolic mirrors (OAPs) is essential to obtaining a high signal-to-noise ratio of the terahertz signal with minimal distortions and abberations. The alignment can be performed in two different ways, using either the pump and probe laser beams or an additional HeNe guide laser that is co-aligned with the pump and probe beam paths. Regardless of alignment method, the initial step is to roughly mark the correct positions of the mirrors on the optical table based on their effective focal lengths and the desired location of the sample position. Optical component mounting tracks should then be placed on the optical table over the planned mirror positions to allow for gross adjustment of the mirror locations as well as easier placement of components such as focusing lenses, antennas, and wave plates. Alignment is often much easier if the mounting tracks are laid parallel to the pump and probe laser beams and the OAP-sample-OAP axis. Every OAP should be mounted on compact x-y translation stages as well as a clamp to allow easy attachment to the mounting rails.

To align the off-axis parabolic mirrors using the pump and probe lasers:

1. Begin by carefully aligning both the probe and laser beams to enter the purge box at the proper beam height and along the desired propagation axes. This is done by placing two identical irises for each beam near where the beams enter the purge box and close to the far wall of the purge box. The beams are aligned when they propagate through the centers of both irises. Adjust the alignment of each beam using two steering mirrors placed prior to the first iris. Often times, incorrect initial alignment of the incoming pump and probe laser beams is the largest contributing factor to OAP misalignment and distortions in the measured terahertz transients.

2. Starting from the generation end of the terahertz beam path, place the first OAP in the marked position. Carefully adjust its vertical position so that the height of the center of the mirror is exactly at the intended beam height. Likewise, adjust the rotation of the mirror about its axis so that the plane formed by the axial direction and the focal direction is parallel to the surface of the optical table. This step should be repeated for each additional mirror after it has been placed on the optical table.

3. Use the pump laser beam to align the correct orientation of the first OAP. Use a beam alignment "template" that has a circle of the same diameter as the OAP centered about a crosshair drawn on a card or solid plate. Place this template near the far edge of the optical table (as far from the OAP as possible) such that the crosshair is located at the correct beam height and horizontal postion. Next, place an iris at the intended position of the second OAP. Adjust the x-y position and tilt degrees of freedom of the first OAP until the pump laser beam passes through the center of the iris and the crosshair on the template.

4. Place a thin paper card at the focus of the first OAP, in the location of the antenna. When the pump laser is focused onto this card, it will diffuse the laser light in the fashion of a point source and can be used to align the focal position of the OAPs. Remove the iris at the intended location of the second OAP and adjust the x-y position and tilt degrees of freedom of the first OAP until the image of the diffused laser beam appears exactly within the drawn circle on the template, without ellipsoidal distortions. The position of the card along the pump laser propagation axis can also be used as an adjustment degree of freedom.

5. Remove the paper card and replace the iris at the intended position of the second OAP. Repeat alignment of the OAP orientation direction by aligning the pump laser to once again pass through the center of the iris and the crosshair on the template. After the beam is realigned, repeat the sequence of aligning the point source image with the paper card in place and aligning the beam without the paper card several times. The OAP is properly aligned when both the laser beam on the crosshair and focal image within the circle are simultaneously aligned without any additional adjustment needed.

6. Place the second OAP, and place one iris at the location of its focus (the sample location) and another iris at least 40–50 cm beyond the location of the focus. Use these two irises to adjust the correct orientation of the second OAP by ensuring the laser beam passes through both when the paper card is removed. Use only the x-y position and tilt degrees of freedom of the second OAP for these adjustments. Next, place the paper card back and make further adjustments of the second OAP to make sure the image of the diffused laser beam forms a circular spot of the same diameter as the mirror at the intended location of the third OAP. The diffused laser beam should also be able to pass through a small iris aperture of diameter no more than 1–2 mm at the focus position without beam clipping. The diffused beam should also be circular in shape with minimal elliptical distortions on either side of the focus (this can be checked by holding a white paper card in the beam path). As with the first OAP, alternate adjustments with and without the card in place until both the collimated laser beam and the diffused laser image are both aligned.

7. Place the third OAP and one iris at the intended position of the fourth OAP with the alignment template behind. Again, adjust the x-y position and tilt degrees of freedom of only the third OAP until the collimated laser beam passes through the iris and the center of the crosshair without the paper card in place. Put the paper card back in place and make further adjustments of the fourth OAP until the diffused laser spot is circular and fills the template without any

elliptical distortions. At this point, because only three mirrors have been placed and the optical beam path is so far asymmetric, one side of the diffused laser spot may be brighter than the other side. This is not a problem provided the spot is symmetrically shaped.

8. Put the fourth OAP in place. This OAP will have a hole drilled through its center to allow the probe laser beam to pass through. First, adjust the x-y position of the OAP until the probe beam can freely pass without clipping (the z position should already have been fixed to match the beam height). Second, place an iris at the focal position, at the intended location of the detector, and a second iris further along the beam path. As with the other OAPs, align the mirror orientation by ensuring the collimated laser beam passes through both irises without the paper card in place. Place the card back and use the x-y position and tilt degrees of freedom to align the diffused laser spot so that it focuses onto the center of the iris. Check that the beam spot is circular both in front and behind the iris.

9. Ensure that the probe laser beam focuses onto the same spot as the fourth OAP. The focusing lens may have to be adjusted by a minor amount.

10. Remove the paper card from in front of the first OAP and place the photoconductive antenna. The antenna should be mounted on an x-y translation stage. Adjust the position of the antenna so that it is located at the focus of the OAP; keep in mind that due to refraction at the semiconductor substrate-to-air interface the apparent location of the terahertz point source will be located slightly in front of the dipole, so the antenna will have to be moved slightly closer to the first OAP.

11. Place the GaP detector crystal at the focus after the fourth OAP. The crystal should be mounted on an x-y translation stage. The angle of the crystal surface with respect to the incident pump beam is highly sensitive. Orient the crystal such that it is $\sim$1–2° off from perfect normal incidence. The crystal should not be exactly at 90° incidence or the pump laser will be reflected backwards through the system and re-enter the laser cavity.

12. Perform final adjustments of the terahertz signal. The goal is to increase the measured terahertz signal intensity to its maximum possible value while simultaneously increasing the bandwidth of the measured spectrum. First, begin by adjusting the x-y translation stage of the GaP detector crystal until the maximum signal intensity is found. Second, adjust the tilt degrees of freedom of the final OAP to improve the overlap of the terahertz focus and the probe laser focus on the detector crystal. Third, adjust the x-y translation stage of the photoconductive antenna. Repeat this sequence of adjustments until the maximum terahertz signal is achieved. It is important at this stage to not adjust the first three OAPs or the terahertz beam focused on the sample and the detector crystal will contain significant distortions.

Alignment of the OAPs using a HeNe guide laser follows many of the same steps as the previous method. However, instead of using the pump and probe lasers themselves, a *continuous wave* HeNe pointer has to be aligned such that its beam co-propagates

with the pump and probe lasers. Performing the initial alignment of the HeNe laser is nontrivial and a large source of error, but the technique offers the advantage of providing phase information via shear-plate interferometery, which allows flat terahertz wave fronts to be obtained with greater precision and control. To align the off-axis parabolic mirrors using HeNe guide lasers and shear-plate interferometer:

1. Carefully align the HeNe guide laser to accurately co-propagate with the pump and probe lasers.

2. Place the OAPs as described above. Instead of using a paper card at the intended location of the antenna, however, use a small pinhole. In this way coherent radiation can be obtained from the effective point source, which is not possible with a paper diffuser card. Align the OAPs as described above.

3. After placing and aligning each OAP, check the alignment with the shear-plate interferometer. The mirrors are correctly aligned with flat wave fronts when the interference fringes appearing in the viewing window of the shear-plate interferometer are straight and parallel to the reference line.

4. Place the photoconductive antenna and detector crystal and adjust their alignment as described above.

Bibliography

[1] B. Keimer and J. E. Moore, "The physics of quantum materials," *Nature Physics*, vol. 13, no. 11, pp. 1045–1055, 2017.

[2] J. G. Bednorz and K. A. Müller, "Possible High T_c Superconductivity in the Ba-La-Cu-O System," *Zeitschrift für Physik B Condensed Matter*, vol. 64, no. 2, pp. 189–193, 1986.

[3] B. Keimer, S. A. Kivelson, M. R. Norman, S. Uchida, and J. Zaanen, "From quantum matter to high-temperature superconductivity in copper oxides," *Nature*, vol. 518, pp. 179–186, 2015.

[4] E. Fradkin, S. A. Kivelson, and J. M. Tranquada, "Colloquium: Theory of intertwined orders in high temperature superconductors," *Reviews of Modern Physics*, vol. 87, no. 2, pp. 457–482, 2015.

[5] R. E. Glover III and M. Tinkham, "Transmission of Superconducting Films at Millimeter-Microwave and Far Infrared Frequencies," *Physical Review*, vol. 104, no. 3, p. 844, 1956.

[6] R. E. Glover III and M. Tinkham, "Conductivity of Superconducting Films for Photon Energies between 0.3 and $40kT_c$," *Physical Review*, vol. 108, no. 2, p. 243, 1957.

[7] M. Tinkham and R. A. Ferrell, "Determination of the superconducting skin depth from the energy gap and sum rule," *Physical Review Letters*, vol. 2, pp. 331–333, 1959.

[8] M. Tinkham, *Introduction to Superconductivity*, 2nd ed. Mineola, NY: Dover Publications, Inc., 2004.

[9] D. N. Basov, R. D. Averitt, D. Van Der Marel, M. Dressel, and K. Haule, "Electrodynamics of correlated electron materials," *Reviews of Modern Physics*, vol. 83, no. 2, pp. 471–541, 2011.

[10] P. U. Jepsen, D. G. Cooke, and M. Koch, "Terahertz spectroscopy and imaging – Modern techniques and applications," *Laser Photonics Reviews*, vol. 5, no. 1, pp. 124–166, 2011.

[11] D. G. Schlom, "Perspective: Oxide molecular-beam epitaxy rocks!" *APL Materials*, vol. 3, no. 6, p. 062403, 2015.

[12] J. E. Hirsch, "Apparent violation of the conductivity sum rule in certain superconductors," *Physica C: Superconductivity*, vol. 199, no. 3-4, pp. 305–310, 1992.

[13] J. E. Hirsch and F. Marsiglio, "Optical sum rule violation, superfluid weight, and condensation energy in the cuprates," *Physical Review B*, vol. 62, no. 22, pp. 15 131–15 150, 2000.

[14] H. J. A. Molegraaf, C. Presura, D. Van Der Marel, P. H. Kes, and M. Li, "Superconductivity-Induced Transfer of In-Plane Spectral Weight in $Bi_2Sr_2CaCu_2O_{8+\delta}$," *Science*, vol. 295, no. 5563, pp. 2239–2241, 2002.

[15] A. F. Santander-Syro, R. P. S. M. Lobo, N. Bontemps, Z. Konstantinovic, Z. Z. Li, and H. Raffy, "Pairing in cuprates from high-energy electronic states," *Europhysics Letters*, vol. 62, no. 4, p. 568, 2003.

[16] A. V. Boris, N. N. Kovaleva, O. V. Dolgov, T. Holden, C. T. Lin, B. Keimer, and C. Bernhard, "In-Plane Spectral Weight Shift of Charge Carriers in $YBa_2Cu_3O_{6.9}$," *Science*, vol. 304, no. 5671, pp. 708–710, 2004.

[17] S. Maiti and A. V. Chubukov, "Optical integral and sum-rule violation in high-T_c superconductors," *Physical Review B*, vol. 81, no. 24, p. 245111, 2010.

[18] M. B. Salamon, J. Shi, N. Overend, and M. A. Howson, "XY-like critical behavior of the thermodynamic and transport properties of $YBa_2Cu_3O_{7-x}$ in magnetic fields near T_c," *Physical Review B*, vol. 47, no. 9, pp. 5520–5523, 1993.

[19] S. Kamal, D. A. Bonn, N. Goldenfeld, P. J. Hirschfeld, R. Liang, and W. N. Hardy, "Penetration Depth Measurements of 3D XY Critical Behavior in $YBa_2Cu_3O_{6.95}$ Crystals," *Physical Review Letters*, vol. 73, pp. 1845–1848, 1994.

[20] J. Yong, M. J. Hinton, A. McCray, M. Randeria, M. Naamneh, A. Kanigel, and T. R. Lemberger, "Evidence of two-dimensional quantum critical behavior in the superfluid density of extremely underdoped $Bi_2Sr_2CaCu_2O_{8+\delta}$," *Physical Review B*, vol. 85, no. 18, p. 180507, 2012.

[21] I. Hetel, T. Lemberger, and M. Randeria, "Quantum critical behaviour in the superfluid density of strongly underdoped ultrathin copper oxide films," *Nature Physics*, vol. 3, pp. 700–702, 2007.

[22] D. M. Broun, W. A. Huttema, P. J. Turner, S. Özcan, B. Morgan, R. Liang, W. N. Hardy, and D. A. Bonn, "Superfluid Density in a Highly Underdoped $YBa_2Cu_3O_{6+y}$ Superconductor," *Physical Review Letters*, vol. 99, p. 237003, 2007.

[23] P. W. Anderson, "More Is Different," *Science*, vol. 177, no. 4047, pp. 393–396, 1972.

[24] E. T. Whittaker, *A History of the Theories of Aether and Electricity: From the Age of Descartes to the Close of the Nineteenth Century.* Longmans, Green, and Co., London; Hodges, Figgis, and Co., Ltd., Dublin, 1910.

[25] R. Bacon, *Opus Majus*, 1267, translated by J. H. Bridges, *The 'Opus Majus' of Roger Bacon*. London, Edinburgh, Oxford: Williams and Norgate, 1900.

[26] G. Logvenov, A. Gozar, and I. Bozovic, "High-Temperature Superconductivity in a Single Copper-Oxygen Plane," *Science*, vol. 326, no. 5953, pp. 699–702, 2009.

[27] C. Homes, S. Dordevic, M. Strongin, D. Bonn, R. Liang, W. Hardy, S. Komiya, Y. Ando, G. Yu, N. Kaneko, X. Zhao, M. Greven, D. N. Basov, and T. Timusk, "A universal scaling relation in high-temperature superconductors," *Nature*, vol. 430, pp. 539–541, 2004.

[28] J. Zaanen, "Why the temperature is high," *Nature*, vol. 430, no. 6999, pp. 512–513, 2004.

[29] C. Bernhard, T. Holden, A. V. Boris, N. N. Kovaleva, A. V. Pimenov, J. Humlicek, C. Ulrich, C. T. Lin, and J. L. Tallon, "Anomalous oxygen-isotope effect on the in-plane far-infrared conductivity of detwinned $YBa_2Cu_3{}^{16,18}O_{6.9}$," *Physical Review B*, vol. 69, no. 5, p. 052502, 2004.

[30] L. Benfatto, C. Castellani, and T. Giamarchi, "Kosterlitz-Thouless Behavior in Layered Superconductors: The Role of the Vortex Core Energy," *Physical Review Letters*, vol. 98, no. 11, p. 117008, 2007.

[31] L. Benfatto, C. Castellani, and T. Giamarchi, "Broadening of the Berezinskii-Kosterlitz-Thouless superconducting transition by inhomogeneity and finite-size effects," *Physical Review B*, vol. 80, no. 21, p. 214506, 2009.

[32] L. Benfatto, C. Castellani, and T. Giamarchi, "Doping dependence of the vortex-core energy in bilayer films of cuprates," *Physical Review B*, vol. 77, p. 100506(R), 2008.

[33] P. G. Baity, X. Shi, Z. Shi, L. Benfatto, and D. Popović, "Effective two-dimensional thickness for the Berezinskii-Kosterlitz-Thouless-like transition in a highly underdoped $La_{2-x}Sr_xCuO_4$," *Physical Review B*, vol. 93, no. 2, p. 024519, 2016.

[34] B. K. Chakraverty, "Possibility of insulator to superconductor phase transition," *Journal de Physique Lettres*, vol. 40, no. 5, pp. 99–100, 1979.

[35] M. K. Wu, J. R. Ashburn, C. J. Torng, P. H. Hor, R. L. Meng, L. Gao, Z. J. Huang, Y. Q. Wang, and C. W. Chu, "Superconductivity at 93 K in a New Mixed-Phase Y-Ba-Cu-O Compound System at Ambient Pressure," *Physical Review Letters*, vol. 58, no. 9, pp. 908–910, 1987.

[36] C. W. Chu, L. Z. Deng, and B. Lv, "Hole-doped cuprate high temperature superconductors," *Physica C: Superconductivity and its Applications*, vol. 514, pp. 290–313, 2015.

[37] N. Barišić, M. K. Chan, Y. Li, G. Yu, X. Zhao, M. Dressel, A. Smontara, and M. Greven, "Universal sheet resistance and revised phase diagram of the cuprate high-temperature superconductors," *Proceedings of the National Academy of Sciences*, vol. 110, no. 30, pp. 12 235–12 240, 2013.

[38] P. H. Hor, R. L. Meng, Y. Q. Wang, L. Gao, Z. J. Huang, J. Bechtold, K. Forster, and C. W. Chu, "Superconductivity above 90 K in the Square-Planar Compound System $A\mathrm{Ba_2Cu_3O_{6+x}}$ with A = Y, La, Nd, Sm, Eu, Gd, Ho, Er and Lu," *Physical Review Letters*, vol. 58, no. 18, pp. 1891–1894, 1987.

[39] J. Fink, N. Nücker, H. Romberg, M. Alexander, M. B. Maple, J. J. Neumeier, and J. W. Allen, "Evidence against hole filling by Pr in $\mathrm{YBa_2Cu_3O_7}$," *Physical Review B*, vol. 42, no. 7, pp. 4823–4826, 1990.

[40] H. A. Blackstead and J. D. Dow, "Implications of superconductivity of $\mathrm{PrBa_2Cu_3O_7}$," *Solid State Communications*, vol. 115, no. 3, pp. 137–140, 2000.

[41] J. Rossat-Mignod, L. P. Regnault, C. Vettier, P. Bourges, P. Burlet, J. Bossy, J. Y. Henry, and G. Lapertot, "Neutron scattering study of the $\mathrm{YBa_2Cu_3O_{6+x}}$ system," *Physica C: Superconductivity*, vol. 185, pp. 86–92, 1991.

[42] H. A. Mook, M. Yethiraj, G. Aeppli, T. E. Mason, and T. Armstrong, "Polarized Neutron Determination of the Magnetic Excitations in $\mathrm{YBa_2Cu_3O_7}$," *Physical Review Letters*, vol. 70, no. 22, pp. 3490–3493, 1993.

[43] H. F. Fong, B. Keimer, P. W. Anderson, D. Reznik, F. Doğan, and I. A. Aksay, "Phonon and Magnetic Neutron Scattering at 41 meV in $\mathrm{YBa_2Cu_3O_7}$," *Physical Review Letters*, vol. 75, no. 2, pp. 316–319, 1995.

[44] H. F. Fong, P. Bourges, Y. Sidis, L. P. Regnault, A. Ivanov, G. D. Gu, N. Koshizuka, and B. Keimer, "Neutron scattering from magnetic excitations in $\mathrm{Bi_2Sr_2CaCu_2O_{8+\delta}}$," *Nature*, vol. 398, no. 6728, pp. 588–591, 1999.

[45] C. C. Tsuei and J. R. Kirtley, "Pairing symmetry in cuprate superconductors," *Reviews of Modern Physics*, vol. 72, no. 4, pp. 969–1016, 2000.

[46] N. E. Hussey, "Phenomenology of the normal state in-plane transport properties of high-T_c cuprates," *Journal of Physics: Condensed Matter*, vol. 20, no. 12, p. 123201, 2008.

[47] G. R. Stewart, "Unconventional superconductivity," *Advances in Physics*, vol. 66, no. 2, pp. 75–196, 2017.

[48] W. W. Warren Jr, R. E. Walstedt, G. F. Brennert, R. J. Cava, R. Tycko, R. F. Bell, and G. Dabbagh, "Cu Spin Dynamics and Superconducting Precursor Effects in Planes above T_c in $\mathrm{YBa_2Cu_3O_{6.7}}$," *Physical Review Letters*, vol. 62, no. 10, pp. 1193–1196, 1989.

[49] H. Alloul, T. Ohno, and P. Mendels, "^{89}Y NMR Evidence for a Fermi-Liquid Behavior in $\mathrm{YBa_2Cu_3O_{6+x}}$," *Physical Review Letters*, vol. 63, no. 16, pp. 1700–1703, 1989.

[50] C. Homes, T. Timusk, R. Liang, D. Bonn, and W. Hardy, "Optical Conductivity of c Axis Oriented $\mathrm{YBa_2Cu_3O_{6.70}}$: Evidence for a Pseudogap," *Physical Review Letters*, vol. 71, no. 10, pp. 1645–1648, 1993.

[51] T. Timusk and B. Statt, "The pseudogap in high-temperature superconductors: an experimental survey," *Reports on Progress in Physics*, vol. 62, no. 1, pp. 61–121, 1999.

[52] M. Hashimoto, I. M. Vishik, R.-H. He, T. P. Devereaux, and Z.-X. Shen, "Energy gaps in high-transition-temperature cuprate superconductors," *Nature Physics*, vol. 10, no. 7, pp. 483–495, 2014.

[53] V. J. Emery and S. A. Kivelson, "Importance of phase fluctuations in superconductors with small superfluid density," *Nature*, vol. 374, no. 6521, pp. 434–437, 1995.

[54] M. Le Tacon, G. Ghiringhelli, J. Chaloupka, M. M. Sala, V. Hinkov, M. Haverkort, M. Minola, M. Bakr, K. J. Zhou, S. Blanco-Canosa, C. Monney, Y. T. Song, G. L. Sun, C. T. Lin, G. M. De Luca, M. Salluzzo, G. Khaliullin, T. Schmitt, L. Braicovich, and B. Keimer, "Intense paramagnon excitations in a large family of high-temperature superconductors," *Nature Physics*, vol. 7, no. 9, pp. 725–730, 2011.

[55] M. P. M. Dean, G. Dellea, R. S. Springell, F. Yakhou-Harris, K. Kummer, N. B. Brookes, X. Liu, Y. J. Sun, J. Strle, T. Schmitt, L. Braicovich, G. Ghiringhelli, I. Božović, and J. P. Hill, "Persistence of magnetic excitations in $La_{2-x}Sr_xCuO_4$ from the undoped insulator to the heavily overdoped non-superconducting metal," *Nature Materials*, vol. 12, no. 11, pp. 1019–1023, 2013.

[56] H. F. Fong, P. Bourges, Y. Sidis, L. P. Regnault, J. Bossy, A. Ivanov, D. L. Milius, I. A. Aksay, and B. Keimer, "Spin susceptibility in underdoped $YBa_2Cu_3O_{6+x}$," *Physical Review B*, vol. 61, no. 21, pp. 14 773–14 786, 2000.

[57] P. Dai, H. A. Mook, R. D. Hunt, and F. Doğan, "Evolution of the resonance and incommensurate spin fluctuations in superconducting $YBa_2Cu_3O_{6+x}$," *Physical Review B*, vol. 63, no. 5, p. 054525, 2001.

[58] J. Chang, E. Blackburn, A. T. Holmes, N. B. Christensen, J. Larsen, J. Mesot, R. Liang, D. A. Bonn, W. N. Hardy, A. Watenphul, M. v. Zimmermann, E. M. Forgan, and S. M. Hayden, "Direct observation of competition between superconductivity and charge density wave order in $YBa_2Cu_3O_{6.67}$," *Nature Physics*, vol. 8, no. 12, pp. 871–876, 2012.

[59] T. Wu, H. Mayaffre, S. Krämer, M. Horvatić, C. Berthier, W. N. Hardy, R. Liang, D. A. Bonn, and M.-H. Julien, "Magnetic-field-induced charge-stripe order in the high-temperature superconductor $YBa_2Cu_3O_y$," *Nature*, vol. 477, no. 7363, pp. 191–194, 2011.

[60] H.-H. Kim, S. M. Souliou, M. E. Barber, E. Lefrançois, M. Minola, M. Tortora, R. Heid, N. Nandi, R. A. Borzi, G. Garbarino, A. Bosak, J. Porras, T. Loew, M. König, P. M. Moll, A. P. Mackenzie, B. Keimer, C. W. Hicks, and M. Le Tacon, "Uniaxial pressure control of competing orders in a high-temperature superconductor," *Science*, vol. 362, no. 6418, pp. 1040–1044, 2018.

[61] M. Bluschke, A. Frano, E. Schierle, D. Putzky, F. Ghorbani, R. Ortiz, H. Suzuki, G. Christiani, G. Logvenov, E. Weschke, R. J. Birgeneau, E. H. da Silva Neto, M. Minola, S. Blanco-Canosa, and B. Keimer, "Stabilization of three-dimensional charge order in $YBa_2Cu_3O_{6+x}$ via epitaxial growth," *Nature Communications*, vol. 9, p. 2978, 2018.

[62] S. Sachdev, *Quantum Phase Transitions*, 2nd ed. Cambridge: Cambridge University Press, 2011.

[63] A. Gozar, G. Logvenov, L. F. Kourkoutis, A. T. Bollinger, L. A. Giannuzzi, D. A. Muller, and I. Bozovic, "High-temperature interface superconductivity between metallic and insulating copper oxides," *Nature*, vol. 455, no. 7214, pp. 782–785, 2008.

[64] Y. Yu, L. Ma, P. Cai, R. Zhong, C. Ye, J. Shen, G. D. Gu, X. H. Chen, and Y. Zhang, "High-temperature superconductivity in monolayer $Bi_2Sr_2CaCu_2O_{8+\delta}$," *Nature*, vol. 575, no. 7781, pp. 156–163, 2019.

[65] V. L. Ginzburg and L. D. Landau, "On the Theory of Superconductivity," *Zhurnal Eksperimental'noi i Teoreticheskoi Fiziki*, vol. 20, p. 1064, 1950, English translation in: L. D. Landau, Collected papers (Oxford: Pergamon Press, 1965) p. 546.

[66] L. D. Landau and E. M. Lifshitz, *Statistical Physics*, 3rd ed. Oxford: Pergamon Press, 1980.

[67] M. Greiter, "Is electromagnetic gauge invariance spontaneously violated in superconductors?" *Annals of Physics*, vol. 319, no. 1, pp. 217–249, 2005.

[68] S. Elitzur, "Impossibility of spontaneously breaking local symmetries," *Physical Review D*, vol. 12, no. 12, pp. 3978–3982, 1975.

[69] H. E. Stanley, "Dependence of Critical Properties on Dimensionality of Spins," *Physical Review Letters*, vol. 20, no. 12, pp. 589–592, 1968.

[70] K. G. Wilson, "Renormalization Group and Critical Phenomena. I. Renormalization Group and the Kadanoff Scaling Picture," *Physical Review B*, vol. 4, no. 9, pp. 3174–3183, 1971.

[71] K. G. Wilson, "Renormalization Group and Critical Phenomena. II. Phase-Space Cell Analysis of Critical Behavior," *Physical Review B*, vol. 4, no. 9, pp. 3184–3205, 1971.

[72] R. Peierls, "Quelques propriétés typiques des corps solides," *Annales de l'Institut H. Poincaré*, vol. 5, no. 3, pp. 177–222, 1935.

[73] L. D. Landau, "On the Theory of Phase Transitions, Part I," *Zhurnal Eksperimental'noi i Teoreticheskoi Fiziki*, vol. 7, p. 19, 1937, English translation in: L. D. Landau, Collected papers (Oxford: Pergamon Press, 1965) p. 193.

[74] L. D. Landau, "On the Theory of Phase Transitions, Part II," *Zhurnal Eksperimental'noi i Teoreticheskoi Fiziki*, vol. 7, p. 627, 1937, English translation in: L. D. Landau, Collected papers (Oxford: Pergamon Press, 1965) p. 209.

[75] N. D. Mermin and H. Wagner, "Absence of Ferromagnetism or Antiferromagnetism in One- or Two-Dimensional Isotropic Heisenberg Models," *Physical Review Letters*, vol. 17, no. 22, pp. 1133–1136, 1966.

[76] P. C. Hohenberg, "Existence of Long-Range Order in One and Two Dimensions," *Physical Review*, vol. 158, no. 2, pp. 383–386, 1967.

[77] N. D. Mermin, "Crystalline Order in Two Dimensions," *Physical Review*, vol. 176, no. 1, pp. 250–254, 1968.

[78] B. J. Alder and T. E. Wainright, "Phase Transition in Elastic Disks," *Physical Review*, vol. 127, no. 2, pp. 359–361, 1962.

[79] F. Wegner, "Spin-Ordering in a Planar Classical Heisenberg Model," *Zeitschrift für Physik*, vol. 206, pp. 465–470, 1967.

[80] V. L. Berezinskii, "Destruction of Long-Range Order in One-Dimensional and Two-Dimensional Systems Having a Continuous Symmetry Group I. Classical Systems," *Soviet Physics JETP*, vol. 32, no. 3, pp. 493–500, 1971.

[81] H. E. Stanley and T. A. Kaplan, "Possibility of a Phase Transition for the Two-Dimensional Heisenberg Model," *Physical Review Letters*, vol. 17, no. 17, pp. 913–915, 1966.

[82] M. A. Moore, "Additional Evidence for a Phase Transition in the Plane-Rotator and Classical Heisenberg Models for Two-Dimensional Lattices," *Physical Review Letters*, vol. 23, no. 15, pp. 861–863, 1969.

[83] V. L. Berezinskii, "Destruction of Long-Range Order in One-Dimensional and Two-Dimensional Systems Possessing a Continuous Symmetry Group II. Quantum Systems," *Soviet Physics JETP*, vol. 34, no. 3, pp. 610–616, 1972.

[84] J. M. Kosterlitz and D. J. Thouless, "Ordering, metastability and phase transitions in two-dimensional systems," *Journal of Physics C: Solid State Physics*, vol. 6, pp. 1181–1203, 1973.

[85] The Nobel Prize in Physics 2016, "Topological Phase Transitions and Topological Phases of Matter," The Royal Swedish Academy of Sciences, Tech. Rep., October 2016, https://www.nobelprize.org/prizes/physics/2016/press-release/.

[86] J. M. Kosterlitz, "The critical properties of the two-dimensional xy model," *Journal of Physics C: Solid State Physics*, vol. 7, pp. 1046–1060, 1974.

[87] P. Minnhagen, "The two-dimensional Coulomb gas, vortex unbinding, and superfluid-superconducting films," *Reviews of Modern Physics*, vol. 59, pp. 1001–1066, 1987.

[88] J. M. Kosterlitz and D. J. Thouless, "Long range order and metastability in two dimensional solids and superfluids. (Application of dislocation theory)," *Journal of Physics C: Solid State Physics*, vol. 5, no. 11, pp. L124–L126, 1972.

[89] D. R. Nelson and J. M. Kosterlitz, "Universal Jump in the Superfluid Density of Two-Dimensional Superfluids," *Physical Review Letters*, vol. 39, no. 19, pp. 1201–1205, 1977.

[90] P. Minnhagen and G. G. Warren, "Superfluid density of a two-dimensional fluid," *Physical Review B*, vol. 24, no. 5, pp. 2526–2532, 1981.

[91] J. V. José, L. P. Kadanoff, S. Kirkpatrick, and D. R. Nelson, "Renormalization, vortices, and symmetry-breaking perturbations in the two-dimensional planar model," *Physical Review B*, vol. 16, no. 3, pp. 1217–1241, 1977.

[92] J. M. Kosterlitz, "Kosterlitz-Thouless physics: a review of key issues," *Reports on Progress in Physics*, vol. 79, no. 2, p. 026001, 2016.

[93] M. H. W. Chan, A. W. Yanof, and J. D. Reppy, "Superfluidity of Thin ^{4}He Films," *Physical Review Letters*, vol. 32, no. 24, pp. 1347–1350, 1974.

[94] D. J. Bishop and J. D. Reppy, "Study of the Superfluid Transition in Two-Dimensional ^{4}He Films," *Physical Review Letters*, vol. 40, no. 26, pp. 1727–1730, 1978.

[95] D. J. Bishop and J. D. Reppy, "Study of the Superfluid Transition in Two-Dimensional ^{4}He Films," *Physical Review B*, vol. 22, no. 11, pp. 5171–5185, 1980.

[96] I. Rudnick, "Critical Surface Density of the Superfluid Component in ^{4}He Films," *Physical Review Letters*, vol. 40, no. 22, pp. 1454–1455, 1978.

[97] D. J. Thouless, M. Kohmoto, M. P. Nightingale, and M. den Nijs, "Quantized Hall Conductance in a Two-Dimensional Periodic Potential," *Physical Review Letters*, vol. 49, no. 6, pp. 405–408, 1982.

[98] J. E. Avron, D. Osadchy, and R. Seiler, "A Topological Look at the Quantum Hall Effect," *Physics Today*, vol. 56, no. 8, pp. 38–42, 2003.

[99] M. Z. Hasan and C. L. Kane, "Colloquium: Topological insulators," *Reviews of Modern Physics*, vol. 82, no. 4, pp. 3045–3067, 2010.

[100] A. Bansil, H. Lin, and T. Das, "Colloquium: Topological band theory," *Reviews of Modern Physics*, vol. 88, no. 2, p. 021004, 2016.

[101] J. Pearl, "Distinctive Properties of Quantized Vortices in Superconducting Films," in *Low Temperature Physics LT9. Proceedings of the IXth International Conference on Low Temperature Physics*, J. G. Daunt, D. O. Edwards, F. J. Milford, and M. Yaqub, Eds. Plenum Press, New York, 1965, pp. 566–570.

[102] J. Pearl, "Current Distribution in Superconducting Films Carrying Quantized Fluxoids," *Applied Physics Letters*, vol. 5, no. 4, pp. 65–66, 1964.

[103] M. R. Beasley, J. E. Mooij, and T. P. Orlando, "Possibility of Vortex-Antivortex Pair Dissociation in Two-Dimensional Superconductors," *Physical Review Letters*, vol. 42, no. 17, pp. 1165–1168, 1979.

[104] S. Doniach and B. A. Huberman, "Topological Excitations in Two-Dimensional Superconductors," *Physical Review Letters*, vol. 42, no. 17, pp. 1169–1172, 1979.

[105] J. E. Mooij, "Two-Dimensional Transition Superconducting Films," in *Percolation, Localization, and Superconductivity*, ser. NATO ASI Series B, Physics, A. M. Goldman and S. A. Wolf, Eds. Plenum New York, 1984, vol. 109, pp. 325–370.

[106] P. W. Anderson, "Considerations on the Flow of Superfluid Helium," *Reviews of Modern Physics*, vol. 38, no. 2, pp. 298–310, 1966.

[107] S. Teitel and C. Jayaprakash, "Resistive transitions in regular superconducting wire networks," *Journal de Physique Lettres*, vol. 46, no. 1, pp. 33–38, 1985.

[108] R. F. Voss, C. M. Knoedler, and P. M. Horn, "Phase-Slip Shot Noise at the Two-Dimensional Superconducting Transition: Evidence for Vortices?" *Physical Review Letters*, vol. 45, no. 8, pp. 1523–1526, 1980.

[109] V. Ambegaokar, B. I. Halperin, D. R. Nelson, and E. D. Siggia, "Dissipation in Two-Dimensional Superfluids," *Physical Review Letters*, vol. 40, no. 12, pp. 783–786, 1978.

[110] V. Ambegaokar, B. I. Halperin, D. R. Nelson, and E. D. Siggia, "Dynamics of superfluid films," *Physical Review B*, vol. 21, no. 5, pp. 1806–1826, 1980.

[111] B. I. Halperin and D. R. Nelson, "Resistive Transition in Superconducting Films," *Journal of Low Temperature Physics*, vol. 36, no. 5/6, pp. 599–616, 1979.

[112] S. R. Shenoy, "Dynamic conductivity of a two-dimensional Josephson junction array," *Journal of Physics C: Solid State Physics*, vol. 18, pp. 5163–5188, 1985.

[113] A. M. Kadin, K. Epstein, and A. M. Goldman, "Renormalization and the Kosterlitz-Thouless transition in a two-dimensional superconductor," *Physical Review B*, vol. 27, no. 11, pp. 6691–6702, 1983.

[114] K. Epstein, A. M. Goldman, and A. M. Kadin, "Vortex-Antivortex Pair Dissociation in Two-Dimensional Superconductors," *Physical Review Letters*, vol. 47, no. 7, pp. 534–537, 1981.

[115] A. F. Hebard and A. T. Fiory, "Critical-Exponent Measurements of a Two-Dimensional Superconductor," *Physical Review Letters*, vol. 50, no. 20, pp. 1603–1606, 1983.

[116] W. Zhao, Q. Wang, M. Liu, W. Zhang, Y. Wang, M. Chen, Y. Guo, K. He, X. Chen, Y. Wang, J. Wang, X. Xie, Q. Niu, L. Wang, X. Ma, J. K. Jain, M. H. W. Chan, and Q.-K. Xue, "Evidence for Berezinskii–Kosterlitz–Thouless transition in atomically flat two-dimensional Pb superconducting films," *Solid StateCommunications*, vol. 165, pp. 59–63, 2013.

[117] S. A. Wolf, D. U. Gubser, and Y. Imry, "Universal Current Scaling in the Critical Region of a Two-Dimensional Superconducting Phase Transition," *Physical Review Letters*, vol. 42, no. 5, pp. 324–327, 1979.

[118] G. Venditti, J. Biscaras, S. Hurand, N. Bergeal, J. Lesueur, A. Dogra, R. C. Budhani, M. Mondal, J. Jesudasan, P. Raychaudhuri, S. Caprara, and L. Benfatto, "Nonlinear *I-V* characteristics of two-dimensional superconductors: Berezinskii-Kosterlitz-Thouless physics versus inhomogeneity," *Physical Review B*, vol. 100, p. 064506, 2019.

[119] D. J. Resnick, J. C. Garland, J. T. Boyd, S. Shoemaker, and R. S. Newrock, "Kosterlitz-Thouless Transition in Proximity-Coupled Superconducting Arrays," *Physical Review Letters*, vol. 47, no. 21, pp. 1542–1545, 1981.

[120] D. W. Abraham, C. J. Lobb, M. Tinkham, and T. M. Klapwijk, "Resistive transition in two-dimensional arrays of superconducting weak links," *Physical Review B*, vol. 26, no. 9, pp. 5268–5271, 1982.

[121] R. W. Crane, N. P. Armitage, A. Johansson, G. Sambandamurthy, D. Shahar, and G. Grüner, "Fluctuations, dissipation, and nonuniversal superfluid jumps in two-dimensional superconductors," *Physical Review B*, vol. 75, p. 094506, 2007.

[122] K. Medvedyeva, B. J. Kim, and P. Minnhagen, "Analysis of current-voltage characteristics of two-dimensional superconductors: Finite-size scaling behavior in the vicinity of the Kosterlitz-Thouless transition," *Physical Review B*, vol. 62, no. 21, pp. 14 531–14 540, 2000.

[123] J. Holzer, R. S. Newrock, C. J. Lobb, T. Aouaroun, and S. T. Herbert, "Finite-size effects and dynamical scaling in two-dimensional Josephson junction arrays," *Physical Review B*, vol. 63, p. 184508, 2001.

[124] A. Gurevich and V. M. Vinokur, "Size effects in the nonlinear resistance and flux creep in a virtual Berezinskii-Kosterlitz-Thouless state of superconducting films," *Physical Review Letters*, vol. 100, no. 22, p. 227007, 2008.

[125] A. T. Fiory, A. F. Hebard, and W. I. Glaberson, "Superconducting phase transitions in indium/indium-oxide thin-film composites," *Physical Review B*, vol. 28, no. 9, pp. 5075–5087, 1983.

[126] A. F. Hebard and A. T. Fiory, "Evidence for the Kosterlitz-Thouless Transition in Thin Superconducting Aluminum Films," *Physical Review Letters*, vol. 44, no. 4, pp. 291–294, 1980.

[127] A. Kamlapure, M. Mondal, M. Chand, A. Mishra, J. Jesudasan, V. Bagwe, L. Benfatto, V. Tripathi, and P. Raychaudhuri, "Measurement of magnetic penetration depth and superconducting energy gap in very thin epitaxial NbN films," *Applied Physics Letters*, vol. 96, no. 7, p. 072509, 2010.

[128] J. Yong, T. R. Lemberger, L. Benfatto, K. Ilin, and M. Siegel, "Robustness of the Berezinskii-Kosterlitz-Thouless transition in ultrathin NbN films near the superconductor-insulator transition," *Physical Review B*, vol. 87, p. 184505, 2013.

[129] S. J. Turneaure, T. R. Lemberger, and J. M. Graybeal, "Dynamic impedance of two-dimensional superconducting films near the superconducting transition," *Physical Review B*, vol. 63, no. 17, p. 174505, 2001.

[130] A. Yazdani, W. White, M. Hahn, M. Gabay, M. Beasley, and A. Kapitulnik, "Observation of Kosterlitz-Thouless-type melting of the disordered vortex lattice in thin films of a-MoGe," *Physical Review Letters*, vol. 70, no. 4, pp. 505–508, 1993.

[131] S. Misra, L. Urban, M. Kim, G. Sambandamurthy, and A. Yazdani, "Measurements of the Magnetic-Field-Tuned Conductivity of Disordered Two-Dimensional $Mo_{43}Ge_{57}$ and InO_x Superconducting Films: Evidence for a Universal Minimum Superfluid Response," *Physical Review Letters*, vol. 110, no. 3, p. 037002, 2013.

[132] J. Bardeen and M. J. Stephen, "Theory of the motion of vortices in superconductors," *Physical Review*, vol. 140, no. 4A, pp. A1197–A1207, 1965.

[133] P. A. Bancel and K. E. Gray, "Search for Vortex Unbinding in Two-Dimensional Superconductors," *Physical Review Letters*, vol. 46, no. 2, pp. 148–152, 1981.

[134] P. Minnhagen, "Kosterlitz-Thouless transition for a two-dimensional superconductor: Magnetic-field dependence from a Coulomb-gas analogy," *Physical Review B*, vol. 23, no. 11, pp. 5745–5761, 1981.

[135] B. Jeanneret, P. Flückiger, J. L. Gavilano, C. Leemann, and P. Martinoli, "Critical phase fluctuations in superconducting wire networks," *Physical Review B*, vol. 40, no. 16, p. 11374(R), 1989.

[136] M. Wallin, "Phenomenological dynamics for two-dimensional superfluids," *Physical Review B*, vol. 41, no. 10, pp. 6575–6581, 1990.

[137] M. Mondal, S. Kumar, M. Chand, A. Kamlapure, G. Saraswat, G. Seibold, L. Benfatto, and P. Raychaudhuri, "Role of the Vortex-Core Energy on the Berezinskii-Kosterlitz-Thouless Transition in Thin Films of NbN," *Physical Review Letters*, vol. 107, no. 21, p. 217003, 2011.

[138] L. Benfatto, C. Castellani, and T. Giamarchi, "Berezinskii-Kosterlitz-Thouless Transition within the Sine-Gordon Approach: The Role of the Vortex-Core Energy," in *40 Years of Berezinskii-Kosterlitz-Thouless Theory*. World Scientific, 2013, pp. 161–199.

[139] P. Minnhagen, "Nonuniversal Jumps and the Kosterlitz-Thouless Transition," *Physical Review Letters*, vol. 54, no. 21, pp. 2351–2354, 1985.

[140] P. Minnhagen, "New renormalization equations for the Kosterlitz-Thouless transition," *Physical Review B*, vol. 32, no. 5, pp. 3088–3102, 1985.

[141] P. Minnhagen and M. Wallin, "New phase diagram for the two-dimensional Coulomb gas," *Physical Review B*, vol. 36, no. 10, pp. 5620–5623, 1987.

[142] P. Minnhagen and M. Wallin, "Results for the phase diagram of the two-dimensional Coulomb gas," *Physical Review B*, vol. 40, no. 7, pp. 5109–5130, 1989.

[143] J. Lee, J. M. Kosterlitz, and E. Granato, "Monte Carlo study of frustrated XY models on a triangular and square lattice," *Physical Review B*, vol. 43, no. 13, p. 11531(R), 1991.

[144] A. Diehl, M. C. Barbosa, and Y. Levin, "Sine-Gordon mean field theory of a Coulomb gas," *Physical Review E*, vol. 56, no. 1, pp. 619–622, 1997.

[145] W. Liu, M. Kim, G. Sambandamurthy, and N. P. Armitage, "Dynamical study of phase fluctuations and their critical slowing down in amorphous superconducting films," *Physical Review B*, vol. 84, no. 2, p. 024511, 2011.

[146] R. Ganguly, D. Chaudhuri, P. Raychaudhuri, and L. Benfatto, "Slowing down of vortex motion at the Berezinskii-Kosterlitz-Thouless transition in ultrathin NbN films," *Physical Review B*, vol. 91, no. 5, p. 054514, 2015.

[147] I. Maccari, L. Benfatto, and C. Castellani, "Broadening of the Berezinskii-Kosterlitz-Thouless transition by correlated disorder," *Physical Review B*, vol. 96, no. 6, p. 060508(R), 2017.

[148] I. Maccari, L. Benfatto, and C. Castellani, "The BKT Universality Class in the Presence of Correlated Disorder," *Condensed Matter*, vol. 3, no. 1, p. 8, 2018.

[149] A. B. Harris, "Effect of random defects on the critical behaviour of Ising models," *Journal of Physics C: Solid State Physics*, vol. 7, no. 9, pp. 1671–1692, 1968.

[150] A. Larkin and A. Varlamov, *Theory of Fluctuations in Superconductors*. Oxford, UK: Clarendon Press, 2005.

[151] P. A. Lee and S. R. Shenoy, "Effective Dimensionality Change of Fluctuations in Superconductors in a Magnetic Field," *Physical Review Letters*, vol. 28, no. 16, pp. 1025–1028, 1972.

[152] D. J. Thouless, "Critical Fluctuations of a Type-II Superconductor in a Magnetic Field," *Physical Review Letters*, vol. 34, no. 15, pp. 946–949, 1975.

[153] D. S. Fisher, M. P. A. Fisher, and D. A. Huse, "Thermal fluctuations, quenched disorder, phase transitions, and transport in type-II superconductors," *Physical Review B*, vol. 43, no. 1, pp. 130–159, 1991.

[154] V. Pasler, P. Schweiss, C. Meingast, B. Obst, H. Wühl, A. I. Rykov, and S. Tajima, "3D-XY Critical Fluctuations of the Thermal Expansivity in Detwinned $YBa_2Cu_3O_{7-\delta}$ Single Crystals Near Optimal Doping," *Physical Review Letters*, vol. 81, no. 5, pp. 1094–1097, 1998.

[155] A. Junod, A. Erb, and C. Renner, "Specific heat of high temperature superconductors in high fields at T_c: from BCS to the Bose-Einstein condensation," *Physica C: Superconductivity*, vol. 317, pp. 333–344, 1999.

[156] N.-C. Yeh and C. C. Tsuei, "Quasi-two-dimensional phase fluctuations in bulk superconducting $YBa_2Cu_3O_7$ single crystals," *Physical Review B*, vol. 39, no. 13, pp. 9708–9711, 1989.

[157] V. I. Nizhankovskiy and K. Rogacki, "BKT transition observed in magnetic and electric properties of $YBa_2Cu_3O_{7-\delta}$ single crystals," *Physical Review B*, vol. 100, p. 104510, 2019.

[158] S. N. Artemenko and A. Kruglov, "Structure of 2D vortex in a layered high-T_c superconductor," *Physics Letters A*, vol. 143, no. 9, pp. 485–488, 1990.

[159] J. R. Clem, "Two-dimensional vortices in a stack of thin superconducting films: A model for high-temperature superconducting multilayers," *Physical Review B*, vol. 43, no. 10, pp. 7837–7846, 1991.

[160] O. Cyr-Choinière, R. Daou, F. Laliberté, C. Collignon, S. Badoux, D. LeBoeuf, J. Chang, B. J. Ramshaw, D. A. Bonn, W. N. Hardy, R. Liang, J.-Q. Yan, J.-G. Cheng, J.-S. Zhou, J. B. Goodenough, S. Pyon, T. Takayama, H. Takagi, N. Doiron-Leyraud, and L. Taillefer, "Pseudogap temperature T^* of cuprate superconductors from the Nernst effect," *Physical Review B*, vol. 97, p. 064502, 2018.

[161] C. Meingast, V. Pasler, P. Nagel, A. Rykov, S. Tajima, and P. Olsson, "Phase Fluctuations and the Pseudogap in $YBa_2Cu_3O_x$," *Physical Review Letters*, vol. 86, pp. 1606–1609, 2001.

[162] M. S. Grbić, M. Požek, D. Paar, V. Hinkov, M. Raichle, D. Haug, B. Keimer, N. Barišić, and A. Dulčić, "Temperature range of superconducting fluctuations above T_c in $YBa_2Cu_3O_{7-\delta}$ single crystals," *Physical Review B*, vol. 83, p. 144508, 2011.

[163] A. Dubroka, M. Rössle, K. W. Kim, V. K. Malik, D. Munzar, D. N. Basov, A. A. Schafgans, S. J. Moon, C. T. Lin, D. Haug, V. Hinkov, B. Keimer, T. Wolf, J. G. Storey, J. L. Tallon, and C. Bernhard, "Evidence of a Precursor Superconducting Phase at Temperatures as High as 180 K in $RBa_2Cu_3O_{7-\delta}$ ($R = \mathrm{Y, Gd, Eu}$) Superconducting Crystals from Infrared Spectroscopy," *Physical Review Letters*, vol. 106, p. 047006, 2011.

[164] M. Franz and A. P. Iyengar, "Superfluid Density of Strongly Underdoped Cuprate Superconductors from a Four-Dimensional XY Model," *Physical Review Letters*, vol. 96, no. 4, p. 047007, 2006.

[165] G. Blatter, M. V. Feigel'man, V. B. Geshkenbein, A. I. Larkin, and V. M. Vinokur, "Vortices in high-temperature superconductors," *Reviews of Modern Physics*, vol. 66, pp. 1125–1388, 1994.

[166] K. H. Fischer, "Kosterlitz-Thouless transition in layered high-T_c superconductors," *Physica C: Superconductivity*, vol. 210, no. 1-2, pp. 179–187, 1993.

[167] Q. Li, X. X. Xi, X. D. Wu, A. Inam, S. Vadlamannati, W. L. McLean, T. Venkatesan, R. Ramesh, D. M. Hwang, J. A. Martinez, and L. Nazar, "Interlayer Coupling effect in High-T_c Superconductors Probed by $YBa_2Cu_3O_{7-\ x}/PrBa_2Cu_3O_{7-x}$ Superlattices," *Physical Review Letters*, vol. 64, no. 25, pp. 3086–3089, 1990.

[168] D. H. Lowndes, D. P. Norton, and J. D. Budai, "Superconductivity in Nonsymmetric Epitaxial $YBa_2Cu_3O_{7-x}/PrBa_2Cu_3O_{7-x}$ Superlattices: The Superconducting Behavior of Cu-O Bilayers," *Physical Review Letters*, vol. 65, no. 9, pp. 1160–1163, 1990.

[169] T. Terashima, K. Shimura, Y. Bando, Y. Matsuda, A. Fujiyama, and S. Komiyama, "Superconductivity of One-Unit-Cell Thick $YBa_2Cu_3O_7$ Thin Film," *Physical Review Letters*, vol. 67, no. 10, pp. 1362–1365, 1991.

[170] Q. Y. Ying and H. S. Kwok, "Kosterlitz-Thouless transition and conductivity fluctuations in Y-Ba-Cu-O thin films," *Physical Review B*, vol. 42, no. 4, pp. 2242–2247, 1990.

[171] S. Vadlamannati, Q. Li, T. Venkatesan, W. L. McLean, and P. Lindenfeld, "Enhanced Kosterlitz-Thouless transition in $YBa_2Cu_3O_{7-x}/PrBa_2Cu_3O_{7-x}$ multilayers as a measure of two-dimensionality," *Physical Review B*, vol. 44, no. 13, pp. 7094–7097, 1991.

[172] M. Ban, T. Ichiguchi, and T. Onogi, "Power laws in the resistive state in high-T_c superconductors," *Physical Review B*, vol. 40, no. 7, pp. 4419–4422, 1989.

[173] M. Rasolt, T. Edis, and Z. Tešanović, "Kosterlitz-Thouless Transition and Charge Redistribution in the Superconductivity of YBCO/PBCO Superlattices," *Physical Review Letters*, vol. 66, no. 22, pp. 2927–2930, 1991.

[174] Y. Matsuda, S. Komiyama, T. Terashima, K. Shimura, and Y. Bando, "Disappearance of Hall Resistance in One-Unit-Cell-Thick $YBa_2Cu_3O_{7-\delta}$: Evidence of Free Vortex-Antivortex Excitation," *Physical Review Letters*, vol. 69, no. 22, pp. 3228–3231, 1992.

[175] Y. Matsuda, S. Komiyama, T. Onogi, T. Terashima, K. Shimura, and Y. Bando, "Thickness dependence of the Kosterlitz-Thouless transition in ultrathin $YBa_2Cu_3O_{7-\delta}$ films," *Physical Review B*, vol. 48, pp. 10 498–10 503, 1993.

[176] J. M. Repaci, C. Kwon, Q. Li, X. Jiang, T. Venkatessan, R. E. Glover, C. J. Lobb, and R. S. Newrock, "Absence of a Kosterlitz-Thouless transition in ultrathin $YBa_2Cu_3O_{7-\delta}$ films," *Physical Review B*, vol. 54, pp. R9674–R9677, 1996.

[177] A. T. Fiory, A. F. Hebard, P. M. Mankiewich, and R. E. Howard, "Renormalization of the Mean-Field Superconducting Penetration Depth in Epitaxial $YBa_2Cu_3O_7$ Films," *Physical Review Letters*, vol. 61, no. 12, pp. 1419–1422, 1988.

[178] V. A. Gasparov, "Berezinskii-Kosterlitz-Thouless transition and fluctuation paraconductivity in $YBa_2Cu_3O_7$ single crystal films," *Physica C: Superconductivity*, vol. 178, no. 4-6, pp. 449–455, 1991.

[179] J. Kötzler, D. Görlitz, S. Skwirblies, and A. Wriedt, "Loss of Superconducting Phase Coherence in $YBa_2Cu_3O_7$ Films: Vortex-Loop Unbinding and Kosterlitz-Thouless Phenomena," *Physical Review Letters*, vol. 87, no. 12, p. 127005, 2001.

[180] Ö. Festin, P. Svedlindh, F. Rönnung, and D. Winkler, "Vortex fluctuations in high-T_c thin films close to the resistive transition," *Physical Review B*, vol. 70, no. 2, p. 024511, 2004.

[181] V. Gasparov, G. Tsydynzhapov, I. Batov, and Q. Li, "Temperature and Frequency Dependence of Complex Conductance of Ultrathin $YBa_2Cu_3O_{7-x}$ Films: Observation of Vortex-Antivortex Pair Unbinding," *Journal of Low Temperature Physics*, vol. 139, pp. 49–63, 2005.

[182] Y. Zuev, M. Seog Kim, and T. R. Lemberger, "Correlation between Superfluid Density and T_C of Underdoped $YBa_2Cu_3O_{6+x}$ Near the Superconductor-Insulator Transition," *Physical Review Letters*, vol. 95, p. 137002, 2005.

[183] J.-M. Triscone, Ø. Fischer, O. Brunner, L. Antognazza, A. D. Kent, M. G. Karkut *et al.*, "$YBa_2Cu_3O_7/PrBa_2Cu_3O_7$ Superlattices: Properties of Ultrathin Superconducting Layers Separated by Insulating Layers," *Physical Review Letters*, vol. 64, no. 7, pp. 804–807, 1990.

[184] A. Kebede, C.-S. Jee, J. Schwegler, J. E. Crow, T. Mihalisin, G. H. Myer, R. E. Salomon, P. Schlottmann, M. V. Kuric, S. H. Bloom, and R. P. Guertin, "Magnetic ordering and superconductivity in $Y_{1-x}Pr_xBa_2Cu_3O_{7-y}$," *Physical Review B*, vol. 40, no. 7, pp. 4453–4462, 1989.

[185] J. L. Peng, P. Klavins, R. N. Shelton, H. B. Radousky, P. A. Hahn, and L. Bernardez, "Upper critical field and normal-state properties of single-phase $Y_{1-x}Pr_xBa_2Cu_3O_{7-\delta}$ compounds," *Physical Review B*, vol. 40, no. 7, pp. 4517–4526, 1989.

[186] H. D. Yang, M. W. Lin, C. H. Luo, H. L. Tsay, and T. F. Young, "Effects of Ca substitution on the structural, electrical and magnetic properties of $PrBa_2Cu_3O_{7-y}$," *Physica C: Superconductivity*, vol. 203, no. 3-4, pp. 320–326, 1992.

[187] S. N. Artemenko, I. G. Gorlova, and Y. I. Latyshev, "Vortex motion and kosterlitz-thouless transition in superconducting single crystals $Bi_2Sr_2CaCu_2O_x$," *Physics Letters A*, vol. 138, no. 8, pp. 428–434, 1989.

[188] S. Martin, A. T. Fiory, R. M. Fleming, G. P. Espinosa, and A. S. Cooper, "Vortex-Pair Excitation near the Superconducting Transition of $Bi_2Sr_2CaCu_2O_8$ Crystals," *Physical Review Letters*, vol. 62, no. 6, pp. 677–680, 1989.

[189] A. K. Pradhan, S. J. Hazell, J. W. Hodby, C. Chen, Y. Hu, and B. M. Wanklyn, "Observation of the Kosterlitz-Thouless transition and of vortex fluctuations in superconducting single crystals of Bi-based cuprates," *Physical Review B*, vol. 47, no. 17, pp. 11 374–11 378, 1993.

[190] D. H. Kim, A. M. Goldman, J. H. Kang, and R. T. Kampwirth, "Kosterlitz-Thouless transition in $Tl_2Ba_2CaCu_2O_8$ thin films," *Physical Review B*, vol. 40, no. 13, pp. 8834–8839, 1989.

[191] S. H. Han, Y. Eltsev, and Ö. Rapp, "Three-dimensional XY critical fluctuations of the dc electrical conductivity in $Bi_2Sr_2CaCu_2O_{8+\delta}$ single crystals," *Physical Review B*, vol. 61, no. 17, pp. 11 776–11 779, 2000.

[192] K. D. Osborn, D. J. Van Harlingen, V. Aji, N. Goldenfeld, S. Oh, and J. N. Eckstein, "Critical dynamics of superconducting $Bi_2Sr_2CaCu_2O_{8+\delta}$ films," *Physical Review B*, vol. 68, no. 14, p. 144516, 2003.

[193] S. Weyeneth, T. Schneider, and E. Giannini, "Evidence for Kosterlitz-Thouless and three-dimensional XY critical behavior in $Bi_2Sr_2CaCu_2O_{8+\delta}$," *Physical Review B*, vol. 79, no. 21, p. 214504, 2009.

[194] C. T. Rogers, K. E. Myers, J. N. Eckstein, and I. Bozovic, "Brownian motion of vortex-antivortex excitations in very thin films of $Bi_2Sr_2CaCu_2O_8$," *Physical Review Letters*, vol. 69, no. 1, pp. 160–163, 1992.

[195] J. Corson, R. Mallozzi, J. Orenstein, J. N. Eckstein, and I. Bozovic, "Vanishing of phase coherence in underdoped $Bi_2Sr_2CaCu_2O_{8+\delta}$," *Nature*, vol. 398, no. 6724, pp. 221–223, 1999.

[196] L. S. Bilbro, R. V. Aguilar, G. Logvenov, O. Pelleg, I. Božović, and N. P. Armitage, "Temporal correlations of superconductivity above the transition temperature in $La_{2-x}Sr_xCuO_4$ probed by terahertz spectroscopy," *Nature Physics*, vol. 7, no. 4, pp. 298–302, 2011.

[197] H. Kitano, T. Ohashi, A. Maeda, and I. Tsukada, "Critical microwave-conductivity fluctuations across the phase diagram of superconducting $La_{2-x}Sr_xCuO_4$ thin films," *Physical Review B*, vol. 73, no. 9, p. 092504, 2006.

[198] B. Leridon, J. Vanacken, T. Wambecq, and V. V. Moshchalkov, "Paraconductivity of underdoped $La_{2-x}Sr_xCuO_4$ thin-film superconductors using high magnetic fields," *Physical Review B*, vol. 76, no. 1, p. 012503, 2007.

[199] V. A. Gasparov and I. Božović, "Magnetic field and temperature dependence of complex conductance of ultrathin $La_{1.65}Sr_{0.45}CuO_4/La_2CuO_4$ films," *Physical Review B*, vol. 86, no. 9, p. 094523, 2012.

[200] M. Dressel and G. Grüner, *Electrodynamics of Solids: Optical Properties of Electrons in Matter*. Cambridge, UK: Cambridge University Press, 2002.

[201] J. C. Maxwell, "On Physical Lines of Force, parts I–IV," *The London, Edinburgh, and Dublin Philosophical Magazine and Journal of Science, Fourth Series*, vol. 21 & 23, 1861.

[202] J. C. Maxwell, "A Dynamical Theory of the Electromagnetic Field," *Philosophical Transactions of the Royal Society of London*, vol. 155, pp. 459–512, 1865.

[203] J. D. Jackson, *Classical Electrodynamics*, 3rd ed. Hoboken, NJ: John Wiley & Sons, Inc., 1999.

[204] A. Zangwill, *Modern Electrodynamics*. Cambridge, UK: Cambridge University Press, 2013.

[205] M. Longair, *Maxwell's Enduring Legacy: A Scientific History of the Cavendish Laboratory*. Cambridge, UK: Cambridge University Press, 2016.

[206] N. W. Ashcroft and D. N. Mermin, *Solid State Physics*. Belmont, CA: Brooks/Cole Cengage Learning, 1976.

[207] M. Born and E. Wolf, *Principles of Optics*, 7th ed. Cambridge, UK: Cambridge University Press, 1999.

[208] W. C. Röntgen, "On a New Kind of Rays," *Nature*, vol. 53, no. 1369, pp. 274–276, 1896.

[209] A. A. C. Swinton, "Professor Röntgen's Discovery," *Nature*, vol. 53, no. 1369, pp. 276–277, 1896.

[210] J. J. Thomson, "Cathode Rays," *The London, Edinburgh, and Dublin Philosophical Magazine and Journal of Science, Fifth Series*, vol. 44, no. 269, pp. 293–316, 1897.

[211] P. Drude, "Zur Elektronentheorie der Metalle," *Annalen der Physik*, vol. 306, pp. 566–613, 1900.

[212] P. Drude, "Zur Elektronentheorie der Metalle; II. Teil. Galvanomagnetische und thermomagnetische Effecte," *Annalen der Physik*, vol. 308, pp. 369–402, 1900.

[213] P. Drude, "Zur Ionentheorie der Metalle," *Physikalische Zeitschrift*, vol. 1, pp. 161–165, 1900.

[214] F. Wooten, *Optical Properties of Solids*. New York, NY: Academic Press, 1972.

[215] P. K. L. Drude, *Physik des Äthers auf elektromagnetischer Grundlage*. Stuttgart: F. Enke, 1894.

[216] M. Scheffler, M. Dressel, M. Jourdan, and H. Adrian, "Extremely slow Drude relaxation of correlated electrons," *Nature*, vol. 438, no. 7071, pp. 1135–1137, 2005.

[217] M. Dressel and M. Scheffler, "Verifying the Drude response," *Annalen der Physik*, vol. 15, no. 7-8, pp. 535–544, 2006.

[218] S. L. Adler, "Quantum Theory of the Dielectric Constant in Real Solids," *Physical Review*, vol. 126, no. 2, pp. 413–420, 1962.

[219] N. Wiser, "Dielectric Constant with Local Field Effects Included," *Physical Review*, vol. 129, no. 1, pp. 62–69, 1963.

[220] M. E. Peskin and D. V. Schroeder, *An Introduction to Quantum Field Theory*, D. Pines, Ed. Boca Raton, FL: CRC Press, Taylor & Francis Group, 1995.

[221] A. Altland and B. Simons, *Condensed Matter Field Theory*, 2nd ed. Cambridge, UK: Cambridge University Press, 2010.

[222] H. Bruus and K. Flensberg, *Many-Body Quantum Theory in Condensed Matter Physics*. Oxford, UK: Oxford University Press, 2004.

[223] R. A. Ferrell and R. E. Glover, "Conductivity of superconducting films: A sum rule," *Physical Review*, vol. 109, pp. 1398–1399, 1958.

[224] L. Genzel, "Far-Infrared Fourier Transform Spectroscopy," in *Millimeter and Submillimeter Wave Spectroscopy of Solids*, G. Grüner, Ed. Berlin Heidelberg: Springer-Verlag, 1998, ch. 5, pp. 169–220.

[225] Y. N. Pchelnikov, "Old Know-How in Helix TWT Development in the USSR," *AIP Conference Proceedings*, vol. 691, pp. 112–122, 2003.

[226] B. Epsztein, "Oscillateur à tube à ondes progressives avec propagation de l'énergie électromagnétique en sens inverse du faisceau," French Patent FR1 035 379A, April 15, 1953.

[227] R. Kompfner, "Backward Wave Tube," U.S. Patent US2 985 790A, May 23, 1961.

[228] R. Kompfner, "The Invention of Traveling Wave Tubes," *IEEE Transactions on Electron Devices*, vol. 23, no. 7, pp. 730–738, 1976.

[229] J. C. Wiltse, "History of Millimeter and Submillimeter Waves," *IEEE Transactions on Microwave Theory and Techniques*, vol. 32, no. 9, pp. 1118–1127, 1984.

[230] J. H. Booske, "Plasma physics and related challenges of millimeter-wave-to-terahertz and high power microwave generation," *Physics of Plasmas*, vol. 15, no. 5, 2008.

[231] D. F. Minenna, F. André, Y. Elskens, J. F. Auboin, F. Doveil, J. Puech, and É. Duverdier, "The traveling-wave tube in the history of telecommunication," *European Physical Journal H*, vol. 44, no. 1, pp. 1–36, 2019.

[232] G. Kozlov and A. Volkov, "Coherent Source Submillimeter Wave Spectroscopy," in *Millimeter and Submillimeter Wave Spectroscopy of Solids*, G. Grüner, Ed. Berlin Heidelberg: Springer-Verlag, 1998, ch. 3, pp. 51–109.

[233] J. H. Booske, R. J. Dobbs, C. D. Joye, C. L. Kory, G. R. Neil, G. S. Park, J. Park, and R. J. Temkin, "Vacuum electronic high power terahertz sources," *IEEE Transactions on Terahertz Science and Technology*, vol. 1, no. 1, pp. 54–75, 2011.

[234] H. R. Johnson, "Backward-Wave Oscillators," *Proceedings of the IRE*, vol. 43, no. 6, pp. 684–697, 1955.

[235] P. Palluel and A. K. Goldberger, "The O-Type Carcinotron Tube," *Proceedings of the IRE*, vol. 44, no. 3, pp. 333–345, 1956.

[236] R. Kompfner and N. T. Williams, "Backward-Wave Tubes," *Proceedings of the IRE*, vol. 41, no. 11, pp. 1602–1611, 1953.

[237] P. Siegel, "Terahertz technology," *IEEE Transactions on Microwave Theory and Techniques*, vol. 50, no. 3, pp. 910–928, mar 2002.

[238] G. P. Gallerano and S. Biedron, "Overview of terahertz radiation sources," *Proceedings of the 2004 FEL Conference*, pp. 216–221, 2004.

[239] M. Tonouchi, "Cutting-edge terahertz technology," *Nature Photonics*, vol. 1, no. 2, pp. 97–105, 2007.

[240] P. Chevalier, A. Amirzhan, F. Wang, M. Piccardo, S. G. Johnson, F. Capasso, and H. O. Everitt, "Widely tunable compact terahertz gas lasers," *Science*, vol. 366, no. 6467, pp. 856–860, 2019.

[241] B. S. Williams, "Terahertz quantum-cascade lasers," *Nature Photonics*, vol. 1, no. 9, pp. 517–525, 2007.

[242] B. Gorshunov, A. Volkov, I. Spektor, A. Prokhorov, A. Mukhin, M. Dressel, S. Uchida, and A. Loidl, "Terahertz BWO-spectrosopy," *International Journal of Infrared and Millimeter Waves*, vol. 26, no. 9, pp. 1217–1240, 2005.

[243] O. Stenzel, *The Physics of Thin Film Optical Spectra: An Introduction.* Berlin Heidelberg: Springer-Verlag, 2005.

[244] M. A. Ordal, R. J. Bell, R. W. Alexander Jr, L. L. Long, and M. R. Querry, "Optical properties of fourteen metals in the infrared and far infrared: Al, Co, Cu, Au, Fe, Pb, Mo, Ni, Pd, Pt, Ag, Ti, V, and W." *Applied Optics*, vol. 24, no. 24, pp. 4493–4495, 1985.

[245] J. Neu and C. A. Schmuttenmaer, "Tutorial: An introduction to terahertz time domain spectroscopy (THz-TDS)," *Journal of Applied Physics*, vol. 124, p. 231101, 2018.

[246] P. Y. Han, M. Tani, M. Usami, S. Kono, R. Kersting, and X.-C. Zhang, "A direct comparison between terahertz time-domain spectroscopy and far-infrared Fourier transform spectroscopy," *Journal of Applied Physics*, vol. 89, no. 4, pp. 2357–2359, 2001.

[247] M. C. Nuss and J. Orenstein, "Terahertz Time-Domain Spectroscopy," in *Millimeter and Submillimeter Wave Spectroscopy of Solids*, G. Grüner, Ed. Berlin Heidelberg: Springer-Verlag, 1998, ch. 2, pp. 7–50.

[248] A. Dreyhaupt, S. Winnerl, T. Dekorsy, and M. Helm, "High-intensity terahertz radiation from a microstructured large-area photoconductor," *Applied Physics Letters*, vol. 86, p. 121114, 2005.

[249] P. A. Elzinga, F. E. Lytle, Y. Jian, G. B. King, and N. M. Laurendeau, "Pump/Probe Spectroscopy by Asynchronous Optical Sampling," *Applied Spectroscopy*, vol. 41, no. 1, pp. 2–4, 1987.

[250] P. A. Elzinga, R. J. Kneisler, F. E. Lytle, Y. Jian, G. B. King, and N. M. Laurendeau, "Pump/probe method for fast analysis of visible spectral signatures utilizing asynchronous optical sampling," *Applied Optics*, vol. 26, no. 19, pp. 4303–4309, 1987.

[251] A. Bartels, R. Cerna, C. Kistner, A. Thoma, F. Hudert, C. Janke, and T. Dekorsy, "Ultrafast time-domain spectroscopy based on high-speed asynchronous optical sampling," *Review of Scientific Instruments*, vol. 78, p. 035107, 2007.

[252] G. Klatt, R. Gebs, C. Janke, T. Dekorsy, and A. Bartels, "Rapid-scanning terahertz precision spectrometer with more than 6 THz spectral coverage," *Optics Express*, vol. 17, no. 25, pp. 22 847–22 854, 2009.

[253] R. Gebs, G. Klatt, C. Janke, T. Dekorsy, and A. Bartels, "High-speed asynchronous optical sampling with sub-50fs time resolution," *Optics Express*, vol. 18, no. 6, pp. 5974–5983, 2010.

[254] W. Withayachumnankul, J. F. O'Hara, W. Cao, I. Al-Naib, and W. Zhang, "Limitation in thin-film sensing with transmission-mode terahertz time-domain spectroscopy," *Optics Express*, vol. 22, no. 1, pp. 972–986, 2014.

[255] J. Vázquez-Cabo, P. Chamorro-Posada, F. J. Fraile-Peláez, O. Rubiños López, J. M. López-Santos, and P. Martín-Ramos, "Windowing of THz time-domain spectroscopy signals: A study based on lactose," *Optics Communications*, vol. 336, pp. 386–396, 2016.

[256] W. A. Fladung, "Windows used for impact testing," in *Proceedings of the 15th International Modal Analysis Conference, Orlando, FL.* SPIE International Society for Optical Engineering, 1997, pp. 1662–1666.

[257] W. Fladung and R. Rost, "Application and correction of the exponential window for frequency response functions," *Mechanical Systems and Signal Processing*, vol. 11, no. 1, pp. 23–36, 1997.

[258] W. Withayachumnankul and M. Naftaly, "Fundamentals of Measurement in Terahertz Time-Domain Spectroscopy," *Journal of Infrared, Millimeter, and Terahertz Waves*, vol. 35, pp. 610–637, 2014.

[259] N. Laman and D. Grischkowsky, "Terahertz conductivity of thin metal films," *Applied Physics Letters*, vol. 93, p. 051105, 2008.

[260] M. A. Helal, T. Mori, and S. Kojima, "Softening of infrared-active mode of perovskite $BaZrO_3$ proved by terahertz time-domain spectroscopy," *Applied Physics Letters*, vol. 106, p. 182904, 2015.

[261] H. G. Tompkins and E. A. Irene, *Handbook of Ellipsometry.* William Andrew, 2005.

[262] T. I. Larkin, "Excitonic Fano resonances in Ta_2NiSe_5 and Ta_2NiS_5," Ph.D. dissertation, University of Stuttgart, 2016.

[263] Y. Saito, T. Nojima, and Y. Iwasa, "Highly crystalline 2D superconductors," *Nature Reviews Materials*, vol. 2, no. 1, pp. 1–18, 2016.

[264] I. Bozovic, J. N. Eckstein, N. Bozovic, and J. O'Donnell, "RHEED Studies of *a*-Axis Oriented $DyBa_2Cu_3O_7$ Films Grown by ALL-MBE," *MRS Online Proceedings Library Archive*, vol. 502, 1997.

[265] L. A. Tietz, C. B. Carter, D. K. Lathrop, S. E. Russek, R. A. Buhrman, and J. R. Michael, "Crystallography of $YBa_2Cu_3O_{6+x}$ thin film-substrate interfaces," *Journal of Materials Research*, vol. 4, no. 5, pp. 1072–1081, 1989.

[266] T. Venkatesan, X. D. Wu, B. Dutta, A. Inam, M. S. Hegde, D. M. Hwang, C. C. Chang, L. Nazar, and B. Wilkens, "High-temperature superconductivity in ultrathin films of $YBa_2Cu_3O_{7-x}$," *Applied Physics Letters*, vol. 54, no. 6, pp. 581–583, 1989.

[267] X. X. Xi, J. Geerk, G. Linker, Q. Li, and O. Meyer, "Preparation and superconducting properties of ultrathin $YBa_2Cu_3O_{7-x}$ films," *Applied Physics Letters*, vol. 54, no. 23, pp. 2367–2369, 1989.

[268] H.-U. Habermeier, "Science and technology of cuprate-based high temperature superconductor thin films, heterostructures and superlattices–the first 30 years," *Low Temperature Physics*, vol. 42, no. 10, pp. 840–862, 2016.

[269] C. Dekker, P. J. M. Wöltgens, R. H. Koch, B. W. Hussey, and A. Gupta, "Absence of a Finite-Temperature Vortex-Glass Phase Transition in Two-Dimensional $YBa_2Cu_3O_{7-\delta}$ Films," *Physical Review Letters*, vol. 69, no. 18, p. 2717, 1992.

[270] I. N. Chan, D. C. Vier, O. Nakamura, J. Hasen, J. Guimpel, S. Schultz, and I. K. Schuller, "Thickness dependence of the superconducting transition temperature of YBCO," *Physics Letters A*, vol. 175, no. 3-4, pp. 241–245, 1993.

[271] F. Baiutti, G. Christiani, and G. Logvenov, "Towards precise defect control in layered oxide structures by using oxide molecular beam epitaxy," *Beilstein Journal of Nanotechnology*, vol. 5, no. 1, pp. 596–602, 2014.

[272] D. G. Schlom, J. N. Eckstein, E. S. Hellman, S. K. Streiffer, J. S. Harris Jr, M. R. Beasley, J. C. Bravman, T. H. Geballe, C. Webb, K. E. Von Dessonneck, and F. Turner, "Molecular beam epitaxy of layered Dy-Ba-Cu-O compounds," *Applied Physics Letters*, vol. 53, no. 17, pp. 1660–1662, 1988.

[273] D. Putzky, P. Radhakrishnan, Y. Wang, P. Wochner, G. Christiani, M. Minola, P. A. van Aken, G. Logvenov, E. Benckiser, and B. Keimer, "Strain-induced structural transition in $DyBa_2Cu_3O_{7-x}$ films grown by atomic layer-by-layer molecular beam epitaxy," *Applied Physics Letters*, vol. 117, no. 7, p. 072601, 2020.

[274] J. Kircher, M. Alouani, M. Garriga, P. Murugaraj, J. Maier, C. Thomsen, M. Cardona, O. K. Andersen, and O. Jepsen, "Anisotropy of the dielectric function in $YBa_2Cu_3O_6$," *Physical Review B*, vol. 40, pp. 7368–7371, 1989.

[275] J. Kircher, M. K. Kelly, S. Rashkeev, M. Alouani, D. Fuchs, and M. Cardona, "Anisotropy and oxygen-stoichiometry dependence of the dielectric tensor of $YBa_2Cu_3O_{7-\delta}$ $(0 \leq \delta \leq 1)$," *Physical Review B*, vol. 44, no. 1, p. 217, 1991.

[276] S. L. Cooper, A. L. Kotz, M. A. Karlow, M. V. Klein, W. C. Lee, J. Giapintzakis, and D. M. Ginsberg, "Development of the optical conductivity with doping in single-domain $YBa_2Cu_3O_{6+x}$," *Physical Review B*, vol. 45, pp. 2549–2552, 1992.

[277] F. Rullier-Albenque, H. Alloul, and R. Tourbot, "Influence of Pair Breaking and Phase Fluctuations on Disordered High T_c Cuprate Superconductors," *Physical Review Letters*, vol. 91, p. 047001, 2003.

[278] M. Chiao, R. W. Hill, C. Lupien, L. Taillefer, P. Lambert, R. Gagnon, and P. Fournier, "Low-energy quasiparticles in cuprate superconductors: A quantitative analysis," *Physical Review B*, vol. 62, pp. 3554–3558, 2000.

[279] K. Tomimoto, I. Terasaki, A. I. Rykov, T. Mimura, and S. Tajima, "Impurity effects on the superconducting coherence length in Zn- or Ni-doped $YBa_2Cu_3O_{6.9}$ single crystals," *Physical Review B*, vol. 60, pp. 114–117, 1999.

[280] S. Kamal, R. Liang, A. Hosseini, D. A. Bonn, and W. N. Hardy, "Magnetic penetration depth and surface resistance in ultrahigh-purity $YBa_2Cu_3O_{7-\delta}$ crystals," *Physical Review B*, vol. 58, pp. R8933–R8936, 1998.

[281] N. R. Lee-Hone, J. S. Dodge, and D. M. Broun, "Disorder and superfluid density in overdoped cuprate superconductors," *Physical Review B*, vol. 96, p. 024501, 2017.

[282] L. C. Hebel and C. P. Slichter, "Nuclear Spin Relaxation in Normal and Superconducting Aluminum," *Physical Review*, vol. 113, no. 6, pp. 1504–1519, 1959.

[283] P. C. Hammel, M. Takigawa, R. H. Heffner, Z. Fisk, and K. C. Ott, "Spin dynamics at oxygen sites in yba 2 cu 3 o 7," *Physical Review Letters*, vol. 63, no. 18, p. 1992, 1989.

[284] F. Marsiglio, "Coherence effects in electromagnetic absorption in superconductors," *Physical Review B*, vol. 44, no. 10, p. 5373, 1991.

[285] D. B. Romero, C. D. Porter, D. B. Tanner, L. Forro, D. Mandrus, L. Mihaly, G. L. Carr, and G. P. Williams, "Quasiparticle Damping in $Bi_2Sr_2CaCu_2O_8$ and $Bi_2Sr_2CuO_6$," *Physical Review Letters*, vol. 68, no. 10, p. 1590, 1992.

[286] F. Gao, D. B. Romero, D. B. Tanner, J. Talvacchio, and M. G. Forrester, "Infrared properties of epitaxial $La_{2-x}Sr_xCuO_4$ thin films in the normal and superconducting states," *Physical Review B*, vol. 47, no. 2, p. 1036, 1993.

[287] F. Gao, G. L. Carr, C. D. Porter, D. B. Tanner, G. P. Williams, C. J. Hirschmugl, B. Dutta, X. D. Wu, and S. Etemad, "Quasiparticle damping and the coherence peak in $YBa_2Cu_3O_{7-\delta}$," *Physical Review B*, vol. 54, no. 1, p. 700, 1996.

[288] D. A. Bonn, R. Liang, T. M. Riseman, D. J. Baar, D. C. Morgan, K. Zhang, P. Dosanjh, T. L. Duty, A. MacFarlane, G. D. Morris, J. H. Brewer, W. N. Hardy, C. Kallin, and A. J. Berlinsky, "Microwave determination of the quasiparticle scattering time in $YBa_2Cu_3O_{6.95}$," *Physical Review B*, vol. 47, no. 17, pp. 11 314–11 328, 1993.

[289] A. Hosseini, R. Harris, S. Kamal, P. Dosanjh, J. Preston, R. Liang, W. N. Hardy, and D. A. Bonn, "Microwave spectroscopy of thermally excited quasiparticles in $YBa_2Cu_3O_{6.99}$," *Physical Review B*, vol. 60, pp. 1349–1359, 1999.

[290] H. J. Fink, "Microwave surface impedance of $YBa_2Cu_3O_{6.99}$: Comparison of theory and experiment," *Physical Review Letters*, vol. 61, pp. 6346–6351, 2000.

[291] R. Kubo, "Statistical-Mechanical Theory of Irreversible Processes. I. General Theory and Simple Applications to Magnetic and Conduction Problems," *Journal of the Physical Society of Japan*, vol. 12, no. 6, pp. 570–586, 1957.

[292] L. Benfatto and S. G. Sharapov, "Optical-conductivity sum rule in cuprates and unconventional charge density waves: a short review," *Low Temperature Physics*, vol. 32, no. 6, pp. 533–545, 2006.

[293] A. Toschi, M. Capone, M. Ortolani, P. Calvani, S. Lupi, and C. Castellani, "Temperature Dependence of the Optical Spectral Weight in the Cuprates: Role of Electron Correlations," *Physical Review Letters*, vol. 95, no. 9, p. 097002, 2005.

[294] K. Haule and G. Kotliar, "Strongly correlated superconductivity: A plaquette dynamical mean-field theory study," *Physical Review B*, vol. 76, no. 10, p. 104509, 2007.

[295] W. N. Hardy, D. A. Bonn, D. C. Morgan, R. Liang, and K. Zhang, "Precision measurements of the temperature dependence of λ in $YBa_2Cu_3O_{6.95}$: Strong evidence for nodes in the gap function," *Physical Review Letters*, vol. 70, pp. 3999–4002, 1993.

[296] P. J. Hirschfeld and N. Goldenfeld, "Effect of strong scattering on the low-temperature penetration depth of a d-wave superconductor," *Physical Review B*, vol. 48, no. 6, p. 4219, 1993.

[297] Z.-B. Wu, D. Putzky, A. K. Kundu, H. Li, S. Yang, Z. Du, S. H. Joo, J. Lee, Y. Zhu, G. Logvenov, B. Keimer, F. Kazuhiro, T. Valla, I. Božović, and I. K. Drozdov, "Homogeneous superconducting gap in $DyBa_2Cu_3O_{7-\delta}$ synthesized by oxide molecular beam epitaxy," *Physical Review Materials*, vol. 4, no. 12, p. 124801, 2020.

[298] S. Teitel and C. Jayaprakash, "Phase transtions in frustrated two-dimensional XY models," *Physical Review B*, vol. 27, no. 1, p. 598, 1983.

[299] R. F. Voss and R. A. Webb, "Phase coherence in a weakly coupled array of 20 000 Nb Josephson junctions," *Physical Review B*, vol. 25, no. 5, p. 3446, 1982.

[300] M. M. Doria, E. H. Brandt, and F. Peeters, "Magnetization of a superconducting film in a perpendicular magnetic field," *Physical Review B*, vol. 78, no. 5, p. 054407, 2008.

[301] L. Benfatto, C. Castellani, and T. Giamarchi, "Sine-Gordon Description of Beresinskii-Kosterlitz-Thouless Vortices in Superconductors Immersed in an External Magnetic Field," *Physical Review Letters*, vol. 99, no. 20, p. 207002, 2007.

[302] Y. J. Uemura, G. M. Luke, B. J. Sternlieb, J. H. Brewer, J. F. Carolan, W. N. Hardy, R. Kadono, J. R. Kempton, R. F. Kiefl, S. R. Kreitzman *et al.*, "Universal Correlations Between T_c and n_s/m^* (Carrier Density over Effective Mass)

in High-T_c Cuprate Superconductors," *Physical Review Letters*, vol. 62, no. 19, p. 2317, 1989.

[303] M. Varela, Z. Sefrioui, D. Arias, M. A. Navacerrada, M. Lucía, M. A. López de la Torre, C. León, G. D. Loos, F. Sánchez-Quesada, and J. Santamaría, "Intracell Changes in Epitaxially Strained $YBa_2Cu_3O_{7-x}$ Ultrathin Layers in $YBa_2Cu_3O_{7-x}/PrBa_2Cu_3O_7$ Superlattices," *Physical Review Letters*, vol. 83, pp. 3936–3939, 1999.

[304] D. N. Basov, R. Liang, D. A. Bonn, W. N. Hardy, B. Dabrowski, M. Quijada, D. B. Tanner, J. P. Rice, D. M. Ginsberg, and T. Timusk, "In-Plane Anisotropy of the Penetration Depth in $YBa_2Cu_3O_{7-x}$ and $YBa_2Cu_4O_8$ Superconductors," *Physical Review Letters*, vol. 74, no. 4, p. 598, 1995.

[305] R. F. Kiefl, M. D. Hossain, B. M. Wojek, S. R. Dunsiger, G. D. Morris, T. Prokscha, Z. Salman, J. Baglo, D. A. Bonn, R. Liang, W. N. Hardy, A. Suter, and E. Morenzoni, "Direct measurement of the London penetration depth in $YBa_2Cu_3O_{6.92}$ using low-energy μSR," *Physical Review B*, vol. 81, no. 18, p. 180502, 2010.

[306] C. Yang, Y. Liu, Y. Wang, L. Feng, Q. He, J. Sun, Y. Tang, C. Wu, J. Xiong, W. Zhang, X. Lin, H. Yao, H. Liu, G. Fernandes, J. Xu, J. M. Valles, J. Wang, and Y. Li, "Intermediate bosonic metallic state in the superconductor-insulator transition," *Science*, vol. 366, no. 6472, pp. 1505–1509, 2019.

[307] P. R. Smith, D. H. Auston, and M. C. Nuss, "Subpicosecond Photoconducting Dipole Antennas," *IEEE Journal of Quantum Electronics*, vol. 24, no. 2, pp. 255–260, 1988.

[308] Y. H. Lee, A. Chavez-Pirson, S. W. Koch, H. M. Gibbs, S. H. Park, J. Morhange, A. Jeffery, N. Peyghambarian, L. Banyai, A. C. Gossard, and W. Wiegmann, "Room-Temperature Optical Nonlinearities in GaAs," *Physical Review Letters*, vol. 57, no. 19, pp. 2446–2449, 1986.

[309] S. E. Ralph and D. Grischkowsky, "Terahertz spectroscopy and source characterization by optoelectronic interferometry," *Applied Physics Letters*, vol. 60, no. 9, pp. 1070–1072, 1992.

[310] X.-C. Zhang and D. H. Auston, "Optoelectronic measurement of semiconductor surfaces and interfaces with femtosecond optics," *Journal of Applied Physics*, vol. 71, no. 1, pp. 326–338, 1992.

[311] P. U. Jepsen, R. H. Jacobsen, and S. R. Keiding, "Generation and detection of terahertz pulses from biased semiconductor antennas," *Journal of the Optical Society of America B*, vol. 13, no. 11, pp. 2424–2436, 1996.

[312] N. M. Burford and M. O. El-Shenawee, "Review of terahertz photoconductive antenna technology," *Optical Engineering*, vol. 56, no. 1, p. 010901, 2017.

[313] M. Tani, S. Matsuura, K. Sakai, and S.-i. Nakashima, "Emission characteristics of photoconductive antennas based on low-temperature-grown GaAs and semi-insulating GaAs," *Applied Optics*, vol. 36, no. 30, pp. 7853–7859, 1997.

[314] D. H. Auston, K. P. Cheung, and P. R. Smith, "Picosecond photoconducting Hertzian dipoles," *Applied Physics Letters*, vol. 45, no. 3, pp. 284–286, 1984.

[315] M. Ashida, "Ultra-Broadband Terahertz Wave Detection Using Photoconductive Antenna," *Japanese Journal of Applied Physics*, vol. 47, no. 10, pp. 8221–8225, 2008.

[316] S. Kono, M. Tani, P. Gu, and K. Sakai, "Detection of up to 20 THz with a low-temperature-grown GaAs photoconductive antenna gated with 15 fs light pulses," *Applied Physics Letters*, vol. 77, no. 25, pp. 4104–4106, 2000.

[317] S. Kono, M. Tani, and K. Sakai, "Coherent detection of mid-infrared radiation up to 60 THz with an LT-GaAs photoconductive antenna," *IEE Proceedings - Optoelectronics*, vol. 149, no. 3, pp. 105–109, 2002.

[318] Y. C. Shen, P. C. Upadhya, H. E. Beere, E. H. Linfield, A. G. Davies, I. S. Gregory, C. Baker, W. R. Tribe, and M. J. Evans, "Generation and detection of ultrabroadband terahertz radiation using photoconductive emitters and receivers," *Applied Physics Letters*, vol. 85, no. 2, pp. 164–166, 2004.

[319] C. Fattinger and D. Grischkowsky, "Terahertz beams," *Applied Physics Letters*, vol. 54, no. 6, pp. 490–492, 1989.

[320] P. U. Jepsen and S. R. Keiding, "Radiation patterns from lens-coupled terahertz antennas," *Optics Letters*, vol. 20, no. 8, pp. 807–809, 1995.

[321] J. Van Rudd and D. M. Mittleman, "Influence of substrate-lens design in terahertz time-domain spectroscopy," *Journal of the Optical Society of America B*, vol. 19, no. 2, pp. 319–329, 2002.

[322] G. Gallot and D. Grischkowsky, "Electro-optic detection of terahertz radiation," *Journal of the Optical Society of America B*, vol. 16, no. 8, pp. 1204–1212, 1999.

[323] L. Xu, X.-C. Zhang, and D. H. Auston, "Terahertz beam generation by femtosecond optical pulses in electrooptic materials," *Applied Physics Letters*, vol. 61, no. 15, pp. 1784–1786, 1992.

[324] A. Rice, Y. Jin, X. F. Ma, X.-C. Zhang, D. Bliss, J. Larkin, and M. Alexander, "Terahertz optical rectification from ⟨110⟩ zinc-blende crystals," *Applied Physics Letters*, vol. 64, no. 11, pp. 1324–1326, 1994.

[325] Q. Wu and X.-C. Zhang, "Freespace electrooptic sampling of terahertz beams," *Applied Physics Letters*, vol. 67, no. 24, pp. 3523–3525, 1995.

[326] Q. Wu, T. D. Hewitt, and X.-C. Zhang, "Two-dimensional electro-optic imaging of THz beams," *Applied Physics Letters*, vol. 69, no. 8, pp. 1026–1028, 1996.

[327] Q. Wu and X.-C. Zhang, "7 terahertz broadband GaP electro-optic sensor," *Applied Physics Letters*, vol. 70, no. 14, pp. 1784–1786, 1997.

[328] A. S. Barker, Jr., "Dielectric Dispersion and Phonon Line Shape in Gallium Phosphide," *Physical Review*, vol. 165, no. 3, pp. 917–922, 1968.

[329] R. W. Boyd, *Nonlinear Optics*, 3rd ed. Academic Press, Inc., 2008.

[330] D. F. Parsons and P. D. Coleman, "Far Infrared Optical Constants of Gallium Phosphide," *Applied Optics*, vol. 10, no. 7, pp. 1683–1685, 1971.

[331] D. E. Aspnes and A. A. Studna, "Dielectric functions and optical parameters of Si, Ge, GaP, GaAs, GaSb, InP, InAs, and InSb from 1.5 to 6.0 eV," *Physical Review B*, vol. 27, no. 2, pp. 985–1009, 1983.

[332] A. Nahata, A. S. Weling, and T. F. Heinz, "A wideband coherent terahertz spectroscopy system using optical rectification and electro-optic sampling," *Applied Physics Letters*, vol. 69, no. 16, pp. 2321–2323, 1996.

[333] J.-C. Diels and W. Rudolph, *Ultrashort Laser Pulse Phenomena*, 2nd ed. Academic Press, 2006.

[334] P. J. Wrzesinski, D. Pestov, V. V. Lozovoy, J. R. Gord, M. Dantus, and S. Roy, "Group-velocity-dispersion measurements of atmospheric and combustion-related gases using an ultrabroadband-laser source," *Optics Express*, vol. 19, no. 6, pp. 5163–5170, 2011.

[335] R. Trebino, *Frequency-Resolved Optical Gating: The Measurement of Ultrashort Laser Pulses*. Boston, MA: Springer, 2002.

[336] N. J. Laurita, B. Cheng, R. Barkhouser, V. A. Neumann, and N. P. Armitage, "A Modified $8f$ Geometry with Reduced Optical Aberrations for Improved Time Domain Terahertz Spectroscopy," *Journal of Infrared, Millimeter, and Terahertz Waves*, vol. 37, no. 9, pp. 894–902, 2016.

[337] M. van Exter, C. Fattinger, and G. D, "Terahertz time-domain spectroscopy of water vapor," *Optics Letters*, vol. 14, no. 20, pp. 1128–1130, 1989.

[338] H.-B. Liu, H. Zhong, N. Karpowicz, Y. Chen, and X.-C. Zhang, "Terahertz Spectroscopy and Imaging for Defense and Security Applications," *Proceedings of the IEEE*, vol. 95, no. 8, pp. 1514–1527, 2007.

Acknowledgements

Completing a PhD thesis is no easy task and it is not something that is accomplished alone. During the last few years I have been graciously afforded many opportunities to grow both professionally and personally in ways that I could never have imagined before. These experiences have certainly become core to my identity as a scientist. As this chapter of my life draws to a close and I begin the exciting prospect of taking the next step forward in my career, I would like to take a moment to thank the people who have helped to make this thesis possible.

First and foremost, I thank Prof. Bernhard Keimer for inviting me to perform my doctoral work in his department at the Max Planck Institute for Solid State Research. He has certainly done a lot to foster a collegial, creative, and productive scientific environment and I greatly appreciate his guidance, insight, and encouragement during my time in Stuttgart. I have been inspired by his commitment to practicing science at the highest level and from his example I have learned many key lessons on how to be the best scientist that I can be. Furthermore, Prof. Keimer's support and funding has made it possible for me to access numerous state-of-the-art experimental facilities available nowhere else in the world as well as to participate in various international collaborations and conferences during the course of my studies.

Second, I thank my day-to-day supervisor, Alexander (Sasha) Boris, for his patient support during these years. Sasha has been a wonderful teacher, mentor, and travel partner—both on beamtimes and to conferences. I greatly appreciate his support especially during the challenging times following journal article submission and when equipment would not cooperate. He is also an absolutely top-notch scientist and it has been a pleasure having the opportunity to learn from him.

Next, I give thanks to members of the Institute with whom I've had the pleasure of collaborating. In particular, I thank Timofei Larkin for fruitful scientific discussions, advice, friendship, and his hospitality during my conference travels in Russia. Many thanks to Gideok Kim for engaging conversations, which constitute some of the highlights of my time in Stuttgart. I greatly appreciate the assistance with sample preparation and ellipsometry measurements that I have received from Gennady Logvenov, Georg Christiani, Daniel Putzky, Ksenia Rabinovich, and Xiaotong Shi. I also gratefully acknowledge Stefan Kaiser, Hao Chu, and Min-Jae Kim for introducing me to the world of non-equilibrium and pump-probe terahertz spectroscopy, inviting me to participate in their exciting Higgs mode experiments on the cuprates, and serving as harmonious travel mates during our trips to the beamline in Dresden.

I must extend my gratitute to Heiko Uhlig and, especially, Benjamin Bruha for their technical assistance, laboratory expertise, and cheerful conversation. There were many instances when my experiments would never have gotten running without their help, and these two were always willing to go above and beyond the call of duty to

get things on track.

A hallmark of a truly great scientific environment is exposure to a group of colleagues who provide encouragement, insightful discussions, and continually push each other to grow and be better scientists. In this regard I am deeply grateful to the current and former members of the Department of Solid State Spectroscopy for their role in cultivating a high quality environment in which to learn and do research. In particular, I thank Daniel Pröpper, Matthias Hepting, Eva Benckiser, Matteo Minola, Katrin Fürsich, Giniyat Khaliullin, Huimei Liu, Lichen Wang, Martin Bluschke, Joel Bertinshaw, Matthieu Le Tacon, Chris Dietl, Alireza Akbari, Hun-ho Kim, Roberto Ortiz, Toshinao Loew, Juan Porras, Hakuto Suzuki, Suguru Nakata, Max Krautloher, Emilie Lefrançois, Padma Radhakrishnan, Cissy Suen, Rebecca Pons, Laura Guasco, Hlynur Gretarsson, Valentin Zimmermann, and Sonja Balkema.

I am particularly grateful to Matthias Hepting, Katrin Fürsich, and Valentin Zimmermann for helping me with the German language version of the abstract.

There are also a number of people within the Institute but external to the Department of Solid State Spectroscopy who have helped to make my time in Stuttgart both possible and enjoyable. Many thanks to Dirk Manske, Peter Specht, Birgit King, Frank Gottschalk, Michael Eppard, Florian Pasler, Dominik Böttcher, and Günter Majer.

I have had the wonderful opportunity to perform experiments at numerous external facilities and learn from skilled members of the international scientific community during my journey as a student. I express my appreciation to Yves-Laurent Mathis of the Karlsruhe Research Accelerator; Sergey Kovalev, Zhe Wang, and Michael Gensch of the TELBE beamline at Helmholtz Zentrum Dresden-Rossendorf; Ryo Shimano of the University of Tokyo; Steven Kivelson of Stanford; Dmitri Basov of Columbia University; Steve Dodge and Nicholas Lee-Hone of Simon Fraser University; Rolando Valdés Aguilar, Mohit Randeria, Ezekiel Johnston-Halperin, Chris Hammel, and Ciriyam Jayaprakash of Ohio State University; Martin Dressel and Lapo Bogani of the University of Stuttgart; and Yi Gu, Fred Gittes, Michael Allen, and Peter Engels of Washington State University.

I thank my parents and my sister for their support, encouragement, and sharing in my triumphs and tribulations from five thousand miles away and across an ocean. This achievement without a doubt would not have been possible without their help during the past many years.

Last but certainly not least, I thank my wife, Rebecca, whose love and support during this thesis writing process helped me to finally cross the finish line.

List of Publications and Conference Contributions

Publications

5. R. D. Dawson, K. S. Rabinovich, D. Putzky, G. Christiani, G. Logvenov, B. Keimer, and A. V. Boris. "Approaching Two-Dimensional Superconductivity in Ultrathin $DyBa_2Cu_3O_{7-\delta}$." *Physical Review Letters* **125**, 237001 (2020).

4. H. Chu, M.-J. Kim, K. Katsumi, S. Kovalev, R. D. Dawson, L. Schwarz, N. Yoshikawa, G. Kim, D. Putzky, Z. Z. Li, H. Raffy, S. Germanskiy, J.-C. Deinert, N. Awari, I. Ilyakov, B. Green, M. Chen, M. Bawatna, G. Cristiani, G. Logvenov, Y. Gallais, A. V. Boris, B. Keimer, A. Schnyder, D. Manske, M. Gensch, Z. Wang, R. Shimano, and S. Kaiser. "Phase-resolved Higgs response in superconducting cuprates." *Nature Communications* **11**, 1793 (2020).

3. T. I. Larkin, R. D. Dawson, M. Höppner, T. Takayama, M. Isobe, Y.-L. Mathis, H. Takagi, B. Keimer, and A. V. Boris. "Infrared phonon spectra of quasi-one-dimensional Ta_2NiSe_5 and Ta_2NiS_5." *Physical Review B* **98**, 125113 (2018).

2. Afsoon Soudi, Robert D. Dawson, and Yi Gu. "Quantitative Heat Dissipation Characteristics in Current-Carrying GaN Nanowires Probed by Combining Scanning Thermal Microscopy and Spatially Resolved Raman Spectroscopy." *ACS Nano* **5**, 255 (2011).

1. Afsoon Soudi, Rodolfo Lopez, Jr., Robert D. Dawson, and Yi Gu. "Anharmonic phonon coupling in vapor-liquid-solid grown ZnO nanowires." *Applied Physics Letters* **95**, 193111 (2009).

Conference Contributions & Speaking

8. **Invited** – "Thickness dependence of superfluid density scaling in $DyBa_2Cu_3O_{7-x}$ thin films," Condensed Matter Seminar, Simon Fraser University Department of Physics, Vancouver, Canada, November 6, 2019.

7. "Thickness dependence of superfluid density scaling in $DyBa_2Cu_3O_{7-x}$ thin films." March Meeting of the American Physical Society, Denver, Colorado, March 5, 2020. (Conference canceled; accepted abstract appears online)

6. "Terahertz Spectroscopy of Superconducting $DyBa_2Cu_3O_{7-x}$ Thin Films." Ringberg Symposium on Unconventional Superconductors and Spin Liquids, Ringberg Castle, Rottach-Egern, Bavaria, Germany, October 13-18, 2019.

5. "Terahertz spectroscopy of excitonic insulator candidate Ta_2NiSe_5". March Meeting of the American Physical Society, Boston, Massachusetts, March 5, 2019.

4. "Closing the terahertz gap: a composite approach toward measuring continuous dielectric functions from microwave to visible wavelengths." TERA-2018, the 3rd International Conference on Terahertz and Microwave Radiation: Generation, Detection, and Applications. Nizhniy Novgorod, Russia, October 22, 2018.

3. "Terahertz and infrared spectroscopic study of in-gap excitations in epitaxial $DyBa_2Cu_3O_7$ thin films" March Meeting of the German Physical Society (DPG), Berlin, Germany, March 12, 2018.

2. "Terahertz and infrared spectroscopy of in-gap excitations in DyBCO thin films." MPI-FKF Workshop on Strongly Correlated Electron Systems, Ringberg Castle, Rottach-Egern, Bavaria, Germany, November 9, 2017.

1. "Wide-band spectroscopic study of in-gap excitations in epitaxial $DyBa_2Cu_3O_{7-\delta}$ superconducting films." March Meeting of the American Physical Society, New Orleans, Louisiana, March 13, 2017.